Single Particle Microscopic and Spectroscopic Chemical Analysis of Primary and Secondary Aerosols

by

Amy L. Bondy

A dissertation submitted in partial fulfillment
of the requirements for the degree of
Doctor of Philosophy
(Chemistry)
in The University of Michigan
2018

Doctoral Committee:

Assistant Professor Andrew P. Ault, Chair
Professor Mark M. Banaszak Holl
Professor Emeritus Michael D. Morris
Assistant Professor Kerri A. Pratt
Professor Edward T. Zellers

Amy L. Bondy

albondy@umich.edu

ORCID iD: 0000-0002-7585-5244

DEDICATION

For my mom and in memory of my dad, who have always been my biggest fans

ACKNOWLEDGEMENTS

I first need to thank my advisor, Dr. Andrew Ault, for all of your guidance and mentorship over the past four and a half years. This new journey through graduate school for both of us—me as a student and you as an advisor—has been an exciting learning experience. You provided me with the tools, expertise, and mentorship needed to grow as a scholar and an independent researcher. Without your hard work, dedication as an advisor, and timely arrival at Michigan, none of this would have been possible.

I would also like to thank my dissertation committee, Dr. Mark Banaszak Holl, Dr. Michael Morris, Dr. Kerri Pratt, and Dr. Edward Zellers for your helpful advice and support over the years. Specifically, I would like to thank Dr. Kerri Pratt and Dr. Mark Banaszak Holl, who as collaborators on research projects, have provided extensive guidance and feedback on much of my work.

I would like to thank the supportive group of Ault-Pratt lab members, past and present, for all your research-related help, as well as sharing in my joys and commiserating in my troubles throughout graduate school. Specifically, I would like to acknowledge Becky Craig, who has been my fellow Ault-lab member since our closet-lab days, as well as a roommate and great friend. Additionally, I would like to thank Dr. Jessica Axson, who joined our small group shortly thereafter, providing a voice of knowledge from the "other side" of graduate school, and plentiful knowledge about pets. I would like to thank Dr. William Collin for your mentorship and friendship, particularly in the beginning years of graduate school when I didn't know anything. I would like to thank Dr. Matthew Gunsch for your companionship traversing graduate school together, from Space Cadet pinball, to giving me pointers about dissertation writing. I would also like to thank Sydney Niles, who not only provided significant help with a challenging research project, but who became a good friend during grad school. More recently, Nicole Olson and Nancy Lei have taught me that I am ready for the next phase of my career, as their questions have helped me realize how much I've learned over the years. Thank you for the mental relief

these past few months with discussions of cats, and Nancy for accompanying me to weekly cardio hip-hop stress relief sessions. In addition to these individuals, I would like to thank Rachel Kirpes, Dr. Peter Peterson, Steven McNamera, Ryan Cook, Nate May, Hongru Shen, Isabel Colon-Bernal, and Dr. Luke Peterson for your help and friendship over the years.

Along with my research-related friendships, I also would like to thank my best friends Dr. Gabrielle McGuire and Meghan Patterson for your friendship throughout all my schooling, and putting up with my nerdiness. Thank you to my BFF Byung Joo Lee, who was only every a phone call away. I would also like to thank all my softball-related friends for keeping me sane and helping me live a balanced work-play life. I want to give a shout out to all the wonderful women involved with FEMMES at U of M, who share my enthusiasm for cool science experiments. Importantly, I would also like to thank my undergraduate advisor, Dr. Krisanu Bandyopadhyay, who introduced me to research and first told me about graduate school possibilities with chemistry.

Last, but most important, I need to thank my family for all of their love, support, understanding, and encouragement throughout my entire academic career. Look guys, I'm finally going finish my career as a professional student, and get a "real job!" My parents have been incredibly proud and supportive of me the entire time, from inviting me over for dinner and not letting me leave without leftovers, little gifts from my mom "just because," and helping with my annual move knowing that my new home would be short-lived. My dad especially, was extremely proud of me, which provided necessary motivation through this tough final year of school. My sisters, Danielle, Jessica, and Sarah provided a listening ear and much needed mental distractions with family fun, and my niece Casey inspired me during our awesome sleepover parties to continue loving science. Finally, my boyfriend Dave has been there for me through thick and thin, travelling the world at my side and bringing me all the Chinese, Arby's and pizza I could want. Thank you for your love and support, I couldn't imagine moving forward with my career without you.

TABLE OF CONTENTS

LIST OF FIGURES

LIST OF TABLES

LIST OF EQUATIONS

LIST OF APPENDICES

ABSTRACT

Atmospheric aerosols have significant impacts on climate and human health. Particle physicochemical properties including chemical composition, distribution of chemical species (i.e. mixing state), morphology, and phase have been tied to their climate and health-related effects, yet our understanding of these properties is still limited. In this dissertation, aerosol particles from the southeastern U.S. were collected and studied using single particle microscopy and spectroscopy methods. In addition, new methods were developed to improve our understanding of their chemical composition and to better predict climate-relevant properties.

The Southern Oxidant and Aerosol Study (SOAS), completed in the summer of 2013, was held at a rural, forested location in Alabama impacted by regional pollution. Particles collected during SOAS were analyzed using scanning electron microscopy with energy dispersive X-ray spectroscopy (SEM-EDX), Raman microspectroscopy, and scanning transmission X-ray microscopy with near edge X-ray absorption fine structure (STXM-NEXAFS) to identify particle sources and degree of chemical aging during transport. Although mixed organic carbon with ammonium sulfate particles dominated number concentrations during SOAS, time periods with high concentrations of mineral dust and sea spray aerosol (SSA) were identified. Chemical mixing state calculations for submicron and micron-sized particles quantified the degree of internal mixing during three distinct time periods, showing that the degree of aerosol aging varied throughout SOAS. Additionally, during two SSA-rich events, SSA was frequently aged by reactions with nitric acid and sulfuric acid leading to chloride depletion within particles, though 24 % of SSA still contained chloride. The frequent observation of SSA at this inland site and the range of chloride depletion observed suggest that SSA may represent an underappreciated inland sink for NO_x/SO_2 oxidation products and source of halogen gases that can act as oxidants.

To more thoroughly characterize organic aerosol from SOAS, a Raman fingerprint was identified for organosulfates derived from isoprene oxidation products, a significant component

of secondary organic aerosol (SOA) in the southeastern U.S. In this analysis, the vibrational modes of key organosulfates were identified using Raman microspectroscopy and density functional theory (DFT), allowing organosulfates to be distinguished from inorganic sulfate within complex ambient SOA. Complementary to Raman microspectroscopy which provides molecular information for particles > 1 μm, atomic force microscopy-infrared spectroscopy (AFM-IR) was applied to aerosol particles for the first time to detect trace organic and inorganic species and probe chemical variation within individual particles down to 150 nm in diameter. With its high spatial resolution, AFM-IR has the potential to advance our understanding of aerosol impacts on climate and health for particles < 500 nm in diameter by improving analytical capabilities to study water uptake, heterogeneous reactivity, and viscosity. Finally, organic-sulfate SOA particles collected during SOAS were observed to have liquid-liquid phase separation with a range of internal morphologies, including core-shell and more complex internal morphologies. Backward air mass trajectory modelling indicated that SOA morphology was dependent on aerosol lifetime, as well as temperature and relative humidity history. Taken together, these analyses of aerosol particle sources, atmospheric aging, internal morphologies, and chemical compositions provide an increased understanding of particle chemistry, mixing state, and internal structure in the southeastern United States.

Chapter 1.
Introduction

1.1. Characteristics of Atmospheric Aerosols

Atmospheric aerosols can have global effects by scattering or absorbing solar radiation, through the modification of cloud properties, or by impacting concentrations of trace gases in the atmosphere (2005; Prather et al., 2008). From a human health perspective, high concentrations of aerosols have been linked to cardiovascular disease and mortality, with 10 % of deaths associated with air pollution globally (Kennedy, 2007; Dominici et al., 2006). Aerosols have also been shown to significantly influence climate, however there is significant error associated with quantifying the magnitude of these effects (Forster, 2007).

The size distribution of aerosols in the atmosphere ranges from 1 nm – 100 μm, with particle number concentrations peaking with diameters at 100 nm, and mass distribution diameters peaking at 500 nm and 6 μm (Seinfeld, 2006; Heal et al., 2012). Coarse particles (diameter > 2.5 μm), accounting for the majority of particle mass, are generated by mechanical processes and consist of mineral dust, sea salt, and primary biological particles such as pollen. Fine particles (diameter < 2.5 μm), accounting for the largest number concentrations of particles in the atmosphere, are generally produced from combustion sources and the low volatility products formed from gas-phase precursors (Seinfeld, 2006). While large airborne particles are generally deposited within hours to days, fine particles can remain airborne for weeks (Poschl, 2005; Prather et al., 2008). Size is a key factor determining particle health and climate impacts. For example, particles < 1 μm can penetrate deeply into the alveoli while larger particles are filtered out (Hinds, 1999). Furthermore, particles larger than 120 nm can act efficiently as cloud condensation nuclei (CCN), modifying the properties of clouds, while particles < 40 nm require unrealistically high supersaturation for activation (Dusek et al., 2006). In addition to size, chemical composition can affect particle impacts on health and climate. Work by Petters and Kreidenweis (2007), Hatch et al. (2011) and Estillore et al. (2016) suggest the presence of

hygroscopic organic compounds in aerosols, such as organosulfates, could enhance the cloud-formation ability of submicron organic aerosol.

Aerosols originate from a variety of natural (biogenic) and human-influenced (anthropogenic) sources. Primary particles such as mineral dust, soot, or sea spray aerosol are emitted directly from a source. Secondary particles such as secondary organic aerosol (SOA), are formed from the oxidation and condensation of volatile species emitted to the atmosphere as gases. One of the challenges in determining the effects of aerosols on climate and health is that particles are constantly changing after emission. Throughout their lifetime, aerosols can undergo heterogeneous reactions or coagulation, modifying their size, chemical composition, cloud-forming ability, or optical properties. As aerosol impacts are closely tied to the properties of individual particles, understanding the chemical composition and distribution of species within populations is essential to learning the extent of aerosol influences. Currently, a comprehensive understanding of aerosol particle composition, morphology, phase and internal structures, and transformations through atmospheric aging remains insufficient to fully predict aerosol impacts on the environment. Aerosol particles can undergo numerous reactions in the atmosphere with gaseous and condensed phase species including inorganic and organic acids, and oxidized nitrogen, sulfur, and organic species (Bondy et al., 2017b; Wang et al., 2015; Ravishankara, 1997). Although atmospheric chemical and physical processes are complex, recent work has advanced considerably in the past decade (Laskin et al., 2016).

The southeastern United States is ideal for studying biogenic-anthropogenic interactions due to the high natural emissions of organic compounds and proximity of natural emissions to anthropogenic pollution sources. Recently isoprene, the most abundant non-methane volatile organic compound, has been shown to contribute significantly to SOA in the region through oxidation and formation of gas-phase products with lower volatility that partition to the particle phase (Glasius and Goldstein, 2016). Additionally, organosulfates, many which have isoprene as the precursor, have been estimated to contribute up to 10 % of the total organic aerosol mass in the southeastern United States (Tolocka and Turpin, 2012), increasing the hygroscopicity of organic aerosol. The exact contribution of key species such as isoprene-derived organosulfates, as well as their formation pathways are currently an active area of research, as there are large uncertainties related to chemistry in the region. In order to evaluate aerosol impacts, a deeper understanding of aerosol chemical composition is needed

1.2. Particle Chemical Mixing State

The distribution of chemical species within an aerosol population is referred to as its chemical mixing state, which can be described in terms of external and internal mixtures (Figure 1.1). An external mixture consists of particles that contain only one pure species per particle, while an internal mixture describes a population where each particle contains equal amounts of each species (Riemer and West, 2013; Posfai and Buseck, 2010). Multiple researchers examining particle chemical mixing state have observed externally and internally mixed particles, primarily at urban locations, with more internally mixed particles formed during stagnated air masses, during serious pollution events, as particles were transported away from their sources, and at higher altitudes (Moffet et al., 2010b; Fu et al., 2012; Pratt and Prather, 2010). However, ambient aerosols cannot typically be categorized into either external or internal mixtures, but rather have complex mixing states that can vary as a function of particle size, altitude, and age. As changes in chemical composition affect particle properties such as reactivity, hygroscopicity, toxicity, and optical properties, it is important to understand the chemical mixing state of individual particles in a population (Jacobson, 2001; Chung and Seinfeld, 2005; Zaveri et al., 2010).

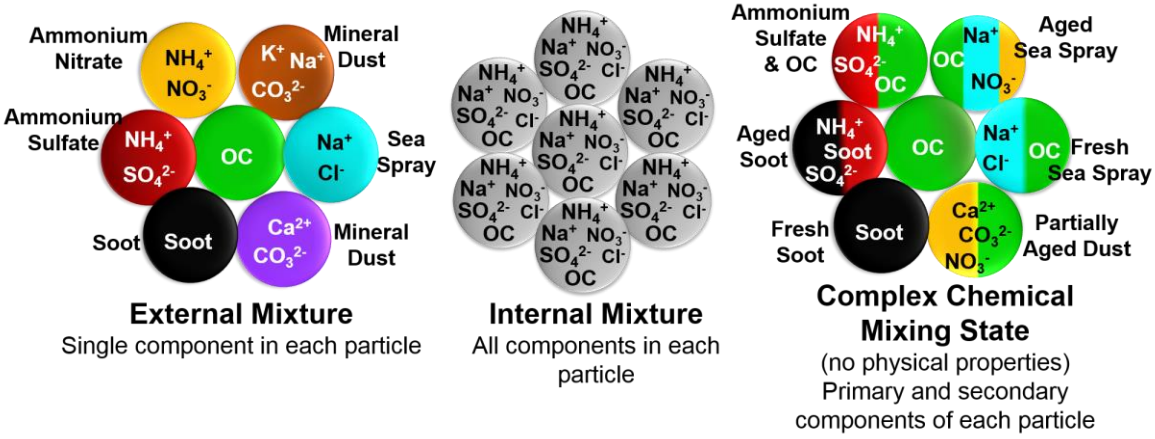

Figure 1.1. Representations of particle composition in external mixtures, internal mixtures, and a particle population with a complex mixing state. Chemical mixing state provides information on primary versus secondary components, but does not provide information concerning the distribution of chemical components within individual particles or other physical properties. Note that the locations of the colors in the chemical mixing state particles are not meant to convey spatial distribution, only the presence of both primary and secondary components. Concept derived from a figure in Ault and Axson (2017).

In 2013, Riemer and West proposed a metric to quantify aerosol population mixing state using entropy and diversity measures. This method, using single particle mass fractions of

individual chemical components to calculate average particle-specific diversity, bulk population diversity, and a mixing state index, has been applied to five aerosol studies, to date (Dickau et al., 2016; Giorio et al., 2015; Healy et al., 2014; O'Brien et al., 2015a; Fraund et al., 2017). The volatile mixing state of soot, particle composition and particle chemical mixing state from anthropogenic sources in London and Paris, and the mixing state of biogenic and anthropogenic particles during aging and transport in California and the Amazon were all quantified, resulting in populations with complex mixing states. Although there have been recent advancements to better understand and quantify the chemical mixing state of aerosols, since mixing state matters when modeling climate-relevant properties, more studies quantifying mixing state are needed to more accurately describe the chemical mixing state of complex, ambient particles.

1.3. Single Particle Microscopy and Spectroscopy Methods

Spectroscopy and microscopy have long been used to probe individual aerosol particles (Fletcher et al., 2011). Particularly within the past 15-20 years, the use of microscopy methods has dramatically increased due to instrument improvements and an increasing desire to analyze the chemical mixing state of particles (Ault and Axson, 2017). Individually, single particle microscopy allows particle size and morphology to be studied, useful measures when identifying sources and particle evolution during transport. Single particle spectroscopy yields detailed chemical information concerning functional groups or elemental composition of particles, depending on the type of transition being probed (vibrational or electronic). As single particle microscopic and spectroscopic methods provide complementary information, often tandem analysis methods or multiple techniques are used to more thoroughly characterize particle populations (Ault and Axson, 2017; Bondy et al., 2017b; Bondy et al., 2017a; Craig et al., 2017a; Creamean et al., 2016; Ault et al., 2012; Ault et al., 2013; Sobanska et al., 2014; Sobanska et al., 2012). The microscopy and spectroscopy methods used in this work are described in the following sections.

1.3.1. Scanning Electron Microscopy with Energy Dispersive X-ray Spectroscopy (SEM-EDX)

Scanning electron microscopy with energy dispersive X-ray spectroscopy (SEM-EDX) has been extensively used in the past to characterize the size, morphology, phase, and elemental

composition of individual particles collected from field campaigns and laboratory studies (Ault and Axson, 2017; Fletcher et al., 2011; Bondy et al., 2017b; Ghorai et al., 2014; Hopkins et al., 2008; Laskin et al., 2006a; Laskin et al., 2016; Laskin et al., 2002, 2003; Laskin et al., 2005; Laskin et al., 2012; O'Brien et al., 2014; O'Brien et al., 2015a; O'Brien et al., 2015b; Wang et al., 2016; Wang and Laskin, 2014; Wang et al., 2015; Sobanska et al., 2003; Sobanska et al., 2014; Axson et al., 2016b; Creamean et al., 2016; Shen et al., 2016; Axson et al., 2016a; Kim et al., 1987; Andreae et al., 1986). SEM is an analytical technique that has been primarily used to study atmospheric aerosol particles down to 50 nm. SEM uses an electron beam with an accelerating voltage between 5 and 25 kV to image particles collected on a substrate. Depending on the particle composition and substrate, different electron-sample interactions can be used for imaging. Backscattered electrons and secondary electrons provide Z-dependent contrast or detailed morphology, respectively, useful for aerosols containing heavy metals or detailed surface features. Scanning transmission electron microscopy (STEM), used with a high angle annular dark field detector (HAADF), has been used increasingly as the STEM image is also Z-dependent, thickness dependent, and its use improves detection of submicron particles. To chemically characterize aerosol particles, SEM is typically coupled with EDX. EDX measures the elemental composition of particles via the detection of energy-specific X-rays which correspond to particular elements. Elemental mapping with EDX (Figure 1.2) can yield chemical mixing state information, as heterogeneity of elements within individual particles can be probed with sub-100 nm resolution (Conny and Norris, 2011).

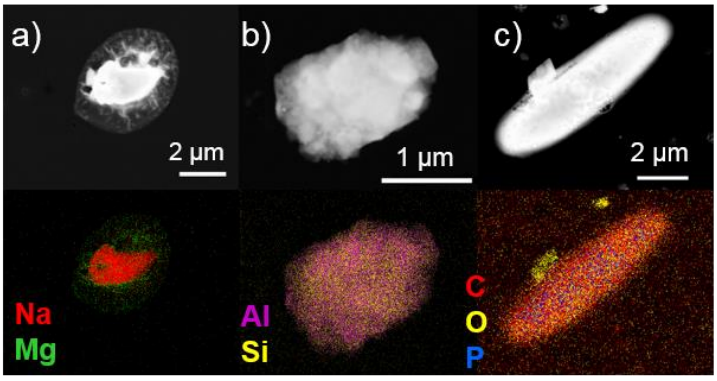

Figure 1.2. Electron images and elemental maps of a a) sea spray aerosol particle, b) mineral dust particle, and c) primary biological particle collected in the southeastern U.S during the SOAS field campaign.

Computer controlled SEM (CCSEM), an automated analysis method, has been developed to improve the throughput of this technique (Laskin et al., 2006a). CCSEM, which automatically detects individual particles based on a light-to-dark threshold followed by EDX spectral acquisition, has been used in a number of diverse applications ranging from detection of sea spray aerosol in coastal and inland locations (Bondy et al., 2017b; Laskin et al., 2012; Laskin et al., 2006b), to analysis of transported mineral dust (Axson et al., 2016b), to detection of lead-containing aerosols from illegal battery recycling operations in an urban center (Shen et al., 2016). To analyze large CCSEM data sets, clustering algorithms such as k-means have been used in several studies (Axson et al., 2016b; Shen et al., 2016; Allen et al., 2015; Bondy et al., 2017b; Ault et al., 2012; Axson et al., 2016a; Craig et al., 2017a). K-means clustering groups particles with similar elemental composition (from EDX spectra) unique to sources, thus particles can be grouped into source-based classes such as sea spray aerosol, mineral dust, and organic aerosol. Furthermore, particle classes such as fresh sea spray aerosol and aged sea spray aerosol can be distinguished, providing information concerning particle evolution (Bondy et al., 2017b; Laskin et al., 2002).

1.3.2. Scanning Transmission X-ray Microscopy with Near Edge X-ray Absorption Fine Structure Spectroscopy (STXM-NEXAFS)

Scanning transmission X-ray microscopy with near edge X-ray absorption fine structure (STXM-NEXAFS) has been used to probe different atmospheric or lab-generated particles (Laskin et al., 2016) including sulfur-containing SSA (Hopkins et al., 2008), soil-derived organic aerosol (Wang et al., 2016), and carbonaceous particles transported from cities (Moffet et al., 2010b; Moffet et al., 2013; O'Brien et al., 2015a). While SEM uses electrons to generate images, STXM microscopy is a synchrotron technique that utilizes “soft” X-ray radiation in the range of ~100-1000 eV. NEXAFS spectra with spatial resolution of 25 nm can probe bonding within particles by focusing on the carbon K-edge, the oxygen K-edge, the nitrogen K-edge, or the L-edges of sulfur and chlorine (Kilcoyne et al., 2003). STXM-NEXAFS is a complementary technique to SEM-EDX because it provides detailed information concerning chemical bonds within particles. Using STXM-NEXAFS, spectra and chemical maps can be collected identifying features such as sp^2-bonded carbon (i.e. soot), COOH groups, potassium in biological particles, and the oxidation states of sulfur in marine aerosol (Hopkins et al., 2008; Moffet et al., 2010b;

Moffet et al., 2010a; Moffet et al., 2013; Pöhlker et al., 2012). Additionally, as NEXAFS is a purely photon-based technique, Beer-Lambert's Law can be used to determine the optical density, or intensity, of peaks in the NEXAFS spectra. Using the ratio of the pre-edge absorption to the post-edge absorption, the ratio of inorganic to organic material can be determined for each pixel, allowing differentiation of inorganic and organic phase-separated regions within particles (Figure 1.3). In this work, STXM-NEXAFS was primarily used to map organic versus inorganic components and identify soot (sp^2 carbon) inclusions within organic aerosol particles.

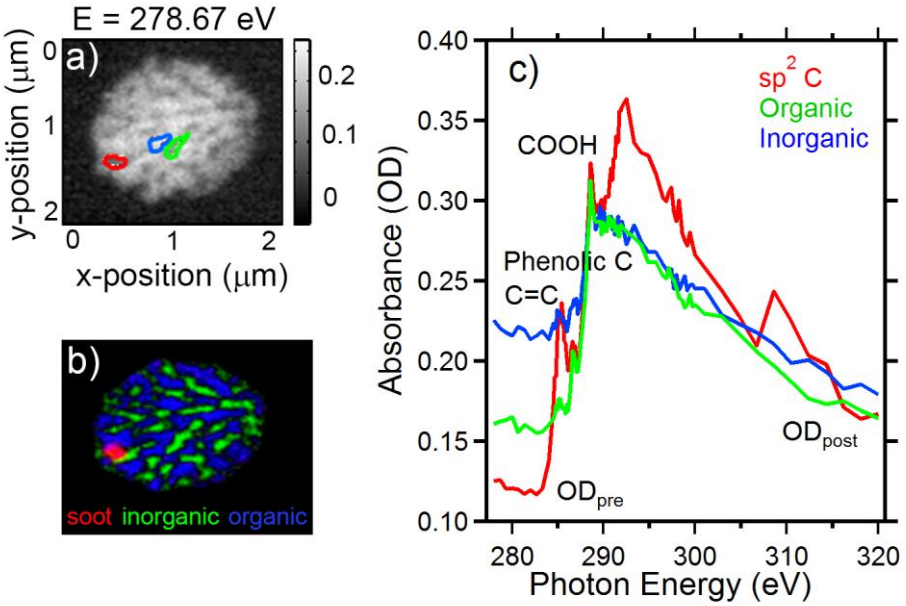

Figure 1.3. a) STXM-NEXAFS images and spectra of an organic-inorganic particle from SOAS. Singular value decomposition maps combining sp^2 carbon (red), organic (green), and inorganic (blue) are depicted in b). The NEXAFS spectra at the carbon K-edge is shown in c).

1.3.3. Raman Microspectroscopy

In the past decade, Raman microspectroscopy of aerosol particles has expanded greatly due to instrument improvements (Ault and Axson, 2017). Raman spectroscopy probes molecular vibrations rather than electronic transitions, yielding information primarily for covalently bonded species. Vibrational methods, such as Raman microspectroscopy, have great potential to provide insight into chemical processes within aerosols (Ault and Axson, 2017), as Raman has been used in recent studies to provide detail on functional groups including $\nu(SO_4^{2-})$, $\nu(NO_3^-)$, ν(C-H), and

ν(O-H) (Craig et al., 2015, 2017a; Ault et al., 2013; Laskina et al., 2013; Deng et al., 2014; Sobanska et al., 2014; Sobanska et al., 2012). Raman microspectroscopy has the potential to probe the chemical species present within individual particles, it can differentiate between bound and free ions (i.e. $NaNO_3$ vs. NO_3^-) (Ault et al., 2014), and recent work by Craig and Rindelaub used Raman microspectroscopy to determine the pH of individual particles (Figure 1.4) (Craig et al., 2017b; Rindelaub et al., 2016). Raman microspectroscopy is useful for aerosol studies because unlike SEM-EDX and STXM-NEXAFS, this technique is performed at ambient pressure. This allows liquid-liquid phase separations to be readily analyzed (Ciobanu et al., 2009), and coupled with relative humidity-controlled cells, the hygroscopic growth of particles can be studied (Estillore et al., 2016; Laskina et al., 2015; Rindelaub et al., 2016). Furthermore, Raman spectroscopy can distinguish species that are challenging for EDX, such as inorganic sulfate and organic sulfate. However one challenge with Raman microspectroscopy is analysis is typically limited to particles > 1 μm due to the diffraction limit of visible light. To probe smaller particles, methods such as surface-enhanced Raman spectroscopy (SERS) (Craig et al., 2015) and tip-enhanced Raman spectroscopy (TERS) (Ofner et al., 2016) have been used to increase Raman signal by coating a substrate surface or tip, respectively, with metal, however uneven signal enhancements require further development. Due to the unique advantages offered by Raman spectroscopy, in this work Raman microspectroscopy was used as a complementary analysis method to other methods such as SEM-EDX and infrared spectroscopy (IR).

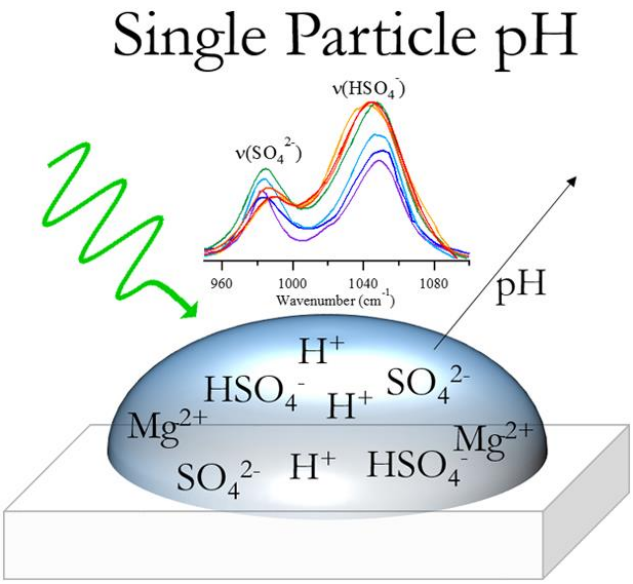

Figure 1.4. Raman microspectroscopy has been used to probe functional groups within individual aerosol particles, yielding information such as the pH of a single particle. Reprinted with permission from Rindelaub, J. D.; Craig, R. L.; Nandy, L.; Bondy, A. L.; Dutcher, C. S.; Shepson, P. B.; Ault, A. P., Direct measurement of pH in individual particles via Raman microspectroscopy and variation in acidity with relative humidity. *J. Phys. Chem. A* **2016,** *120* (6), 911-917. Copyright (2016) American Chemical Society.

1.3.4 Atomic Force Microscopy Infrared Spectroscopy (AFM-IR)

Atomic force microscopy infrared spectroscopy (AFM-IR) has the potential to overcome size limitations of traditional vibrational spectroscopy methods, such as Raman microspectroscopy. The AFM-IR technique is based on the photothermal expansion of a sample detected by an AFM probe, allowing for IR detection with spatial resolution ~50 nm, limited only by the radius of the AFM tip (Dazzi and Policar, 2011; Dazzi and Prater, 2016; Dazzi et al., 2012; Dazzi et al., 2007; Marcott et al., 2012). AFM-IR, a recently developed method, was applied to the analysis of aerosol particles for the first time in this work (Figure 1.5) (Bondy et al., 2017a). Previously, this method has been applied to the analysis of polymer blends and composites (Dazzi et al., 2012), imaging and spectroscopic analysis of single cells (Baldassarre et al., 2016), analysis of tissue (Marcott et al., 2013), and other diverse areas including investigation of metal organic frameworks (Katzenmeyer et al., 2014), perovskite solar cells (Dong et al., 2015), and cultural heritage materials (Dazzi and Prater, 2016; Latour et al., 2016).

This method combines simultaneous single particle imaging with AFM, yielding information on phase, morphology (Krueger et al., 2005), hygroscopicity (Morris, 2016; Hritz et al., 2016), and surface tension (Morris et al., 2015), with chemical functional group information obtained by IR absorption. The subdiffraction limit capability of AFM-IR has the potential to advance understanding of particle impacts on climate and health by improving our ability to study heterogeneous reactivity and chemical mixing state of submicron aerosol particles near the peak of the number size distribution in the atmosphere.

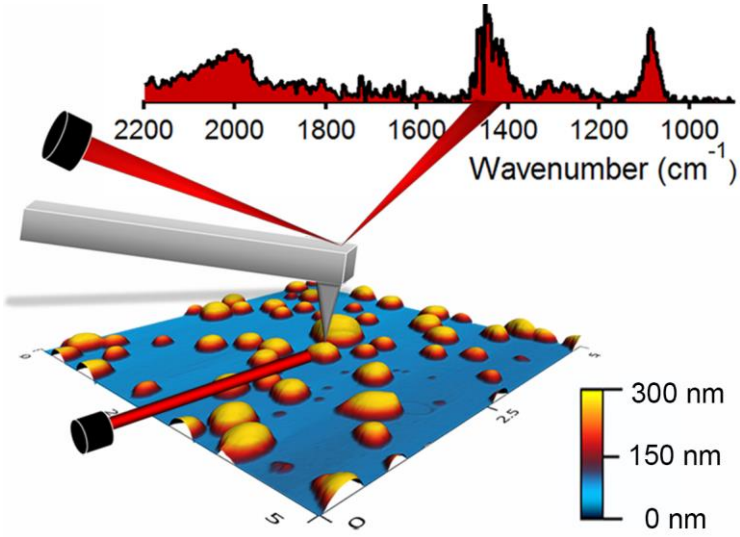

Figure 1.5. AFM-IR combines single particle imaging with vibrational chemical information, yielding size, morphology, and chemical composition for submicron particles. Originally published in Bondy et al. (2017a).

1.4. Research Objectives and Scope of Dissertation

In this dissertation, ambient and laboratory-generated aerosol particles were studied using single particle microscopy and spectroscopy methods to improve our understanding of their chemical mixing state and better predict particle impacts on health and climate. Chapter 2 identifies particle sources and quantifies the chemical mixing state of particles collected during the Southern Oxidant and Aerosol Study (SOAS) in a forested region influenced by transported pollution. Chapter 2 was submitted to *Atmospheric Chemistry and Physics* in January, 2018. Chapter 3 probes the varying degrees of atmospheric processing experienced by one particular class of particles from SOAS, sea spray aerosol (SSA), which were transported hundreds of kilometers inland. Chapter 3 was published in *Environmental Science & Technology* in 2017.

Chapter 4 fundamentally characterizes the vibrational modes of isoprene-derived organosulfates, an important class of organic aerosol in the southeastern United States, using Raman microspectroscopy. This vibrational mode information is then used to identify organosulfates within organic aerosol from SOAS. This work was published in the *Journal of Physical Chemistry A* in 2017. Chapter 5 applies AFM-IR to the analysis of aerosol particles for the first time, detecting trace organic and inorganic species in individual particles down to 200 nm. Chapter 5 was published in *Analytical Chemistry* in 2017. Chapter 6 describes the physicochemical mixing state of SOA from SOAS, illustrating that the separation of organic and inorganic material within particles is dependent on aerosol lifetime and relative humidity history. This work is currently being prepared for submission to *Nature Geoscience*. Combined, these chapters strengthen our understanding of the chemical mixing state of single particles from a variety of sources.

1.5. References

Allen, H. M., Draper, D. C., Ayres, B. R., Ault, A. P., Bondy, A. L., Takahama, S., Modini, R. L., Baumann, K., Edgerton, E., Knote, C., Laskin, A., Wang, B., and Fry, J. L.: Influence of crustal dust and sea spray supermicron particle concentrations and acidity on inorganic NO_3^- aerosol during the 2013 Southern Oxidant and Aerosol Study, Atmos. Chem. Phys., 15, 10669-10685, 2015.

Andreae, M. O., Charlson, R. J., Bruynseels, F., Storms, H., Van Grieken, R., and Maenhaut, W.: Internal mixture of sea salt, silicates, and excess sulfate in marine aerosols, Science, 232, 1620-1623, 1986.

Ault, A. P., Peters, T. M., Sawvel, E. J., Casuccio, G. S., Willis, R. D., Norris, G. A., and Grassian, V. H.: Single-particle SEM-EDX analysis of iron-containing coarse particulate matter in an urban environment: Sources and distribution of iron within Cleveland, Ohio, Environ. Sci. Technol., 46, 4331-4339, 2012.

Ault, A. P., Zhao, D., Ebben, C. J., Tauber, M. J., Geiger, F. M., Prather, K. A., and Grassian, V. H.: Raman microspectroscopy and vibrational sum frequency generation spectroscopy as probes of the bulk and surface compositions of size-resolved sea spray aerosol particles, PCCP, 15, 6206-6214, 2013.

Ault, A. P., Guasco, T. L., Baltrusaitis, J., Ryder, O. S., Trueblood, J. V., Collins, D. B., Ruppel, M. J., Cuadra-Rodriguez, L. A., Prather, K. A., and Grassian, V. H.: Heterogeneous reactivity of nitric acid with nascent sea spray aerosol: Large differences observed between and within individual particles, J. Phys. Chem. Lett., 5, 2493-2500, 2014.

Ault, A. P., and Axson, J. L.: Atmospheric aerosol chemistry: Spectroscopic and microscopic advances, Anal. Chem., 89, 430-452, 2017.

Axson, J. L., May, N. W., Colon-Bernal, I. D., Pratt, K. A., and Ault, A. P.: Lake spray aerosol: A chemical signature from individual ambient particles, Environ. Sci. Technol., 50, 9835-9845, 2016a.

Axson, J. L., Shen, H. R., Bondy, A. L., Landry, C. C., Welz, J., Creamean, J. M., and Ault, A. P.: Transported mineral dust deposition case study at a hydrologically sensitive mountain site: Size and composition shifts in ambient aerosol and snowpack, Aerosol Air Qual. Res., 16, 555-567, 2016b.

Baldassarre, L., Giliberti, V., Rosa, A., Ortolani, M., Bonamore, A., Baiocco, P., Kjoller, K., Calvani, P., and Nucara, A.: Mapping the amide I absorption in single bacteria and mammalian cells with resonant infrared nanospectroscopy, Nanotechnology, 27, 075101, 2016.

Bondy, A. L., Kirpes, R. M., Merzel, R. L., Pratt, K. A., Banaszak Holl, M. M., and Ault, A. P.: Atomic force microscopy-infrared spectroscopy of individual atmospheric aerosol particles: Subdiffraction limit vibrational spectroscopy and morphological analysis, Anal. Chem., 89, 8594-8598, 2017a.

Bondy, A. L., Wang, B., Laskin, A., Craig, R. L., Nhliziyo, M. V., Bertman, S. B., Pratt, K. A., Shepson, P. B., and Ault, A. P.: Inland sea spray aerosol transport and incomplete chloride depletion: Varying degrees of reactive processing observed during SOAS, Environ. Sci. Technol., 51, 9533-9542, 2017b.

Chung, S. H., and Seinfeld, J. H.: Climate response of direct radiative forcing of anthropogenic black carbon, J. Geophys. Res.: Atmos., 110, 2005.

Ciobanu, V. G., Marcolli, C., Krieger, U. K., Weers, U., and Peter, T.: Liquid-liquid phase separation in mixed organic/inorganic aerosol particles, J. Phys. Chem. A, 113, 10966-10978, 2009.

Conny, J. M., and Norris, G. A.: Scanning electron microanalysis and analytical challenges of mapping elements in urban atmospheric particles, Environ. Sci. Technol., 45, 7380-7386, 2011.

Craig, R. L., Bondy, A. L., and Ault, A. P.: Surface enhanced Raman spectroscopy enables observations of previously undetectable secondary organic aerosol components at the individual particle level, Anal. Chem., 87, 7510-7514, 2015.

Craig, R. L., Bondy, A. L., and Ault, A. P.: Computer-controlled Raman microspectroscopy (CC-Raman): A method for the rapid characterization of individual atmospheric aerosol particles, Aerosol Sci. Technol., 51, 1099-1112, 2017a.

Craig, R. L., Nandy, L., Axson, J. L., Dutcher, C. S., and Ault, A. P.: Spectroscopic determination of aerosol pH from acid–base equilibria in inorganic, organic, and mixed systems, J. Phys. Chem. A, 121, 5690-5699, 2017b.

Creamean, J. M., Axson, J. L., Bondy, A. L., Craig, R. L., May, N. W., Shen, H., Weber, M. H., Pratt, K. A., and Ault, A. P.: Changes in precipitating snow chemistry with location and elevation in the California Sierra Nevada, J. Geophys. Res.: Atmos., 121, 7296-7309, 2016.

Dazzi, A., Prazeres, R., Glotin, F., and Ortega, J. M.: Analysis of nano-chemical mapping performed by an AFM-based ("AFMIR") acousto-optic technique, Ultramicroscopy, 107, 1194-1200, 2007.

Dazzi, A., and Policar, C.: Chapter 9 - AFM-IR: photothermal infrared nanospectroscopy: Application to cellular imaging A2 - Pradier, C.M, in: Biointerface Characterization by Advanced IR Spectroscopy, edited by: Chabal, Y. J., Elsevier, Amsterdam, 245-278, 2011.

Dazzi, A., Prater, C. B., Hu, Q., Chase, D. B., Rabolt, J. F., and Marcott, C.: AFM-IR: Combining atomic force microscopy and infrared spectroscopy for nanoscale chemical characterization, Appl. Spectrosc., 66, 1365-1384, 2012.

Dazzi, A., and Prater, C. B.: AFM-IR: Technology and applications in nanoscale infrared spectroscopy and chemical imaging, Chem. Rev., 10.1021/acs.chemrev.6b00448, 2016.

Deng, C., Brooks, S. D., Vidaurre, G., and Thornton, D. C. O.: Using Raman microspectroscopy to determine chemical composition and mixing state of airborne marine aerosols over the Pacific Ocean, Aerosol Sci. Technol., 48, 193-206, 2014.

Dickau, M., Olfert, J., Stettler, M. E. J., Boies, A., Momenimovahed, A., Thomson, K., Smallwood, G., and Johnson, M.: Methodology for quantifying the volatile mixing state of an aerosol, Aerosol Sci. Technol., 50, 759-772, 2016.

Dominici, F., Peng, R. D., Bell, M. L., and et al.: Fine particulate air pollution and hospital admission for cardiovascular and respiratory diseases, JAMA, 295, 1127-1134, 2006.

Dong, R., Fang, Y. J., Chae, J., Dai, J., Xiao, Z. G., Dong, Q. F., Yuan, Y. B., Centrone, A., Zeng, X. C., and Huang, J. S.: High-gain and low-driving-voltage photodetectors based on organolead triiodide perovskites, Adv. Mater., 27, 1912-+, 2015.

Dusek, U., Frank, G. P., Hildebrandt, L., Curtius, J., Schneider, J., Walter, S., Chand, D., Drewnick, F., Hings, S., Jung, D., Borrmann, S., and Andreae, M. O.: Size matters more than chemistry for cloud-nucleating ability of aerosol particles, Science, 312, 1375-1378, 2006.

Estillore, A. D., Hettiyadura, A. P. S., Qin, Z., Leckrone, E., Wombacher, B., Humphry, T., Stone, E. A., and Grassian, V. H.: Water uptake and hygroscopic growth of organosulfate aerosol, Environ. Sci. Technol., 50, 4259-4268, 2016.

Fletcher, R. A., Ritchie, N. W. M., Anderson, I. M., and Small, J. A.: Microscopy and microanalysis of individual collected particles, in: Aerosol Measurement, John Wiley & Sons, Inc., 179-232, 2011.

Forster, P. R., V., Artaxo, P. Berntsen, T. Betts, R. Fahey, D.W. Haywood, J. Lean, J. Lowe, D.C. Myhre, G. Nganga, J. Prinn, R. Raga, G. Schulz, M. Van Dorland, R.: Intergovernmental Panel on Climate Change (IPCC), Cambridge University, Cambridge, United Kingdom, 2007.

Fraund, M., Pham, D., Bonanno, D., Harder, T., Wang, B., Brito, J., de Sá, S., Carbone, S., China, S., Artaxo, P., Martin, S., Pöhlker, C., Andreae, M., Laskin, A., Gilles, M., and Moffet, R.: Elemental mixing state of aerosol particles collected in Central Amazonia during GoAmazon2014/15, Atmosphere, 8, 173, 2017.

Fu, H., Zhang, M., Li, W., Chen, J., Wang, L., Quan, X., and Wang, W.: Morphology, composition and mixing state of individual carbonaceous aerosol in urban Shanghai, Atmos. Chem. Phys., 12, 693-707, 2012.

Ghorai, S., Wang, B., Tivanski, A., and Laskin, A.: Hygroscopic properties of internally mixed particles composed of NaCl and water-soluble organic acids, Environ. Sci. Technol., 48, 2234-2241, 2014.

Giorio, C., Tapparo, A., Dall'Osto, M., Beddows, D. C. S., Esser-Gietl, J. K., Healy, R. M., and Harrison, R. M.: Local and regional components of aerosol in a heavily trafficked street canyon in central London derived from PMF and cluster analysis of single-particle ATOFMS spectra, Environ. Sci. Technol., 49, 3330-3340, 2015.

Glasius, M., and Goldstein, A. H.: Recent discoveries and future challenges in atmospheric organic chemistry, Environ. Sci. Technol., 50, 2754-2764, 2016.

Hatch, L. E., Creamean, J. M., Ault, A. P., Surratt, J. D., Chan, M. N., Seinfeld, J. H., Edgerton, E. S., Su, Y., and Prather, K. A.: Measurements of isoprene-derived organosulfates in ambient aerosols by aerosol time-of-flight mass spectrometry - part 1: Single particle atmospheric observations in Atlanta, Environ. Sci. Technol., 45, 5105-5111, 2011.

Heal, M. R., Kumar, P., and Harrison, R. M.: Particles, air quality, policy and health, Chem. Soc. Rev., 41, 6606-6630, 2012.

Healy, R. M., Riemer, N., Wenger, J. C., Murphy, M., West, M., Poulain, L., Wiedensohler, A., O'Connor, I. P., McGillicuddy, E., Sodeau, J. R., and Evans, G. J.: Single particle diversity and mixing state measurements, Atmos. Chem. Phys., 14, 6289-6299, 2014.

Hinds, W. C.: Aerosol Technology Properties, Behavior, and Measurement of Airborne Particles, 2nd ed., John Wiley & Sons, Inc., New York, 1999.

Hopkins, R. J., Desyaterik, Y., Tivanski, A. V., Zaveri, R. A., Berkowitz, C. M., Tyliszczak, T., Gilles, M. K., and Laskin, A.: Chemical speciation of sulfur in marine cloud droplets and particles: Analysis of individual particles from the marine boundary layer over the California current, J. Geophys. Res.: Atmos., 113, 2008.

Hritz, A. D., Raymond, T. M., and Dutcher, D. D.: A method for the direct measurement of surface tension of collected atmospherically relevant aerosol particles using atomic force microscopy, Atmos. Chem. Phys., 16, 9761-9769, 2016.

Jacobson, M. Z. Z.: Strong radiative heating due to the mixing state of black carbon in atmospheric aerosols, Nature (London), 409, 695-697, 2001.

Katzenmeyer, A. M., Canivet, J., Holland, G., Farrusseng, D., and Centrone, A.: Assessing chemical heterogeneity at the nanoscale in mixed-ligand metal-organic frameworks with the PTIR technique, Angew. Chem. Int. Ed., 53, 2852-2856, 2014.

Kennedy, I. M.: The health effects of combustion-generated aerosols, Proceedings of the Combustion Institute, 31, 2757-2770, 2007.

Kilcoyne, A. L. D., Tyliszczak, T., Steele, W. F., Fakra, S., Hitchcock, P., Franck, K., Anderson, E., Harteneck, B., Rightor, E. G., Mitchell, G. E., Hitchcock, A. P., Yang, L., Warwick, T., and Ade, H.: Interferometer-controlled scanning transmission X-ray microscopes at the Advanced Light Source, Journal of Synchrotron Radiation, 10, 125-136, 2003.

Kim, D. S., Hopke, P. K., Massart, D. L., Kaufman, L., and Casuccio, G. S.: Multivariate analysis of CCSEM auto emission data, Sci. Total Environ., 59, 141-155, 1987.

Krueger, B. J., Ross, J. L., and Grassian, V. H.: Formation of microcrystals, micropuddles, and other spatial inhomogenieties in surface reactions under ambient conditions: An atomic force microscopy study of water and nitric acid adsorption on MgO(100) and $CaCO_3(10\bar{1}4)$, Langmuir, 21, 8793-8801, 2005.

Laskin, A., Iedema, M. J., and Cowin, J. P.: Quantitative time-resolved monitoring of nitrate formation in sea salt particles using a CCSEM/EDX single particle analysis, Environ. Sci. Technol., 36, 4948-4955, 2002.

Laskin, A., Iedema, M. J., and Cowin, J. P.: Time-resolved aerosol collector for CCSEM/EDX single-particle analysis, Aerosol Sci. Technol., 37, 246-260, 2003.

Laskin, A., Iedema, M. J., Ichkovich, A., Graber, E. R., Taraniuk, I., and Rudich, Y.: Direct observation of completely processed calcium carbonate dust particles, Faraday Discuss., 130, 453-468, 2005.

Laskin, A., Cowin, J. P., and Iedema, M. J.: Analysis of individual environmental particles using modern methods of electron microscopy and X-ray microanalysis, J. Electron. Spectrosc. Relat. Phenom., 150, 260-274, 2006a.

Laskin, A., Wang, H., Robertson, W. H., Cowin, J. P., Ezell, M. J., and Finlayson-Pitts, B. J.: A new approach to determining gas-particle reaction probabilities and application to the heterogeneous reaction of deliquesced sodium chloride particles with gas-phase hydroxyl radicals, J. Phys. Chem. A, 110, 10619-10627, 2006b.

Laskin, A., Moffet, R. C., Gilles, M. K., Fast, J. D., Zaveri, R. A., Wang, B., Nigge, P., and Shutthanandan, J.: Tropospheric chemistry of internally mixed sea salt and organic particles: Surprising reactivity of NaCl with weak organic acids, J. Geophys. Res.: Atmos., 117, 2012.

Laskin, A., Gilles, M. K., Knopf, D. A., Wang, B., and China, S.: Progress in the analysis of complex atmospheric particles, in: Annual Review of Analytical Chemistry, Vol 9, edited by: Bohn, P. W., and Pemberton, J. E., Annual Review of Analytical Chemistry, 117-143, 2016.

Laskina, O., Young, M. A., Kleiber, P. D., and Grassian, V. H.: Infrared extinction spectroscopy and micro-Raman spectroscopy of select components of mineral dust mixed with organic compounds, J. Geophys. Res.: Atmos., 118, 6593-6606, 2013.

Laskina, O., Morris, H. S., Grandquist, J. R., Qin, Z., Stone, E. A., Tivanski, A. V., and Grassian, V. H.: Size matters in the water uptake and hygroscopic growth of atmospherically relevant multicomponent aerosol particles, J. Phys. Chem. A, 119, 4489-4497, 2015.

Latour, G., Robinet, L., Dazzi, A., Portier, F., Deniset-Besseau, A., and Schanne-Klein, M. C.: Correlative nonlinear optical microscopy and infrared nanoscopy reveals collagen degradation in altered parchments, Scientific Reports, 6, 2016.

Marcott, C., Kjoller, K., Lo, M., Prater, C., Shetty, R., and Dazzi, A.: Nanoscale IR spectroscopy: AFM-IR - a new technique, Spectroscopy, 27, 60-65, 2012.

Marcott, C., Lo, M., Kjoller, K., Domanov, Y., Balooch, G., and Luengo, G. S.: Nanoscale infrared (IR) spectroscopy and imaging of structural lipids in human stratum corneum using an atomic force microscope to directly detect absorbed light from a tunable IR laser source, Experimental Dermatology, 22, 419-421, 2013.

Moffet, R. C., Henn, T., Laskin, A., and Gilles, M. K.: Automated chemical analysis of internally mixed aerosol particles using X-ray spectromicroscopy at the carbon K-edge, Anal. Chem., 82, 7906-7914, 2010a.

Moffet, R. C., Henn, T. R., Tivanski, A. V., Hopkins, R. J., Desyaterik, Y., Kilcoyne, A. L. D., Tyliszczak, T., Fast, J., Barnard, J., Shutthanandan, V., Cliff, S. S., Perry, K. D., Laskin, A., and Gilles, M. K.: Microscopic characterization of carbonaceous aerosol particle aging in the outflow from Mexico City, Atmos. Chem. Phys., 10, 961-976, 2010b.

Moffet, R. C., Roedel, T. C., Kelly, S. T., Yu, X. Y., Carroll, G. T., Fast, J., Zaveri, R. A., Laskin, A., and Gilles, M. K.: Spectro-microscopic measurements of carbonaceous aerosol aging in central California, Atmos. Chem. Phys., 13, 10445-10459, 2013.

Morris, H. S., Grassian, V. H., and Tivanski, A. V.: Humidity-dependent surface tension measurements of individual inorganic and organic submicrometre liquid particles, Chemical Science, 6, 3242-3247, 2015.

Morris, H. S. S.: Quantifying the hygroscopic growth of individual submicrometer particles with atomic force microscopy, Analytical chemistry (Washington), 88, 3647-3654, 2016.

O'Brien, R. E., Neu, A., Epstein, S. A., MacMillan, A. C., Wang, B., Kelly, S. T., Nizkorodov, S. A., Laskin, A., Moffet, R. C., and Gilles, M. K.: Physical properties of ambient and laboratory-generated secondary organic aerosol, Geophys. Res. Lett., 41, 2014GL060219, 2014.

O'Brien, R. E., Wang, B., Laskin, A., Riemer, N., West, M., Zhang, Q., Sun, Y., Yu, X.-Y., Alpert, P., Knopf, D. A., Gilles, M. K., and Moffet, R. C.: Chemical imaging of ambient aerosol

particles: Observational constraints on mixing state parameterization, J. Geophys. Res.: Atmos., 120, 9591-9605, 2015a.

O'Brien, R. E., Wang, B. B., Kelly, S. T., Lundt, N., You, Y., Bertram, A. K., Leone, S. R., Laskin, A., and Gilles, M. K.: Liquid-liquid phase separation in aerosol particles: Imaging at the nanometer scale, Environ. Sci. Technol., 49, 4995-5002, 2015b.

Ofner, J., Deckert-Gaudig, T., Kamilli, K. A., Held, A., Lohninger, H., Deckert, V., and Lendl, B.: Tip-enhanced Raman spectroscopy of atmospherically relevant aerosol nanoparticles, Anal. Chem., 88, 9766-9772, 2016.

Petters, M. D., and Kreidenweis, S. M.: A single parameter representation of hygroscopic growth and cloud condensation nucleus activity, Atmos. Chem. Phys., 7, 1961-1971, 2007.

Pöhlker, C., Wiedemann, K. T., Sinha, B., Shiraiwa, M., Gunthe, S. S., Smith, M., Su, H., Artaxo, P., Chen, Q., Cheng, Y., Elbert, W., Gilles, M. K., Kilcoyne, A. L. D., Moffet, R. C., Weigand, M., Martin, S. T., Pöschl, U., and Andreae, M. O.: Biogenic potassium salt particles as seeds for secondary organic aerosol in the Amazon, Science, 337, 1075-1078, 2012.

Poschl, U.: Atmospheric aerosols: Composition, transformation, climate and health effects, Angew. Chem. Int. Ed., 44, 7520-7540, 2005.

Posfai, M., and Buseck, P. R.: Nature and climate dffects of individual tropospheric aerosol particles, in: Annual Review of Earth and Planetary Sciences, Vol 38, edited by: Jeanloz, R., and Freeman, K. H., Annual Review of Earth and Planetary Sciences, 17-43, 2010.

Prather, K. A., Hatch, C. D., and Grassian, V. H.: Analysis of atmospheric aerosols, Annu. Rev. Anal. Chem., 1, 485-514, 2008.

Pratt, K. A., and Prather, K. A.: Aircraft measurements of vertical profiles of aerosol mixing states, J. Geophys. Res.: Atmos., 115, 2010.

Ravishankara, A. R.: Heterogeneous and multiphase chemistry in the troposphere, Science, 276, 1058-1065, 1997.

Riemer, N., and West, M.: Quantifying aerosol mixing state with entropy and diversity measures, Atmos. Chem. Phys., 13, 11423-11439, 2013.

Rindelaub, J. D., Craig, R. L., Nandy, L., Bondy, A. L., Dutcher, C. S., Shepson, P. B., and Ault, A. P.: Direct measurement of pH in individual particles via Raman microspectroscopy and variation in acidity with relative humidity, J. Phys. Chem. A, 120, 911-917, 2016.

Seinfeld, J. H. P., S. N.: Atmospheric Chemistry and Physics: From Air Pollution to Climate Change, 2nd ed. ed., Wiley, New York, 2006.

Shen, H. R., Peters, T. M., Casuccio, G. S., Lersch, T. L., West, R. R., Kumar, A., Kumar, N., and Ault, A. P.: Elevated concentrations of lead in particulate matter on the neighborhood-scale in Delhi, India as determined by single particle analysis, Environ. Sci. Technol., 50, 4961-4970, 2016.

Sobanska, S., Coeur, C., Maenhaut, W., and Adams, F.: SEM-EDX characterisation of tropospheric aerosols in the Negev desert (Israel), J. Atmos. Chem., 44, 299-322, 2003.

Sobanska, S., Hwang, H., Choel, M., Jung, H.-J., Eom, H.-J., Kim, H., Barbillat, J., and Ro, C.-U.: Investigation of the chemical mixing state of individual Asian dust particles by the combined

use of electron probe X-ray microanalysis and Raman microspectrometry, Anal. Chem., 84, 3145-3154, 2012.

Sobanska, S., Falgayrac, G., Rimetz-Planchon, J., Perdrix, E., Bremard, C., and Barbillat, J.: Resolving the internal structure of individual atmospheric aerosol particle by the combination of Atomic Force Microscopy, ESEM-EDX, Raman and ToF-SIMS imaging, Microchem. J., 114, 89-98, 2014.

Tolocka, M. P., and Turpin, B.: Contribution of organosulfur compounds to organic aerosol mass, Environ. Sci. Technol., 46, 7978-7983, 2012.

Wang, B., and Laskin, A.: Reactions between water-soluble organic acids and nitrates in atmospheric aerosols: Recycling of nitric acid and formation of organic salts, J. Geophys. Res.: Atmos., 119, 3335-3351, 2014.

Wang, B., O'Brien, R. E., Kelly, S. T., Shilling, J. E., Moffet, R. C., Gilles, M. K., and Laskin, A.: Reactivity of liquid and semisolid secondary organic carbon with chloride and nitrate in atmospheric aerosols, J. Phys. Chem. A, 119, 4498-4508, 2015.

Wang, B. B., Harder, T. H., Kelly, S. T., Piens, D. S., China, S., Kovarik, L., Keiluweit, M., Arey, B. W., Gilles, M. K., and Laskin, A.: Airborne soil organic particles generated by precipitation, Nat. Geosci., 9, 433-+, 2016.

Zaveri, R. A., Barnard, J. C., Easter, R. C., Riemer, N., and West, M.: Particle-resolved simulation of aerosol size, composition, mixing state, and the associated optical and cloud condensation nuclei activation properties in an evolving urban plume, J. Geophys. Res.: Atmos., 115, 2010.

Chapter 2.
Diverse Chemical Mixing State of Aerosol Particles at SOAS in the Southeastern United States

Amy L. Bondy, Daniel Bonanno, Ryan C. Moffet, Bingbing Wang, Alexander Laskin, Andrew P. Ault. Diverse Chemical Mixing State of Aerosol Particles at SOAS in the Southeastern United States. Submitted to *Atmospheric Chemistry and Physics*.

2.1. Introduction

The southeastern United States has experienced neutral to cooling shifts in regional climate over the past century (Portmann et al., 2009; Saxena and Yu, 1998), in contrast to warming observed in the rest of the United States. This has been attributed to increased formation of secondary organic aerosol (SOA) with largely cooling effects due to efficient light scattering and activity in cloud formation (Goldstein et al., 2009; Portmann et al., 2009). Regionally, the main SOA source is oxidation of biogenic volatile organic compounds (BVOCs), followed by condensation onto preexisting particles containing ammonium, sulfate, and nitrate (Chameides et al., 1988; Carlton et al., 2010; Lee et al., 2010; Weber et al., 2007; Anttila et al., 2007; Budisulistiorini et al., 2015a; Xu et al., 2015b; Boyd et al., 2015; Hodas et al., 2014; Nguyen et al., 2015). Most studies of aerosol climate impacts in the southeast have focused on the effects of SOA, as this region has high concentrations of organics, which along with ammonium sulfate, contribute 60-90 % of fine particulate matter ($PM_{2.5}$) (Attwood et al., 2014; Cerully et al., 2015; Nguyen et al., 2014; Boone et al., 2015). However, despite the importance of SOA, the mixing of secondary species (SOA, sulfate, nitrate, etc.) with primary particles is not fully known, particularly for forested locations impacted by regional anthropogenic emissions. The form and extent of mixing between chemical species in individual particles, i.e. mixing state, is critical for climate-relevant properties including light scattering, water uptake, and particle acidity (Artaxo and Orsini, 1987; Metternich et al., 1986; Kunkel et al., 2012; Violaki and

Mihalopoulos, 2010; Cong et al., 2010; Xu et al., 2015a). Therefore, it is important to identify the sources of aerosol particles present in the southeastern United States, as well as their size and mixing state in order to accurately assess their impact on aerosol direct and indirect effects (Li et al.; Posfai and Buseck, 2010; Moise et al., 2015).

Mixing state is described in terms of external and internal mixtures: an external mixture consists of particles that contain only one pure species per particle, while an internal mixture describes particles that contain equal amounts of all chemical species (Riemer and West, 2013; Posfai and Buseck, 2010; Ault and Axson, 2017). The mixing states of ambient aerosol populations are complex and can vary as a function of size, altitude, and particle age (Moffet et al., 2010b; Fu et al., 2012; Healy et al., 2014a; Pratt and Prather, 2010). Aging, or atmospheric processing such as coagulation, condensation of secondary species, and heterogeneous reactions leads to internal mixing, while freshly emitted particles are more externally mixed (Weingartner et al., 1997; Schutgens and Stier, 2014). Here, mixing state is used to describe the distribution of chemical species in a population and is purely based on composition, not including particle morphology or other physical properties (Ault and Axson, 2017). Although the representation of mixing state in models is still an open research question (Riemer and West, 2013), an appropriate description of mixing state is critical for modeling the optical properties (Jacobson, 2001; Chung and Seinfeld, 2005; Zaveri et al., 2010) and cloud condensation nuclei (CCN) activity of particles (Zaveri et al., 2010).

Riemer and West (2013) introduced the mixing state index (χ) to quantify aerosol mixing state. This parameterization uses single particle mass fractions of individual components to calculate the average particle-specific diversity and the bulk population diversity, from which the mixing state index can then be determined. This methodology has been applied to a handful of laboratory and field studies, to date. In the laboratory, Dickau et al. (2016) used aerosol sizing and mass instrumentation to quantify the volatile mixing state of soot. Single particle mass spectrometry data from field studies in London (Giorio et al., 2015) and as part the MEGAPOLI campaign in Paris (Healy et al., 2014b) found mixing state was dependent both upon time of day and air mass origin. Similarly, mixing state parameters were applied to computer controlled scanning electron microscopy/energy dispersive X-ray spectroscopy (CCSEM-EDX) and scanning transmission X-ray microscopy/near edge X-ray absorption fine structure spectroscopy (STXM-NEXAFS) during the Carbonaceous Aerosol and Radiative Effects Study (CARES) in

the Central Valley, CA (O'Brien et al., 2015) and in the Amazon during the GoAmazon campaign (Fraund et al., 2017), finding changes in mixing state were associated with a buildup of organic matter and particle clusters were less diverse at remote sites, respectively. However, additional studies are needed to quantify the chemical mixing state of aerosols, particularly for rural locations.

In this study, we analyzed individual atmospheric particles collected in a rural location influenced by regional pollution in the southeastern United States during the 2013 Southern Oxidant and Aerosol Study (SOAS) to identify their size-resolved chemical composition and mixing state. CCSEM-EDX was used to determine the size, elemental composition, and number fraction of particles containing nonvolatile cations. STXM-NEXAFS was used to characterize chemical bonding of carbonaceous components, specifically distinguishing soot from organic carbon. Mass estimates of particle elemental composition from CCSEM-EDX were calculated using a modified version of the method from O'Brien et al. (2015) to quantify the mixing state parameters for both submicron and supermicron particles during time periods dominated by SOA/sulfate, dust, and sea spray aerosol (SSA), respectively. Additionally, the variability in the mixing state index during these three time periods of interest, showed that submicron aerosol varied between more internal and external mixing states, while supermicron particles were mostly internally mixed. The variety of particle classes, varying extent of secondary processing, and diverse chemical mixing states at this rural, forested site may impact climate-relevant properties of aerosols in the southeastern United States.

2.2. Experimental

2.2.1. Aerosol Sample Collection

Samples of atmospheric particles were collected at the SOAS Centreville, AL site (32.9030 N, 87.2500 W, 242 m AMSL) between June 5 and July 11, 2013 (Hidy et al., 2014; Bondy et al., 2017b). The site was located in a rural forested region near Talladega National Forest, at a location that is part of the SouthEastern Aerosol Research and Characterization Network (SEARCH). Meteorological and filter sample data analyzed from the SEARCH network were used to aid selection of samples for analysis (Figures 2.1 and A.1). Particles were collected near ground level (1 m) using a micro-orifice uniform deposit impactor (MOUDI, MSP Corp. Model 110) sampling at 30 lpm with a PM_{10} cyclone (URG Model 786) to exclude

particles larger than 10 µm. The 50 % size cut-points for the MOUDI used in this analysis had aerodynamic diameters (D_a) of 3.2, 1.8, 1.00, 0.56, 0.32 0.18, 0.10, and 0.056 µm (Marple et al., 1991). Throughout SOAS, particles were impacted onto Cu 200 mesh TEM grids with Carbon Type B thin film (Ted Pella Inc.) for analysis with SEM-EDX and STXM-NEXAFS. Substrates in the MOUDI were collected daily from 8:00-19:00 CST and 20:00-7:00 CST (with 1 hour for substrate exchange), except during intensive periods from June 10th-12th, June 14th-16th, June 29th-July 1st, and July 7th-9th when the sampling schedule was 8:00-11:00, 12:00-15:00, 16:00-19:00, and 20:00-7:00 CST (Table A.1). Samples were collected more frequently during intensive time periods, which were determined by meteorological and gas phase concentrations (Budisulistiorini et al., 2015a). In Figure 2.1, the MOUDI stages analyzed using CCSEM are noted for each sample. After collection, all substrates were sealed and stored at -22°C prior to analysis.

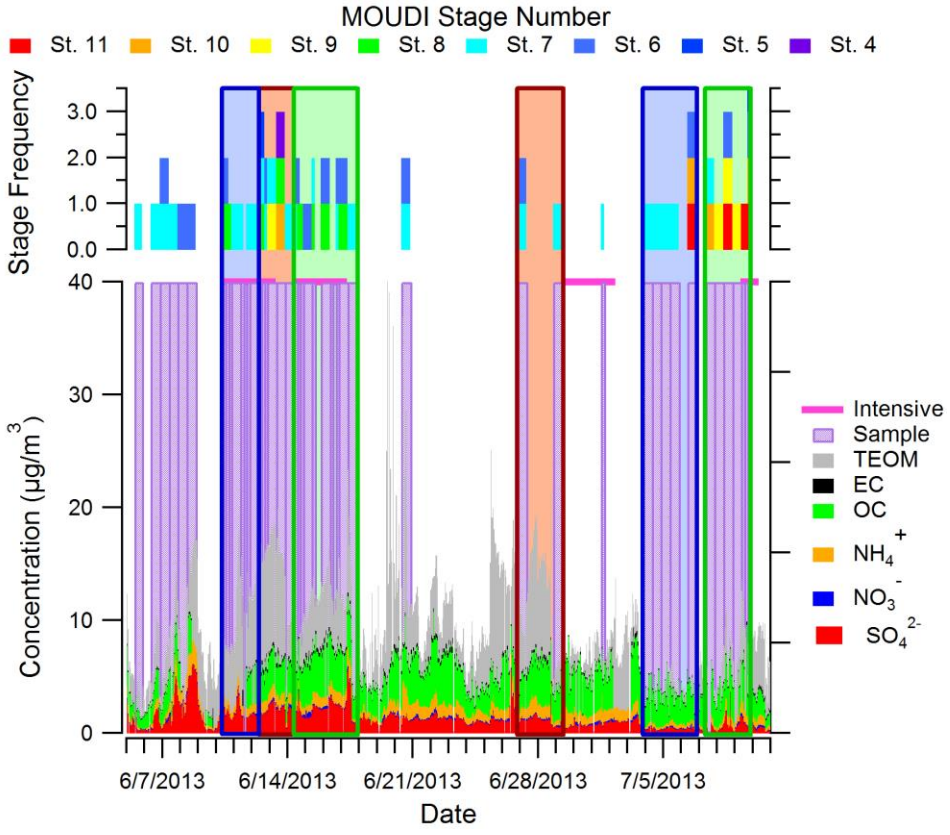

Figure 2.1. SEARCH filter sample data for Centreville, AL during SOAS with purple boxes overlaid for time periods in which CCSEM was run, and the corresponding MOUDI stages that were analyzed. SOA-rich periods denoted with green boxes (June 14-17 and July 7-11, 2013) were studied by Xiong et al. (2015), Pye et al. (2015), Xu et al. (2015c), Hu et al. (2015), and Rattanavaraha et al. (2016); dust-rich periods marked with brown boxes (June 12-13 and June

26-28, 2013) were identified by Allen et al. (2015); and SSA-rich periods marked with blue boxes (June 10-11 and July 3-6, 2013) were identified by Bondy et al. (2017b). Note, due to sample damage and identification of mutually exclusive time periods, only 29 % of SOA-dominant periods, 40 % of dust periods, and 51 % of SSA periods identified in previous studies were analyzed here.

2.2.2. CCSEM-EDX Analysis

Particles on MOUDI stages 4-11 (D_a = 0.056-1.8 µm, Figure 2.1) were analyzed using CCSEM (FEI Quanta environmental SEM) equipped with a field emission gun operating at 20 kV and a high angle annular dark field (HAADF) detector (Laskin et al., 2002; Laskin et al., 2012; Laskin et al., 2006). The SEM was equipped with an EDX spectrometer (EDAX, Inc.) which was used to quantify X-rays of elements with atomic numbers $\geq$ C (Z = 6). A total of ~34,000 particles were analyzed during time periods denoted in Table A.2, which constitute a representative cross section of the campaign. CCSEM analysis captured particle physical parameters including projected area diameter, projected area, and perimeter. Projected area diameter, which is equivalent to the diameter of a circle with the same area as the particle silhouette, is typically larger than aerodynamic diameters measured by other analytical techniques (Hinds, 1999; Bondy et al., 2017a). For a more accurate representation of particle size, projected area diameters were converted to volume equivalent diameter using a conversion factor of 0.49 for SOA/sulfate and biomass burning particles and 0.66 for SSA, determined from atomic force microscopy (AFM) volume calculations of particles from SOAS (Tables A.3 and A.4). EDX spectra from individual particles were analyzed to determine the relative abundance of 14 elements: C, N, O, Na, Mg, Al, Si, P, S, Cl, K, Ca, Ti, and Fe. Note, the Cu signal in the EDX spectra is primarily due to the Cu grid from the substrate and was not included in CCSEM-EDX analysis.

The CCSEM-EDX data sets were analyzed using k-means clustering of the elemental composition following the method described in Ault et al. (2012) using codes written in Matlab R2013b (MathWorks, Inc.). Clusters were grouped into source-based classes by elemental composition, including mineral dust (Sobanska et al., 2003; Laskin et al., 2005; Coz et al., 2009; Axson et al., 2016; Creamean et al., 2016), SSA (Bondy et al., 2017b; Laskin et al., 2002; Hopkins et al., 2008), SOA/sulfate (Sobanska et al., 2003; Moffet et al., 2013; O'Brien et al., 2015), biomass burning aerosol (Li et al., 2003; Posfai et al., 2003), fly ash/metals (Ault et al., 2012; Shen et al., 2016), biological particles (Huffman et al., 2012), and fresh soot (Li et al.,

2003). Soot forms fractal aggregates of graphitic carbon (C) which contain tens to hundreds of small spherical aggregates (Li et al., 2003). However the intense carbon signal due to the carbon film substrate made chemical identification of soot difficult, resulting in false positives from the substrate. Because of their unique morphology, the size distribution of fresh soot particles without a large, secondary organic carbon coating altering the fractal morphology, was manually determined. Then, a scaling factor based on the SEARCH network elemental carbon mass concentrations was applied to the size distribution and this factor was used in the subsequent analysis. More information on this correction for soot can be found in Appendix A, specifically Table A.5.

2.2.3. Mass Calculations and Mixing State Parameters

Mole percent of elements analyzed using CCSEM-EDX were converted to mass fractions using the method described by O'Brien et al (2015) and detailed in Appendix A. Briefly, particle volumes were calculated from projected area diameters assuming the volume of a hemisphere. Particle masses were then calculated (μ_i = density x volume) assuming the following densities for each class: 1.3 g/cm^3 for SOA/sulfate, biomass burning aerosol, and primary biological particles (Nakao et al., 2013; Li et al., 2016; Manninen et al., 2014); 2.0 g/cm^3 for SSA particles (O'Brien et al., 2015); 2.6 g/cm^3 for dust particles (Wagner et al., 2009); and 3.0 g/cm^3 for fly ash particles (Buha et al., 2014). To calculate the mass of each element, the elemental mole percent was converted to a weight percent, which was multiplied by the estimated particle mass.

Diversity parameters were calculated using two different methods in this work: elemental diversity was calculated from CCSEM-EDX results similar to O'Brien et al. (2015), and mixing state parameters due to aging were calculated as described below (which use only two diversity species: the mass fraction of elements associated with externally-mixed particles and the mass fraction of secondary species). To calculate elemental diversity parameters, the mixing entropy of each particle (H_i) and average particle mixing entropy (H_α) were calculated for each particle class as described in detail by Riemer and West (2013):

$$H_i = \sum_{a=1}^{A} p^a{}_i \ln p_i^a \tag{2.1}$$

$$H_\alpha = \sum_{i=1}^{N} p_i H_i \tag{2.2}$$

where p_i is the mass fraction of particle i in the population and $p^a{}_i$ is the mass fraction of element a in particle i. The particle diversity (D_i) was then calculated by taking the exponent of the particle-specific entropy H_i, and the average particle-specific diversity (D_α) was calculated by taking the exponent of H_α. D_α was used as an indicator of elemental diversity for each particle class: SOA/sulfate, biomass burning particles, fly ash, dust, SSA, and biological particles.

In addition to elemental diversity, diversity parameters were calculated to quantify the extent of particle aging. To calculate the mixing state aging parameters for the three time periods of interest, two final mass values were calculated: the mass of single particles in a class based on the sum of elements characteristic to that class, and the mass of secondary species. The elemental mass fractions as a function of size are depicted in Figure A.2. Due to the semi-quantitative nature of the lower Z elements (Laskin et al., 2006) and substrate interferences, we excluded C, N, and O from mixing state calculations, similar to O'Brien et al. The mass associated with SOA/sulfate was solely accounted for by S (if present), and therefore was either ignored or severely underestimated. Fresh biomass particles consisted of K and Cl, fly ash particles contained Al and Si, unreacted dust particles consisted of Na, Mg, Al, Si, K, Ca, Ti, and Fe, fresh SSA particles contained Na, Mg, Cl, K, and Ca, and biological particles contained P, Cl, and K. As a metric for aging, all sulfur was assumed to be secondary within particles, though trace primary sulfur is present in SSA and possibly other classes. Thus, each particle contained between one and two components: a primary source-based composition and secondary aging due to sulfur. Using the mass fractions of only these two components, H_i, H_α, and the population bulk mixing entropy (H_γ) were calculated for each particle class

$$H_\gamma = \sum_{a=1}^{A} -p^a ln p^a \tag{2.3}$$

where p^a is the mass fraction of element a in the population. The bulk population diversity (D_γ) was then calculated by taking the exponent of H_γ. The mixing state index (χ) is then defined as

$$\chi = \frac{D_\alpha - 1}{D_\gamma - 1} \text{ x } 100 \tag{2.4}$$

where χ can range from 0 % for an external mixture to 100 % for an internal mixture.

2.2.4. STXM-NEXAFS Analysis

STXM-NEXAFS measurements of two MOUDI samples (stage 9, 50 % size cut-point of 0.18 µm, 100-200 particles analyzed per sample), June 10 and July 7, 2013 were performed at the carbon K-absorption edge (280-320 eV) to characterize chemical bonding of carbonaceous components, specifically distinguishing soot from organic carbon. STXM was conducted at the Advanced Light Source at Lawrence Berkeley National Laboratory on beamline 5.3.2. The operation of the microscope has been explained in detail by Kilcoyne et al. (2003). The software programs Matlab and Axis 2000 were both used for spectral analysis of the STXM-NEXAFS data as described by Moffet et al. (2010a); (Moffet et al., 2016). Stacks of images taken at sequentially increasing photon energies were used to obtain spatially resolved spectroscopic data at the carbon K-edge. For organic identification, pixels were identified where the post-edge minus the pre-edge (optical density (OD) at 320 eV minus OD 278 eV) was greater than zero. For the inorganic component, particles with a ratio of the pre-edge to the post-edge (OD 278 / OD 320) greater than 0.5 were identified. To identify soot inclusions within particles, individual pixels of STXM images were analyzed and if a pixel contained 35 % or greater C=C, a peak which was identified as soot using graphitic carbon as a standard, then that pixel was identified as a soot region. Additional details on identification of SOA-containing soot inclusions are provided in Appendix A.

2.3. Results and Discussion

2.3.1. Overview of Particle Classes at SOAS

Although SOAS took place in a rural forested region, a variety of particle classes were observed, and SOA/sulfate was not always the dominant individual particle class. Based on the chemical composition, seven main particle classes were identified: SOA/sulfate, biomass burning particles, soot, and fly ash, which are typically present in the submicron (< 1 µm) regime, and mineral dust, SSA, and primary biological particles with characteristic sizes > 1 µm. Figure 2.2 shows SEM images of representative particles from each class and their corresponding EDX spectra. SOA/sulfate particles were identified by the elemental composition of C and O, along with either S, N, or both S and N. As all SOA particles contained inorganic species in addition to organic carbon (based on STXM OD_{pre}/OD_{post} = 0.5, ~20 % by weight), this class is referred to as SOA/sulfate. EDX spectra of SOA/sulfate particles on Si wafers (Figure A.3) confirmed C

and O in the particles, since the carbon film substrate on TEM grids contributes to the signal for C and O in the CCSEM-EDX analysis. The presence of S and/or N in addition to C and O is likely NO_3^- or SO_4^{2-}, based on Raman microspectroscopy (Craig et al., 2017), or organonitrate or organosulfate compounds, which are ubiquitous in the southeastern U.S. (Froyd et al., 2010; Carlton et al., 2009; Ayres et al., 2015). SOA/sulfate particles were typically circular (circularity ranging from 0.95-1, where 1 is perfectly circular, equation A.10), though some SOA/sulfate exhibited liquid-liquid phase separation (LLPS), such as core-shell or more complex morphologies, which will be explained in a future publication. Biomass burning aerosol particles were often circular as well (0.96 circularity), with high concentrations of K and frequently S and Cl, in addition to C and O (organic carbon) (Li et al., 2003; Posfai et al., 2003). Fly ash particles were identified primarily by their spherical morphology (0.93 circularity) since fly ash is generated through high temperature processes (Ault et al., 2012; Chen et al., 2012), in addition to high EDX signals from O along with either Si or Al, likely in the form of SiO_2 or Al_2O_3 respectively. A final class comprised primarily of submicron particles was soot. Fresh soot particles were identified primarily by their morphology consisting of agglomerated spheres, which had substantially smaller diameters than fly ash (Li et al., 2003). Fresh soot was not very prevalent at SOAS, however, but present more frequently within other particles such as SOA, which will be detailed later.

In addition to submicron classes, three classes of particles predominately in the supermicron size range were observed at SOAS. Dust particles were identified by strong signals from O, Al, and Si (aluminosilicates), often along with other elements such as Na, Mg, K, Ca, Ti, and Fe (Sobanska et al., 2003; Laskin et al., 2005; Coz et al., 2009). EDX spectra of SSA particles contained a strong Na signal (Na^+) and weaker Mg signal (Mg^{2+}) in a ~10:1 ratio, as found in seawater (Pilson, 1998), small contributions from K (K^+) and Ca (Ca^{2+}), and counter-ion elements such as N, O, S, or Cl, (NO_3^-, SO_4^{2-}, or Cl^-), depending on whether the SSA was fresh or aged (Bondy et al., 2017b). Finally, biological particles typically contained primarily C due to organic macromolecules, along with lesser amounts of N, O, P, and K, likely in the form of amines, phosphate, and K^+ (Huffman et al., 2012), as seen in Figure 2.2. Overall, various particle classes were detected at SOAS using CCSEM-EDX based on unique chemical composition, morphology, and size.

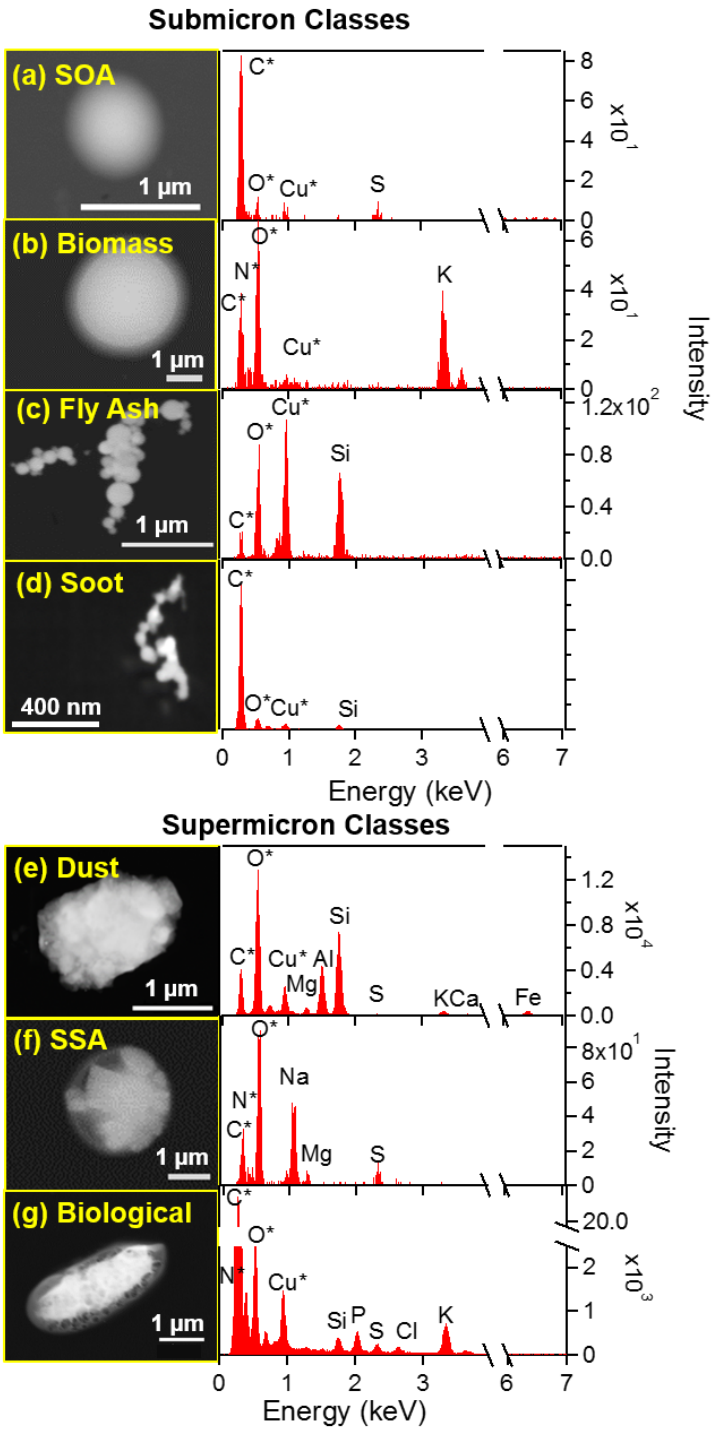

Figure 2.2. SEM images and corresponding EDX spectra for each of the main particle classes identified during SOAS within the submicron: (a) SOA, (b) biomass burning aerosol particles, (c) fly ash, (d) soot, and supermicron: (e) dust, (f) SSA, (g) primary biological, sizes. Note the elements with an asterisk are not quantitative due to interference from the substrate or detector.

STXM-NEXAFS was used to investigate carbonaceous particles since these particles were prevalent at SOAS. The carbon K-edge was probed using this technique, and high spatial resolution information was obtained regarding sp^2 C inclusions within SOA/sulfate, which were identified as soot at 285 eV (Moffet et al., 2010a). In two samples analyzed using STXM-NEXAFS, 6.9 % and 9.9 % of particles by number contained sp^2 C inclusions, suggesting that a small fraction of SOA/sulfate contained soot. In comparison, organic carbon/elemental carbon (OC/EC) bulk analysis by the SEARCH network detected ~2 % elemental carbon by mass, suggesting that although little soot was present overall, a sizeable fraction was present as small inclusions within SOA/sulfate. It is important to consider the mixing state of aerosols when modelling radiative forcing in the region, because internally mixed particles behave differently than pure components. For example, soot coated with secondary organic material may have an enhanced absorption compared to fresh soot or soot-less SOA, though recent work has suggested that soot coatings may not always increase absorption (Ramanathan and Carmichael, 2008; Moffet et al., 2009; Zhang et al., 2008; Healy et al., 2015). These spectra highlight that although seven main particle classes were identified, many of the particles, such as SOA and soot, were partially internally mixed.

2.3.2. Diversity within Particle Classes

Using SEM-EDX elemental mapping, morphology and the spatial distribution of species within individual particles was examined. In Figure 2.3, particles (a-d) were identified as dust based on their morphology and elemental composition. However, only (b-d) are aluminosilicate dust particles; (a) contains high concentrations of Ca and S instead. Based on its chemical composition, this dust particle is most likely gypsum ($CaSO_4 \cdot 2H_2O$) (Hashemi et al., 2011). The elemental map highlights that elements present within the dust class are not homogeneously distributed among all particles. Rather, the dust class consists of externally mixed particles with varying compositions. In addition to dust, two other particle classes are represented in the elemental map in Figure 2.3. Particles (e-f) were identified as aged SSA due to the high concentration of Na and Mg along with S and N (likely SO_4^{2-} and NO_3^-) (Bondy et al., 2017b), and particle (g) is a primary biological particle, possibly coagulated with a small calcium oxide particle based on the morphology and distinctly different elemental compositions of the two components. In addition to differentiating particles among the seven particle classes identified,

SEM-EDX mapping allowed investigation into whether coagulation or chemical aging of particles has occurred within particles due to the presence of localized regions of elements or surface-layer coatings (Conny and Norris, 2011). As seen in Figure 2.3, very few of the particles have a homogeneous distribution of elements, though vacuum analysis and drying can modify internal composition of particles. Rather, Na, Ca, S, and Cl often appear in only a few distinct regions within particles, which can likely be attributed to heterogeneous reactions or limited diffusion. The aluminosilicate dust particle (b) in particular, has localized regions of Ca and S (SO_4^{2-}) on the edges of the particle, signifying that this particle has undergone aging, resulting in a more diverse chemical mixing state. Complex mixing states like this have been observed previously for SSA and dust, showing that these classes of particles can be externally mixed or have surface coatings and inclusions leading to internal mixing, thereby altering their physical and chemical properties (Deboudt et al., 2012; Sobanska et al., 2012; Fitzgerald et al., 2015; Kandler et al., 2011; Sullivan et al., 2007; Sullivan et al., 2009; Kim and Park, 2012; Gantt and Meskhidze, 2013).

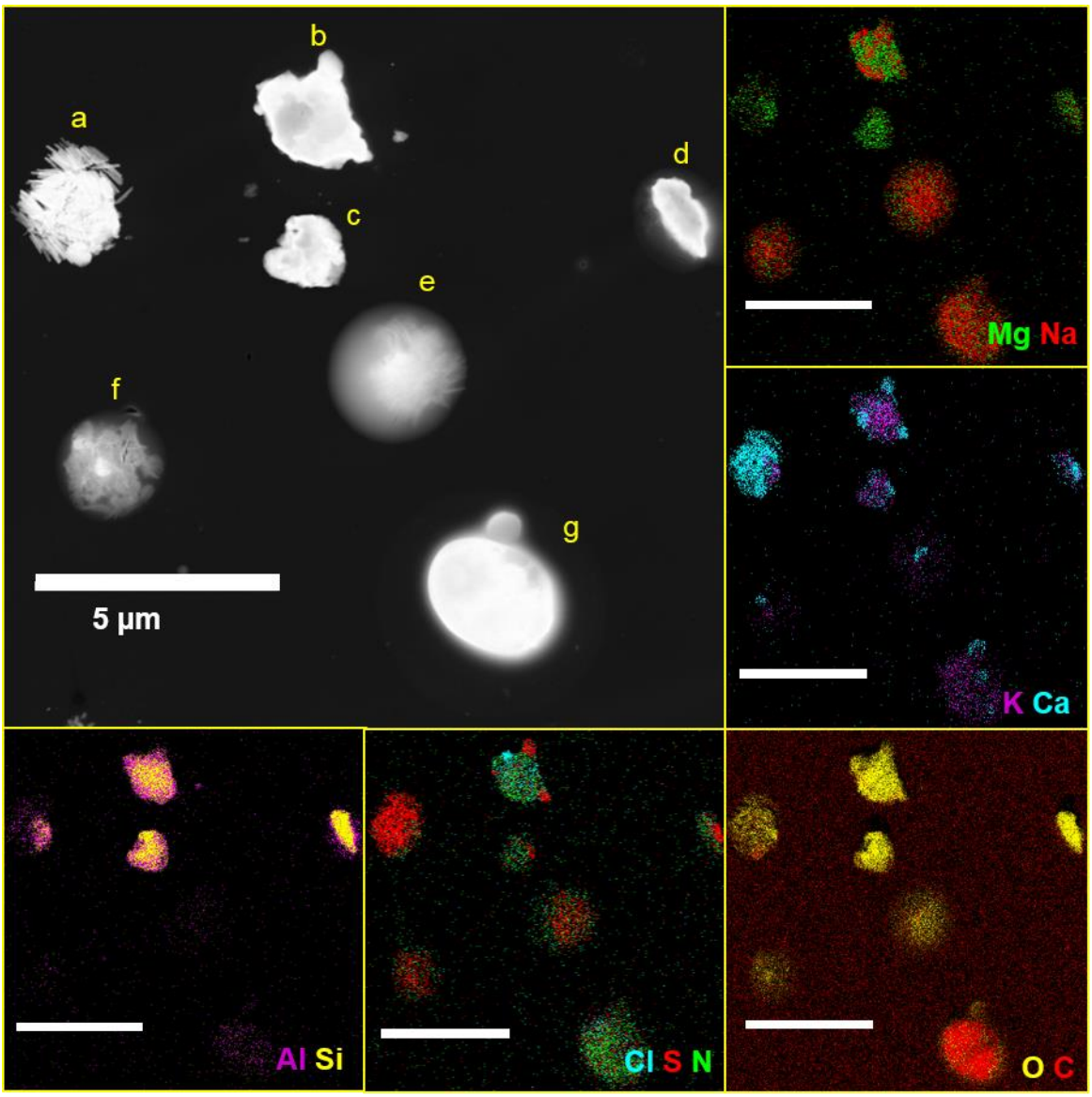

Figure 2.3. SEM image (dark field) and EDX elemental maps of particles indicated that these particle classes had various mixing states. Each of the elemental map panels corresponds to two elements overlaid to show the elemental distributions from the SEM image. The following particle classes are shown: (a-d) dust, (e-f) aged SSA, (g) primary biological.

To probe the chemical diversity of each particle class, Figure 2.4 shows the average EDX elemental percentages for each particle class. The digital color histogram height shows the number fraction of particles in a class containing a specific element, while the color represents the mole % of the element. For example, 100 % of SOA/sulfate by number contain between 50-100 % C (mole %). To quantify elemental diversity of particles, D_{α}, representing the average

number of elements within particles in each class, was calculated. D_α ranges from 1 (when a particle contains only one element) to *A* number of elements. Note, due to interference from the substrate or detector, C, N, and O were not included in D_α calculations. CCSEM-EDX results suggest that SOA/sulfate particles were elementally the least diverse, with D_α = 1.00. However, other studies from SOAS that used an aerosol mass spectrometer (AMS) (Guo et al., 2015; Xu et al., 2015c) or ultra-performance liquid chromatography/electrospray ionization high-resolution quadrupole time-of-flight mass spectrometry (UPLC/ESI-HR-QTOFMS) (Riva et al., 2016; Budisulistiorini et al., 2015b) discovered that a wealth of sources contribute to SOA, resulting in hydrocarbon-like organic aerosol, isoprene-derived organic aerosol, as well as more-oxidized and less-oxidized oxygenated organic aerosol. Their analyses also showed that SO_4^{2-} is the most abundant component aside from organic carbon, with significant concentrations of NH_4^+ followed by NO_3^-, consistent with our observations of 92 % of SOA by number containing S and 68 % containing N (mole %) (Guo et al., 2015; Xu et al., 2015c; Xu et al., 2017; Budisulistiorini et al., 2015b; Riva et al., 2016).

The composition of biomass burning particles was elementally more diverse than SOA (D_α = 1.92), with large contributions from K^+ (1-30 % by mole %) as well as organic carbon (C 20-100 % and O 2-50 % by mole %). However, in addition to these three components, approximately 60 % of particles by number also contained SO_4^{2-} (1-15 % S by mole %), 45% contained NO_3^-/NH_4^+ (1-10 % N by mole %), and 15 % by number contained 1-30 % Cl (mole %). The presence of Cl suggests that some of the biomass burning particles were fresh. However, because sulfate and nitrate, which are indicative of aging (Li et al., 2003), were present more frequently, biomass burning particles detected during SOAS likely had sufficient time during transport for multiphase reactions to occur. The final submicron particle class, fly ash (D_α = 1.92), showed two distinct compositions in addition to aging: fly ash from SOAS consisted of primarily SiO_2, although approximately 15 % by number contained aluminosilicates. Low concentrations of SO_4^{2-} and NO_3^- (1-5 % S and N by mole %) suggest acidic species such as sulfuric and nitric acid reacted with 25 % of fly ash by number.

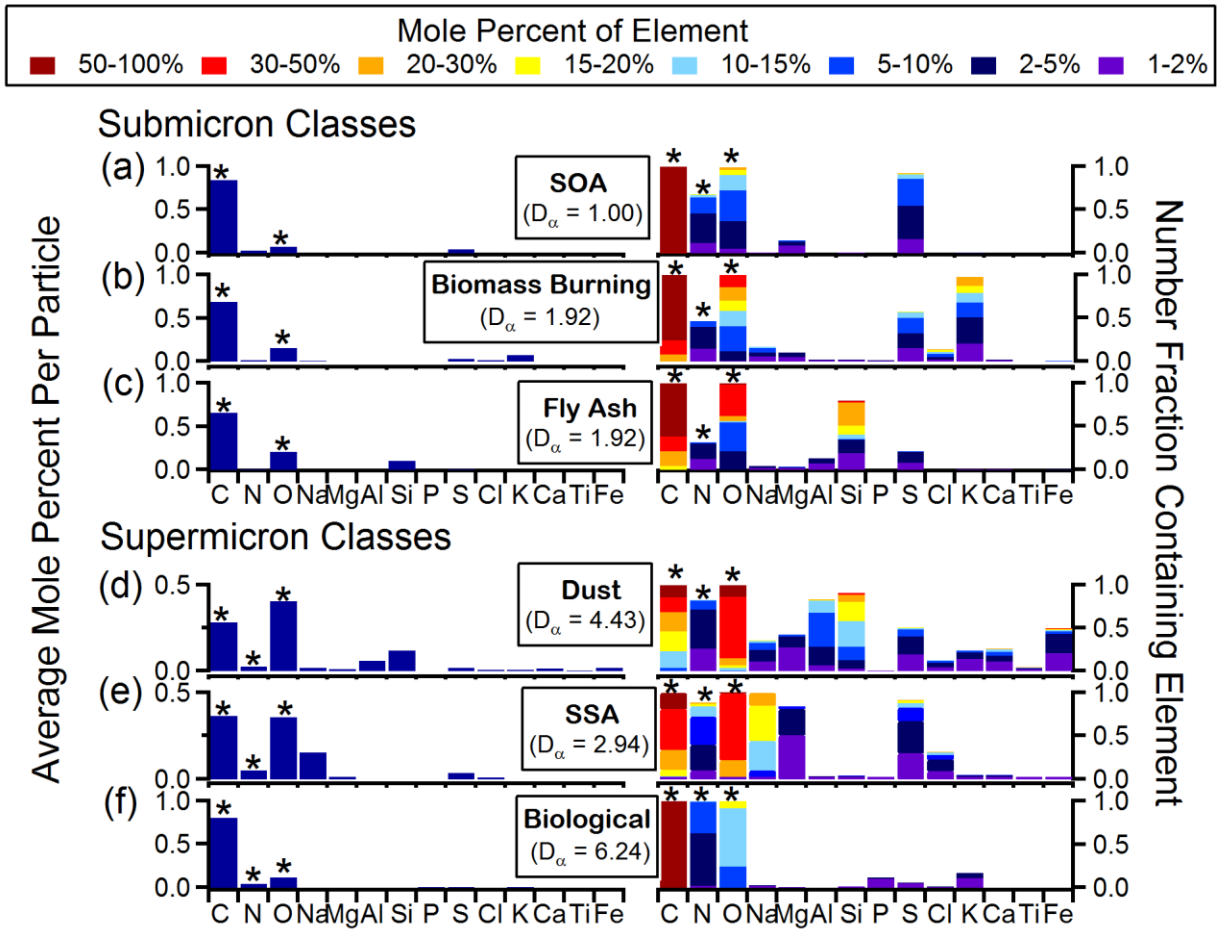

Figure 2.4. Average histograms and digital color histograms of different particle classes from SOAS: (a) SOA, (b) biomass burning, (c) fly ash, (d) dust, (e) SSA, and (f) primary biological. Average spectra are shown on the left as the average mole percent of each element analyzed by CCSEM-EDX (C, N, O, Na, Mg, Al, Si, P, S, Cl, K, Ca, Fe). On the right the digital color histogram heights represent the number fraction of particles containing a specific element, and the colors represent the mole percent of that element. The average particle specific diversity (D_α), representing the average number of elements in each particle, is calculated for each submicron and supermicron class. Note the elements with an asterisk are not quantitative due to interference from the substrate or detector and are not included in D_α.

Within the supermicron particle classes, a range of elemental compositions were observed for dust and SSA (Figure 2.4b). Dust was primarily composed of aluminosilicates (10-100 % O, 1-50 % Si, and 1-50 % Al by mole %), with minor contributions from other chemical species, including CO_3^{2-} or organic coatings (5-100 % C by mole %), NO_3^- (1-10 % N by mole %), SO_4^{2-} (1-10 % S by mole %), Mg^{2+} (1-10 % by mole %), K^+ (1-5 % by mole %), Na^+ (1-10 % by mole %), Ca^{2+} (1-10 % by mole %), and Fe^{2+}/Fe^{3+} (1-30 % by mole %). The frequency of

these minor elements in dust particles varied widely resulting in a high average particle species diversity (D_α = 4.43), with nitrate present in approximately 75 % of the dust population by number, and titanium present in less than 5 %. The diversity of dust indicates various sources and processing throughout SOAS, which likely contributed to time periods with distinct dust compositions due to wind speed, direction, and pollution levels. Allen et al. (2015) detected two high coarse nitrate events during SOAS, the first corresponding to high levels of SSA and dust, and the second primarily dust. The first event exhibited a higher percent of Na^+, not all of which was attributed to SSA due to the low Mg^{2+} to Na^+ molar ratio, while the second event had a higher percent composition of Ca^{2+}. Back trajectory analysis of the air mass origin during the two coarse particle events indicate that although the overall pattern in wind trajectories was similar, slight differences in wind patterns at the beginning of each event may have contributed to the observed differences in composition of the aerosol, suggesting a relatively local origin of the dust during the second event. The elements of SSA were more homogeneously distributed throughout the population than dust (D_α = 2.94), with 100 % of particles by number containing C, O, and Na, 75 % by number containing S, and ~70 % by number containing > 1 % (mole %) N and Mg. SSA particles also showed various degrees of aging with respect to the anions, since chloride can be liberated through multi-phase reactions with acidic species such as HNO_3, H_2SO_4, and organic acids (Bondy et al., 2017b). Partially aged SSA comprised approximately 20 % of particles by number, indicated by Cl^- (1-10 % Cl by mole %) in addition to nitrate and sulfate. Complete chloride depletion and aging by nitrate (1-30 % N by mole %) and sulfate (1-30 % S by mole %) was more ubiquitous though, with each secondary species present in ~90 % of SSA by number. A thorough discussion of the degree of reactive processing of SSA transported inland to Centreville can be found in Chapter 3.

Primary biological particles contained primarily organic carbon (50-100 % C and 5-20 % O by mole %) with minor contributions from PO_4^{3-}, SO_4^{2-}, K^+, in addition to other minor elements (D_α = 6.24). The minor constituents (P, K, S) were not detected in all particles, but only in about 20 % by number. The absence of these minor constituents from EDX spectra is likely the result of low concentrations compared to carbon, and signal below the 1 % detection threshold. Although sulfate is typically an indication of aging by H_2SO_4 in aerosol particles, it is also naturally present in biological particles. Furthermore, because the sulfur signal intensity is on the same scale as the other minor constituents, it is not necessarily from secondary species.

Overall, throughout both the submicron and supermicron particle regimes, particle diversity varied, indicating sources of long and short range transport, and various degrees of aging of particles within each class.

2.3.3. Particle Class Contributions during Events throughout SOAS

Three main time periods (SOA, dust, and SSA) were identified during SOAS that had distinctly different sources and processing (Figure 2.5). Figure 2.5a depicts the size-resolved chemical composition averaged over two SOA-dominated time periods (June 14-17, 2013 and July 7-11, 2013), two dust events (June 11-13, 2013 and June 26-28, 2013), and two SSA events (June 10-11, 2013 and July 3-6, 2013), though only select MOUDI stages were analyzed for each sampling period. During each time period depicted, SOA/sulfate averaged > 60 % of accumulation mode (0.2-1.0 μm), and 2 % of the supermicron (1.0-5.0 μm) particles by number fraction. However, the number fraction of SOA/sulfate was highly variable between the SOA, dust and SSA periods. During the two periods dominated by SOA/sulfate depicted in Figure 2.5a, the number fraction of SOA/sulfate reached up to 95 % in the accumulation mode and up to 70 % of supermicron particles. Because Centreville, AL is a forested site and BVOC emissions, such as isoprene, are high in this region, it is not surprising that SOA/sulfate dominated throughout the majority of the campaign, particularly at small particle sizes. However the fraction of SOA/sulfate > 1 μm is noteworthy, as SOA/sulfate particles are typically considered submicron in size.

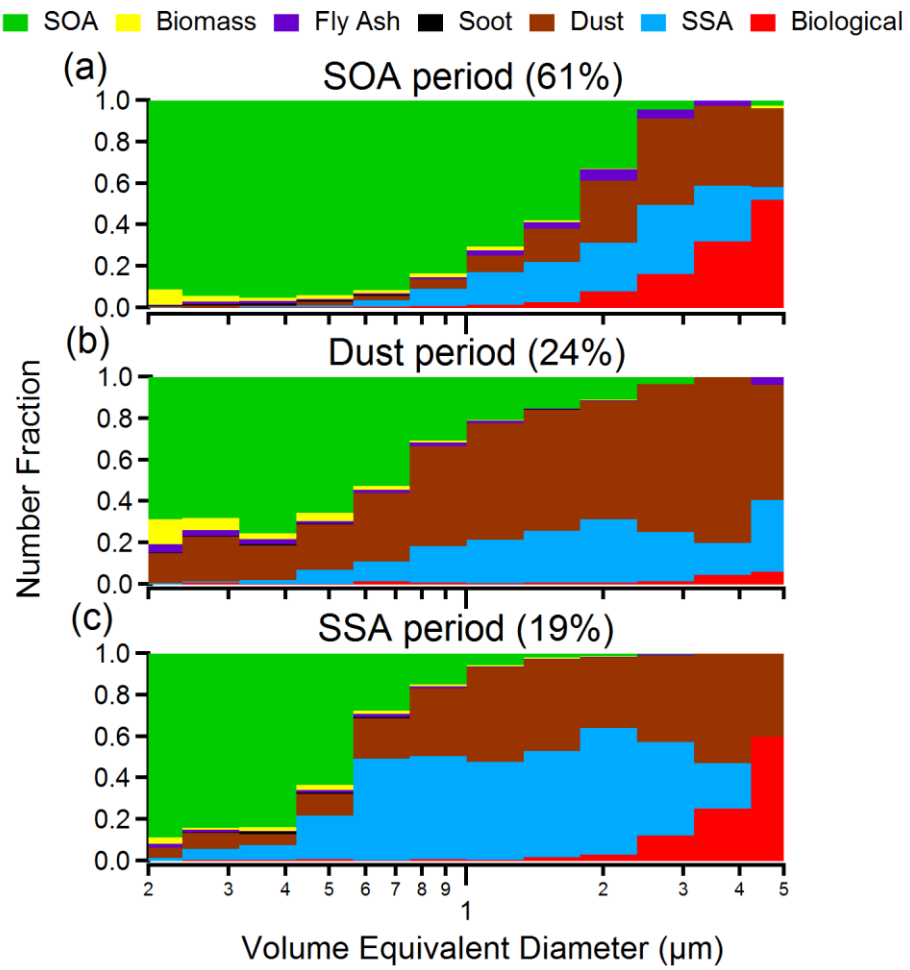

Figure 2.5. Size distributions for specific particle-rich time periods: (a) SOA-rich periods (June 14-17 and July 7-11, 2013), (b) dust-rich periods (June 12-13 and June 26-28, 2013), and (c) SSA-rich periods (June 10-11 and July 3-6, 2013). SOA periods were dominant throughout SOAS (61 % of study), high dust periods occurred 24 % of the time (Allen et al., 2015), and SSA periods dominated 19 % of the time (Bondy et al., 2017) based on literature-defined periods noted in parentheses in the figure. *Literature-identified SSA periods and dust periods overlap from 6/11-6/13, 2013, thus the percentage of high SOA, dust, and SSA periods ≠ 100 %. Only particles with volume equivalent diameters between 0.2 - 5 µm are shown due to too few particles present at larger sizes for quantitative analysis.

Dust was the dominant particle source during two coarse-mode nitrate events (Figure 2.5b) detailed previously by Allen et al. (2015) and defined more narrowly herein as June 11-13 and June 26-28, 2013 to differentiate from SSA transport time periods and account for available CCSEM data. During the dust-dominated time periods analyzed, dust constituted > 55 % of supermicron particles (1.0-5.0 µm) by number, but also contributed, on average, 26 % of accumulation mode particles (0.2-1.0 µm) by number. Similar to dust, SSA contributed

significantly to the overall particle population multiple times throughout the study, comprising approximately 35 % of particles, by number, analyzed during an event in the middle of June (June 10-11, 2013), and at the beginning of July (July 3-6, 2013). Both of these SSA events were also characterized by high number fractions of dust, as observed in Figure 2.5c. During these SSA-rich periods, SSA particles were predominately larger than 1 μm (38 % by number), although notable contributions to accumulation mode number fractions of SSA were also observed (22 % by number from 0.2-1.0 μm). During these two events the degree of atmospheric processing varied, with a considerable number fraction of partially aged SSA present during the second event compared to the first event, which was primarily fully-aged SSA (Bondy et al., 2017b).

2.3.4. Nonvolatile Cations at SOAS

Recently, the presence of soluble nonvolatile cations such as Na^+, Mg^{2+}, K^+, and Ca^{2+} have been predicted to improve thermodynamic modelling results of aerosol acidity when included as inputs (Guo et al., 2017) and assuming all species are internally mixed. As CCSEM-EDX can readily detect metals within individual particles, the number fraction of particles containing Na, Mg, K, Ca, and Fe at sub- and supermicron sizes during the SOA, dust, and SSA events is shown in Figure 2.6. In addition to these metals, Mn was detected within < 3 % particles by number during SOAS, and, given its low fraction, Mn was not included in further analysis. During all events, the number fraction of particles containing nonvolatile cations increased as a function of particle size, with a higher number fraction of metal-containing particles at supermicron sizes (19-94 %) compared to submicron sizes (1-50 %). During all the time periods depicted, Na was present most frequently, closely followed by Mg, indicative of SSA particles. Fewer particles contained K and Ca by comparison, and Fe was present within the lowest number fraction of particles, except for during the dust period when Fe was more frequent. The number fraction of metal-containing particles was not consistent throughout SOAS, but varied dramatically between the SOA, dust, and SSA periods. In general, particles during the dust and SSA events contained higher number fractions of all nonvolatile cations, particularly Na and Mg. However, the variation between specific metals was largely dependent on the dominant particle class during each period.

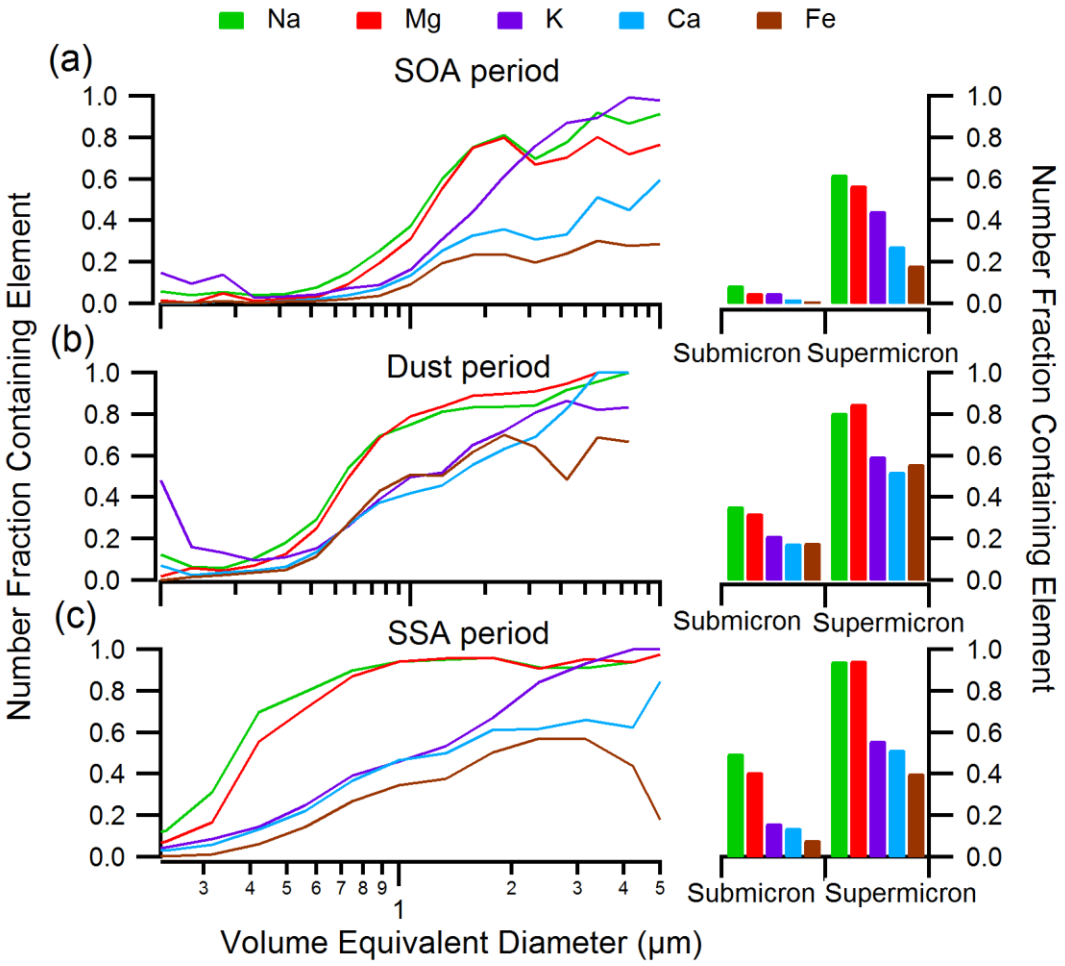

Figure 2.6. (Left) Size-resolved compositions indicate the number fraction of particles containing non-volatile cations Na, Mg, K, Ca, and Fe during the (a) SOA period, (b) dust period, and (c) SSA period. (Right) The number fraction of submicron and supermicron particles during each period containing each non-volatile cation.

Figure 2.7 focuses on the SOA time period and shows the number fraction of particles within each particle class that contains Na, Mg, K, Ca, or Fe (dust and SSA periods are shown in Figure A.4). Within both submicron and supermicron particles, the nonvolatile cations within each class are consistent, though a marginally larger number fraction of supermicron particles contained nonvolatile cations, likely due to detection limits for smaller particles. Less than 5 % of SOA/sulfate particles by number contained any Na, Mg, K, Ca or Fe. Conversely, all other particle classes contained metals within a substantial number of particles. Specifically, all biomass burning particles contained K and fly ash most frequently contained Na, though most fly ash contained Al or Si instead (Figure 2.4). Additionally, a considerable fraction of dust particles contained Na, Mg, K, Ca, or Fe, all SSA contained Na and many contained Mg, and most

primary biological particles contained Na, Mg, and K. Comparing the nonvolatile cations within each class during the SOA, dust, and SSA periods (Figures 2.7 and A.4), the number fractions of metal-containing particles are consistent for each particle class, suggesting than an internal mixing assumption for nonvolatile cations does not accurately represent overall particle composition.

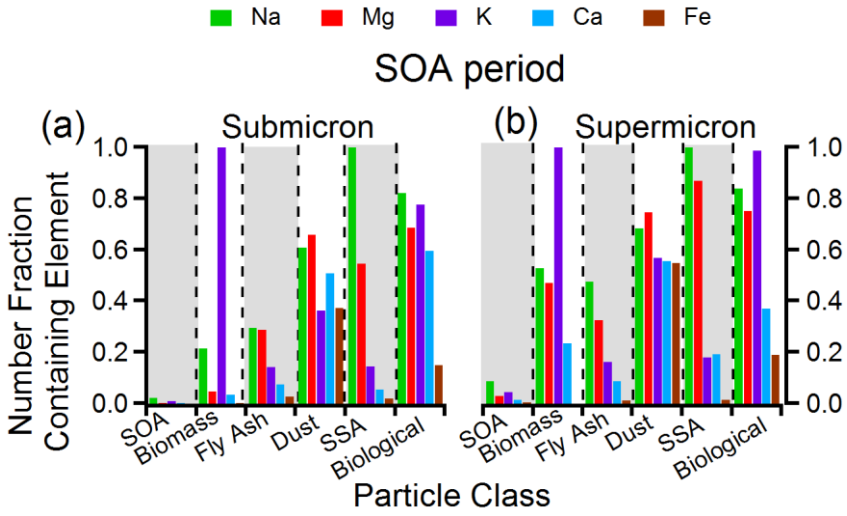

Figure 2.7. Size-resolved particle class compositions indicate the number fraction of particles in each class containing non-volatile cations Na, Mg, and Fe during the SOA period in the (a) submicron and (b) supermicron size range.

2.3.5. Particle Aging

In contrast to nonvolatile cations, the contribution of secondary components within each class varied drastically throughout SOAS. Due to atmospheric reactions and transport of gases from nearby cities, many of the particles analyzed from SOAS were likely not "fresh" from their source, but had undergone secondary processing by species such as HNO_3, SO_2/H_2SO_4, or organic acids. Secondary processing of particles is important because changing their chemical composition can impact light scattering and CCN properties (Giordano et al., 2015; Sedlacek et al., 2012; Chi et al., 2015; Ghorai et al., 2014; Robinson et al., 2013; Chang et al., 2010; Lu et al., 2011; Hiranuma et al., 2013; Moise et al., 2015; Tang et al., 2016). As the chemical composition of particles varied over time, the mixing state index was used to quantify the degree of aging. The degree of secondary processing for each particle class was calculated as the average mass fraction of sulfur per particle, see Figure A.5 and details in Appendix A. Only

sulfur was used as an indicator of aging in this study since carbon had interference from the background and nitrogen is only semiquantitative with CCSEM-EDX (Laskin et al., 2006).

From STXM-NEXAFS, we know that most SOA particles are mixtures of organic and inorganic (mostly ammonium sulfate) components and there are almost no externally mixed organic or ammonium sulfate particles present. As such, based on elemental composition shown in Figure 2.4 and the fact that C, O, and N could not be quantified in this study, particles containing only S in our mixing state analysis are presumed to be SOA/sulfate. A large fraction of sulfur in SOA was likely in the form of sulfate, since sulfate was identified as the major inorganic component within SOA (24 % wt. in fine aerosol) (Budisulistiorini et al., 2015a). Additionally, IEPOX-derived organosulfates and other organosulfates, known to contribute to the organic aerosol fraction in Centreville (Budisulistiorini et al., 2015a; Boone et al., 2015; Xu et al., 2015b; Riva et al., 2016), also contributed to the EDX sulfur content of SOA. The other five particle classes contained substantially less sulfur than SOA; SSA (20-30 wt. % S), biomass burning particles (15-25 wt. % S), dust (5-15 wt. % S), fly ash (2-10 wt. % S), and biological particles (15-25 wt. % S). SSA and biomass burning particles are both readily aged by sulfuric acid forming Na_2SO_4 and K_2SO_4 respectively (Li et al., 2003; Chen et al., 2017; Hopkins et al., 2008), although up to 8 % of sulfate in SSA may have marine origins (Pilson, 1998). Aluminosilicate dust, the most common type of mineral dust detected at SOAS, is also aged by sulfuric acid (Perlwitz et al., 2015; Song et al., 2007; Sullivan et al., 2007). Fly ash detected at SOAS did not contain much sulfur, indicating that it was relatively fresh, or was aged more by other species such as organics, relative to sulfuric acid (Li et al., 2017). Primary biological particles also contained low mass fractions of sulfur. However, as heterogeneous chemistry of this class of particles has not been explored as extensively as the other classes and the sulfur mass fractions did not follow the same trends for the three time periods (Figure A.5), the sulfur content in biological particles may have been, but was not necessarily the result of aging (Estillore et al., 2016).

In addition to differences in aging by sulfur for each particle class, the average mass fraction of sulfur within each class varied during the SOA-rich, dust-rich, and SSA-rich time periods (Figure A.5). Specifically, the average mass fraction of sulfur was significantly higher during the SOA-dominated time period compared to the dust and SSA periods at the 95 % confidence interval for all particle classes aside from biological (Table A.6-A7). However, the

mass fraction of sulfur was not statistically different between the dust and SSA periods for any particle classes (Table A.8). Stagnant air masses, indicated by slower average wind speed at Centreville during the SOA/sulfate period (1.62 ± 0.72) compared to the dust period (2.34 ± 0.95) and SSA period (2.10 ± 0.97), may have led to more aging during the SOA events.

2.3.6. Quantification of Mixing State

To quantify the differences in aging during three described events, the mixing state index was calculated for the SOA, dust, and SSA time periods (Figure 2.8). Because the particle classes present at sub- and supermicron sizes vary dramatically, mixing state indices were calculated separately for the two size ranges. From calculations of the average particle diversity and the bulk diversity (Figure 2.8a), the mixing state index, a ratio measuring how close the population is to an external or internal mixture, could be determined for each time period (Figure 2.8b). The mixing state indices for supermicron particles were generally the highest (χ = 19 %, 15 %, and 11 % during the SSA, dust, and SOA periods, respectively), signifying that supermicron particles were less diverse than submicron particles. The mixing state index for accumulation mode particles during the SOA period was comparable (χ = 10 %), suggesting that submicron particles were more internally mixed during this time period compared to the dust and SSA periods. Overall, Figure 2.8a demonstrates that time periods with low bulk diversity, which contain fewer particle classes, have mixing state indices closer to 100 % (more internally mixed). The supermicron SOA period though, is more internally mixed than expected because although it contains the most individual particle classes (largest bulk diversity, ~5), the particle-specific diversity is highest as well, indicating that this period has a lot of aging by sulfur, contributing to the relatively high mixing state index.

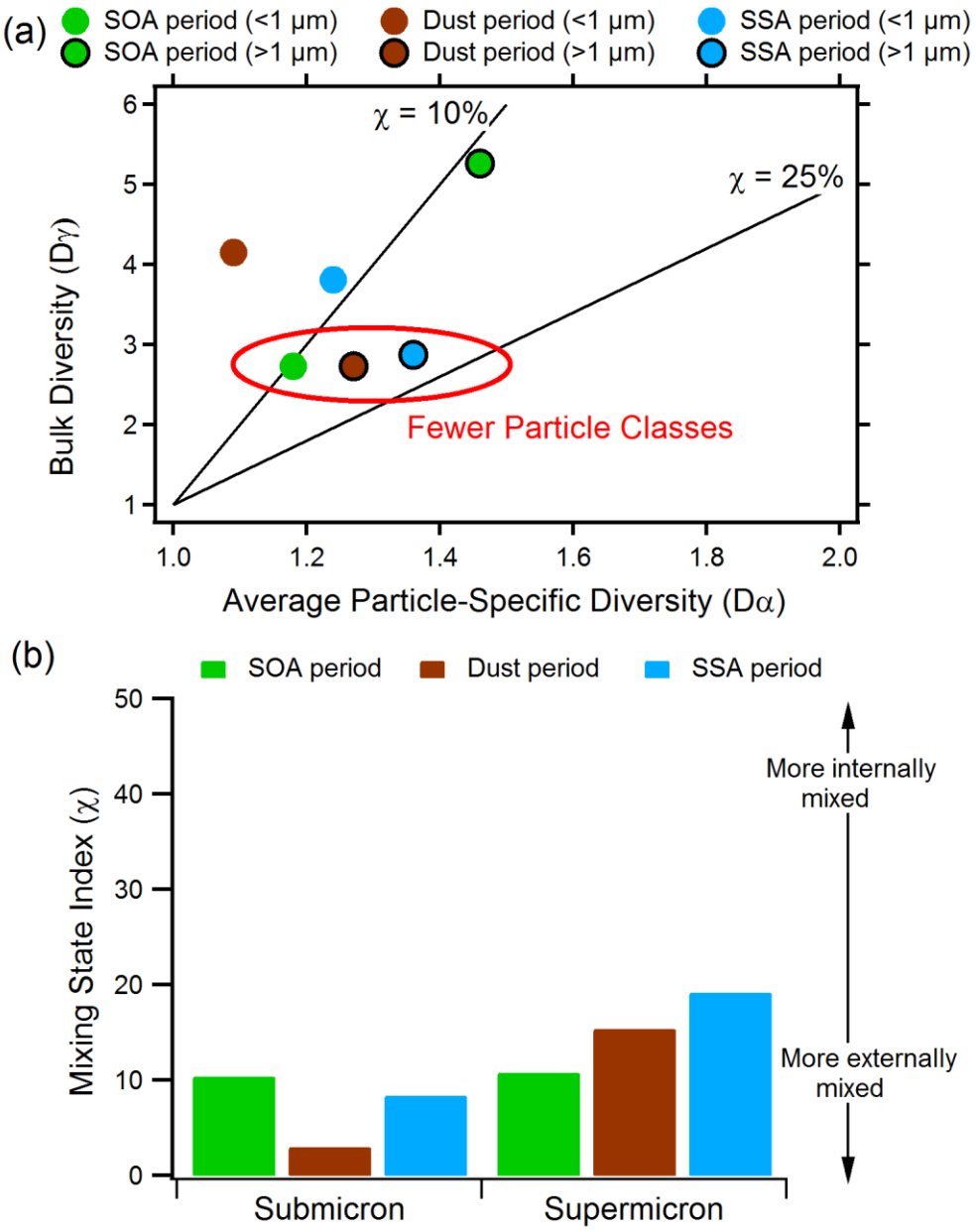

Figure 2.8. (a) Mixing state diagram showing the bulk diversity and average particle-specific diversity and (b) mixing state indices for sub- and supermicron particles during the SOA, dust, and SSA periods. For submicron particles, contributions by different sources impact mixing state.

Mixing state indices of this work are lower than previous reports by Fraund et al. (2017) and O'Brien et al. (2015) (χ > 80 % and χ > 40 %, respectively), who used CCSEM-EDX and STXM-NEXAFS to analyze particles collected in the Amazon and Central Valley, CA. In both studies, calculations using STXM-NEXAFS resulted in low diversity and high mixing state

indices, likely due to the inclusion of organic carbon, which increased particle homogeneity. O'Brien et al. also calculated mixing state indices using solely CCSEM-EDX, similar to our study. From this method, O'Brien found lower mixing state indices using CCSEM-EDX (χ = 41-90 %) compared to mixing state index calculations from STXM-NEXAFS results (χ > 60 %). However, the mixing state index in this previous work increased during high SSA periods and periods characterized by increased mass fractions of K, Ca, Zn, and Al, suggesting that periods with higher average particle-specific diversity were more homogeneous, simply because they contained more elements than periods dominated by carbonaceous particles. To improve upon this inherent challenge associated with quantifying mixing state using CCSEM-EDX, in the current study we calculate mixing state based on the number of particle classes and secondary species (in this study, sulfur) rather than the number of elements within particles. Quantifying mixing state parameters using this approach is consistent with our concept of atmospheric aging since the mixing state index increases as bulk diversity decreases and the mass fraction of secondary species increases, signifying aging increases the degree of internal mixing in a population. This method quantifying aerosol mixing state using single particle methods can be used to show the varying impact of sources and aging between different air masses at the same location.

2.4. Conclusions

Even at rural locations, a variety of particle classes with complex chemical mixing states can contribute to the aerosol population, impacting climate direct and indirect effects. During the SOAS field campaign in Centreville, Alabama, CCSEM-EDX analysis identified the following particle classes: biological, mineral dust, SSA, fly ash, biomass burning aerosol particles, SOA/sulfate, and fresh soot. Although SOA/sulfate dominated the overall aerosol distribution, especially in the accumulation mode (0.2-1.0 μm), it was found to be present at supermicron sizes as well. Additionally, while biological particles, mineral dust, and SSA dominated the supermicron regime, mineral dust and SSA were also observed as significant particle fractions in the accumulation mode. While some of the particle classes indicate nearby regional sources, such as fly ash transported from nearby cities and SOA/sulfate formed from the interaction of biogenic VOCs and anthropogenic pollutants, other classes point toward longer range transport such as SSA transported from the Gulf of Mexico. From the single particle chemical analysis

conducted, complex chemical mixing states of particles with secondary processing by sulfur were observed. Finally, even though the sampling site in Centreville was located in a relatively remote region, long and short range transport of particles was evident based on not only the wide variety of particle classes and degrees of aging within each class, but also on the variation in number concentration over time. The average mass fraction of sulfur within every particle class, aside from primary biological particles, was greater during more stagnant conditions, leading to more internally mixed particle populations.

These findings provide quantitative metrics of the diversity in particle composition and their mixing states characteristic of the southeastern United States, suggesting that many factors and classes of particles beyond SOA/sulfate contribute to the atmospheric aerosol in this region. Submicron mineral dust and SSA may be previously underrepresented sources of CCN in this region, though they are not effectively measured by instruments that only measure non-refractory particles. Although not highly prevalent, ~8 % of SOA by number were found to contain soot inclusions, indicating that some SOA/sulfate may actually absorb in addition to scattering solar radiation, a factor which needs to be considered to accurately model radiative transfer. Additionally, since most of the particles in this region have been chemically aged with sulfuric acid/SO_2, their hygroscopicity and propensity to form CCN will be altered compared to their fresh counterparts. With this information detailing the particle classes and the mixing states during SOAS, further studies can be conducted and inputs for models can be generated to more accurately assess effects of aerosols on climate in this unique region.

2.5. Acknowledgements

This work was supported by startup funds from the University of Michigan. The authors wish to acknowledge EPA (R835409) and NSF (AGS1228496) for providing funding for SOAS sampling. The CCSEM-EDX research was performed at the Environmental Molecular Sciences Laboratory (EMSL), a science user facility located at the Pacific Northwest National Laboratory (PNNL), sponsored by the Office of Biological and Environmental Research of the U.S Department of Energy. PNNL is operated for DOE by Battelle Memorial Institute under contract number DE-AC06-76RL0 1830. Travel funds to PNNL were provided by UM Rackham Graduate School and the UM Office of the Provost. The STXM-NEXAFS particle analysis was performed at beamline 5.3.2 at the Advanced Light Source (ALS) at Lawrence Berkeley

National Laboratory. Additionally, we thank Ann Marie Carlton (Rutgers University, now UC-Irvine), Lindsay Yee (UC-Berkeley), Allen Goldstein (UC-Berkeley), and Jason Surratt (UNC-Chapel Hill) for organizing SOAS and filter sampling, Steven Bertman (Western Michigan University) for field study logistics, as well as Karsten Baumann, and others and for logistical assistance.

2.6. References

Allen, H. M., Draper, D. C., Ayres, B. R., Ault, A. P., Bondy, A. L., Takahama, S., Modini, R. L., Baumann, K., Edgerton, E., Knote, C., Laskin, A., Wang, B., and Fry, J. L.: Influence of crustal dust and sea spray supermicron particle concentrations and acidity on inorganic NO_3^- aerosol during the 2013 Southern Oxidant and Aerosol Study, Atmos. Chem. Phys., 15, 10669-10685, 2015.

Anttila, T., Kiendler-Scharr, A., Mentel, T. F., and Tillmann, R.: Size dependent partitioning of organic material: evidence for the formation of organic coatings on aqueous aerosols, J. Atmos. Chem., 57, 215-237, 2007.

Artaxo, P., and Orsini, C.: PIXE and receptor models applied to remote aerosol source apportionment in Brazil, Nucl. Instrum. Methods Phys. Res., Sect. B, 22, 259-263, 1987.

Attwood, A. R., Washenfelder, R. A., Brock, C. A., Hu, W., Baumann, K., Campuzano-Jost, P., Day, D. A., Edgerton, E. S., Murphy, D. M., Palm, B. B., McComiskey, A., Wagner, N. L., de Sá, S. S., Ortega, A., Martin, S. T., Jimenez, J. L., and Brown, S. S.: Trends in sulfate and organic aerosol mass in the Southeast U.S.: Impact on aerosol optical depth and radiative forcing, Geophys. Res. Lett., 41, 7701-7709, 2014.

Ault, A. P., Peters, T. M., Sawvel, E. J., Casuccio, G. S., Willis, R. D., Norris, G. A., and Grassian, V. H.: Single-particle SEM-EDX analysis of iron-containing coarse particulate matter in an urban environment: Sources and distribution of iron within Cleveland, Ohio, Environ. Sci. Technol., 46, 4331-4339, 2012.

Ault, A. P., and Axson, J. L.: Atmospheric aerosol chemistry: Spectroscopic and microscopic advances, Anal. Chem., 89, 430-452, 2017.

Axson, J. L., Shen, H. R., Bondy, A. L., Landry, C. C., Welz, J., Creamean, J. M., and Ault, A. P.: Transported mineral dust deposition case study at a hydrologically sensitive mountain site: Size and composition shifts in ambient aerosol and snowpack, Aerosol Air Qual. Res., 16, 555-567, 2016.

Ayres, B. R., Allen, H. M., Draper, D. C., Brown, S. S., Wild, R. J., Jimenez, J. L., Day, D. A., Campuzano-Jost, P., Hu, W., de Gouw, J., Koss, A., Cohen, R. C., Duffey, K. C., Romer, P., Baumann, K., Edgerton, E., Takahama, S., Thornton, J. A., Lee, B. H., Lopez-Hilfiker, F. D., Mohr, C., Wennberg, P. O., Nguyen, T. B., Teng, A., Goldstein, A. H., Olson, K., and Fry, J. L.: Organic nitrate aerosol formation via NO_3 + biogenic volatile organic compounds in the southeastern United States, Atmos. Chem. Phys., 15, 13377-13392, 2015.

Bondy, A. L., Kirpes, R. M., Merzel, R. L., Pratt, K. A., Banaszak Holl, M. M., and Ault, A. P.: Atomic force microscopy-infrared spectroscopy of individual atmospheric aerosol particles: Subdiffraction limit vibrational spectroscopy and morphological analysis, Anal. Chem., 89, 8594-8598, 2017a.

Bondy, A. L., Wang, B., Laskin, A., Craig, R. L., Nhliziyo, M. V., Bertman, S. B., Pratt, K. A., Shepson, P. B., and Ault, A. P.: Inland sea spray aerosol transport and incomplete chloride depletion: Varying degrees of reactive processing observed during SOAS, Environ. Sci. Technol., 51, 9533-9542, 2017b.

Boone, E. J., Laskin, A., Laskin, J., Wirth, C., Shepson, P. B., Stirm, B. H., and Pratt, K. A.: Aqueous processing of atmospheric organic particles in cloud water collected via aircraft sampling, Environ. Sci. Technol., 49, 8523-8530, 2015.

Boyd, C. M., Sanchez, J., Xu, L., Eugene, A. J., Nah, T., Tuet, W. Y., Guzman, M. I., and Ng, N. L.: Secondary organic aerosol formation from the β-pinene+NO_3 system: Effect of humidity and peroxy radical fate, Atmos. Chem. Phys., 15, 7497-7522, 2015.

Budisulistiorini, S. H., Li, X., Bairai, S. T., Renfro, J., Liu, Y., Liu, Y. J., McKinney, K. A., Martin, S. T., McNeill, V. F., Pye, H. O. T., Nenes, A., Neff, M. E., Stone, E. A., Mueller, S., Knote, C., Shaw, S. L., Zhang, Z., Gold, A., and Surratt, J. D.: Examining the effects of anthropogenic emissions on isoprene-derived secondary organic aerosol formation during the 2013 Southern Oxidant and Aerosol Study (SOAS) at the Look Rock, Tennessee, ground site, Atmos. Chem. Phys. Discuss., 15, 7365-7417, 2015a.

Budisulistiorini, S. H., Li, X., Bairai, S. T., Renfro, J., Liu, Y., Liu, Y. J., McKinney, K. A., Martin, S. T., McNeill, V. F., Pye, H. O. T., Nenes, A., Neff, M. E., Stone, E. A., Mueller, S., Knote, C., Shaw, S. L., Zhang, Z., Gold, A., and Surratt, J. D.: Examining the effects of anthropogenic emissions on isoprene-derived secondary organic aerosol formation during the 2013 Southern Oxidant and Aerosol Study (SOAS) at the Look Rock, Tennessee ground site, Atmos. Chem. Phys., 15, 8871-8888, 2015b.

Buha, J., Mueller, N., Nowack, B., Ulrich, A., Losert, S., and Wang, J.: Physical and chemical characterization of fly ashes from swiss waste incineration plants and determination of the ash fraction in the nanometer range, Environ. Sci. Technol., 48, 4765-4773, 2014.

Carlton, A. G., Wiedinmyer, C., and Kroll, J. H.: A review of secondary organic aerosol (SOA) formation from isoprene, Atmos. Chem. Phys., 9, 4987-5005, 2009.

Carlton, A. G., Pinder, R. W., Bhave, P. V., and Pouliot, G. A.: To what extent can biogenic SOA be controlled?, Environ. Sci. Technol., 44, 3376-3380, 2010.

Cerully, K. M., Bougiatioti, A., Hite Jr, J. R., Guo, H., Xu, L., Ng, N. L., Weber, R., and Nenes, A.: On the link between hygroscopicity, volatility, and oxidation state of ambient and water-soluble aerosols in the southeastern United States, Atmos. Chem. Phys., 15, 8679-8694, 2015.

Chameides, W. L., Lindsay, R. W., Richardson, J., and Kiang, C. S.: The role of biogenic hydrocarbons in urban photochemical smog: Atlanta as a case study, Science, 241, 1473-1475, 1988.

Chang, R. Y. W., Slowik, J. G., Shantz, N. C., Vlasenko, A., Liggio, J., Sjostedt, S. J., Leaitch, W. R., and Abbatt, J. P. D.: The hygroscopicity parameter (kappa) of ambient organic aerosol at a field site subject to biogenic and anthropogenic influences: relationship to degree of aerosol oxidation, Atmos. Chem. Phys., 10, 5047, 2010.

Chen, H., Laskin, A., Baltrusaitis, J., Gorski, C. A., Scherer, M. M., and Grassian, V. H.: Coal fly ash as a source of iron in atmospheric dust, Environ. Sci. Technol., 46, 2112-2120, 2012.

Chen, J., Li, C., Ristovski, Z., Milic, A., Gu, Y., Islam, M. S., Wang, S., Hao, J., Zhang, H., He, C., Guo, H., Fu, H., Miljevic, B., Morawska, L., Thai, P., Lam, Y. F., Pereira, G., Ding, A., Huang, X., and Dumka, U. C.: A review of biomass burning: emissions and impacts on air quality, health and climate in China, Sci. Total Environ., 579, 1000-1034, 2017.

Chi, J. W., Li, W. J., Zhang, D. Z., Zhang, J. C., Lin, Y. T., Shen, X. J., Sun, J. Y., Chen, J. M., Zhang, X. Y., Zhang, Y. M., and Wang, W. X.: Sea salt aerosols as a reactive surface for inorganic and organic acidic gases in the Arctic troposphere, Atmos. Chem. Phys., 15, 11341-11353, 2015.

Chung, S. H., and Seinfeld, J. H.: Climate response of direct radiative forcing of anthropogenic black carbon, J. Geophys. Res.: Atmos., 110, 2005.

Cong, Z., Kang, S., Dong, S., Liu, X., and Qin, D.: Elemental and individual particle analysis of atmospheric aerosols from high Himalayas, Environ. Monit. Assess., 160, 323-335, 2010.

Conny, J. M., and Norris, G. A.: Scanning electron microanalysis and analytical challenges of mapping elements in urban atmospheric particles, Environ. Sci. Technol., 45, 7380-7386, 2011.

Coz, E., Gómez-Moreno, F. J., Pujadas, M., Casuccio, G. S., Lersch, T. L., and Artíñano, B.: Individual particle characteristics of North African dust under different long-range transport scenarios, Atmos. Environ., 43, 1850-1863, 2009.

Craig, R. L., Bondy, A. L., and Ault, A. P.: Computer-controlled Raman microspectroscopy (CC-Raman): A method for the rapid characterization of individual atmospheric aerosol particles, Aerosol Sci. Technol., 51, 1099-1112, 2017.

Creamean, J. M., Axson, J. L., Bondy, A. L., Craig, R. L., May, N. W., Shen, H., Weber, M. H., Pratt, K. A., and Ault, A. P.: Changes in precipitating snow chemistry with location and elevation in the California Sierra Nevada, J. Geophys. Res.: Atmos., 121, 7296-7309, 2016.

Deboudt, K., Gloter, A., Mussi, A., and Flament, P.: Red-ox speciation and mixing state of iron in individual African dust particles, J. Geophys. Res.: Atmos., 117, 2012.

Dickau, M., Olfert, J., Stettler, M. E. J., Boies, A., Momenimovahed, A., Thomson, K., Smallwood, G., and Johnson, M.: Methodology for quantifying the volatile mixing state of an aerosol, Aerosol Sci. Technol., 50, 759-772, 2016.

Estillore, A. D., Trueblood, J. V., and Grassian, V. H.: Atmospheric chemistry of bioaerosols: heterogeneous and multiphase reactions with atmospheric oxidants and other trace gases, Chemical Science, 7, 6604-6616, 2016.

Fitzgerald, E., Ault, A. P., Zauscher, M. D., Mayol-Bracero, O. L., and Prather, K. A.: Comparison of the mixing state of long-range transported Asian and African mineral dust, Atmos. Environ., 115, 19-25, 2015.

Fraund, M., Pham, D., Bonanno, D., Harder, T., Wang, B., Brito, J., de Sá, S., Carbone, S., China, S., Artaxo, P., Martin, S., Pöhlker, C., Andreae, M., Laskin, A., Gilles, M., and Moffet, R.: Elemental mixing state of aerosol particles collected in Central Amazonia during GoAmazon2014/15, Atmosphere, 8, 173, 2017.

Froyd, K. D., Murphy, S. M., Murphy, D. M., de Gouw, J. A., Eddingsaas, N. C., Wennberg, P. O., and Thiemens, M. H.: Contribution of isoprene-derived organosulfates to free tropospheric aerosol mass, Proc. Natl. Acad. Sci. U. S. A., 107, 21360-21365, 2010.

Fu, H., Zhang, M., Li, W., Chen, J., Wang, L., Quan, X., and Wang, W.: Morphology, composition and mixing state of individual carbonaceous aerosol in urban Shanghai, Atmos. Chem. Phys., 12, 693-707, 2012.

Gantt, B., and Meskhidze, N.: The physical and chemical characteristics of marine primary organic aerosol: A review, Atmos. Chem. Phys., 13, 3979-3996, 2013.

Ghorai, S., Wang, B., Tivanski, A., and Laskin, A.: Hygroscopic properties of internally mixed particles composed of NaCl and water-soluble organic acids, Environ. Sci. Technol., 48, 2234-2241, 2014.

Giordano, M., Espinoza, C., and Asa-Awuku, A.: Experimentally measured morphology of biomass burning aerosol and its impacts on CCN ability, Atmos. Chem. Phys., 15, 1807-1821, 2015.

Giorio, C., Tapparo, A., Dall'Osto, M., Beddows, D. C. S., Esser-Gietl, J. K., Healy, R. M., and Harrison, R. M.: Local and regional components of aerosol in a heavily trafficked street canyon in central London derived from PMF and cluster analysis of single-particle ATOFMS spectra, Environ. Sci. Technol., 49, 3330-3340, 2015.

Goldstein, A. H., Koven, C. D., Heald, C. L., and Fung, I. Y.: Biogenic carbon and anthropogenic pollutants combine to form a cooling haze over the southeastern United States, Proc. Natl. Acad. Sci. U. S. A., 106, 8835-8840, 2009.

Guo, H., Xu, L., Bougiatioti, A., Cerully, K. M., Capps, S. L., Hite, J. R., Jr., Carlton, A. G., Lee, S. H., Bergin, M. H., Ng, N. L., Nenes, A., and Weber, R. J.: Fine-particle water and pH in the southeastern United States, Atmos. Chem. Phys., 15, 5211-5228, 2015.

Guo, H., Nenes, A., and Weber, R. J.: The underappreciated role of nonvolatile cations on aerosol ammonium-sulfate molar ratios, Atmos. Chem. Phys. Discuss., 2017, 1-19, 2017.

Hashemi, S. S., Baghernejad, M., and Khademi, H.: Micromorphology of gypsum crystals in southern Iranian soils under different moisture regimes, J. Agric. Sci. Technol., 13, 273-288, 2011.

Healy, R. M., Evans, G. J., Murphy, M., Juranyi, Z., Tritscher, T., Laborde, M., Weingartner, E., Gysel, M., Poulain, L., Kamilli, K. A., Wiedensohler, A., O'Connor, I. P., McGillicuddy, E., Sodeau, J. R., and Wenger, J. C.: Predicting hygroscopic growth using single particle chemical composition estimates, J. Geophys. Res.: Atmos., 119, 9567-9577, 2014a.

Healy, R. M., Riemer, N., Wenger, J. C., Murphy, M., West, M., Poulain, L., Wiedensohler, A., O'Connor, I. P., McGillicuddy, E., Sodeau, J. R., and Evans, G. J.: Single particle diversity and mixing state measurements, Atmos. Chem. Phys., 14, 6289-6299, 2014b.

Healy, R. M., Wang, J. M., Jeong, C. H., Lee, A. K. Y., Willis, M. D., Jaroudi, E., Zimmerman, N., Hilker, N., Murphy, M., Eckhardt, S., Stohl, A., Abbatt, J. P. D., Wenger, J. C., and Evans, G. J.: Light-absorbing properties of ambient black carbon and brown carbon from fossil fuel and biomass burning sources, J. Geophys. Res.: Atmos., 120, 6619-6633, 2015.

Hidy, G. M., Blanchard, C. L., Baumann, K., Edgerton, E., Tanenbaum, S., Shaw, S., Knipping, E., Tombach, I., Jansen, J., and Walters, J.: Chemical climatology of the southeastern United States, 1999-2013, Atmos. Chem. Phys., 14, 11893-11914, 2014.

Hinds, W. C.: Aerosol Technology Properties, Behavior, and Measurement of Airborne Particles, 2nd ed., John Wiley & Sons, Inc., New York, 1999.

Hiranuma, N., Brooks, S. D., Moffet, R. C., Glen, A., Laskin, A., Gilles, M. K., Liu, P., Macdonald, A. M., Strapp, J. W., and McFarquhar, G. M.: Chemical characterization of

individual particles and residuals of cloud droplets and ice crystals collected on board research aircraft in the ISDAC 2008 study, J. Geophys. Res.: Atmos., 118, 6564-6579, 2013.

Hodas, N., Sullivan, A. P., Skog, K., Keutsch, F. N., Collett, J. L., Decesari, S., Facchini, M. C., Carlton, A. G., Laaksonen, A., and Turpin, B. J.: Aerosol liquid water driven by anthropogenic nitrate: implications for lifetimes of water-soluble organic gases and potential for secondary organic aerosol formation, Environ. Sci. Technol., 48, 11127-11136, 2014.

Hopkins, R. J., Desyaterik, Y., Tivanski, A. V., Zaveri, R. A., Berkowitz, C. M., Tyliszczak, T., Gilles, M. K., and Laskin, A.: Chemical speciation of sulfur in marine cloud droplets and particles: Analysis of individual particles from the marine boundary layer over the California current, J. Geophys. Res.: Atmos., 113, 2008.

Hu, W. W., Campuzano-Jost, P., Palm, B. B., Day, D. A., Ortega, A. M., Hayes, P. L., Krechmer, J. E., Chen, Q., Kuwata, M., Liu, Y. J., de Sá, S. S., McKinney, K., Martin, S. T., Hu, M., Budisulistiorini, S. H., Riva, M., Surratt, J. D., St. Clair, J. M., Isaacman-Van Wertz, G., Yee, L. D., Goldstein, A. H., Carbone, S., Brito, J., Artaxo, P., de Gouw, J. A., Koss, A., Wisthaler, A., Mikoviny, T., Karl, T., Kaser, L., Jud, W., Hansel, A., Docherty, K. S., Alexander, M. L., Robinson, N. H., Coe, H., Allan, J. D., Canagaratna, M. R., Paulot, F., and Jimenez, J. L.: Characterization of a real-time tracer for isoprene epoxydiols-derived secondary organic aerosol (IEPOX-SOA) from aerosol mass spectrometer measurements, Atmos. Chem. Phys., 15, 11807-11833, 2015.

Huffman, J. A., Sinha, B., Garland, R. M., Snee-Pollmann, A., Gunthe, S. S., Artaxo, P., Martin, S. T., Andreae, M. O., and Pöschl, U.: Size distributions and temporal variations of biological aerosol particles in the Amazon rainforest characterized by microscopy and real-time UV-APS fluorescence techniques during AMAZE-08, Atmos. Chem. Phys., 12, 11997, 2012.

Jacobson, M. Z. Z.: Strong radiative heating due to the mixing state of black carbon in atmospheric aerosols, Nature (London), 409, 695-697, 2001.

Kandler, K., Lieke, K., Benker, N., Emmel, C., Küpper, M., Müller-Ebert, D., Ebert, M., Scheuvens, D., Schladitz, A., Schütz, L., and Weinbruch, S.: Electron microscopy of particles collected at Praia, Cape Verde, during the Saharan Mineral Dust Experiment: particle chemistry, shape, mixing state and complex refractive index, Tellus B, 63, 2011.

Kilcoyne, A. L. D., Tyliszczak, T., Steele, W. F., Fakra, S., Hitchcock, P., Franck, K., Anderson, E., Harteneck, B., Rightor, E. G., Mitchell, G. E., Hitchcock, A. P., Yang, L., Warwick, T., and Ade, H.: Interferometer-controlled scanning transmission X-ray microscopes at the Advanced Light Source, Journal of Synchrotron Radiation, 10, 125-136, 2003.

Kim, J.-S., and Park, K.: Atmospheric aging of Asian dust particles during long range transport, Aerosol Sci. Technol., 46, 913-924, 2012.

Kunkel, D., Lawrence, M. G., Tost, H., Kerkweg, A., Jockel, P., and Borrmann, S.: Urban emission hot spots as sources for remote aerosol deposition, Geophys. Res. Lett., 39, 2012.

Laskin, A., Iedema, M. J., and Cowin, J. P.: Quantitative time-resolved monitoring of nitrate formation in sea salt particles using a CCSEM/EDX single particle analysis, Environ. Sci. Technol., 36, 4948-4955, 2002.

Laskin, A., Iedema, M. J., Ichkovich, A., Graber, E. R., Taraniuk, I., and Rudich, Y.: Direct observation of completely processed calcium carbonate dust particles, Faraday Discuss., 130, 453-468, 2005.

Laskin, A., Cowin, J. P., and Iedema, M. J.: Analysis of individual environmental particles using modern methods of electron microscopy and X-ray microanalysis, J. Electron. Spectrosc. Relat. Phenom., 150, 260-274, 2006.

Laskin, A., Moffet, R. C., Gilles, M. K., Fast, J. D., Zaveri, R. A., Wang, B., Nigge, P., and Shutthanandan, J.: Tropospheric chemistry of internally mixed sea salt and organic particles: Surprising reactivity of NaCl with weak organic acids, J. Geophys. Res.: Atmos., 117, 2012.

Lee, S., Wang, Y. H., and Russell, A. G.: Assessment of secondary organic carbon in the southeastern United States: A review, Journal of the Air & Waste Management Association, 60, 1282-1292, 2010.

Li, C., Hu, Y., Chen, J., Ma, Z., Ye, X., Yang, X., Wang, L., Wang, X., and Mellouki, A.: Physiochemical properties of carbonaceous aerosol from agricultural residue burning: Density, volatility, and hygroscopicity, Atmos. Environ., 140, 94-105, 2016.

Li, J., Posfai, M., Hobbs, P. V., and Buseck, P. R.: Individual aerosol particles from biomass burning in southern Africa: 2, Compositions and aging of inorganic particles, J. Geophys. Res.: Atmos., 108, 2003.

Li, W., Shao, L., Zhang, D., Ro, C.-U., Hu, M., Bi, X., Geng, H., Matsuki, A., Niu, H., and Chen, J.: A review of single aerosol particle studies in the atmosphere of East Asia: Morphology, mixing state, source, and heterogeneous reactions, J. Cleaner Prod., http://dx.doi.org/10.1016/j.jclepro.2015.04.050

Li, W., Xu, L., Liu, X., Zhang, J., Lin, Y., Yao, X., Gao, H., Zhang, D., Chen, J., Wang, W., Harrison, R. M., Zhang, X., Shao, L., Fu, P., Nenes, A., and Shi, Z.: Air pollution–aerosol interactions produce more bioavailable iron for ocean ecosystems, Sci. Adv., 3, 2017.

Lu, J. W., Flores, J. M., Lavi, A., Abo-Riziq, A., and Rudich, Y.: Changes in the optical properties of benzo[a]pyrene-coated aerosols upon heterogeneous reactions with NO_2 and NO_3, PCCP, 13, 6484-6492, 2011.

Manninen, H. E., Back, J., Sihto-Nissila, S. L., Huffman, J. A., Pessi, A. M., Hiltunen, V., Aalto, P. P., Hidalgo, P. J., Hari, P., Saarto, A., Kulmala, M., and Petaja, T.: Patterns in airborne pollen and other primary biological aerosol particles (PBAP), and their contribution to aerosol mass and number in a boreal forest, Boreal Environment Research, 19, 383-405, 2014.

Marple, V. A., Rubow, K. L., and Behm, S. M.: A microorifice uniform deposit impactor (MOUDI)-description, calibration and use, Aerosol Sci. Technol., 14, 434-446, 1991.

Metternich, P., Georgii, H. W., and Groeneveld, K. O.: Application of particle induced X-ray emission to aerosol long-range transport studies—transport pathways of pollution aerosol over the Atlantic ocean and Europe, Atmos. Res., 20, 3-9, 1986.

Moffet, R. C., Prather, K. A., and Thiemens, M. H.: In-situ measurements of the mixing state and optical properties of soot with implications for radiative forcing estimates, Proc. Natl. Acad. Sci. U. S. A., 106, 11872-11877, 2009.

Moffet, R. C., Henn, T., Laskin, A., and Gilles, M. K.: Automated chemical analysis of internally mixed aerosol particles using X-ray spectromicroscopy at the carbon K-edge, Anal. Chem., 82, 7906-7914, 2010a.

Moffet, R. C., Henn, T. R., Tivanski, A. V., Hopkins, R. J., Desyaterik, Y., Kilcoyne, A. L. D., Tyliszczak, T., Fast, J., Barnard, J., Shutthanandan, V., Cliff, S. S., Perry, K. D., Laskin, A., and Gilles, M. K.: Microscopic characterization of carbonaceous aerosol particle aging in the outflow from Mexico City, Atmos. Chem. Phys., 10, 961-976, 2010b.

Moffet, R. C., Roedel, T. C., Kelly, S. T., Yu, X. Y., Carroll, G. T., Fast, J., Zaveri, R. A., Laskin, A., and Gilles, M. K.: Spectro-microscopic measurements of carbonaceous aerosol aging in central California, Atmos. Chem. Phys., 13, 10445-10459, 2013.

Moffet, R. C., O'Brien, R. E., Alpert, P. A., Kelly, S. T., Pham, D. Q., Gilles, M. K., Knopf, D. A., and Laskin, A.: Morphology and mixing of black carbon particles collected in central California during the CARES field study, Atmos. Chem. Phys., 16, 14515-14525, 2016.

Moise, T., Flores, J. M., and Rudich, Y.: Optical properties of secondary organic aerosols and their changes by chemical processes, Chem. Rev., 115, 4400-4439, 2015.

Nakao, S., Tang, P., Tang, X., Clark, C. H., Qi, L., Seo, E., Asa-Awuku, A., and Cocker Iii, D.: Density and elemental ratios of secondary organic aerosol: Application of a density prediction method, Atmos. Environ., 68, 273-277, 2013.

Nguyen, T. K. V., Petters, M. D., Suda, S. R., Guo, H., Weber, R. J., and Carlton, A. G.: Trends in particle-phase liquid water during the Southern Oxidant and Aerosol Study, Atmos. Chem. Phys., 14, 10911-10930, 2014.

Nguyen, T. K. V., Capps, S. L., and Carlton, A. G.: Decreasing aerosol water is consistent with OC trends in the southeast U.S, Environ. Sci. Technol., 49, 7843-7850, 2015.

O'Brien, R. E., Wang, B., Laskin, A., Riemer, N., West, M., Zhang, Q., Sun, Y., Yu, X.-Y., Alpert, P., Knopf, D. A., Gilles, M. K., and Moffet, R. C.: Chemical imaging of ambient aerosol particles: Observational constraints on mixing state parameterization, J. Geophys. Res.: Atmos., 120, 9591-9605, 2015.

Perlwitz, J. P., Pérez García-Pando, C., and Miller, R. L.: Predicting the mineral composition of dust aerosols – Part 1: Representing key processes, Atmos. Chem. Phys., 15, 11593-11627, 2015.

Pilson, M. E. Q.: An introduction to the chemistry of the sea, Cambridge University Press, 1998.

Portmann, R. W., Solomon, S., Hegerl, G. C., and Held, I. M.: Spatial and seasonal patterns in climate change, temperatures, and precipitation across the United States, Proc. Natl. Acad. Sci. U. S. A., 106, 7324-7329, 2009.

Posfai, M., Simonics, R., Li, J., Hobbs, P. V., and Buseck, P. R.: Individual aerosol particles from biomass burning in southern Africa: 1. Compositions and size distributions of carbonaceous particles, J. Geophys. Res.: Atmos., 108, 2003.

Posfai, M., and Buseck, P. R.: Nature and climate dffects of individual tropospheric aerosol particles, in: Annual Review of Earth and Planetary Sciences, Vol 38, edited by: Jeanloz, R., and Freeman, K. H., Annual Review of Earth and Planetary Sciences, 17-43, 2010.

Pratt, K. A., and Prather, K. A.: Aircraft measurements of vertical profiles of aerosol mixing states, J. Geophys. Res.: Atmos., 115, 2010.

Pye, H. O. T., Luecken, D. J., Xu, L., Boyd, C. M., Ng, N. L., Baker, K. R., Ayres, B. R., Bash, J. O., Baumann, K., Carter, W. P. L., Edgerton, E., Fry, J. L., Hutzell, W. T., Schwede, D. B., and Shepson, P. B.: Modeling the current and future roles of particulate organic nitrates in the southeastern United States, Environ. Sci. Technol., 49, 14195-14203, 2015.

Ramanathan, V., and Carmichael, G.: Global and regional climate changes due to black carbon, Nature Geosci., 1, 221-227, 2008.

Rattanavaraha, W., Chu, K., Budisulistiorini, S. H., Riva, M., Lin, Y. H., Edgerton, E. S., Baumann, K., Shaw, S. L., Guo, H., King, L., Weber, R. J., Neff, M. E., Stone, E. A., Offenberg, J. H., Zhang, Z., Gold, A., and Surratt, J. D.: Assessing the impact of anthropogenic pollution on isoprene-derived secondary organic aerosol formation in $PM_{2.5}$ collected from the Birmingham, Alabama, ground site during the 2013 Southern Oxidant and Aerosol Study, Atmos. Chem. Phys., 16, 4897-4914, 2016.

Riemer, N., and West, M.: Quantifying aerosol mixing state with entropy and diversity measures, Atmos. Chem. Phys., 13, 11423-11439, 2013.

Riva, M., Budisulistiorini, S. H., Zhang, Z., Gold, A., and Surratt, J. D.: Chemical characterization of secondary organic aerosol constituents from isoprene ozonolysis in the presence of acidic aerosol, Atmos. Environ., 130, 5-13, 2016.

Robinson, C. B., Schill, G. P., Zarzana, K. J., and Tolbert, M. A.: Impact of organic coating on optical growth of ammonium sulfate particles, Environ. Sci. Technol., 47, 13339-13346, 2013.

Saxena, V. K., and Yu, S. C.: Searching for a regional fingerprint of aerosol radiative forcing in the southeastern US, Geophys. Res. Lett., 25, 2833-2836, 1998.

Schutgens, N. A. J., and Stier, P.: A pathway analysis of global aerosol processes, Atmos. Chem. Phys., 14, 11657-11686, 2014.

Sedlacek, A. J., III, Lewis, E. R., Kleinman, L., Xu, J., and Zhang, Q.: Determination of and evidence for non-core-shell structure of particles containing black carbon using the Single-Particle Soot Photometer (SP2), Geophys. Res. Lett., 39, 2012.

Shen, H. R., Peters, T. M., Casuccio, G. S., Lersch, T. L., West, R. R., Kumar, A., Kumar, N., and Ault, A. P.: Elevated concentrations of lead in particulate matter on the neighborhood-scale in Delhi, India as determined by single particle analysis, Environ. Sci. Technol., 50, 4961-4970, 2016.

Sobanska, S., Coeur, C., Maenhaut, W., and Adams, F.: SEM-EDX characterisation of tropospheric aerosols in the Negev desert (Israel), J. Atmos. Chem., 44, 299-322, 2003.

Sobanska, S., Hwang, H., Choel, M., Jung, H.-J., Eom, H.-J., Kim, H., Barbillat, J., and Ro, C.-U.: Investigation of the chemical mixing state of individual Asian dust particles by the combined use of electron probe X-ray microanalysis and Raman microspectrometry, Anal. Chem., 84, 3145-3154, 2012.

Song, C. H., Kim, C. M., Lee, Y. J., Carmichael, G. R., Lee, B. K., and Lee, D. S.: An evaluation of reaction probabilities of sulfate and nitrate precursors onto East Asian dust particles, J. Geophys. Res.: Atmos., 112, 2007.

Sullivan, R. C., Guazzotti, S. A., Sodeman, D. A., and Prather, K. A.: Direct observations of the atmospheric processing of Asian mineral dust, Atmos. Chem. Phys., 7, 1213-1236, 2007.

Sullivan, R. C., Moore, M. J. K., Petters, M. D., Kreidenweis, S. M., Roberts, G. C., and Prather, K. A.: Effect of chemical mixing state on the hygroscopicity and cloud nucleation properties of calcium mineral dust particles, Atmos. Chem. Phys., 9, 3303-3316, 2009.

Tang, M. J., Cziczo, D. J., and Grassian, V. H.: Interactions of water with mineral dust aerosol: Water adsorption, hygroscopicity, cloud condensation, and ice nucleation, Chem. Rev., 116, 4205-4259, 2016.

Violaki, K., and Mihalopoulos, N.: Water-soluble organic nitrogen (WSON) in size-segregated atmospheric particles over the Eastern Mediterranean, Atmos. Environ., 44, 4339-4345, 2010.

Wagner, F., Bortoli, D., Pereira, S., Costa, M. J., Silva, A. M., Weinzierl, B., Esselborn, M., Petzold, A., Rasp, K., Heinold, B., and Tegen, I. N. A.: Properties of dust aerosol particles transported to Portugal from the Sahara desert, Tellus B, 61, 297-306, 2009.

Weber, R. J., Sullivan, A. P., Peltier, R. E., Russell, A., Yan, B., Zheng, M., de Gouw, J., Warneke, C., Brock, C., Holloway, J. S., Atlas, E. L., and Edgerton, E.: A study of secondary organic aerosol formation in the anthropogenic-influenced southeastern United States, J. Geophys. Res.: Atmos., 112, 2007.

Weingartner, E., Burtscher, H., and Baltensperger, U.: Hygroscopic properties of carbon and diesel soot particles, Atmos. Environ., 31, 2311-2327, 1997.

Xiong, F., McAvey, K. M., Pratt, K. A., Groff, C. J., Hostetler, M. A., Lipton, M. A., Starn, T. K., Seeley, J. V., Bertman, S. B., Teng, A. P., Crounse, J. D., Nguyen, T. B., Wennberg, P. O., Misztal, P. K., Goldstein, A. H., Guenther, A. B., Koss, A. R., Olson, K. F., de Gouw, J. A., Baumann, K., Edgerton, E. S., Feiner, P. A., Zhang, L., Miller, D. O., Brune, W. H., and Shepson, P. B.: Observation of isoprene hydroxynitrates in the southeastern United States and implications for the fate of NO_x, Atmos. Chem. Phys., 15, 11257-11272, 2015.

Xu, J. Z., Zhang, Q., Wang, Z. B., Yu, G. M., Ge, X. L., and Qin, X.: Chemical composition and size distribution of summertime $PM_{2.5}$ at a high altitude remote location in the northeast of the Qinghai-Xizang (Tibet) Plateau: Insights into aerosol sources and processing in free troposphere, Atmos. Chem. Phys., 15, 5069-5081, 2015a.

Xu, L., Guo, H., Boyd, C. M., Klein, M., Bougiatioti, A., Cerully, K. M., Hite, J. R., Isaacman-VanWertz, G., Kreisberg, N. M., Knote, C., Olson, K., Koss, A., Goldstein, A. H., Hering, S. V., de Gouw, J., Baumann, K., Lee, S.-H., Nenes, A., Weber, R. J., and Ng, N. L.: Effects of anthropogenic emissions on aerosol formation from isoprene and monoterpenes in the southeastern United States, Proc. Natl. Acad. Sci., 112, 37-42, 2015b.

Xu, L., Suresh, S., Guo, H., Weber, R. J., and Ng, N. L.: Aerosol characterization over the southeastern United States using high-resolution aerosol mass spectrometry: spatial and seasonal variation of aerosol composition and sources with a focus on organic nitrates, Atmos. Chem. Phys., 15, 7307-7336, 2015c.

Xu, L., Guo, H., Weber, R. J., and Ng, N. L.: Chemical characterization of water-soluble organic aerosol in contrasting rural and urban environments in the southeastern United States, Environ. Sci. Technol., 51, 78-88, 2017.

Zaveri, R. A., Barnard, J. C., Easter, R. C., Riemer, N., and West, M.: Particle-resolved simulation of aerosol size, composition, mixing state, and the associated optical and cloud condensation nuclei activation properties in an evolving urban plume, J. Geophys. Res.: Atmos., 115, 2010.

Zhang, R., Khalizov, A. F., Pagels, J., Zhang, D., Xue, H., and McMurry, P. H.: Variability in morphology, hygroscopicity, and optical properties of soot aerosols during atmospheric processing, Proc. Natl. Acad. Sci. U. S. A., 105, 10291-10296, 2008.

Chapter 3.
Inland Sea Spray Aerosol Transport and Incomplete Chloride Depletion: Varying Degrees of Reactive Processing Observed during SOAS

Adapted with permission from Bondy, A. L., Wang, B., Laskin, A., Craig, R. L., Nhliziyo, M. V., Bertman, S. B., Pratt, K. A., Shepson, P. B., and Ault, A. P.: Inland sea spray aerosol transport and incomplete chloride depletion: Varying degrees of reactive processing observed during SOAS, Environ. Sci. Technol., 51, 9533-9542, 2017.

3.1. Introduction

Reactions of sea spray aerosol (SSA) with inorganic acids (HNO_3 and H_2SO_4) have long been observed in the polluted marine atmosphere and through controlled laboratory experiments (Ault et al., 2013a; Gard et al., 1998; Hopkins et al., 2008; De Haan et al., 1999; Ravishankara and Longfellow, 1999; Reid and Sayer, 2002; Rossi, 2003; Gibson et al., 2006; Finlayson-Pitts, 2009; Allen et al., 1996; Ault et al., 2014; Duce, 1969; Robbins et al., 1959; Martens et al., 1973; Clarke and Radojevic, 1984; Okada et al., 1978; Mamane and Gottlieb, 1990; Mamane and Mehler, 1987; McInnes et al., 1994; Sievering et al., 1991; Cadle, 1972; ten Brink, 1998; Pakkanen, 1996; Odowd et al., 1997; Ravishankara, 1997; Keene et al., 1990). Through multiphase reactions with key pollutants (NO_x and SO_2) and their oxidation products, SSA can impact nitrogen, sulfur, and oxidant budgets (Rossi, 2003; Ravishankara, 1997; Pakkanen, 1996; De Haan et al., 1999; Finlayson-Pitts, 2009; Schroeder and Urone, 1974; Pósfai et al., 1994). In addition to acting as a sink, particle phase SSA reactions are also a source of halogen gases (HCl, Cl_2, $ClNO_2$, etc.) (Finlayson-Pitts et al., 1989; Eldering et al., 1991; Roberts et al., 2008; Clegg and Brimblecombe, 1985; Robbins et al., 1959; Dasgupta et al., 2007; Keene et al., 1990). A generalized acid reaction leading to the release of $HCl_{(g)}$ is shown in Reaction 1 where HA denotes atmospheric acids such as HNO_3, H_2SO_4, or CH_3SO_2OH.

$$HA_{(g,\,aq)} + NaCl_{(aq,s)} \rightarrow NaA_{(aq,s)} + HCl_{(g)} \quad (1)$$

Chloride displacement by liberation of $HCl_{(g)}$ in individual SSA has been observed from heterogeneous reactions of SSA with nitric acid (Gard et al., 1998; Clegg and Brimblecombe, 1985; Robbins et al., 1959; Eldering et al., 1991). This prominent SSA multiphase reaction has been widely studied and modeled (Roth and Okada, 1998; Kerminen et al., 1998; Pakkanen, 1996; Zhuang et al., 1999; McInnes et al., 1994; Eldering et al., 1991; Liu et al., 2007; Mamane and Gottlieb, 1990; Saul et al., 2006; ten Brink, 1998; Cadle, 1972; Robbins et al., 1959; Gard et al., 1998). Aged SSA may also contain sulfur species (in excess of seawater concentrations) due to reactions with H_2SO_4 or CH_3SO_2OH, formed from the oxidation of SO_2 or dimethyl sulfide (DMS) (Gaston et al., 2010; Hopkins et al., 2008; McInnes et al., 1994). While not thermodynamically favored for bulk aqueous chemistry, SO_2 can be oxidized to H_2SO_4 in SSA because the oxidation of SO_2 occurs considerably faster than in pure water due to other oxidants (H_2O_2) or chloride ion catalysis (Clarke and Radojevic, 1984). More recently, laboratory and field studies have shown that NaCl can react with weak organic acids, such as malonic and citric acid, in addition to inorganic acids, releasing $HCl_{(g)}$ (Ghorai et al., 2014; Laskin et al., 2012; Wang et al., 2015). Furthermore, SSA can undergo reactions with other reactive nitrogen gases such as N_2O_5 to form $NO_3^-{}_{(aq)}$ and $ClNO_{2(g)}$ (Finlayson-Pitts et al., 1989; Thornton and Abbatt, 2005; Woods et al., 2013; Ryder et al., 2014; Roberts et al., 2008; Allen et al., 1996; Bertram and Thornton, 2009; Bertram et al., 2009). As SSA can react with a variety of species during transport, understanding the extent of processing by identifying the particle-phase reaction products formed when HCl is liberated, is necessary for a thorough understanding of the multiphase chemistry experienced by SSA during transport to sites far from coastal environments.

While SSA has been shown to act as an important sink for oxidized forms of NO_x and SO_2 in coastal regions, relatively few measurements have focused on SSA transported inland. Thus, the potential for inland SSA to have regional impacts after multiphase reactions, such as acting as a sink for HNO_3 and H_2SO_4 impacting nitrate deposition patterns (Matsumoto et al., 2009), is poorly understood (Gantt et al., 2015). To date, inland SSA has been detected with concentrations ranging from 1-20 μg/m^3 at locations 100 to > 1000 km from their source in Israel (Foner and Ganor, 1992), Buenos Aires (Dos Santos et al., 2012), Ecuador (Giannoni et al., 2016), Arkansas (Chalbot et al., 2013), California (O'Brien et al., 2015; Laskin et al., 2012;

Moffet et al., 2013), Alaska (Shaw, 1991), Antarctica (Udisti et al., 2012; Hara et al., 2004), Spain (Silva et al., 2007), Sweden (Gustafsson and Franzen, 2000), and across the European continent (Manders et al., 2010) (Figure B.1, Table B.1). However, most sites are still somewhat close to the ocean (100-250 km) or in areas that are typically downwind of the ocean. Studies have relied primarily on bulk analysis methods, which use Cl^- or Na^+ concentrations, the ratio of Cl^-/Na^+, or the ratio of Cl^-/ Mg^{2+} to identify SSA (Foner and Ganor, 1992; Dos Santos et al., 2012; Chalbot et al., 2013; Shaw, 1991; Silva et al., 2007; Giannoni et al., 2016; Hara et al., 2004; Manders et al., 2010; Udisti et al., 2012). While some studies only detected fresh SSA (since Cl^- was used as a marker) (Foner and Ganor, 1992), aged SSA were detected in the majority of the studies using the Cl^-/Na^+ mass ratio which ranged from 0-1.8 (Gustafsson and Franzen, 2000; Ueda et al., 2014; Silva et al., 2007; Udisti et al., 2012; Shaw, 1991; Chalbot et al., 2013; Giannoni et al., 2016; Dos Santos et al., 2012) (Cl^-/Na^+ = 1.81 in seawater) (Pilson, 1998). Since $HCl_{(g)}$ can be released from SSA by the reactions discussed above, ratios involving Cl^- can lead to an underestimation of inland SSA concentrations (Pakkanen, 1996). Additionally, Na^+, Mg^{2+}, and Cl^- can also be present from other sources, such as mineral dust(Sullivan et al., 2007) and incineration (Moffet et al., 2008), further complicating the use of these ion ratios in bulk samples to accurately identify SSA.

Single particle analysis overcomes challenges related to bulk average concentrations and ion ratios and allows for particle-by-particle comparison of SSA to seawater ion ratios, such as Na^+/Mg^{2+} (Ault and Axson, 2017; Noble and Prather, 1997; Gard et al., 1998; Ault et al., 2013a; Ault et al., 2013c; Gaston et al., 2010; Guasco et al., 2014; Prather et al., 2013; Hopkins et al., 2008; Laskin et al., 2002; Laskin et al., 2012; Ghorai et al., 2014; Ault et al., 2014; Ault et al., 2013b). By not using chloride to identify SSA, more detailed analysis of the extent of multiphase reactions that individual particles have undergone can be conducted. Scanning electron microscopy with energy dispersive x-ray spectroscopy (SEM-EDX) has been used extensively to identify fresh and aged SSA (SSA depleted in chloride), measure particle size and morphology, and analyze distributions of elements within individual particles (Laskin et al., 2002; Ault et al., 2013a; Ghorai et al., 2014; Hopkins et al., 2008; Geng et al., 2014; Sobanska et al., 2003; Prather et al., 2013; Laskin et al., 2012; Liu et al., 2007; Ali et al., 2014; Laskin et al., 2006b; Laskin et al., 2003; Ault et al., 2013b). SEM-EDX also has potential to provide a wealth of information regarding concentrations of SSA and extent of aging at inland locations where few single particle

studies have been conducted (Allen et al., 2015; Moffet et al., 2013; Laskin et al., 2012; O'Brien et al., 2015).

In this study, individual SSA particles were analyzed to determine the degree of aging as a function of particle size during the Southern Oxidant and Aerosol Study (SOAS) in 2013 near Centreville, Alabama. Computer controlled SEM-EDX (CCSEM-EDX) was used to identify and analyze particles to determine elemental composition, size, and morphology. Computer controlled Raman microspectroscopy (CC-Raman) (Craig et al., 2017a) was used to identify secondary species (nitrate and sulfate) and trace organics. A previous SOAS publication investigated the impact of mineral dust aerosol on nitrate, but only briefly mentioned SSA influence (Allen et al., 2015). Herein, two chemically distinct time periods with high SSA concentrations and different extents of aging were identified. Backward air mass trajectory analysis, in conjunction with weighted potential source contribution function analysis (WPSCF), and local meteorological data were used to investigate differences in atmospheric processing between these two SSA events. The presence of partially aged SSA transported inland may serve as sinks for HNO_3 and SO_2/H_2SO_4, as well as a source of oxidants in inland locations.

3.2. Methods

3.2.1. Field Site Description and Sample Collection

Aerosol samples were collected as part of SOAS near Centreville, AL (32.9030 N, 87.2500 W, 242 m above mean sea level) (Hidy et al., 2014). Centreville is located in a rural, forested region near Talladega National Forest approximately 320 km north of the Gulf of Mexico. Samples for single particle analysis were collected between June 5 and July 11, 2013 near ground level (1 m) using a micro-orifice uniform deposit impactor (MOUDI, MSP Corp. Model 110) sampling at 30 lpm with a PM_{10} cyclone (URG Model 786). The 50 % aerodynamic diameter size cut-points for the MOUDI sampling stages used in this analysis were 1.8, 1.0, 0.56, and 0.32 μm (Marple et al., 1991). Particles were impacted onto 200 mesh carbon-type-B Formvar grids and quartz substrates (Ted Pella Inc.) for analysis with SEM-EDX and Raman, respectively. Samples were collected from 8:00-19:00 Central Standard Time (CST) and 20:00-7:00 CST, except during intensive periods when the schedule was 8:00-11:00, 12:00-15:00, 16:00-19:00, and 20:00-7:00 CST. Intensive time periods were scheduled based on predicted

meteorological parameters and gas phase concentrations (Budisulistiorini et al., 2015). After collection, all substrates were sealed and stored at -22 °C prior to analysis.

3.2.2. Computer-Controlled Scanning Electron Microscopy with Energy Dispersive X-ray Spectroscopy Analysis

Particles were analyzed using a FEI Quanta environmental SEM equipped with a field emission gun operating at 20 kV and a high angle annular dark field (HAADF) detector (Laskin et al., 2002; Laskin et al., 2006a). The SEM is equipped with an EDX spectrometer (EDAX, Inc.). The CCSEM automated analysis captured single-particle physical parameters including projected area diameter and perimeter. EDX spectra from individual particles were analyzed to determine the relative abundance of 15 elements: C, N, O, Na, Mg, Al, Si, P, S, Cl, K, Ca, Ti, Fe, and Zn. For SOAS, a total of 34,266 particles were analyzed, including 4,047 SSA particles. Single-particle data from the CCSEM-EDX analysis was examined in Matlab R2013b (MathWorks, Inc.) using k-means clustering of individual particle EDX spectra following a previously described method (2012; Shen et al., 2016). Clusters were grouped by elemental composition into source-based classes, including SSA (Hopkins et al., 2008; Laskin et al., 2012; Ault et al., 2013b). The particles identified as SSA in this study are unlikely to be influenced by other species such as dust, since the SSA particles contained negligible amounts of common soil elements such as Si and Al. SSA data from two samples (July 4 20:00-July 5 7:00 and July 5 8:00-19:00) were excluded from analysis due to possible influence from fireworks (Liu et al., 1997; Li et al., 2013; Martin-Alberca and Garcia-Ruiz, 2014).

3.2.3. Computer-controlled Raman Microspectroscopy

Raman microspectroscopy was performed using a Horiba LabRAM HR Evolution Raman spectrometer coupled with a confocal optical microscope (100x long working distance objective, Olympus, 0.9 numerical aperture). The instrument was equipped with a Nd:YAG laser source (50 mW, 532 nm), a charge-coupled device (CCD), and a 600 groove/mm diffraction grating (1.8 cm^{-1} spectral resolution). The instrument was calibrated daily using the Stokes Raman signal of pure Si at 521 cm^{-1}. The laser power was adjusted with a neutral density filter, and four accumulations each with 15 s acquisition time were used to collect spectra for the range of 500 to 4000 cm^{-1}. Approximately 200 particles (0.8-6.4 μm projected area diameter) from each SSA

event (June 12, 2013 12:00-15:00 and July 4, 2013 8:00-19:00) were analyzed using CC-Raman to investigate secondary species, including nitrate, sulfate, and organics, using the method described by Craig et al. (2017a).

3.2.4. Hybrid Single Particle Lagrangian Integrated Trajectory Model and Weighted Potential Source Contribution Function Analysis

The NOAA HYSPLIT model (Draxler and Rolph, 2003) was run hourly at 100, 200, 500, 1000, and 3000 m (120 hours backwards) in conjunction with WPSCF receptor modeling (Wang et al., 2009) to examine the air mass histories of SSA during two SSA events: June 10-13, 2013 and July 3-8, 2013. PSCF values for each grid cell were calculated by counting the number of trajectories that ended at each grid cell, *n(i,j)*. The number of samples with trajectories that end at a grid cell that exhibit concentrations higher than an arbitrary criterion value is defined as *m(i,j)*. The PSCF value for the ij^{th} cell is defined as:

$$PSCF(i,j) = \frac{m(i,j)}{n(i,j)} \tag{3.1}$$

Since small values of n_{ij} are likely to produce high uncertainties in PSCF analysis, an empirical weight function *W(i,j)* was applied for low n_{ij} values. In this analysis, a criterion of 6 % SSA (the median SSA number fraction during SOAS) was applied, and an arbitrary weight function was used (Polissar et al., 2001):

$$W(n_{ij}) = \begin{cases} 1.0 & n_{ij}>120 \\ 0.7 & 40<n_{ij}<120 \\ 0.42 & 20<n_{ij}<40 \\ 0.17 & 0<n_{ij}<20 \end{cases} \tag{3.2}$$

3.3. Results and Discussion

3.3.1. SSA Partially-Aged Classes at SOAS

Individual SSA particles were identified during SOAS by the presence of sodium and magnesium in a ~10:1 ratio (by atomic percent), which is equivalent to their molar ratio in seawater (Pilson, 1998). This fingerprint has been used to identify SSA in both laboratory and field studies using SEM-EDX, including both fresh and aged (depleted in chloride) SSA (Laskin et al., 2002; DeMott et al., 2016; Ault et al., 2014; Ault et al., 2013b). For EDX analysis it is typical to report atomic percentages of specific elements, which are equivalent to the mole percent of a specific element within the total particle. To facilitate comparison to bulk analyses,

we report mole percentages and mole ratios in the analysis below. Details on identification of SSA through molar ratios are given in Appendix B and Table B.2. Though primary biological and other organic particles have been observed to be emitted from marine environments (Orellana et al., 2011; Guasco et al., 2014), due to their relatively smaller contributions and challenges differentiating these types of particles from organic or biological particles emitted from terrestrial sources at SOAS, only salt-containing SSA are discussed hereafter. Using CCSEM-EDX to identify SSA helps avoid misclassifying particles where Cl^- has been fully depleted via multiphase reactions. SSA particles identified during SOAS were classified into two categories: 1) partially aged (Cl/Na mole ratio $\geq$ 0.1) and 2) aged or fully processed (Cl/Na mole ratio < 0.1). There is no "fresh" category of SSA, as no SSA particles were observed without some chloride depletion. Chloride enrichment factors, calculated by dividing the Cl^-/Na^+ mass ratio of the aerosol sample by the Cl^-/Na^+ ratio of seawater, are commonly used in ion chromatography to differentiate aged and fresh SSA (Newberg et al., 2005). However, the complete Cl loss in many particles made this approach impractical, and the simpler ratio of Cl/Na frequently used in EDX analysis (Laskin et al., 2012), is used herein. A molar threshold of 0.1 Cl/Na (1.16 in seawater) is used where particles with this ratio contain $\geq$ 10 % of the chloride content (molar) of fresh SSA, and are therefore $\leq$ 90 % depleted in chloride.

Within the fully aged category, particles were sub-classified into sulfate-dominated (aged-sulfate, mole % S $\geq$ 1, mole % N < 1%) and mixed (aged-nitrate/sulfate, mole % S $\geq$ 1, mole % N $\geq$ 1). These thresholds were selected to minimize false positives due to background interferences. Figure 3.1 shows example images and EDX spectra of SSA particles from each of these three categories (partially aged, fully aged (aged-sulfate), and fully aged (aged-nitrate/sulfate), with all three particles showing varying degrees of chloride depletion and the presence of nitrate and/or sulfate. For the elements Cl, N, and S associated with key anionic species (Cl^-, NO_3^-, SO_4^{2-}), in the representative particle from the partially aged class more Cl (9 %) was present than N (2 %) and S (2 %) by mole %. In comparison, the two aged classes contain substantially less Cl, with the particle from the aged-sulfate class containing 0 % Cl, 13 % S, and 1 % N, and the particle from the aged-nitrate/sulfate class containing 0 % Cl, 3 % S, and 2 % N by mole %. Although EDX only measures elemental composition, whenever nitrogen and sulfur were present in the EDX spectra, elemental maps always showed collocation with oxygen, suggesting that these elements were present in the form of nitrate and sulfate (Figure

3.1a). Raman microspectroscopy of particles from the same time period also showed frequent nitrate and sulfate vibrational modes, supporting this assignment (Figure B.2). A future publication will focus on Raman mode analysis of particles from all sources at SOAS.

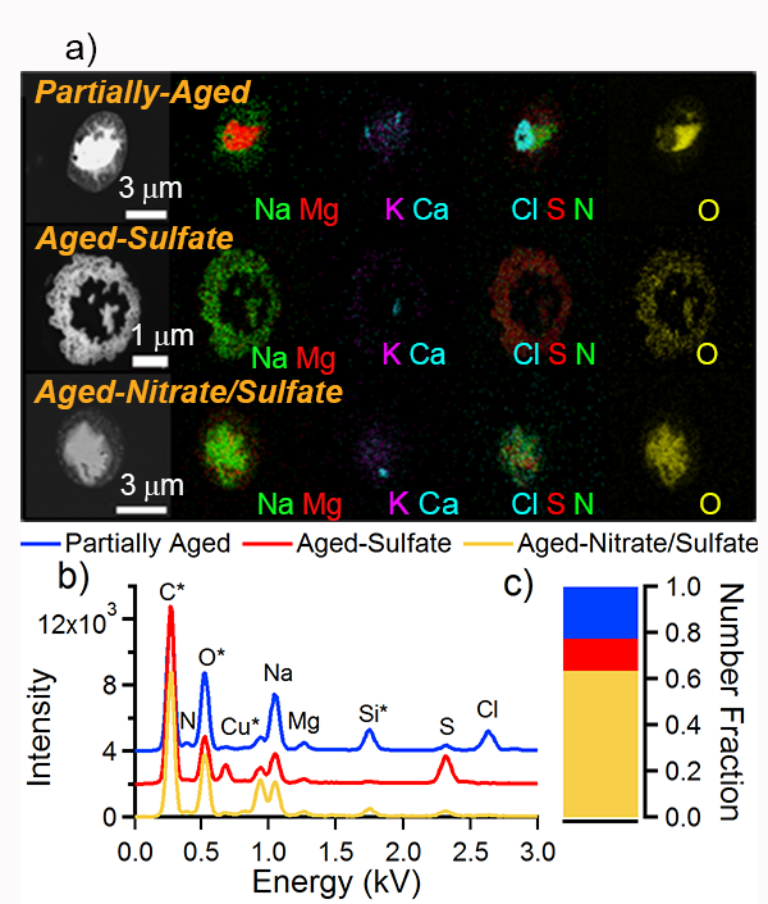

Figure 3.1. a) SEM images and elemental maps of particles representing the three SSA classes observed during SOAS: partially aged, aged-sulfate, and aged-nitrate/sulfate, b) corresponding EDX spectra, and c) bar graph depicting the abundance of each SSA class by number fraction. *Note, these elements are not quantitative due to interference from the substrate or detector. Standard error for the abundance of each class is below 0.01. A table with error values is located in Appendix B (Table B.2).

Elemental maps of particles representative of the three SSA classes in Figure 3.1a show the distribution of elements within each individual particle after impaction. In agreement with prior results (Ault et al., 2013a; Hoffman et al., 2004; Ziemann and McMurry, 1997), the partially aged and aged SSA particles did not have elements homogeneously distributed spatially or a cubic efflorescence pattern typical of $NaCl_{(s)}$, suggesting the structures were not due to analysis under vacuum. Rather, spherical structures, some of which were core-shell, were

observed. The distribution of elements with sodium, chloride (represented by Cl), and sulfate (represented by S) on the interior and magnesium and nitrate (represented by N) on the exterior is particularly apparent for the partially aged particle. In this particle, nitrate may have been enhanced at the surface, with chloride present within the core, due to reactions on an effloresced particle with a solid core. The enhancement of sodium rather than magnesium within the core suggests, unlike aged-nitrate/sulfate particles with the opposite cation organization, that the reaction is incomplete since cation rearrangement had not occurred (Ault et al., 2013a). Although three main classes of SSA were identified, a large variety of compositions and spatial distributions, even within a single particle category, were observed necessitating an investigation of compositional variability.

The average EDX elemental percentages for all three types of SSA were observed to be depleted in chloride, although the extent of depletion varied, as seen in Figure 3.2. The partially aged class (24 % of SSA by number) contained chloride in all the particles, with mole percentages of Cl ranging from 1-44 %, with averages of 5 % Cl, 2 % S, and 5 % N. Aged-sulfate particles (15 % of SSA by number) were completely depleted in chloride and did not contain nitrate, but contained up to 15 % S with an average of 6 % S (mole %). Aged-nitrate/sulfate particles, which accounted for the majority (61 % by number) of SSA analyzed, had minimal chloride (Cl/Na mole fraction < 0.1) with nitrate and sulfate present in all particles (up to 15 % N and S with an average of 5 % N and 4 % S by mole %). Less than 1 % by number of SSA particles contained more than 10 % Cl (with fresh SSA particles containing 49 % Cl by mole percentage), indicating a substantial degree of processing during transport from the Gulf of Mexico.

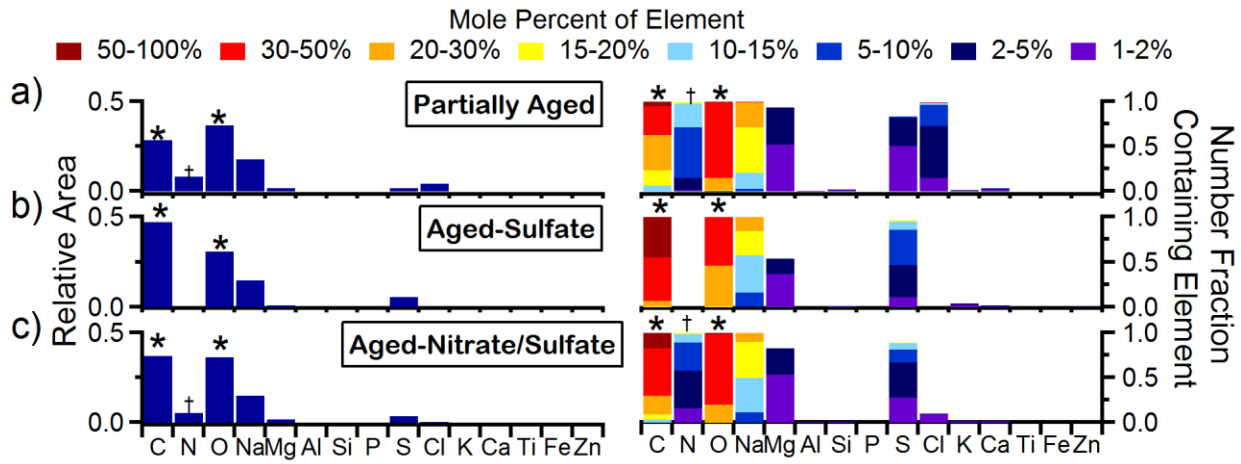

Figure 3.2. Average mole percent per particle and digital color histograms of three different particle classes of SSA: a) partially aged, b) aged-sulfate, and c) aged-nitrate/sulfate. Average histograms are shown on the left as the elemental mole fraction across the elements analyzed by CCSEM-EDX. On the right, the digital color histogram heights represent the number fraction of particles containing a specific element, and the colors represent the mole percent of that element. Since analysis was conducted under vacuum, these mole percentages do not include moles of water. *Note these elements (C, O) are not quantitative due to interference from the substrate or detector, and † may have interfering signal from the carbon and oxygen EDX peaks.

3.3.2. Comparison of Two SSA Events

During SOAS two events (Event 1: June 10th-13th and Event 2: July 3rd-8th) were identified that had high number percentages of SSA in the accumulation and coarse modes, 11 % and 35 %, respectively, compared to the 6 % median number percentage of SSA for all of the SOAS samples analyzed (Figure B.3). During these events SSA are a substantial fraction of total $PM_{2.5}$ mass. The highly aged character from Figure 3.2 is supported by the mean pH of 0.9 ± 0.6 reported for $PM_{2.5}$ at the site (Guo et al., 2015; Weber et al., 2016). When compared to the pH range of 7.0 to 9.0 which is typical for freshly-emitted SSA (Keene et al., 1990), HCl volatilization is predicted under these highly acidic conditions at Centreville (Keene et al., 1990), though limited methods for direct pH determination are available (Rindelaub et al., 2016; Craig et al., 2017b). To compare SSA aging during these events, the number fraction of SSA in each particle class was analyzed as a function of projected area diameter (Figure 3.3a). For comparison, the composition of SSA during the rest of the campaign, which accounted for approximately 20 % of SSA by number, is also shown. For all SSA detected during SOAS, size plays an important role in chemical composition: sulfate-containing particles were present from

0.5 to 5 µm (stats were poor < 0.5 µm), particles containing nitrate were mostly > 1 µm, and partially aged particles containing chloride were generally > 2 µm. Figure 3.3b shows the number fraction of particles containing any Cl, N, or S (mole percent > 1 %) in the particle. These data further support that within partially aged and aged SSA categories sulfate is concentrated in submicron particles, while chloride and nitrate are primarily in the supermicron size range. In addition to quantifying the number fraction of particles that contain nitrate, sulfate, and chloride, the average mole percent relative to sodium of each element was analyzed to determine their per particle concentrations as a function of size. Figure 3.3b shows that for all SSA, the number fraction of particles containing Cl increased with diameter with similar mole fractions of Cl (~0.2) within the largest particles analyzed. On the other hand, the mole fractions of N and S in SSA are inversely related. While submicron particles are very S-rich, as diameter increases, the mole fraction of S within particles decreases and the mole fraction of N increases.

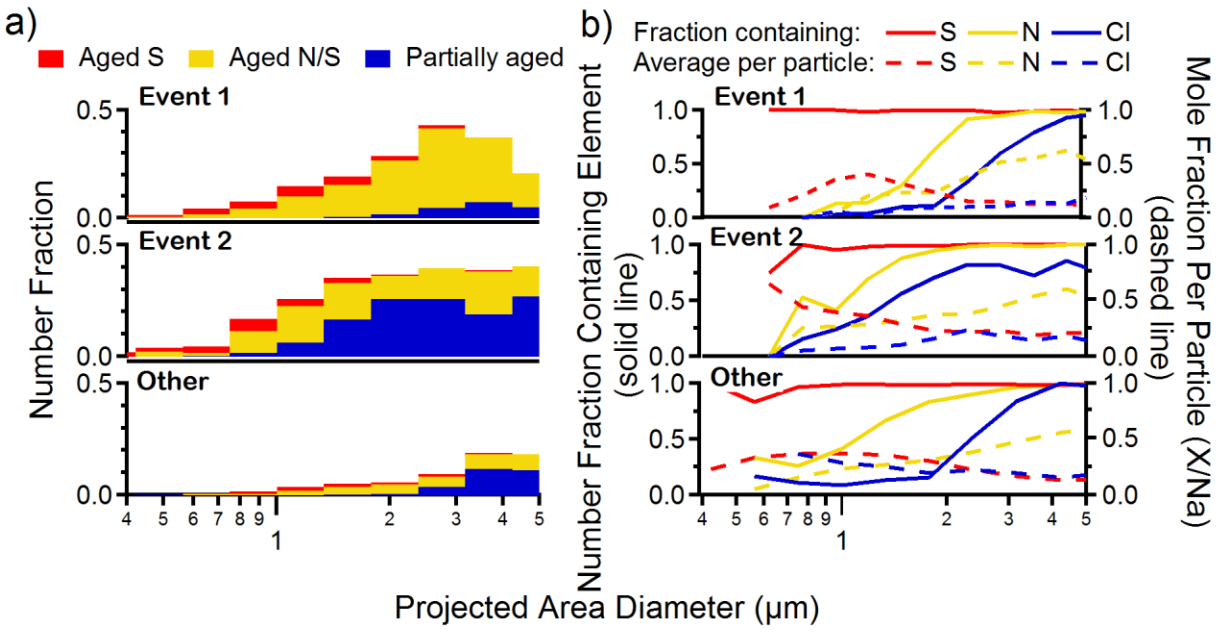

Figure 3.3. a) Aged-sulfate, aged-nitrate/sulfate, and partially aged SSA depicted as a function of size during two SSA-rich periods: June 10-13th (Event 1), July 3-8th (Event 2), and throughout the rest of SOAS (other). During these two events, SSA is present at both submicron and supermicron sizes. b) Size-resolved SSA composition indicates the number fraction of SSA containing Cl, N, and/or S. The solid line corresponds to the number fraction containing the element, while the dashed line corresponds to the mole fraction per particle relative to sodium.

The size dependence of nitrate and sulfate within SSA particles provides insight into the mechanism for the uptake of HNO_3 and SO_2. In general, the accumulation of sulfate in SSA by

reaction with SO_2 is diffusion limited. Therefore, it occurs most readily in $PM_{2.5}$, particularly accumulation mode particles (diameters 0.1-1.0 μm) (Kerminen et al., 1998; Zhuang et al., 1999; Ueda et al., 2014; Gurciullo et al., 1999). Additionally, sulfate may accumulate in small particles because H_2SO_4, formed from the aqueous-phase or gas-phase oxidation of SO_2 in deliquesced particles and droplets, dissociates instantly to HSO_4^-, H^+, and SO_4^{2-} and stays in the particle phase after uptake or formation, as opposed to the higher vapor pressure HNO_3 (Skinner and Sambles, 1972). Over time, the accumulation of sulfate will acidify the particles, and more HNO_3 volatilization will lead to a "distillation effect" where more sulfate accumulates within the smaller particles and any pre-existing nitrate is displaced. Thus, NO_3^- will be present primarily in supermicron SSA (Kerminen et al., 1998; Pakkanen, 1996; Zhuang et al., 1999), preferentially particles ~1 μm since the net uptake for nitric acid onto NaCl is highest for micron-sized particles with large surface areas (Liu et al., 2007). However, the reaction may not go to completion for large SSA since the uptake of HNO_3 is diffusion-limited above 1 μm (Liu et al., 2007), leading to partially aged SSA particles. In short, the irreversible uptake of SO_2 on SSA is kinetically limited while the uptake of HNO_3 is kinetically limited for large particles and thermodynamically controlled for small particles, resulting in sulfate accumulation in submicron particles, and nitrate accumulation in supermicron particles.

In addition to composition varying as a function of size, SSA composition was different for the two events. During Event 1 in June, aged-nitrate/sulfate SSA account for the majority of SSA particles by number, consistent with work by Allen et al. (Allen et al., 2015), who showed coarse particle nitrate was high from June 9-13th during SOAS. In contrast, during Event 2 the partially aged SSA particles accounts for the majority of SSA by number. For particles (> 4 μm), chloride is present in $\geq$ 70 % of particles during both events. However, during Event 1, only 6 % of submicron SSA, by number, contain chloride, while 33 % of submicron SSA contain chloride during Event 2, showing different extents of chloride depletion. This high fraction of particles that are not fully depleted in chloride may have important implications for the nitrogen budget, with partially aged SSA acting as an inland sink for NO_x oxidation products.

Ternary diagrams (Figure 3.4) show percentages of Cl, N and S with respect to the sum of Cl + N + S in individual particles by mole percent, as in Equations 3.1-3.3 shown below:

$$Cl\ \% = \frac{Cl}{Cl+N+S} \times 100\ \% \quad (3.3)$$

$$N\ \% = \frac{N}{Cl+N+S} \times 100\ \% \quad (3.4)$$

$$S\ \% = \frac{S}{Cl+N+S} \times 100\ \% \quad (3.5)$$

These plots highlight differences in aging processes between the SSA events. During Event 1 two populations are observed: 1) particles containing varying amounts of N and S with complete Cl depletion, and 2) particles containing varying amounts of N and Cl with minimal S. As also shown in Figure 3.3b, Cl is in the largest particles and the largest S enrichments are in the smallest particles, with lower relative mole fractions of S (1-2 %) observed in particles > 2.5 μm (although all particles 0.5-5 μm contained some amount of S). High relative percentages of N ($\geq$ 60 %) are found in all SSA $\geq$ 1 μm, suggesting particles were within a favorable size range for maximal uptake of HNO_3. In comparison, during Event 2, particles were smaller than the first event with average diameters < 2.5 μm, and contained less N relative to S and Cl. To highlight the variation of N, the average relative percent of N, S, and Cl were calculated for each event, represented by the asterisks in Figure 3.4. The average N % is much higher during Event 1 (65 %) than during Event 2 (36 %), indicating that SSA during this event were aged to a greater extent by HNO_3. Conversely, the average mole percentage of S increased (21 % during Event 1 to 56 % during Event 2), and Cl remained approximately constant (13 % during Event 1, 8 % during Event 2), even though the particles were much smaller during Event 2. The presence of chloride in a higher number fraction during Event 2, particularly in SSA < 2.5 μm, may suggest an inhibition of multiphase reactions due to the particles not behaving as ideal aqueous droplets (e.g. effloresced particles or particles coated with organic material inhibiting uptake) (McNeill et al., 2006) or transport at higher altitudes with lower HNO_3 and SO_2 concentrations.

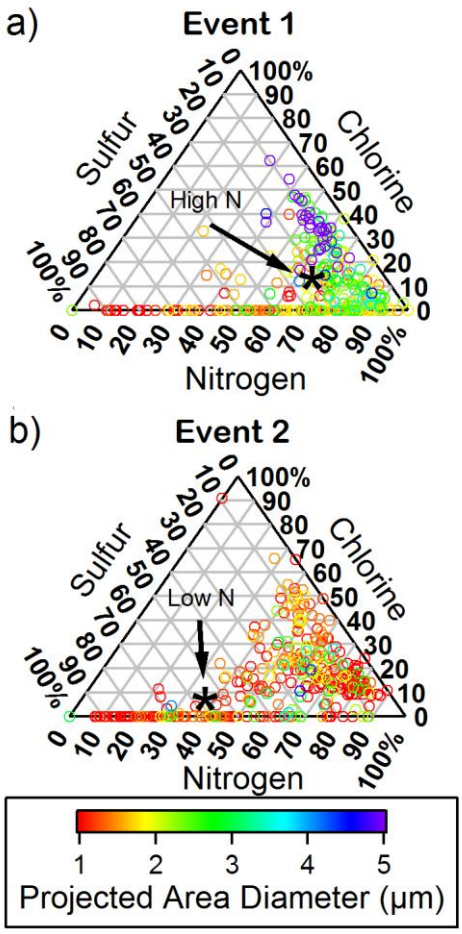

Figure 3.4. Ternary plots showing the relative percent of sulfate (S), chloride (Cl), and nitrate (N) in individual SSA particles collected from SOAS as a function of particle diameter for a) Event 1 and b) Event 2. Only every 5th (Event 1) or 3rd (Event 2) particle, respectively, is shown on the plots above to better show trends. The asterisk shows the average SSA composition during each event, with SSA from Event 1 containing substantially more nitrogen than SSA from Event 2.

To examine the air mass history during the two high-SSA events, HYSPLIT analysis with WPSCF was used. Shown in Figure 3.5, the SSA collected at rural, forested Centreville originated from the Gulf of Mexico and were transported inland. However, throughout these two SSA events, the particles arrived at Centreville via different transport routes, speeds, and altitudes. During Event 1, the air mass arrived from the southwest after passing over Louisiana and Mississippi; while during Event 2, the air mass approached Centreville directly from the south after travelling over Alabama and the Florida panhandle. Figure 3.5c shows example HYSPLIT backward air mass trajectories from Event 1, where the air mass spends ~24 h over land, while the backward air mass trajectories for Event 2 only spent ~10 h over land. The air

masses from Event 1 travelled within the boundary layer over land, but due to differences in chemical composition from aerosol emitted from freshwater (Axson et al., 2016; May et al., 2016), we are confident these particles are of marine origin and not from lakes or rivers the air mass passes over en route to Centreville. In contrast to Event 1, the air mass influencing Event 2 was primarily in the free troposphere until the last few hours prior to arrival at Centreville. Although the transport time from the Gulf of Mexico was 2-3 times longer for the more aged SSA Event 1, exposure to different pollutant levels on the two trajectories, rather than diffusion-limited reactions over the transport time scale, likely led to the differences in SSA composition. To support this, the theoretical uptake of HNO_3 onto SSA completely aging particles was calculated to take ~4 hours (Table B.3), which is much shorter than the transport times of particles during SOAS, particularly during Event 1. Meteorological data indicated that immediately preceding Event 2, Centreville experienced heavy rainfall (Nguyen et al., 2014; Xiong et al., 2015) leading to a reduction of gaseous HNO_3 (Allen et al., 2015), while Event 1 SSA experienced no precipitation. Specifically, Event 2 gas-phase measurements of NO_y (0.51 ppb) and HNO_3 (0.03 ppb) were much lower compared to concentrations of NO_y (1.28 ppb) and HNO_3 (0.23 ppb) during Event 1 (Figure B.4), which may be indicative of changes in regional NO_y and HNO_3 concentrations along the transport paths though values likely vary along the trajectory to the site. The high concentrations of HNO_3 and NO_y during Event 1 may account for the highly nitrate-aged SSA analyzed during that period, compared to the high concentrations of partially aged SSA detected during Event 2.

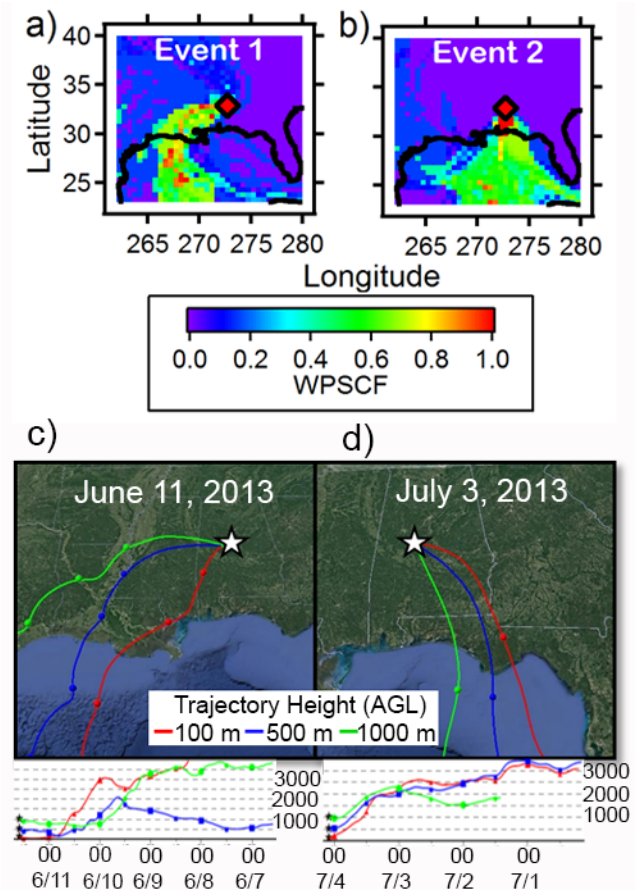

Figure 3.5. WPSCF trajectory analysis of SSA a) Event 1 and b) Event 2 ending at Centreville, AL. WPSCF data is shown for SSA > 6 % (median % SSA during SOAS) by number according to CCSEM-EDX analysis and clustering. Example HYSPLIT 120 h backward air mass trajectories during Event 1 ending at Centreville on c) June 11, 2013 at 8:00am and Event 2, d) July 3, 2013 at 8:00pm. The red trajectory corresponds with trajectories ending at 100 m AGL, blue with 500 m AGL, and green with 1000 m AGL. *Circles on trajectory are spaced 12 h apart. Map data for 5C and 5D: © Google, Image Landsat/Copernicus; Data SIO, NOAA, U.S. Navy, NGA, GEBCO.

3.3.3. Chloride Depletion within Inland SSA

The importance of transport time for predicting whether chloride has been fully depleted from a particle is shown in Figure 3.6 by the average chloride depletion in SSA (mole %) as a function of air mass transport time from the Gulf (% Cl depletion calculations in Appendix B). During Event 1, SSA experienced much longer transport times, with 30 h median transport times from the ocean based on backward air mass trajectories 500 m above ground level (Figure 3.5a). Air masses that were transported for 20-29 h contained slightly more chloride (98 % Cl depleted,

by mole %) compared to air masses that had transport times of 30-68 h (99 % Cl depleted), although the difference is not statistically significant (Table B.4), suggesting the reactions were not diffusion-limited on these time scales. By comparison, SSA during Event 2 had a median transport time of 10 h over land and contained substantially more chloride. Air masses with transport times of 7-8 h were on average 87 % chloride depleted (mole %), which is statistically different at the 90 % confidence interval from the 95 % chloride depletion of SSA that travelled over land for more than 10 h. Thus, the combination of transport time and heavy precipitation leading to wet deposition of NO_y species likely caused differing chloride levels during the two SSA events.

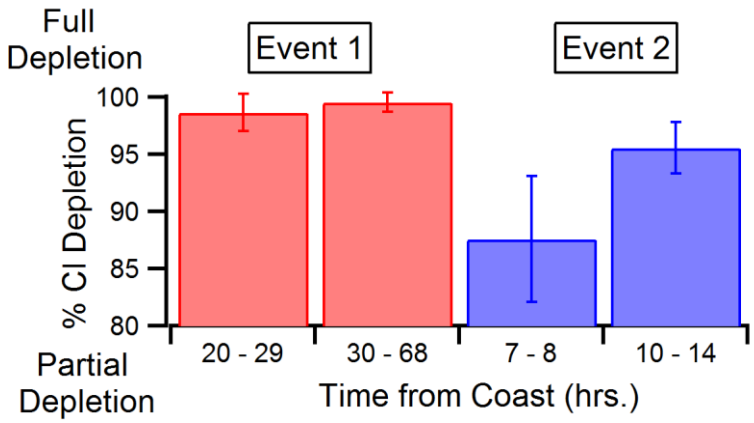

Figure 3.6. Average mole % of chloride depleted from SSA particles after transport from the ocean during Event 1 and Event 2. Five sampling times were averaged for each category during Event 1, and two and three sampling times were averaged for the Event 2 categories, respectively. Error bars represent one standard deviation from the mean. The time from the coast is calculated in hours using HYSPLIT.

To estimate the maximum contribution of SSA chloride depletion on the atmospheric oxidant budget, the mass of chlorine released during transport during Event 1 was calculated. First, the SSA mass concentration was calculated based on the Na^+ concentration ($\mu mol/m^3$) measured using a Monitor for Aerosols and Gases (MARGA) at the Centreville site (Allen et al., 2015), shown by CCSEM-EDX to be SSA. The seawater Cl^-/Na^+ ratio (1.81) (Pilson, 1998) was applied to calculate the original Cl^- concentration, and an average of 98 % (mole) chloride depletion, as determined by CCSEM-EDX (Figure 3.6), was applied to calculate moles of chlorine that partitioned to the gas-phase during transport. During Event 1, when most chloride was depleted, a maximum of ~620 ppt of HCl (17 $\mu mol/m^3$ Cl; from 15 $\mu mol/m^3$ of Na^+) is released into the atmosphere. Since much lower concentrations of HCl (~180 ppt during this

same time period) were measured at the Centreville site (Allen et al., 2015), most HCl (or Cl_2, $ClNO_2$) was likely released during transport from the ocean. These results indicate that under specific conditions, SSA may act as a source of Cl inland modifying the oxidant budget, and, if complete depletion does not occur during transport, SSA may exist as a source of HCl and a sink for oxidized NO_x species at inland locations.

3.4. Conclusions

SSA impact atmospheric chemistry and climate as they undergo multiphase reactions in the atmosphere, thereby acting as sinks for NO_x oxidation products and SO_2 as well as a source of gaseous halogen species (e.g. HCl and $ClNO_2$) (Finlayson-Pitts, 2009; De Haan et al., 1999; Gibson et al., 2006; Reid and Sayer, 2002; Rossi, 2003; Ravishankara and Longfellow, 1999; Gantt and Meskhidze, 2013). During the summer 2013 SOAS field campaign in Centreville, Alabama, SSA particles comprised up to 81 % of supermicron (1-10 μm) and 48 % of submicron (0.2-1.0 μm) particles, by number, during two multi-day events. Since Centreville, AL is an inland site located approximately 320 km from the coast, most of the SSA was depleted in chloride and enriched in nitrate and sulfate due to transport and reactions with acidic species. Still, 24 % of all SSA particles sampled, by number, contained detectable chloride (Cl/Na mole ratio $\geq$ 0.1), suggesting that complete chloride depletion frequently did not occur. During Event 2, shorter transport times and subsidence from aloft during periods of low $HNO_{3(g)}$ led to particles where less than 90 % of chloride had been depleted, although additional factors, such as the presence of an organic coating, could have impacted SSA reactivity during transport.

The findings suggest chloride-containing SSA exist at inland sites may have important implications for the nitrogen and oxidant budgets in the southeastern U.S or other inland sites, as these SSA will likely undergo further reactions during continued transport inland. Thus, SSA may act as an underappreciated inland sink for NO_x and SO_2 oxidation products, and source of reactive halogen-containing gases. Additionally, SSA could act as an inland cloud condensation nuclei source, indirectly impacting climate through cloud formation. The outcomes of this study provide insight regarding secondary chemistry involving aerosols in the southeastern U.S. Additional studies at inland sites, particularly less-polluted ones, are needed to examine effects on oxidation products of NO_x, SO_2, and the oxidant budget from halogen production.

3.5. Acknowledgements

A.L.B. performed CCSEM analysis with assistance by B.W. and A.L. R.L.C assisted with Raman analysis. M.V.N. collected samples during SOAS. S.B.B., K.A.P., and P.B.S. helped plan sample collection. The authors acknowledge EPA (R835409) for SOAS sampling funding. CCSEM was performed at EMSL at PNNL. PNNL is operated for the U.S Department of Energy by Battelle Memorial Institute under contract number DE-AC06-76RL0 1830. Travel funds to PNNL were provided by UM Rackham Graduate School and the UM Office of the Provost. We wish to thank the Southeastern Aerosol Research and Characterization (SEARCH) program for NO_y and HNO_3 measurements. Additionally, we thank Annmarie Carlton (Rutgers University, now UC-Irvine), Lindsay Yee (UC-Berkeley), Jason Surratt (UNC-Chapel Hill), and Allen Goldstein (UC-Berkeley) for organizing SOAS and the filter sampling effort, as well as Karsten Baumann and others for logistical assistance.

3.6. References

Ali, H. M., Iedema, M., Yu, X. Y., and Cowin, J. P.: Ionic strength dependence of the oxidation of SO_2 by H_2O_2 in sodium chloride particles, Atmos. Environ., 89, 731-738, 2014.

Allen, H. C., Laux, J. M., Vogt, R., FinlaysonPitts, B. J., and Hemminger, J. C.: Water-induced reorganization of ultrathin nitrate films on NaCl: Implications for the tropospheric chemistry of sea salt particles, J. Phys. Chem., 100, 6371-6375, 1996.

Allen, H. M., Draper, D. C., Ayres, B. R., Ault, A. P., Bondy, A. L., Takahama, S., Modini, R. L., Baumann, K., Edgerton, E., Knote, C., Laskin, A., Wang, B., and Fry, J. L.: Influence of crustal dust and sea spray supermicron particle concentrations and acidity on inorganic NO_3^- aerosol during the 2013 Southern Oxidant and Aerosol Study, Atmos. Chem. Phys., 15, 10669-10685, 2015.

Ault, A. P., Peters, T. M., Sawvel, E. J., Casuccio, G. S., Willis, R. D., Norris, G. A., and Grassian, V. H.: Single-particle SEM-EDX analysis of iron-containing coarse particulate matter in an urban environment: sources and distribution of iron within Cleveland, Ohio, Environ. Sci. Technol., 46, 4331-4339, 2012.

Ault, A. P., Guasco, T. L., Ryder, O. S., Baltrusaitis, J., Cuadra-Rodriguez, L. A., Collins, D. B., Ruppel, M. J., Bertram, T. H., Prather, K. A., and Grassian, V. H.: Inside versus outside: Ion redistribution in nitric acid reacted sea spray aerosol particles as determined by single particle analysis, J. Am. Chem. Soc., 135, 14528-14531, 2013a.

Ault, A. P., Moffet, R. C., Baltrusaitis, J., Collins, D. B., Ruppel, M. J., Cuadra-Rodriguez, L. A., Zhao, D., Guasco, T. L., Ebben, C. J., Geiger, F. M., Bertram, T. H., Prather, K. A., and Grassian, V. H.: Size-dependent changes in sea spray aerosol composition and properties with different seawater conditions, Environ. Sci. Technol., 47, 5603-5612, 2013b.

Ault, A. P., Zhao, D., Ebben, C. J., Tauber, M. J., Geiger, F. M., Prather, K. A., and Grassian, V. H.: Raman microspectroscopy and vibrational sum frequency generation spectroscopy as probes of the bulk and surface compositions of size-resolved sea spray aerosol particles, PCCP, 15, 6206-6214, 2013c.

Ault, A. P., Guasco, T. L., Baltrusaitis, J., Ryder, O. S., Trueblood, J. V., Collins, D. B., Ruppel, M. J., Cuadra-Rodriguez, L. A., Prather, K. A., and Grassian, V. H.: Heterogeneous reactivity of nitric acid with nascent sea spray aerosol: Large differences observed between and within individual particles, J. Phys. Chem. Lett., 5, 2493-2500, 2014.

Ault, A. P., and Axson, J. L.: Atmospheric aerosol chemistry: Spectroscopic and microscopic advances, Anal. Chem., 89, 430-452, 2017.

Axson, J. L., May, N. W., Colon-Bernal, I. D., Pratt, K. A., and Ault, A. P.: Lake spray aerosol: A chemical signature from individual ambient particles, Environ. Sci. Technol., 50, 9835-9845, 2016.

Bertram, T. H., and Thornton, J. A.: Toward a general parameterization of N_2O_5 reactivity on aqueous particles: the competing effects of particle liquid water, nitrate and chloride, Atmos. Chem. Phys., 9, 8351-8363, 2009.

Bertram, T. H., Thornton, J. A., Riedel, T. P., Middlebrook, A. M., Bahreini, R., Bates, T. S., Quinn, P. K., and Coffman, D. J.: Direct observations of N_2O_5 reactivity on ambient aerosol particles, Geophys. Res. Lett., 36, 2009.

Budisulistiorini, S. H., Li, X., Bairai, S. T., Renfro, J., Liu, Y., Liu, Y. J., McKinney, K. A., Martin, S. T., McNeill, V. F., Pye, H. O. T., Nenes, A., Neff, M. E., Stone, E. A., Mueller, S., Knote, C., Shaw, S. L., Zhang, Z., Gold, A., and Surratt, J. D.: Examining the effects of anthropogenic emissions on isoprene-derived secondary organic aerosol formation during the 2013 Southern Oxidant and Aerosol Study (SOAS) at the Look Rock, Tennessee ground site, Atmos. Chem. Phys., 15, 8871-8888, 2015.

Cadle, R. D.: Formation and chemical reactions of atmospheric particles, J. Colloid Interface Sci., 39, 25-31, 1972.

Chalbot, M. C., McElroy, B., and Kavouras, I. G.: Sources, trends and regional impacts of fine particulate matter in southern Mississippi valley: Significance of emissions from sources in the Gulf of Mexico coast, Atmos. Chem. Phys., 13, 3721-3732, 2013.

Clarke, A. G., and Radojevic, M.: Oxidation rates of SO_2 in sea-water and sea-salt aerosols, Atmos. Environ. (1967-1989), 18, 2761-2767, 1984.

Clegg, S. L., and Brimblecombe, P.: Potential degassing of hydrogen chloride from acidified sodium chloride droplets, Atmos. Environ. (1967-1989), 19, 465-470, 1985.

Craig, R. L., Bondy, A. L., and Ault, A. P.: Computer-controlled Raman microspectroscopy (CC-Raman): A method for the rapid characterization of individual atmospheric aerosol particles, Aerosol Sci. Technol., 10.1080/02786826.2017.1337268, 1-14, 2017a.

Craig, R. L., Nandy, L., Axson, J. L., Dutcher, C. S., and Ault, A. P.: Spectroscopic determination of aerosol pH from acid–base equilibria in inorganic, organic, and mixed systems, J. Phys. Chem. A, 121, 5690-5699, 2017b.

Dasgupta, P. K., Campbell, S. W., Al-Horr, R. S., Ullah, S. M. R., Li, J., Amalfitano, C., and Poor, N. D.: Conversion of sea salt aerosol to $NaNO_3$ and the production of HCl: Analysis of temporal behavior of aerosol chloride/nitrate and gaseous HCl/HNO_3 concentrations with AIM, Atmos. Environ., 41, 4242-4257, 2007.

De Haan, D. O., Brauers, T., Oum, K., Stutz, J., Nordmeyer, T., and Finlayson-Pitts, B. J.: Heterogeneous chemistry in the troposphere: experimental approaches and applications to the chemistry of sea salt particles, Int. Rev. Phys. Chem., 18, 343-385, 1999.

DeMott, P. J., Hill, T. C. J., McCluskey, C. S., Prather, K. A., Collins, D. B., Sullivan, R. C., Ruppel, M. J., Mason, R. H., Irish, V. E., Lee, T., Hwang, C. Y., Rhee, T. S., Snider, J. R., McMeeking, G. R., Dhaniyala, S., Lewis, E. R., Wentzell, J. J. B., Abbatt, J., Lee, C., Sultana, C. M., Ault, A. P., Axson, J. L., Diaz Martinez, M., Venero, I., Santos-Figueroa, G., Stokes, M. D., Deane, G. B., Mayol-Bracero, O. L., Grassian, V. H., Bertram, T. H., Bertram, A. K., Moffett, B. F., and Franc, G. D.: Sea spray aerosol as a unique source of ice nucleating particles, Proc. Natl. Acad. Sci., 113, 5797-5803, 2016.

Dos Santos, M., Dawidowski, L., Smichowski, P., Graciela Ulke, A., and Gomez, D.: Factors controlling sea salt abundances in the urban atmosphere of a coastal South American megacity, Atmos. Environ., 59, 483-491, 2012.

Duce, R. A.: On source of gaseous chlorine in marine atmosphere, J. Geophys. Res., 74, 4597-4599, 1969.

Eldering, A., Solomon, P. A., Salmon, L. G., Fall, T., and Cass, G. R.: Hydrochloric acid-A regional perspective on concentrations and formation in the atmosphere of southern California, Atmos. Environ., Part A, 25, 2091-2102, 1991.

Finlayson-Pitts, B. J., Ezell, M. J., and Pitts, J. N.: Formation of chemically active chlorine compounds by reactions of atmospheric NaCl particles with gaseous N_2O_5 and $ClONO_2$, Nature, 337, 241-244, 1989.

Finlayson-Pitts, B. J.: Reactions at surfaces in the atmosphere: Integration of experiments and theory as necessary (but not necessarily sufficient) for predicting the physical chemistry of aerosols, PCCP, 11, 7760-7779, 2009.

Foner, H. A., and Ganor, E.: The chemical and mineralogical composition of some urban atmospheric aerosols in Israel, Atmos. Environ., Part B, 26, 125-133, 1992.

Gantt, B., and Meskhidze, N.: The physical and chemical characteristics of marine primary organic aerosol: A review, Atmos. Chem. Phys., 13, 3979-3996, 2013.

Gantt, B., Kelly, J. T., and Bash, J. O.: Updating sea spray aerosol emissions in the Community Multiscale Air Quality (CMAQ) model version 5.0.2, Geosci. Model Dev., 8, 3733-3746, 2015.

Gard, E. E., Kleeman, M. J., Gross, D. S., Hughes, L. S., Allen, J. O., Morrical, B. D., Fergenson, D. P., Dienes, T., Galli, M. E., Johnson, R. J., Cass, G. R., and Prather, K. A.: Direct observation of heterogeneous chemistry in the atmosphere, Science, 279, 1184-1187, 1998.

Gaston, C. J., Pratt, K. A., Qin, X., and Prather, K. A.: Real-time detection and mixing state of methanesulfonate in single particles at an inland urban location during a phytoplankton bloom, Environ. Sci. & Technol., 44, 1566-1572, 2010.

Geng, H., Hwang, H., Liu, X., Dong, S., and Ro, C. U.: Investigation of aged aerosols in size-resolved Asian dust storm particles transported from Beijing, China, to Incheon, Korea, using low-Z particle EPMA, Atmos. Chem. Phys., 14, 3307-3323, 2014.

Ghorai, S., Wang, B., Tivanski, A., and Laskin, A.: Hygroscopic properties of internally mixed particles composed of NaCl and water-soluble organic acids, Environ. Sci. Technol., 48, 2234-2241, 2014.

Giannoni, S. M., Trachte, K., Rollenbeck, R., Lehnert, L., Fuchs, J., and Bendix, J.: Atmospheric salt deposition in a tropical mountain rainforest at the eastern Andean slopes of south Ecuador - Pacific or Atlantic origin?, Atmos. Chem. Phys., 16, 10241-10261, 2016.

Gibson, E. R., Hudson, P. K., and Grassian, V. H.: Physicochemical properties of nitrate aerosols: Implications for the atmosphere, J. Phys. Chem. A, 110, 11785-11799, 2006.

Guasco, T. L., Cuadra-Rodriguez, L. A., Pedler, B. E., Ault, A. P., Collins, D. B., Zhao, D., Kim, M. J., Ruppel, M. J., Wilson, S. C., Pomeroy, R. S., Grassian, V. H., Azam, F., Bertram, T. H., and Prather, K. A.: Transition metal associations with primary biological particles in sea spray aerosol generated in a wave channel, Environ. Sci. Technol., 48, 1324-1333, 2014.

Guo, H., Xu, L., Bougiatioti, A., Cerully, K. M., Capps, S. L., Hite, J. R., Jr., Carlton, A. G., Lee, S. H., Bergin, M. H., Ng, N. L., Nenes, A., and Weber, R. J.: Fine-particle water and pH in the southeastern United States, Atmos. Chem. Phys., 15, 5211-5228, 2015.

Gurciullo, C., Lerner, B., Sievering, H., and Pandis, S. N.: Heterogeneous sulfate production in the remote marine environment: cloud processing and sea-salt particle contributions, J. Geophys. Res.: Atmos., 104, 21719-21731, 1999.

Gustafsson, M. E. R., and Franzen, L. G.: Inland transport of marine aerosols in southern Sweden, Atmos. Environ., 34, 313-325, 2000.

Hara, K., Osada, K., Kido, M., Hayashi, M., Matsunaga, K., Iwasaka, Y., Yamanouchi, T., Hashida, G., and Fukatsu, T.: Chemistry of sea-salt particles and inorganic halogen species in Antarctic regions: compositional differences between coastal and inland stations, J. Geophys. Res.: Atmos., 109, 2004.

Hidy, G. M., Blanchard, C. L., Baumann, K., Edgerton, E., Tanenbaum, S., Shaw, S., Knipping, E., Tombach, I., Jansen, J., and Walters, J.: Chemical climatology of the southeastern United States, 1999-2013, Atmos. Chem. Phys., 14, 11893-11914, 2014.

Hoffman, R. C., Laskin, A., and Finlayson-Pitts, B. J.: Sodium nitrate particles: Physical and chemical properties during hydration and dehydration, and implications for aged sea salt aerosols, J. Aerosol Sci, 35, 869-887, 2004.

Hopkins, R. J., Desyaterik, Y., Tivanski, A. V., Zaveri, R. A., Berkowitz, C. M., Tyliszczak, T., Gilles, M. K., and Laskin, A.: Chemical speciation of sulfur in marine cloud droplets and particles: Analysis of individual particles from the marine boundary layer over the California current, J. Geophys. Res.: Atmos., 113, 2008.

Keene, W. C., Pszenny, A. A. P., Jacob, D. J., Duce, R. A., Galloway, J. N., Schultz-Tokos, J. J., Sievering, H., and Boatman, J. F.: The geochemical cycling of reactive chlorine through the marine troposphere, Global Biogeochem. Cycles, 4, 407-430, 1990.

Kerminen, V. M., Teinila, K., Hillamo, R., and Pakkanen, T.: Substitution of chloride in sea-salt particles by inorganic and organic anions, J. Aerosol Sci., 29, 929-942, 1998.

Laskin, A., Iedema, M. J., and Cowin, J. P.: Quantitative time-resolved monitoring of nitrate formation in sea salt particles using a CCSEM/EDX single particle analysis, Environ. Sci. Technol., 36, 4948-4955, 2002.

Laskin, A., Iedema, M. J., and Cowin, J. P.: Time-resolved aerosol collector for CCSEM/EDX single-particle analysis, Aerosol Sci. Technol., 37, 246-260, 2003.

Laskin, A., Cowin, J. P., and Iedema, M. J.: Analysis of individual environmental particles using modern methods of electron microscopy and X-ray microanalysis, J. Electron. Spectrosc. Relat. Phenom., 150, 260-274, 2006a.

Laskin, A., Wang, H., Robertson, W. H., Cowin, J. P., Ezell, M. J., and Finlayson-Pitts, B. J.: A new approach to determining gas-particle reaction probabilities and application to the heterogeneous reaction of deliquesced sodium chloride particles with gas-phase hydroxyl radicals, J. Phys. Chem. A, 110, 10619-10627, 2006b.

Laskin, A., Moffet, R. C., Gilles, M. K., Fast, J. D., Zaveri, R. A., Wang, B., Nigge, P., and Shutthanandan, J.: Tropospheric chemistry of internally mixed sea salt and organic particles: Surprising reactivity of NaCl with weak organic acids, J. Geophys. Res.: Atmos., 117, 2012.

Li, W. J., Shi, Z. B., Yan, C., Yang, L. X., Dong, C., and Wang, W. X.: Individual metal-bearing particles in a regional haze caused by firecracker and firework emissions, Sci. Total Environ., 443, 464-469, 2013.

Liu, D.-Y., Rutherford, D., Kinsey, M., and Prather, K. A.: Real-time monitoring of pyrotechnically derived aerosol particles in the troposphere, Anal. Chem., 69, 1808-1814, 1997.

Liu, Y., Cain, J. P., Wang, H., and Laskin, A.: Kinetic study of heterogeneous reaction of deliquesced NaCl particles with gaseous HNO_3 using particle-on-substrate stagnation flow reactor approach, J. Phys. Chem. A, 111, 10026-10043, 2007.

Mamane, Y., and Mehler, M.: On the nature of nitrate particles in a coastal urban area, Atmos. Environ. (1967-1989), 21, 1989-1994, 1987.

Mamane, Y., and Gottlieb, J.: Heterogeneous reaction of nitrogen oxides on sea salt and mineral particles—a single particle approach, J. Aerosol Sci, 21, S225-S228, 1990.

Manders, A. M. M., Schaap, M., Querol, X., Albert, M. F. M. A., Vercauteren, J., Kuhlbusch, T. A. J., and Hoogerbrugge, R.: Sea salt concentrations across the European continent, Atmos. Environ., 44, 2434-2442, 2010.

Marple, V. A., Rubow, K. L., and Behm, S. M.: A microorifice uniform deposit impactor (MOUDI)-description, calibration and use, Aerosol Sci. Technol., 14, 434-446, 1991.

Martens, C. S., Wesolowski, J. J., Harriss, R. C., and Kaifer, R.: Chlorine loss from Puerto Rican and San Francisco Bay area marine aerosols, J. Geophys. Res., 78, 8778-8792, 1973.

Martin-Alberca, C., and Garcia-Ruiz, C.: Analytical techniques for the analysis of consumer fireworks, Trac-Trends Anal. Chem., 56, 27-36, 2014.

Matsumoto, K., Minami, H., Uyama, Y., and Uematsu, M.: Size partitioning of particulate inorganic nitrogen species between the fine and coarse mode ranges and its implication to their deposition on the surface ocean, Atmos. Environ., 43, 4259-4265, 2009.

May, N. W., Axson, J. L., Watson, A., Pratt, K. A., and Ault, A. P.: Lake spray aerosol generation: a method for producing representative particles from freshwater wave breaking, Atmos. Meas. Tech., 9, 4311-4325, 2016.

McInnes, L. M., Covert, D. S., Quinn, P. K., and Germani, M. S.: Measurements of chloride depletion and sulfur enrichment in individual sea-salt particles collected from the remote marine boundary layer, J. Geophys. Res.: Atmos., 99, 8257-8268, 1994.

McNeill, V. F., Patterson, J., Wolfe, G. M., and Thornton, J. A.: The effect of varying levels of surfactant on the reactive uptake of N_2O_5 to aqueous aerosol, Atmos. Chem. Phys., 6, 1635-1644, 2006.

Moffet, R. C., Desyaterik, Y., Hopkins, R. J., Tivanski, A. V., Gilles, M. K., Wang, Y., Shutthanandan, V., Molina, L. T., Abraham, R. G., Johnson, K. S., Mugica, V., Molina, M. J., Laskin, A., and Prather, K. A.: Characterization of Aerosols Containing Zn, Pb, and Cl from an Industrial Region of Mexico City, Environ. Sci. Technol., 42, 7091-7097, 2008.

Moffet, R. C., Roedel, T. C., Kelly, S. T., Yu, X. Y., Carroll, G. T., Fast, J., Zaveri, R. A., Laskin, A., and Gilles, M. K.: Spectro-microscopic measurements of carbonaceous aerosol aging in central California, Atmos. Chem. Phys., 13, 10445-10459, 2013.

Newberg, J. T., Matthew, B. M., and Anastasio, C.: Chloride and bromide depletions in sea-salt particles over the northeastern Pacific Ocean, J. Geophys. Res.: Atmos., 110, 13, 2005.

Nguyen, T. K. V., Petters, M. D., Suda, S. R., Guo, H., Weber, R. J., and Carlton, A. G.: Trends in particle-phase liquid water during the Southern Oxidant and Aerosol Study, Atmos. Chem. Phys., 14, 10911-10930, 2014.

Noble, C. A., and Prather, K. A.: Real-time single particle monitoring of a relative increase in marine aerosol concentration during winter rainstorms, Geophys. Res. Lett., 24, 2753-2756, 1997.

O'Brien, R. E., Wang, B., Laskin, A., Riemer, N., West, M., Zhang, Q., Sun, Y., Yu, X.-Y., Alpert, P., Knopf, D. A., Gilles, M. K., and Moffet, R. C.: Chemical imaging of ambient aerosol particles: Observational constraints on mixing state parameterization, J. Geophys. Res.: Atmos., 120, 9591-9605, 2015.

Odowd, C. D., Smith, M. H., Consterdine, I. E., and Lowe, J. A.: Marine aerosol, sea-salt, and the marine sulphur cycle: A short review, Atmos. Environ., 31, 73-80, 1997.

Okada, K., Ishizaka, Y., Masuzawa, T., and Isono, K.: Chlorine deficiency in coastal aerosols, J. Meteorol. Soc. Jpn., 56, 501-507, 1978.

Orellana, M. V., Matrai, P. A., Leck, C., Rauschenberg, C. D., Lee, A. M., and Coz, E.: Marine microgels as a source of cloud condensation nuclei in the high Arctic, Proc. Natl. Acad. Sci. U. S. A., 108, 13612-13617, 2011.

Pakkanen, T. A.: Study of formation of coarse particle nitrate aerosol, Atmos. Environ., 30, 2475-2482, 1996.

Pilson, M. E. Q.: An introduction to the chemistry of the sea, Cambridge University Press, 1998.

Polissar, A. V., Hopke, P. K., and Harris, J. M.: Source regions for atmospheric aerosol measured at Barrow, Alaska, Environ. Sci. Technol., 35, 4214-4226, 2001.

Pósfai, M., Anderson, J. R., Buseck, P. R., Shattuck, T. W., and Tindale, N. W.: Constituents of a remote pacific marine aerosol: A TEM study, Atmos. Environ., 28, 1747-1756, 1994.

Prather, K. A., Bertram, T. H., Grassian, V. H., Deane, G. B., Stokes, M. D., DeMott, P. J., Aluwihare, L. I., Palenik, B. P., Azam, F., Seinfeld, J. H., Moffet, R. C., Molina, M. J., Cappa, C. D., Geiger, F. M., Roberts, G. C., Russell, L. M., Ault, A. P., Baltrusaitis, J., Collins, D. B., Corrigan, C. E., Cuadra-Rodriguez, L. A., Ebben, C. J., Forestieri, S. D., Guasco, T. L., Hersey, S. P., Kim, M. J., Lambert, W. F., Modini, R. L., Mui, W., Pedler, B. E., Ruppel, M. J., Ryder, O. S., Schoepp, N. G., Sullivan, R. C., and Zhao, D.: Bringing the ocean into the laboratory to probe the chemical complexity of sea spray aerosol, Proc. Natl. Acad. Sci. U. S. A., 110, 7550-7555, 2013.

Ravishankara, A. R.: Heterogeneous and multiphase chemistry in the troposphere, Science, 276, 1058-1065, 1997.

Ravishankara, A. R., and Longfellow, C. A.: Reactions on tropospheric condensed matter, Physical Chemistry Chemical Physics, 1, 5433-5441, 1999.

Reid, J. P., and Sayer, R. M.: Chemistry in the clouds: The role of aerosols in atmospheric chemistry, Sci. Prog., 85, 263, 2002.

Rindelaub, J. D., Craig, R. L., Nandy, L., Bondy, A. L., Dutcher, C. S., Shepson, P. B., and Ault, A. P.: Direct measurement of pH in individual particles via Raman microspectroscopy and variation in acidity with relative humidity, J. Phys. Chem. A, 120, 911-917, 2016.

Robbins, R. C., Cadle, R. D., and Eckhardt, D. L.: The conversion of sodium chloride to hydrogen chloride in the atmosphere, J. Meteorol., 16, 53-56, 1959.

Roberts, J. M., Osthoff, H. D., Brown, S. S., and Ravishankara, A. R.: N_2O_5 oxidizes chloride to Cl_2 in acidic atmospheric aerosol, Science, 321, 1059-1059, 2008.

Rossi, M. J.: Heterogeneous reactions on salts, Chem. Rev., 103, 4823-4882, 2003.

Roth, B., and Okada, K.: On the modification of sea-salt particles in the coastal atmosphere, Atmos. Environ., 32, 1555-1569, 1998.

Ryder, O. S., Ault, A. P., Cahill, J. F., Guasco, T. L., Riedel, T. P., Cuadra-Rodriguez, L. A., Gaston, C. J., Fitzgerald, E., Lee, C., Prather, K. A., and Bertram, T. H.: On the role of particle inorganic mixing state in the reactive uptake of N_2O_5 to ambient aerosol particles, Environ. Sci. Technol., 48, 1618-1627, 2014.

Saul, T. D., Tolocka, M. P., and Johnston, M. V.: Reactive uptake of nitric acid onto sodium chloride aerosols across a wide range of relative humidities, J. Phys. Chem. A, 110, 7614-7620, 2006.

Schroeder, W. H., and Urone, P.: Formation of nitrosyl chloride from salt particles in air, Environ. Sci. Tech., 8, 756-758, 1974.

Shaw, G. E.: Aerosol chemical-components in Alaska air masses. 2. Sea salt and marine product, J. Geophys. Res.: Atmos., 96, 22369-22372, 1991.

Shen, H. R., Peters, T. M., Casuccio, G. S., Lersch, T. L., West, R. R., Kumar, A., Kumar, N., and Ault, A. P.: Elevated concentrations of lead in particulate matter on the neighborhood-scale in Delhi, India as determined by single particle analysis, Environ. Sci. Technol., 50, 4961-4970, 2016.

Sievering, H., Boatman, J., Galloway, J., Keene, W., Kim, Y., Luria, M., and Ray, J.: Heterogeneous sulfur conversion in sea-salt aerosol particles-the role of aerosol water-content and size distribution, Atmos. Environ., Part A, 25, 1479-1487, 1991.

Silva, B., Rivas, T., Garcia-Rodeja, E., and Prieto, B.: Distribution of ions of marine origin in Galicia (NW Spain) as a function of distance from the sea, Atmos. Environ., 41, 4396-4407, 2007.

Skinner, L. M., and Sambles, J. R.: The Kelvin equation—a review, J. Aerosol Sci, 3, 199-210, 1972.

Sobanska, S., Coeur, C., Maenhaut, W., and Adams, F.: SEM-EDX characterisation of tropospheric aerosols in the Negev desert (Israel), J. Atmos. Chem., 44, 299-322, 2003.

Sullivan, R. C., Guazzotti, S. A., Sodeman, D. A., and Prather, K. A.: Direct observations of the atmospheric processing of Asian mineral dust, Atmos. Chem. Phys., 7, 1213-1236, 2007.

ten Brink, H. M.: Reactive uptake of HNO_3 and H_2SO_4 in sea-salt (NaCl) particles, J. Aerosol Sci, 29, 57-64, 1998.

Thornton, J. A., and Abbatt, J. P. D.: N_2O_5 reaction on submicron sea salt aerosol: kinetics, products, and the effect of surface active organics, J. Phys. Chem. A, 109, 10004-10012, 2005.

Udisti, R., Dayan, U., Becagli, S., Busetto, M., Frosini, D., Legrand, M., Lucarelli, F., Preunkert, S., Severi, M., Traversi, R., and Vitale, V.: Sea spray aerosol in central Antarctica. Present atmospheric behaviour and implications for paleoclimatic reconstructions, Atmos. Environ., 52, 109-120, 2012.

Ueda, S., Hirose, Y., Miura, K., and Okochi, H.: Individual aerosol particles in and below clouds along a Mt. Fuji slope: modification of sea-salt-containing particles by in-cloud processing, Atmos. Res., 137, 216-227, 2014.

Wang, B., O'Brien, R. E., Kelly, S. T., Shilling, J. E., Moffet, R. C., Gilles, M. K., and Laskin, A.: Reactivity of liquid and semisolid secondary organic carbon with chloride and nitrate in atmospheric aerosols, J. Phys. Chem. A, 119, 4498-4508, 2015.

Wang, Y. Q., Zhang, X. Y., and Draxler, R. R.: TrajStat: GIS-based software that uses various trajectory statistical analysis methods to identify potential sources from long-term air pollution measurement data, Environ. Model. Softw., 24, 938-939, 2009.

Weber, R. J., Guo, H. Y., Russell, A. G., and Nenes, A.: High aerosol acidity despite declining atmospheric sulfate concentrations over the past 15 years, Nature Geosci., 9, 282-285, 2016.

Woods, E., III, Heylman, K. D., Gibson, A. K., Ashwell, A. P., and Rossi, S. R.: Effects of NO_y aging on the dehydration dynamics of model sea spray aerosol, J. Phys. Chem. A, 117, 4214-4222, 2013.

Xiong, F., McAvey, K. M., Pratt, K. A., Groff, C. J., Hostetler, M. A., Lipton, M. A., Starn, T. K., Seeley, J. V., Bertman, S. B., Teng, A. P., Crounse, J. D., Nguyen, T. B., Wennberg, P. O., Misztal, P. K., Goldstein, A. H., Guenther, A. B., Koss, A. R., Olson, K. F., de Gouw, J. A., Baumann, K., Edgerton, E. S., Feiner, P. A., Zhang, L., Miller, D. O., Brune, W. H., and Shepson, P. B.: Observation of isoprene hydroxynitrates in the southeastern United States and implications for the fate of NO_x, Atmos. Chem. Phys., 15, 11257-11272, 2015.

Zhuang, H., Chan, C. K., Fang, M., and Wexler, A. S.: Formation of nitrate and non-sea-salt sulfate on coarse particles, Atmos. Environ., 33, 4223-4233, 1999.

Ziemann, P. J., and McMurry, P. H.: Spatial distribution of chemical components in aerosol particles as determined from secondary electron yield measurements: Implications for mechanisms of multicomponent aerosol crystallization, J. Colloid Interface Sci., 193, 250-258, 1997.

Chapter 4.
Isoprene-Derived Organosulfates: Vibrational Mode Analysis by Raman Spectroscopy, Acidity-Dependent Spectral Modes, and Observation in Individual Atmospheric Particles

Adapted with permission from Bondy, A. L., Craig, R. L., Zhang, Z., Gold, A., Surratt, J. D., Ault, A. P. Isoprene-derived organosulfates: Vibrational mode analysis by Raman spectroscopy, acidity-dependent spectral modes, and observation in individual atmospheric particles, *Journal of Phys. Chem. A*, DOI: 10.1021/acs.jpca.7b10587. Copyright 2017 American Chemical Society.

4.1. Introduction

Isoprene is a biogenic volatile organic compound (BVOC) emitted by broadleaf trees and is the largest global emission of all non-methane VOCs (~600 Tg y^{-1}) (Guenther et al., 2006). Atmospheric oxidation of isoprene leads to lower volatility products that partition to the particle phase, forming secondary organic aerosol (SOA) (Hallquist et al., 2009; Martin et al., 2010; Carlton et al., 2009; Glasius and Goldstein, 2016), which has been estimated to constitute 30 % to 50 % of the global SOA budget (Carlton et al., 2009). SOA-containing particles impact climate by scattering and absorbing solar radiation or acting as cloud condensation nuclei (CCN) (Jacobson et al., 2000). Recent work has also shown that exposure of human lung cells to atmospherically relevant isoprene-derived SOA induces oxidative stress (Kramer et al., 2016; Lin et al., 2016; Lin et al., 2017). Furthermore, chronic obstructive pulmonary disease (COPD), which can worsen due to oxidative stress in the human respiratory system (Barnes et al., 2003; Repine et al., 1997), is higher in the southeastern United States where isoprene-derived SOA contributes large mass fractions (up to 40 %) of submicron organic aerosol (Dominici et al., 2006; Budisulistiorini et al., 2016; Rattanavaraha et al., 2017). Therefore, understanding the formation and evolution of isoprene-derived SOA is important for understanding the overall impact of aerosols on climate and health.

Organosulfates are a major class of compounds in SOA, estimated to contribute 5-10 % of the total organic aerosol mass over the continental U.S. (Tolocka and Turpin, 2012). Due to their high polarity and water solubility, these hygroscopic compounds could enhance the CCN activity of organic aerosol (Estillore et al., 2016). Isoprene-derived organosulfates formed from reactions of sulfate with isoprene oxidation products in the particle phase are often reported as the most abundant organosulfates in ambient aerosols (Hatch et al., 2011a, b; Froyd et al., 2010; Surratt et al., 2008), with mass concentrations of up to 8 % of organic matter (He et al., 2014; Lin et al., 2013; Liao et al., 2015; Budisulistiorini et al., 2015). The isoprene-derived organosulfates detected in ambient aerosol formed under low-NO_x conditions are the diastereomeric methyltetrol sulfate ester racemates (Froyd et al., 2010; Hatch et al., 2011a, b; Gomez-Gonzalez et al., 2008; He et al., 2014; Stone et al., 2012; Lin et al., 2013; Lin et al., 2012; Riva et al., 2016; Surratt et al., 2008; Liao et al., 2015; Surratt et al., 2007a), while under high-NO_x conditions, racemic 2-methylglyceric acid sulfate ester is also detected (Hatch et al., 2011a, b; Surratt et al., 2008; He et al., 2014; Lin et al., 2013; Gomez-Gonzalez et al., 2008; Surratt et al., 2007a). A simplified scheme of reactions leading to the formation of isoprene-derived organosulfates under low- and high-NO_x conditions is shown in Figure 4.1. The sulfate esters form via a nucleophilic oxirane ring-opening reaction by sulfate. Sulfate attacks δ-isoprene epoxydiol (δ-IEPOX), an isomer of IEPOX formed in significant proportion (Bates et al., 2014), under low-NO_x conditions at the primary carbon (C1) to yield racemic 3-methylerythritol sulfate ester ((*2S,3R)/(2R,3S)*-2,3,4-trihydroxy-3-methylbutyl sulfate) and racemic 3-methylthreitol sulfate ester ((*2R,3R)/(2S,3S)*-2,3,4-trihydroxy-3-methylbutyl sulfate) (Darer et al., 2011; Surratt et al., 2010; Minerath and Elrod, 2009). Two high NO_x isoprene-oxidation products, methacrylic acid epoxide (MAE; 2-methyloxirane-2-carboxylic acid) and hydroxymethyl-methyl-α-lactone (HMML), yield racemic 2-methylglyceric acid sulfate ester (2-carboxyl-2-hydroxylpropyl sulfate). Methyltetrol sulfate esters have been observed in more than 65 % of particles in the southeastern U.S and are among the most abundant individual organic compounds in atmospheric aerosol (Froyd et al., 2010; Hatch et al., 2011a). Although previous studies in China and the southeastern United States showed that 2-methylglyceric acid sulfate ester is not as abundant in ambient aerosol as the methyltetrol sulfate esters, it nevertheless accounted for ~0.5 % of organic matter by mass (He et al., 2014; Lin et al., 2013). Isoprene-derived organosulfates have long atmospheric lifetimes and thus are substantial contributors to

ambient organic aerosol (Darer et al., 2011). The sulfate esters can undergo hydrolysis within particles (hydrolysis lifetime, 60 to 460 h, depending on particle acidity) (Darer et al., 2011; Hu et al., 2011), leading to the formation of the diastereomeric 2-methyltetrol racemates (erythritol and threitol) and racemic 2-methylglyceric acid (2,3-dihydroxy-2-methylpropanoic acid) (Surratt et al., 2006; Darer et al., 2011; Hu et al., 2011; Gomez-Gonzalez et al., 2008; Lin et al., 2013; Surratt et al., 2010; Nguyen et al., 2015). The prevalence of these organosulfates and their hydrolysis products as well as their continuing chemistry in the aerosol phase, has recently elicited considerable research interest (Surratt et al., 2007a; Chan et al., 2010; Ebben et al., 2014; Lin et al., 2012; Surratt et al., 2008; Surratt et al., 2006; Glasius and Goldstein, 2016; Upshur et al., 2014).

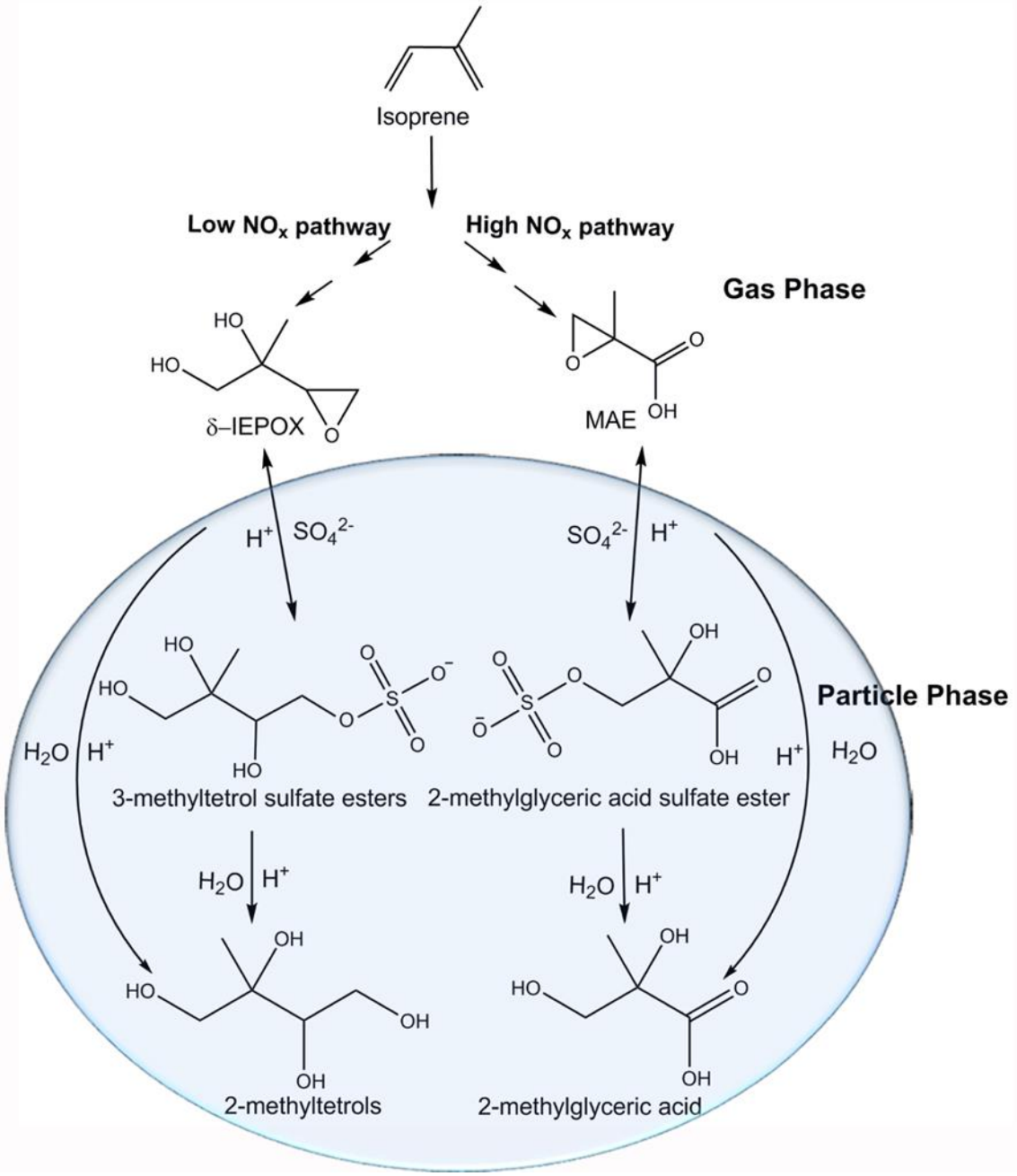

Figure 4.1. Scheme leading to the formation of isoprene-derived SOA compounds: 3-methyltetrol sulfate esters, 2-methyltetrols, 2-methylglyceric acid sulfate ester, and 2-methylglyceric acid. Both the high- and low-NO_x pathways are shown (Lin et al., 2013; Surratt et al., 2010; Nguyen et al., 2015). For simplicity, only one isomer of each respective compound is shown. 2-Methylglyceric acid, 2-methylglyceric acid sulfate ester, 2-methyltetrols, and the 3-methyltetrol sulfate esters are present in the particle phase, while the epoxides are in the gas phase.

Currently, identification and quantitation of isoprene-derived organosulfates in individual aerosol particles has been limited due to the complexity of SOA particles (thousands of species

are often present in attoliter volumes), instrumental difficulties in differentiating organosulfates from inorganic sulfate, and a lack of authentic standards. Most methods currently used to detect organosulfate species have been offline mass spectrometry-focused, relying on filter extractions followed by ultra-performance liquid chromatography/electrospray ionization high-resolution quadrupole time-of-flight mass spectrometry (UPLC/ESI-HR-QTOFMS) (Surratt et al., 2008; Gomez-Gonzalez et al., 2008; Yassine et al., 2012; Hettiyadura et al., 2015; Boone et al., 2015; Budisulistiorini et al., 2015; Riva et al., 2016; Lin et al., 2013; Lin et al., 2012; Stone et al., 2012; He et al., 2014; Surratt et al., 2007a; Iinuma et al., 2009; Nguyen et al., 2015; Surratt et al., 2007b; Surratt et al., 2010). Online analysis has been attempted by Farmer et al. (2010), who used an online aerosol mass spectrometer (AMS) to analyze an isoprene organosulfate surrogate standard, though due to extensive fragmentation, this compound could not be differentiated from inorganic sulfate in ambient aerosol. Some spectroscopic analysis has been done on organosulfates using Fourier transform infrared spectroscopy (Takahama et al., 2011; Schwartz et al., 2010; Maria et al., 2003; Frossard et al., 2011; Russell et al., 2009), but identification has focused on a single lower frequency vibration (C-S of methane sulfonic acid at 876 cm^{-1}), rather than the entire fingerprint region, making interpretation challenging. Although bulk methods are typically used to detect and quantify organosulfates, they provide information limited to average aerosol composition and do not provide information concerning the abundance of organosulfate-containing particles.

Single particle mass spectrometry methods have been used to provide information regarding the mixing state of organosulfates. Hatch et al. detected isoprene-derived organosulfates using aerosol time-of-flight mass spectrometry (ATOFMS), and observed high fractions during two field studies in Atlanta, Georgia (Hatch et al., 2011a, b). Froyd et al. (2010) detected significant levels of isoprene-derived organosulfates in the free troposphere by particle ablation laser mass spectrometry (PALMS). These studies revealed that isoprene-derived organosulfates not only account for a sizeable fraction of organic aerosol mass, but are ubiquitous, present in more than 70 % of aerosols over the continental U.S. (Froyd et al., 2010; Hatch et al., 2011a). However, issues such as fragmentation and shot-to-shot variability for laser desorption/ionization in both the ATOFMS and PALMS make quantifying organosulfates particularly challenging (Froyd et al., 2010; Hatch et al., 2011a; Liao et al., 2015).

In contrast to bulk analysis and single particle mass spectrometry methods, Raman microspectroscopy is a nondestructive technique that can be used to analyze the vibrational modes of functional groups within individual particles (Ault and Axson, 2017; Ault et al., 2013; Craig et al., 2015, 2017a; Craig et al., 2017b; Ivleva et al., 2007; Popovicheva et al., 2012; Rindelaub et al., 2016; Deng et al., 2014; Baustian et al., 2012; Lee and Chan, 2007; Lee and Chan, 2010; Reid et al., 2007; Schweiger, 1990; Ivleva et al., 2013; Catelani et al., 2014). In addition to identifying vibrational modes, Raman microspectroscopy is sensitive to changes in bonding and molecular environment, such as aqueous versus solid particles (Ault et al., 2014) or acidity-dependent protonation states (Craig et al., 2017b; Rindelaub et al., 2016). Since Raman scattering, unlike mass spectrometry, is not dependent on particle ionization and fragmentation patterns (Farmer et al., 2010; Froyd et al., 2010), it can be used to differentiate classes of compounds within SOA, such as inorganic sulfate and organosulfates, since each class exhibits unique vibrational modes. Previous Raman studies of ambient SOA identified nitrates, sulfates, carbonates, alcohols/water, silicates and aluminosilicates, soot, hydrocarbons, and humic like substances within individual particles (Craig et al., 2015; Ivleva et al., 2007; Popovicheva et al., 2012; Deng et al., 2014; Baustian et al., 2012). However, despite the rich vibrational spectra that Raman can provide, the complexity of ambient SOA makes unambiguous identification of specific constituents challenging. In order to identify isoprene-derived organosulfates within ambient SOA particles using Raman spectroscopy, a thorough analysis of their vibrational modes is therefore necessary.

Herein, the Raman vibrational spectra of the atmospherically-relevant 3-methylerythritol/3-methylthreitol sulfate ester mixture derived from δ-IEPOX and 2-methylglyceric acid sulfate ester derived from MAE and HMML are recorded and observed band frequencies are compared to calculated frequencies. Raman spectra of the organosulfate hydrolysis products, 2-methyltetrols and 2-methylglyceric acid, were examined to assist in the identification of the organosulfate-related modes. Density functional theory (DFT), in conjunction with published frequencies of small-molecule organosulfates, was used to predict optimized structures of the isoprene-derived organosulfates and to assign vibrational modes in experimental Raman spectra. Acidity-dependent shifts of key modes were identified. Furthermore, key organosulfate-related Raman modes were observed in ambient atmospheric aerosol particles collected from the southeastern United States. This study identifies signature

Raman vibrational modes for isoprene-derived organosulfates that can be used to identify these compounds in chamber studies and ambient particles.

4.2. Methods

4.2.1 Reagents

2-Methylglyceric acid, racemic 2-methylglyceric acid sulfate ester potassium salt (81 %), a diastereomeric mixture of racemic 2-methyltetrols (racemic 2-methylerythritol and racemic 2-methylthreitol), and sodium salts of the 3-methyltetrol sulfate esters (86 %) (racemic 3-methylerythritol sulfate ester and racemic 3-methylthreitol sulfate ester) were synthesized by the Surratt group and used without further purification (Budisulistiorini et al., 2015; Rattanavaraha et al., 2016; Hettiyadura et al., 2015; An et al., 1992). Synthetic details for the 3-methyltetrol sulfate esters and 2-methyltetrols are given in Appendix C. 2-Methylglyceric acid was synthesized by a published method (An et al., 1992). 2-Methylglyceric acid sulfate ester potassium salt was synthesized with a slight modification of the published method (Hettiyadura et al., 2015) using methylglyceric acid as the starting material. Trace quantities of inorganic sulfate are present in the 3-methyltetrol and 2-methylglyceric acid sulfate esters. Target structures were verified by proton nuclear magnetic resonance spectroscopy (^{1}H NMR), Fourier transform infrared spectroscopy (FTIR) and energy dispersive X-ray spectroscopy (EDX) (Figures C.1-C.8).

4.2.2. Raman Microspectroscopy

Aqueous 0.05 M solutions of 2-methylglyceric acid, 2-methylglyceric acid sulfate ester, 2-methyltetrols, and 3-methyltetrol sulfate esters were prepared by dissolution in 18.3 MΩ Milli-Q water. For Raman analysis, 2 μL droplets (~1 mm diameter) were deposited onto quartz substrates (Ted Pella). Additionally, aerosol particles were generated by nebulizing aqueous 0.05 M solutions of 2-methylglyceric acid sulfate ester and 3-methyltetrol sulfate esters onto quartz using a concentric glass nebulizer (TR-30-A1, Meinhard). Particles from aerosolized compounds, with projected area diameters ranging from ~3.5 to 9 μm, produced identical, but lower intensity Raman spectra as large droplets of the aqueous solutions, therefore only Raman spectra of the organosulfate solutions are shown in the subsequent analysis. See Appendix C for Raman spectra of aerosolized compounds and pure crystals/liquids (Figures C.9-C.12).

The standards were probed using a Raman microspectrometer (LabRAM HR Evolution, HORIBA, Ltc.) at ambient temperature and relative humidity. The Raman spectrometer was coupled with a confocal optical microscope (100x long working distance Olympus objective, 0.9 numerical aperture) and equipped with a Nd:YAG laser source (50 mW, 532 nm) operated with a neutral density (ND) filter at 100 % and CCD detector. The 1800 g/mm diffraction grating yielded a spectral resolution of ~0.7 cm^{-1}. The instrument was calibrated daily using a silicon wafer standard against the Stokes Raman signal of pure Si at 520 cm^{-1}. Spectra were collected with three accumulations at 60-second acquisition times for the following spectral ranges: 500-4000 cm^{-1} (2-methylglyceric acid sulfate ester and 2-methyltetrols), 500-2200 cm^{-1} and 2200-4000 cm^{-1} (2-methylglyceric acid), 500-1800 cm^{-1} and 2500-4000 (3-methyltetrol sulfate esters). For 2-methylglyceric acid and the 3-methyltetrol sulfate esters, the lower frequency ranges (500-2200 cm^{-1} and 500-1800 cm^{-1}, respectively) and the higher frequency range (2500-4000 cm^{-1}) were collected separately using the same number of accumulations and acquisition time described previously to minimize water evaporation.

To explore the nature of the carboxylic acid vibrational mode and identify the cause of spectral variation between 2-methylglyceric acid sulfate ester and 2-methylglyceric acid, the effect of pH was studied. Assuming a similar pK_a for 2-methylglyceric acid compared to glyceric acid (pK_a glyceric acid ~3.5), the pH of an aqueous solution of 2-methylglyceric acid was adjusted from 1.3 to approximately 1.8, 3, and 10 through the addition of NaOH, measured using pH paper. Raman spectra were collected of the aqueous solutions of 2-methylglyceric acid at each pH from 500 to 4000 cm^{-1} using three accumulations, 10-second acquisition times, and a 600 g/mm diffraction grating with a spectral resolution of ~1.7 cm^{-1}.

4.2.3. Density Functional Theory Calculations

Geometry optimization, Raman shift, and Raman scattering activity calculations were performed using Gaussian 09W (Frisch et al., 2009). Initial geometry optimizations were performed using DFT with the CAM-B3LYP functional and 3-21G basis set. An additional geometry optimization was performed and Raman vibrational mode frequencies were calculated at the DFT CAM-B3LYP level of theory with the 6-311 ++ G(2d,p) basis set, using an ultrafine pruned grid and tight optimization criteria. All calculations are unscaled and run using water as a solvent. Calculated Raman frequencies and activity were used, in conjunction with literature

(Okabayashi et al., 1974; Koda and Nomura, 1985; Kato and Kurimoto, 1977; Chihara, 1960; Larkin, 2011; Picquart, 1986; Kartha et al., 1984), to assign vibrational modes to the experimental Raman spectra collected for each compound. The DFT calculations for 2-methylglyceric acid sulfate ester, 3-methylerythritol sulfate ester, and 3-methylthreitol sulfate ester were performed with a -1 charge on the compounds. Since the DFT calculated frequencies for the sulfate functional group-related modes deviate from literature frequencies, multiple functionals and basis sets were tested for methyl sulfate, a model compound (Table C.1), and CAM-B3LYP was selected for the following analysis as a compromise between accuracy and calculation expense.

4.2.4. Ambient Aerosol Collection

Ambient particles from the Southern Oxidant and Aerosol Study (SOAS) during the summer of 2013 were analyzed for isoprene-derived organosulfate Raman signatures. Description of the site and particle collection is provided elsewhere (Bondy et al., 2017; Allen et al., 2015; Hidy et al., 2014). Briefly, particles were impacted on quartz substrates (Ted Pella Inc.) using a micro-orifice uniform deposit impactor (MOUDI, Model 110, MSP Corp.) in Centreville, AL, a rural, forested region near Talladega National Forest with high isoprene emissions. After collection, all substrates were sealed and stored at -22 °C prior to analysis. Individual particles were analyzed using computer controlled-Raman microspectroscopy (CC-Raman), according to the method described previously by Craig et al. (2017a).

4.3. Results and Discussion

4.3.1. Signature Raman Modes for Isoprene-Derived Organosulfates

To identify Raman signatures for isoprene-derived organosulfates, differences between the experimental spectra of the organosulfates and their hydrolysis products were noted. Figure 4.2 shows experimental Raman spectra of the organosulfates and their hydrolysis products overlaid with intensities normalized to the modes at 1460 cm^{-1} and 2950 cm^{-1} (the most intense modes in the low- and high-frequency regions, respectively, excluding possible sulfate modes). Distinct modes present in the spectra of both organosulfates at ~1065 cm^{-1} and ~850 cm^{-1}, assigned to the organosulfate functional group, are highlighted. Aside from the sulfate modes, key spectral differences include a very intense inorganic sulfate mode (from synthesis or

hydrolysis) present in the spectrum of the 3-methyltetrol sulfate ester mixture at 982 cm^{-1}, and differences in the carbonyl stretching region (1400-1750 cm^{-1}) for 2-methylglyceric acid sulfate ester and 2-methylglyceric acid which will be explored in more detail below.

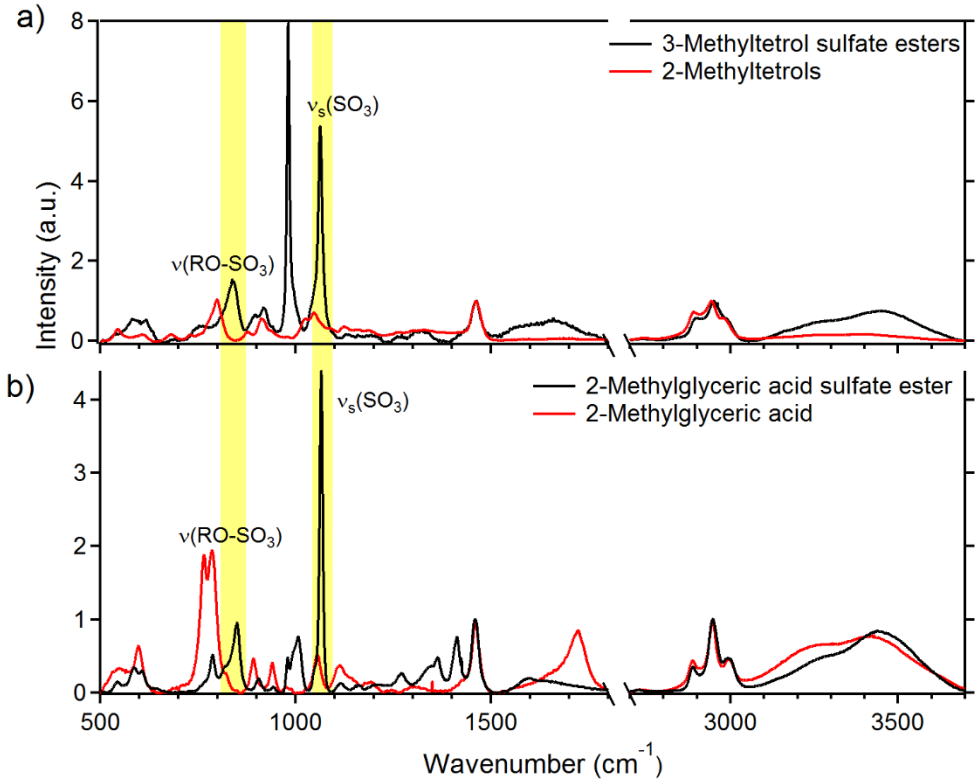

Figure 4.2. Experimental Raman spectra of a) the 3-methyltetrol sulfate esters overlaid with 2-methyltetrols, and b) 2-methylglyceric acid sulfate ester overlaid with 2-methylglyceric acid.

4.3.2. Experimental Raman Spectra and DFT Calculated Frequencies for the 3-Methyltetrol Sulfate Esters and 2-Methyltetrols

To correlate the spectral differences observed in Figure 4.2 with the presence of the organosulfate functional group, quantum chemical calculations were performed for the 3-methyltetrol sulfate esters, 2-methyltetrols, 2-methylglyceric acid sulfate ester, and 2-methylglyceric acid. Figure 4.3a shows experimental Raman modes within the fingerprint region (500-1500 cm^{-1}) and at higher frequencies (2700-3500 cm^{-1}) for the mixture of diastereomeric 3-methyltetrol sulfate esters in an aqueous solution. Using DFT, the Raman activity (Figure 4.3b) was calculated for the minimum-energy geometry of each diastereomer (Figure 4.3c and 4.3d). The optimal geometries, with the terminal (C4) hydroxyl group twisted toward the sulfate group,

were used in the subsequent analysis, although the energies were not substantially different for other conformers (difference < 0.2 kcal)

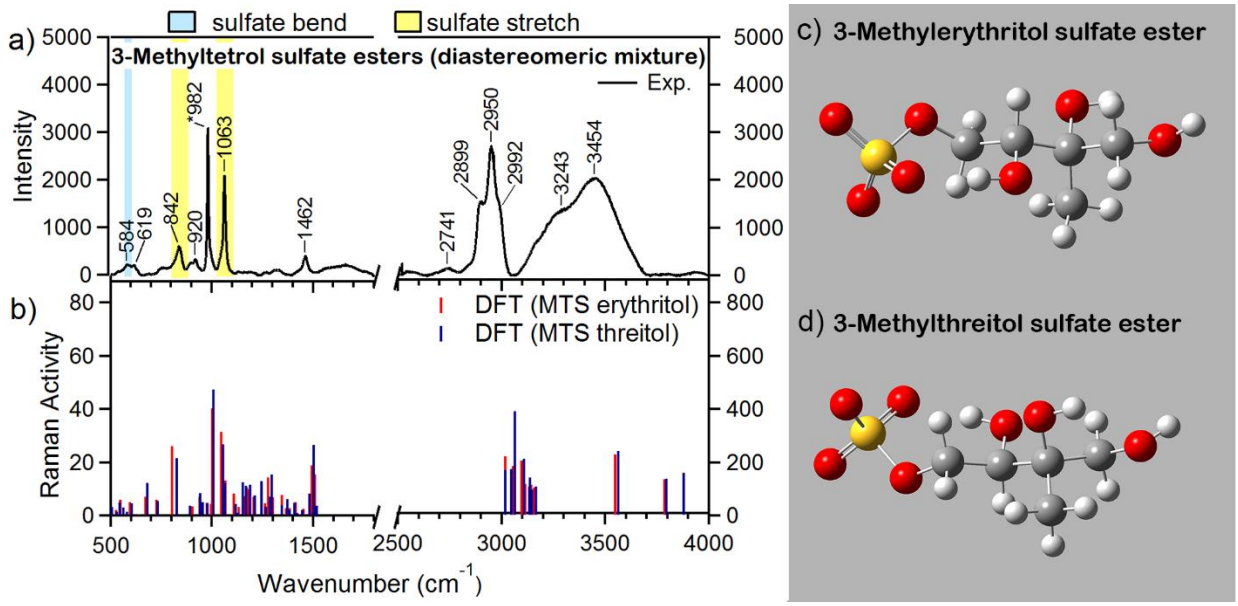

Figure 4.3. Aqueous phase a) experimental and b) calculated Raman spectra of the 3-methyltetrol sulfate esters. In panel a, the sulfate bending mode is highlighted in blue, and the sulfate stretching modes in yellow. DFT optimized structures of c) 3-methylerythritol sulfate ester and d) 3-methylthreitol sulfate ester. Note that the intensity scale of the lower frequency modes in the DFT spectra (500-1800 cm^{-1}) is 10x less intense than that of the higher frequency modes (2500-4000 cm^{-1}).

Comparison of the calculated spectra of the 3-methyltetrol sulfate esters with the experimental spectrum shows general qualitative agreement between calculated and observed Raman shifts and intensities (Table 4.1, Table C.2). However, some discrepancies were observed within the fingerprint region, in addition to the blue-shifted ν(C-H) and ν(O-H) modes due to anharmonicity associated with light atoms (Siebert and Hildebrandt, 2008). Table 4.1 lists tentative Raman assignments for the experimentally observed modes and the DFT-calculated frequencies, assigned by comparing the observed modes to those predicted via DFT, as well as published Raman measurements of alkyl sulfates, discussed later in detail (Chihara, 1960; Okabayashi et al., 1974; Kartha et al., 1984; Kato and Kurimoto, 1977; Picquart, 1986; Larkin, 2011; Koda and Nomura, 1985). Bands assigned to the organosulfate stretching modes are ν(RO-SO_3) at 842 cm^{-1} and $\nu_s(SO_3)$ at 1063 cm^{-1}. Additionally, a very strong band at 982 cm^{-1} in the observed spectrum likely corresponds to the $\nu_s(SO_4^{2-})$ of aqueous sulfate (Vargas Jentzsch et al., 2013; Ben Mabrouk et al., 2013), a residual species from the synthesis. A very weak mode at 584

cm^{-1} may be related to $\delta(SO_3)$; however, this assignment is ambiguous because of low intensity and interfering background signal from the quartz substrate. All the observed sulfate-related modes are blue-shifted from the calculated frequencies, likely due to issues associated with DFT predicting frequencies for charged species (electron density is localized within the sulfate group). As the differences between calculated and observed frequencies were significant for the sulfate-related functional group, published Raman measurements of alkyl sulfates and spectral differences between the 3-methyltetrol sulfate esters and 2-methyltetrols were used to assign these modes, discussed later in detail. In addition to the modes related to the sulfate functional group, Raman intensity at 920 cm^{-1} and 1462 cm^{-1} correspond to $\delta(CH_2)$ and $\delta(CH_3)$ (Avzianova and Brooks, 2013; De Gelder et al., 2007; Larkin, 2011; Furić et al., 1992; Lee and Chan, 2007; McLaughlin et al., 2002). Raman modes in the observed spectrum at 2741, 2899, 2950, and 2992 cm^{-1} correspond to $\nu_s(CH_2)$, $\nu_s(CH_3)$, $\nu_a(CH_2)$ and $\nu_a(CH_3)$ (Craig et al., 2015; Larkin, 2011), respectively, and bands at 3243 and 3454 cm^{-1} correspond to ν(O-H) (Furić et al., 1992).

Table 4.1. Experimentally observed Raman modes, DFT calculated frequencies, and tentative assignments for the 3-methyltetrol sulfate esters.

Observed (cm^{-1})	Calculated: 3-methylerythritol sulfate ester (cm^{-1})	Calculated: 3-methylthreitol sulfate ester (cm^{-1})	Assignment
584 (vw)[a,b]	561[a]	546[a]	$\delta(SO_3)$ (Picquart, 1986; Chihara, 1960; Kartha et al., 1984; Kato and Kurimoto, 1977; Okabayashi et al., 1974)
842 (m)[a]	727[a]	732[a]	$\nu(RO\text{-}SO_3)$ (Picquart, 1986; Kartha et al., 1984; Okabayashi et al., 1974; Larkin, 2011)
920 (w)	939	954	$\delta(CH_2$ & $CH_3)$ (De Gelder et al., 2007)
982 (vs)[c]			$\nu_s(SO_4)$ (salt) (Vargas Jentzsch et al., 2013; Ben Mabrouk et al., 2013)
1063 (s)[a]	1047[a]	1054[a]	$\nu_s(SO_3)$ (Chihara, 1960; Kartha et al., 1984; Koda and Nomura, 1985; Okabayashi et al., 1974; Larkin, 2011)
1462 (m)	1500	1503	$\delta(CH_2$ & $CH_3)$ (McLaughlin et al., 2002; De Gelder et al., 2007; Furić et al., 1992; Avzianova and Brooks, 2013; Larkin, 2011; Lee and Chan, 2007)
2899 (s)	3055	3048	$\nu_s(CH_3)$ (Craig et al., 2015; Larkin, 2011)
2950 (vs)	3066	3066	$\nu_a(CH_2)$ (Larkin, 2011; Craig et al., 2015)
2992 (s)	3097	3110	$\nu_a(CH_3)$ (Larkin, 2011; Craig et al., 2015)
3243 (s)	3786	3795	ν(O-H) (Furić et al., 1992)
3454 (vs)	3877	3878	ν(O-H) (Furić et al., 1992)

[a] Frequencies highlighted in blue correspond to bending modes associated with the organosulfate group, while frequencies highlighted in yellow correspond to organosulfate-related stretching modes.

[b] Possible $\delta(SO_3)$ mode, difficult to differentiate from background.

[c] Contamination in sample.

Assignment of the sulfate modes was confirmed by comparison of the experimental and calculated modes of the sulfate esters with the experimental and calculated modes (using DFT-optimized conformations) of the mixture of diastereomeric 2-methyltetrols (Figure 4.4, Table 4.2, Table C.3) (Darer et al., 2011; Hu et al., 2011). This approach is based on the assumption that the sulfate group will not cause major perturbation of other structural modes. In accord with this premise, the experimental spectrum of the 2-methyltetrols (Figure 4.4a) contained modes in the fingerprint region at 914 and 1462 cm^{-1} indicative of $\delta(CH_2)$ and $\delta(CH_3)$ (Furić et al., 1992; Larkin, 2011; Lee and Chan, 2007; De Gelder et al., 2007; Avzianova and Brooks, 2013; McLaughlin et al., 2002). In the high frequency region, modes at 2751, 2895, 2942, and 2983 cm^{-1} correspond to $\nu_s(CH_2)$, $\nu_s(CH_3)$, $\nu_a(CH_2)$ and $\nu_a(CH_3)$ (Craig et al., 2015; Larkin, 2011),

respectively, closely corresponding to similar modes identified in the spectrum of the sulfate ester mixture. Modes at 3262 and 3435 cm^{-1} correspond to ν(O-H) (Furić et al., 1992). In addition, the spectrum of the 2-methyltetrols showed moderate intensity Raman modes at 799 cm^{-1} (δ(C-OH)) (Larkin, 2011) and 1048 cm^{-1} (ν(C-O)) (De Gelder et al., 2007; Avzianova and Brooks, 2013), and a weak mode at 1125 cm^{-1} (ν(C-OH), Table 4.2) (Avzianova and Brooks, 2013; Larkin, 2011). As observed for 3-methyltetrol sulfate ester, the DFT calculated frequencies and intensities for the polyol and carbon backbone-related modes δ(C-H, CH_2, & CH_3), δ(C-OH), ν(C-C), ν(C-O) had generally good agreement with the experimentally observed frequencies in the fingerprint region. The calculated frequencies for the high frequency region however, were blue-shifted as in the 3-methyltetrol sulfate esters.

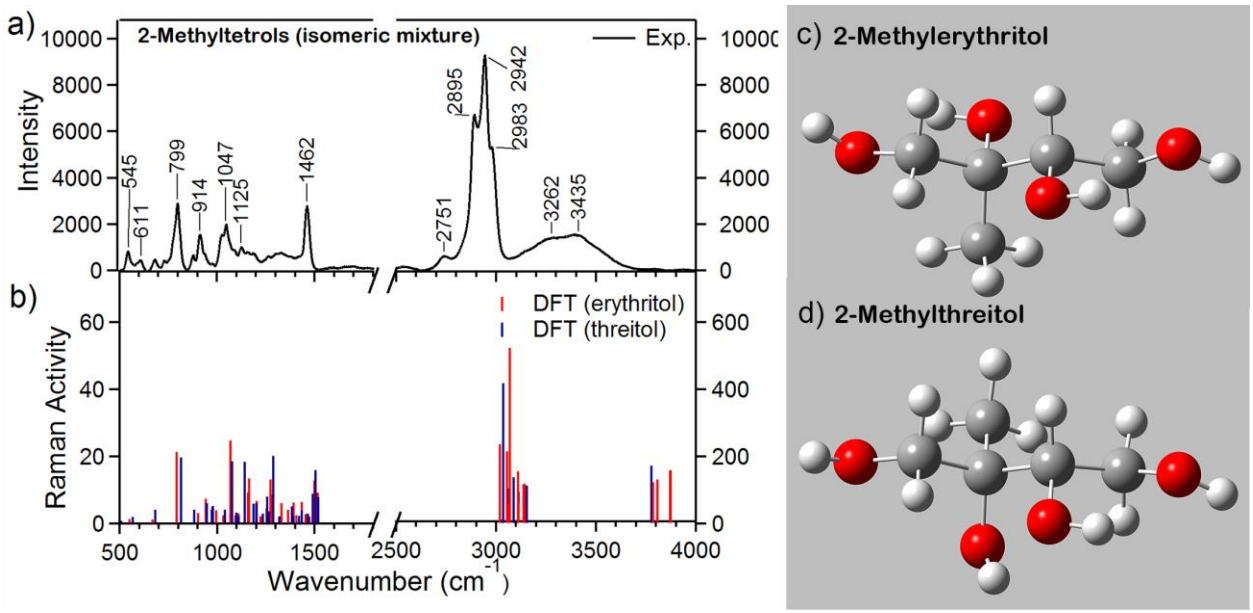

Figure 4.4 Aqueous phase a) experimental and b) DFT calculated Raman spectra of the 2-methyltetrols (2-methylerythritol and 2-methylthreitol). DFT optimized structures of c) 2-methylerythritol and d) 2-methylthreitol. Note, the lower frequency modes in the DFT spectra (500-1800 cm^{-1}) are on an intensity scale 10x lower than the higher frequency region (2500-4000 cm^{-1}).

Table 4.2. Experimentally observed Raman modes, DFT calculated frequencies, and tentative assignments for the 2-methyltetrols.

Observed (cm^{-1})	Calculated: 2-methylerythritol (cm^{-1})	Calculated: 2-methylthreitol (cm^{-1})	Assignment
545 (m)	550	566	δ(C-H) (Leyton et al., 2008)
799 (s)	792	814	δ(C-OH) (Larkin, 2011)
878 (w)	902	883	ν(C-C) (Avzianova and Brooks, 2013)
914 (m)	942	946	δ(CH_2 & CH_3) (De Gelder et al., 2007)
1047 (m)	1069	1078	ν(C-O) (Larkin, 2011; De Gelder et al., 2007; Avzianova and Brooks, 2013)
1125 (w)	1159	1142	ν(C-OH) (Avzianova and Brooks, 2013; Larkin, 2011)
1462 (s)	1498	1505	δ(CH_2 & CH_3) (Avzianova and Brooks, 2013; McLaughlin et al., 2002; De Gelder et al., 2007; Furić et al., 1992; Larkin, 2011; Lee and Chan, 2007)
2895 (s)	3054	3035	ν_s(CH_3) (Larkin, 2011; Craig et al., 2015)
2942 (vs)	3067	3069	ν_a(CH_2) (Larkin, 2011; Craig et al., 2015)
2983 (s)	3110	3088	ν_a(CH_3) (Larkin, 2011; Craig et al., 2015)
3262 (s)	3785	3777	ν(O-H) (Furić et al., 1992)
3435 (s)	3875	3873	ν(O-H) (Furić et al., 1992)

4.3.3. Experimental Raman Spectra and DFT Calculated Frequencies for 2-Methylglyceric Acid Sulfate Ester and 2-Methylglyceric Acid

The molecular geometry of the high-NO_x isoprene-derived organosulfate, 2-methylglyceric acid sulfate ester, was optimized and Raman modes assigned in a manner analogous to that for the 3-methyltetrol sulfate esters (Figure 4.5, Table 4.3, Tables C.4-C.5). Unlike the 3-methyltetrol sulfate esters, neither the C2-OH nor the carboxyl-OH is oriented toward the sulfate group in the lowest energy structure. Rather, both hydroxyl groups are oriented to allow hydrogen bonding with the carbonyl oxygen. General agreement was observed between the DFT calculated frequencies and intensities and the experimentally observed mode frequencies, aside from shifting related to the sulfate functional group. Similar to the 3-methyltetrol sulfate esters, modes related to the sulfate functional group were identified for 2-methylglyceric acid sulfate ester at 850 cm^{-1} (ν(RO-SO_3)) and 1066 cm^{-1} (ν_s(SO_3)). An additional weak mode at 587 cm^{-1} may be δ(SO_3); however, background interference from the substrate makes this assignment ambiguous. Although much less intense relative to ν_s(SO_3) tentatively

associated with inorganic sulfate in the Raman spectrum of the 3-methyltetrol sulfate esters, a mode at 979 cm^{-1} may also be due to inorganic sulfate (Ben Mabrouk et al., 2013; Vargas Jentzsch et al., 2013). A mode at 1008 cm^{-1} was assigned to the ν(C-O) vibration, red-shifted from the 1047 cm^{-1} mode observed in the 2-methyltetrols. As the frequency was substantially lower in 2-methylglyceric acid sulfate ester and in a region where inorganic sulfate modes are present, EDX verified that the mode was not related to inorganic sulfate with divalent cations (Ca^{2+} or Mg^{2+}) (Figure C.8) (Vargas Jentzsch et al., 2013).

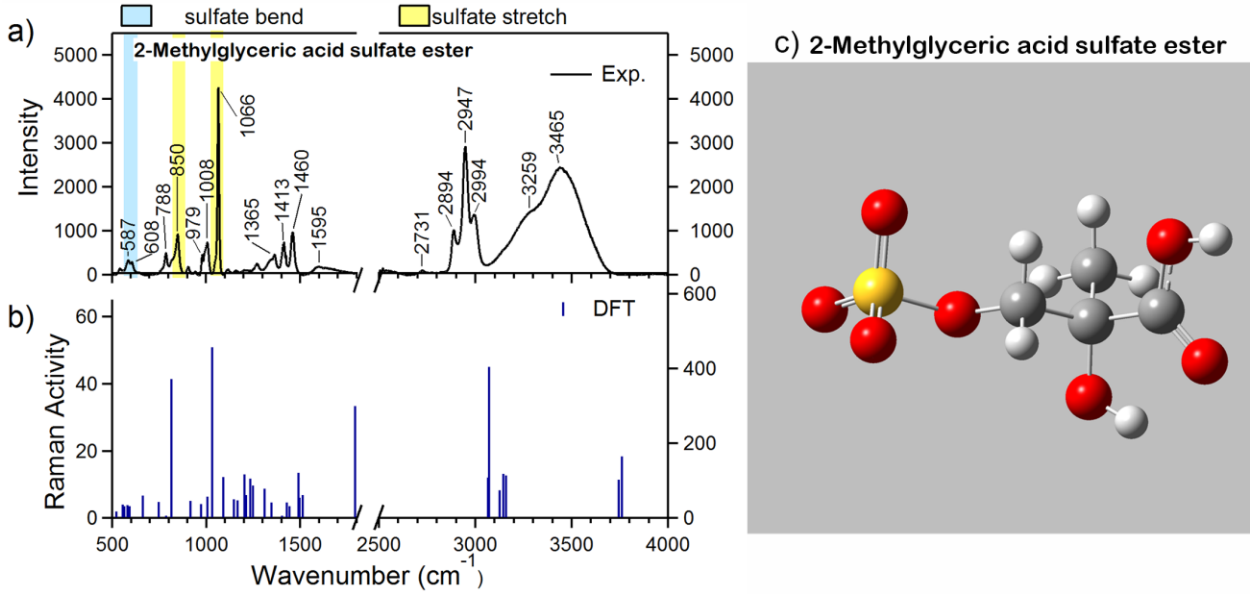

Figure 4.5. Aqueous phase a) experimental and b) DFT-calculated Raman spectra of 2-methylglyceric acid sulfate ester. The blue region corresponds to a sulfate-related bending mode, while yellow regions correspond to sulfate-related stretching modes. c) DFT-optimized structure of 2-methylglyceric acid sulfate acid, a high-NO_x particle-phase isoprene oxidation product. Note that the lower frequency modes in the DFT spectra (500-1800 cm^{-1}) were less intense than the higher frequency region (2500-4000 cm^{-1}), and are magnified 10x.

Table 4.3. Experimentally observed Raman modes, DFT-calculated frequencies, and tentative assignments for 2-methyglyceric acid sulfate ester.

Observed (cm^{-1})	Calculated (cm^{-1})	Assignment
587 (w)[a, b]	564[a]	$\delta(SO_3)$ (Picquart, 1986; Chihara, 1960; Kartha et al., 1984; Kato and Kurimoto, 1977; Okabayashi et al., 1974)
608 (w)	580	δ(O-H) (Cooney et al., 1994)
788 (m)		δ(C-OH), δ(O-H) (Larkin, 2011)
850 (s)[a]	748[a]	$\nu(RO\text{-}SO_3)$ (Larkin, 2011; Picquart, 1986; Kartha et al., 1984; Okabayashi et al., 1974)
979 (m)[c]		$\nu_s(SO_4)$ (salt) (Vargas Jentzsch et al., 2013; Ben Mabrouk et al., 2013)
1008 (m)	973	ν(C-O) (Okabayashi et al., 1974; Koda and Nomura, 1985; Kartha et al., 1984; Chihara, 1960)
1066 (vs)[a]	1031[a]	$\nu_s(SO_3)$ (Larkin, 2011; Chihara, 1960; Kartha et al., 1984; Koda and Nomura, 1985; Okabayashi et al., 1974)
1365 (m)	1310	$\delta(CH_2$ & $CH_3)$ (Avzianova and Brooks, 2013; De Gelder et al., 2007)
1413 (m)[d]		$\nu_{s(}COO^-)$ (Fayer, 2013)
1460 (s)	1491	$\delta(CH_2$ & $CH_3)$ (Larkin, 2011; McLaughlin et al., 2002; De Gelder et al., 2007; Furić et al., 1992; Avzianova and Brooks, 2013)
1595 (vw)[d]		$\nu_{as(}COO^-)$ (Fayer, 2013)
2894 (s)	3072	$\nu_s(CH_3)$ (Craig et al., 2015; Larkin, 2011)
2947 (vs)	3146	$\nu_a(CH_2)$ (Craig et al., 2015; Larkin, 2011)
2994 (s)	3160	$\nu_a(CH_3)$ (Craig et al., 2015; Larkin, 2011)
3259 (vs)	3745	ν(O-H) (Furić et al., 1992)
3465 (vs)	3761	ν(O-H) (Furić et al., 1992)

[a] Frequencies highlighted in blue correspond to bending modes associated with the organosulfate group, while frequencies highlighted in yellow correspond to organosulfate-related stretching modes.

[b] Possible $\delta(SO_3)$ mode, however difficult to differentiate from background.

[c] Indicates contamination.

[d] Experimental results indicate carboxylate ion rather than carboxylic acid group is present.

Figure 4.6 shows measured and computed Raman spectra and the DFT lowest-energy structure for 2-methylglyceric acid. As expected, ν(C-O) (1053 and 1056 cm^{-1} respectively) (De Gelder et al., 2007; Avzianova and Brooks, 2013), $\delta(CH_2)$ and δ(O-H) (1112-1116 cm^{-1}) (Larkin, 2011; Avzianova and Brooks, 2013), $\delta(CH_2$ and $CH_3)$ (940-941 and 1460-1462 cm^{-1}) (Larkin, 2011; Avzianova and Brooks, 2013; Lee and Chan, 2007; De Gelder et al., 2007; Furić et al., 1992), ν(C-H) (2731-2737 cm^{-1}, 2894-2896 cm^{-1}, 2947-2946 cm^{-1}, and 2992-2994 cm^{-1}) (Craig et al., 2015; Larkin, 2011), and ν(O-H) (3212-3259 cm^{-1} and 3436-3465 cm^{-1}, Tables 4.3 and 4.4) (Furić et al., 1992) are present in the sulfate esters and their hydrolysis products. As in

the 2-methyltetrols, the frequencies of the experimentally-observed modes in the fingerprint region agreed with the DFT calculated frequencies. Other distinctive Raman modes specific to 2-methylglyceric acid sulfate ester and 2-methylglyceric acid include modes related to the carboxylic acid functional group (1595 and 1724 cm^{-1}) and the acidic δ(C-OH) at 788 cm^{-1} (Larkin, 2011).

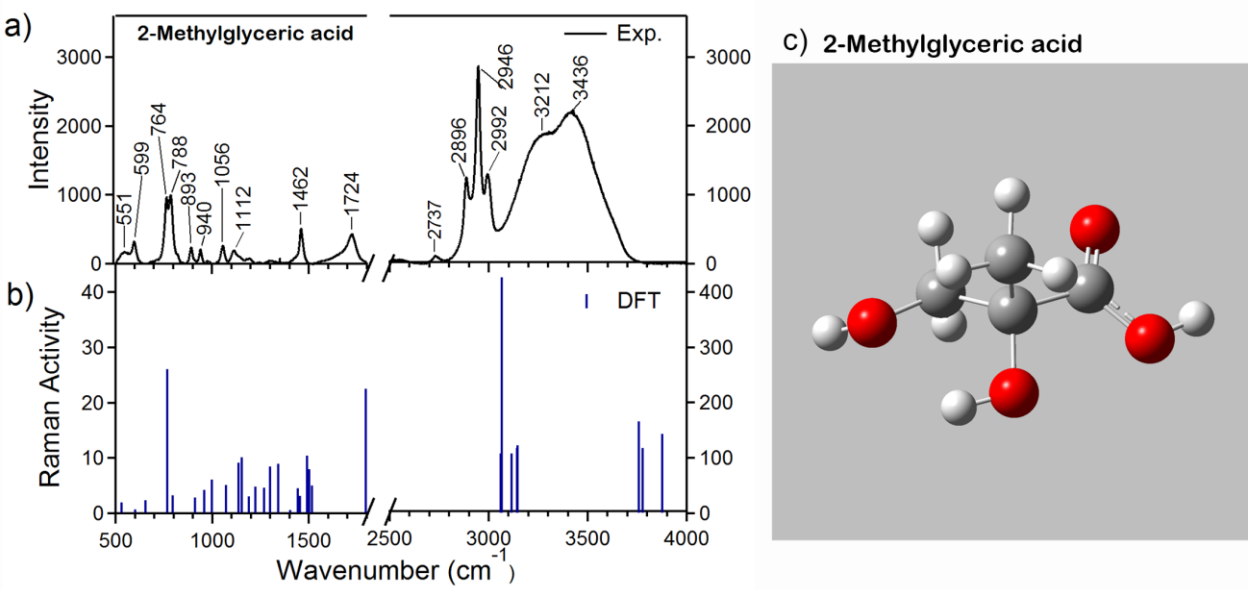

Figure 4.6. Aqueous phase a) experimental and b) DFT-calculated Raman spectra of 2-methylglyceric acid, the hydrolysis product of 2-methylglyceric acid sulfate ester. c) DFT-optimized structure of 2-methylglyceric acid. Note that the lower frequency modes in the DFT spectra (500-1800 cm^{-1}) were less intense than the higher frequency region (2500-4000 cm^{-1}), and are magnified 10x.

Table 4.4. Experimentally observed Raman modes, DFT-calculated frequencies, and tentative assignments for 2-methyglyceric acid.

Observed (cm^{-1})	Calculated (cm^{-1})	Assignment
551 (m)	531	δ(C-H) (Leyton et al., 2008)
599 (m)	602	δ(O-H) (Cooney et al., 1994)
764 (vs)	769	δ(O-C-O) (Avzianova and Brooks, 2013; Zhou et al., 2014)
788 (vs)	794	δ(C-OH), δ(O-H) (Larkin, 2011)
893 (m)	912	ν(C-C) (Avzianova and Brooks, 2013)
940 (m)	958	δ(CH_2 & CH_3), ν(C-C) (De Gelder et al., 2007)
1056 (m)	1072	ν(C-O) (De Gelder et al., 2007; Avzianova and Brooks, 2013)
1112 (m)	1136	ν(C-OH) (Avzianova and Brooks, 2013; Larkin, 2011)
1462 (s)	1491	δ(CH_2 & CH_3) (Larkin, 2011; McLaughlin et al., 2002; De Gelder et al., 2007; Furić et al., 1992; Avzianova and Brooks, 2013)
1724 (s)	1794	ν(C=O), δ(O-H) (Zhou et al., 2014)
2896 (s)	3067	$\nu_s(CH_3)$ (Craig et al., 2015)
2946 (vs)	3116	$\nu_a(CH_2)$ (Craig et al., 2015)
2992 (s)	3147	$\nu_a(CH_3)$ (Craig et al., 2015)
3212 (vs)	3759	ν(O-H) (Furić et al., 1992)
3436 (vs)	3778	ν(O-H) (Furić et al., 1992)

4.3.4. pH-Dependent Raman Modes for 2-Methylglyceric Acid Sulfate Ester and 2-Methylglyceric Acid

In 2-methylglyceric acid, the ν(C=O) present at 1724 cm^{-1} is consistent with the COOH functional group (Zhou et al., 2014; Fayer, 2013), while 2-methylglyceric acid sulfate ester modes at 1595 cm^{-1} and 1413 cm^{-1} correspond to $\nu_s(COO^-)$ and $\nu_a(COO^-)$, respectively (Fayer, 2013). As the pK_a of 2-methylglyceric acid, similar to glyceric acid, is ~3.5 (Pure et al., 1979), the aqueous 2-methylglyceric acid pH of ~1.3 was below and the 2-methylglyceric acid sulfate ester pH of ~5 was above the pK_a. To explore the effect of the carboxylic acid protonation state on the vibrational spectra, Raman spectra of 2-methylglyceric acid were acquired as a function of pH and compared to the Raman spectrum of the sulfate ester (Figure 4.7). At pH 1.3 the initial Raman spectrum of 2-methylglyceric acid showed a medium-intensity ν(C=O) mode at 1724 cm^{-1}. As pH increased (1.3-10), this mode disappeared and a weak mode due to $\nu_a(COO^-)$ appeared at ~1594 cm^{-1}, the same frequency observed for 2-methylglyceric acid sulfate ester. Additionally, as pH increased the emergence of a medium-intensity mode in 2-methylglyceric acid at ~1415 cm^{-1} (1413 cm^{-1} in 2-methylglyceric acid sulfate ester) shows that 2-

methylglyceric acid and 2-methylglyceric acid sulfate ester adopt a carboxylate structure rather than a carboxylic acid at higher pH (Fayer, 2013). Methods using Raman peak ratios of acids and conjugate bases have shown promise in laboratory studies (Rindelaub et al., 2016; Craig et al., 2017b), but additional laboratory and chamber studies are necessary to extrapolate this metric to additional systems and ultimately, ambient aerosol.

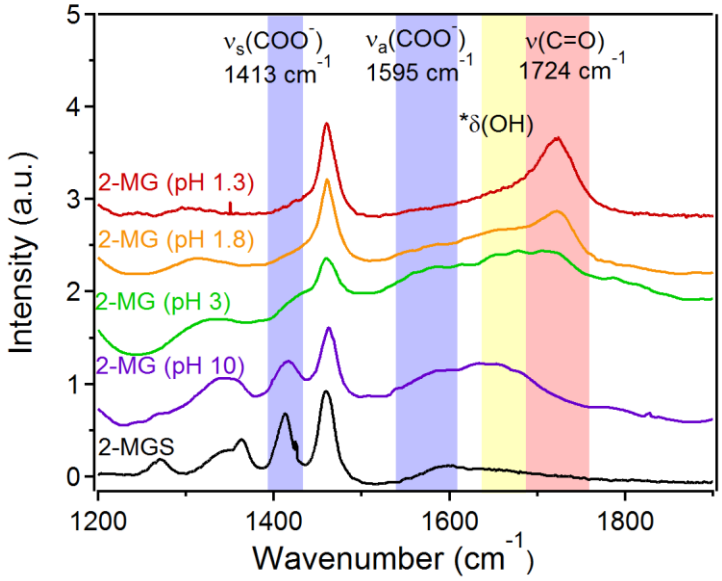

Figure 4.7. Aqueous phase experimental Raman spectra of 2-methylglyceric acid sulfate ester (2-MGS) and 2-methylglyceric acid (2-MG) at varying pH. Note the δ(OH) emergence ~1640 is primarily due to the addition of NaOH (Lappi et al., 2004).

4.3.5. Comparison of Experimental Calculated Organosulfate Frequencies to Literature Modes

In general, the DFT calculated modes appear to be red-shifted from experimental values for the sulfate functional group stretching modes, likely due to shortcomings using DFT for ionic compounds, making the calculated Raman activities difficult to interpret with respect to the experimental values. Due to the differences between DFT-calculated frequencies and experimentally observed values, frequencies associated with $\delta(SO_3)$, $\nu(RO\text{-}SO_3)$, and $\nu_s(SO_3)$ in previous experiments on small-molecule organosulfates were used to verify the assignment of the sulfate functional group-related modes in the isoprene-derived organosulfates (Table 4.5). One mode likely associated with the $\delta(SO_3)$ vibration had strong enough intensity to be observed experimentally at 584 cm^{-1} (DFT 546 and 561 cm^{-1}) and 587 cm^{-1} (DFT 564 cm^{-1}) in the 3-

methyltetrol sulfate esters and 2-methylglyceric acid sulfate ester, respectively. These modes correspond to $\delta_s(SO_3)$ Raman modes reported for sodium and potassium methyl sulfates (559-561 cm^{-1}) (Chihara, 1960; Okabayashi et al., 1974), sodium, potassium, and lanthanum ethyl sulfates (565-574 cm^{-1}) (Okabayashi et al., 1974; Kato and Kurimoto, 1977), sodium propyl sulfate, sodium butyl sulfate, sodium hexyl sulfate, sodium octyl sulfate, sodium decyl sulfate, and sodium dodecyl sulfate (580-598 cm^{-1}) (Okabayashi et al., 1974; Picquart, 1986), and sodium, potassium lithium, ammonium, and cesium palmityl sulfates (583-601 cm^{-1}) (Kartha et al., 1984). The $\nu(RO\text{-}SO_3)$ modes in the isoprene-derived organosulfates were assigned at 842 and 850 cm^{-1} for the 3-methyltetrol sulfate esters and 2-methylglyceric acid sulfate ester, respectively, compared to the calculated modes at 727 and 732 and 748 cm^{-1}. Although the experimentally assigned $\nu(RO\text{-}SO_3)$ modes do not closely match the calculated modes, the experimentally-observed vibrational modes correlate well with reported modes observed experimentally. Particularly good agreement was observed with long chain alkyl sulfates such as sodium dodecyl sulfate (838-841 cm^{-1}) (Picquart, 1986; Larkin, 2011) and the palmityl sulfate compounds (792-856 cm^{-1}) (Kartha et al., 1984), as increasing chain length tends to blue-shift the frequencies.

Finally, the $\nu_s(SO_3)$ mode was assigned to the 3-methyltetrol sulfate esters at 1063 cm^{-1} (DFT-calculated 1047 and 1054 cm^{-1}) and 2-methylglyceric acid sulfate ester at 1066 cm^{-1} (calculated 1031 cm^{-1}). The frequency of the $\nu_s(SO_3)$ mode experimentally observed for the isoprene-derived organosulfates is in agreement with previous observations of other organosulfates by Larkin (2011), Chihara (1960), Okabayashi et al. (1974), Picquart (1986), Kartha et al. (1984), and Koda and Nomura (1985) (1050-1095 cm^{-1}), though Kato and Kurimoto (1977) reported modes with lower frequencies for potassium and lanthanum ethyl sulfate (1006-1010 cm^{-1}). The similar frequencies observed between the isoprene-derived organosulfates and the small-molecule organosulfates suggest that these organosulfate-related modes could be used to identify isoprene-, terpene-, or other VOC-derived organosulfates in atmospheric particles.

Table 4.5. Literature Raman mode frequencies related to the sulfate-functional group for small molecule organosulfates.

Organosulfate compound	$\delta(SO_3)$ (cm^{-1})	$\delta(SO_3)$ (cm^{-1})	$\nu(RO\text{-}SO_3)$ (cm^{-1})	$\nu_s(SO_3)$ (cm^{-1})	$\nu_a(SO_3)$ (cm^{-1})	$\nu_a(SO_3)$ (cm^{-1})
3-methyltetrol sulfate esters[a]	584		842	1063		
2-methylglyceric acid sulfate ester[a]	587		850	1066		
sodium methyl sulfate (Okabayashi et al., 1974; Koda and Nomura, 1985)	561	591, 617	785	1063-1064		
potassium methyl sulfate (Chihara, 1960; Okabayashi et al., 1974)	559	615	781	1063	1221	1257
sodium ethyl sulfate (Okabayashi et al., 1974)	574	622	795	1063		
potassium ethyl sulfate (Kato and Kurimoto, 1977)	574	621		1010	1110	1200
lanthanum ethyl sulfate $9H_2O$ (Kato and Kurimoto, 1977)	565-570	612-615		1006-1008	1105-1109	1203-1225
sodium propyl sulfate to sodium dodecyl sulfate (Okabayashi et al., 1974)[b]	580-584	619-625	822-839	1062-1065		
sodium dodecyl sulfate (Picquart, 1986; Larkin, 2011)	598	635	838-841	1086		
sodium palmityl sulfate (Kartha et al., 1984)	593	623-629	828-838	1084	1197-1218	1220-1235, 1261
potassium palmityl sulfate (Kartha et al., 1984)	583	632	810	1067	1220	1248, 1276
lithium palmityl sulfate (Kartha et al., 1984)	601	631	856	1095	1196	1270
ammonium palmityl sulfate (Kartha et al., 1984)	587	629	814	1063	1196	1276
cesium palmityl sulfate (Kartha et al., 1984)	584	626	792	1050	1204, 1239	1254, 1276

[a] Gray shading indicates the experimental organosulfate results from this study.

[b] Includes sodium propyl sulfate, sodium butyl sulfate, sodium hexyl sulfate, sodium octyl sulfate, sodium decyl sulfate, and sodium dodecyl sulfate.

In addition to the three sulfate-related modes experimentally observed in the isoprene-derived organosulfates, a $\delta(SO_3)$ mode (591-635 cm^{-1}) and two $\nu_a(SO_3)$ modes (1105-1239, 1200-1276 cm^{-1}) too weak to be distinguished from background noise were identified in some of the previous organosulfate studies (Okabayashi et al., 1974; Chihara, 1960; Kato and Kurimoto, 1977; Picquart, 1986; Kartha et al., 1984). These corresponding modes, calculated for 3-

methylerythritol sulfate ester and 3-methylthreitol sulfate ester, were 596/602 cm^{-1} for $\delta(SO_3)$, and 1188/1184 and 1245 cm^{-1} for $\nu_a(SO_3)$ (Table C.2). Though these modes were observed in some of the other studies, the more complex polyol structures for the isoprene-derived organosulfates made observation and identification of these modes challenging since multiple ν(C-O), ν(C-C), and $\delta(CH_2)$ vibrations were present in the spectra from 1100-1300 cm^{-1}. Additionally, the DFT-calculated modes were present at 556 cm^{-1} for $\delta(SO_3)$, and at 1211 and 1235 cm^{-1} for the $\nu_a(SO_3)$ modes of 2-methylglyceric acid sulfate ester (Table C.4). Because a range of frequencies related to the sulfate functional group vibrational modes were observed in previous studies, and because mode shifting was observed based on molecular environment, alkyl chain length, and associated cation, additional Raman analysis of organosulfates in both chamber and ambient SOA is necessary to identify key vibrational modes.

4.3.6. Organosulfate Raman Signatures in Ambient Particles

In addition to the analysis of authentic isoprene-derived standards, Raman organosulfate signatures were identified in atmospheric particles. During the Southern Oxidant and Aerosol Study (SOAS) in summer 2013, ambient concentrations of organosulfates were on average 100-200 ng m^{-3}, with concentrations up to 1 μg m^{-3} (Budisulistiorini et al., 2017; Rattanavaraha et al., 2016). As organosulfates were a significant component of bulk organic aerosol sampled during SOAS, organosulfates in spectra of individual particles could be identified in a preliminary Raman microspectroscopy study using the vibrational modes identified in this study. The Raman spectrum of an ambient organic/sulfate particle is shown in Figure 4.8. Modes at 2848, 2883, 2898, and 2928 cm^{-1} characteristic of $\nu(CH_2)$ and $\nu(CH_3)$ and a strong mode at 980 cm^{-1} characteristic of $\nu_s(SO_4^{2-})$ were used to identify the particle as organic/sulfate. Furthermore, modes at 1064 cm^{-1} and a shoulder at 847 cm^{-1} consistent with the $\nu_s(SO_3)$ and $\nu(RO\text{-}SO_3)$ modes of isoprene-derived organosulfates were observed. Although ambient particles may contain tens to hundreds of chemical species making identification of specific species challenging, these two modes suggest isoprene- or terpene-derived organosulfates are likely present within this ambient particle. We have demonstrated here that the strong $\nu_s(SO_3)$ mode could be used in future studies, particularly alongside the $\nu(RO\text{-}SO_3)$ mode, to identify organosulfates in aerosols from chamber studies or ambient measurements.

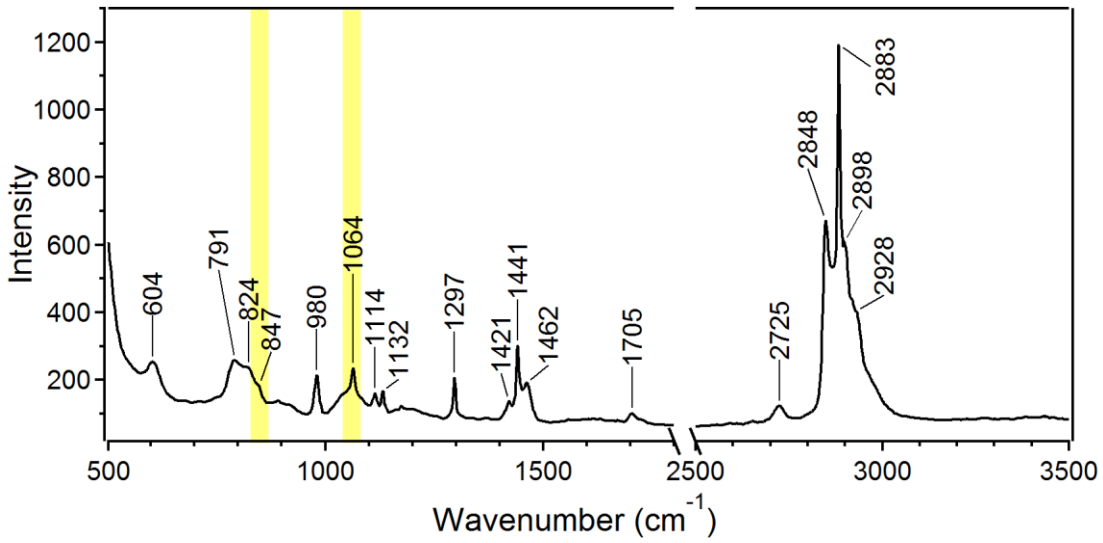

Figure 4.8. Raman spectrum of an organic/sulfate ambient particle with projected area diameter of 3.4 μm (volume equivalent diameter ~2 μm) from Centreville, Alabama. The medium-intensity modes at 1064 cm^{-1} and shoulder at 847 cm^{-1} (highlighted in yellow) likely correspond to the organosulfate $\nu_s(SO_3)$ and $\nu(RO\text{-}SO_3)$ and modes, respectively.

4.4. Conclusions

Raman microspectroscopy and DFT computations were used to investigate vibrational mode assignments for 2-methylglyceric acid sulfate ester and 3-methyltetrol sulfate esters, along with their hydrolysis products, 2-methylglyceric acid and 2-methyltetrols. The frequencies assigned to the sulfate functional group-related modes of the 3-methyltetrol sulfate esters and 2-methylglyceric acid sulfate ester are similar, and agree well with previous assignments made for simpler alkyl sulfates. Two strong organosulfate modes, $\nu(RO\text{-}SO_3)$ at 842-850 cm^{-1} and $\nu_s(SO_3)$ at 1063-1066 cm^{-1} were observed. An additional weak mode at 584-587 cm^{-1} was observed for these compounds; however, due to background noise the organosulfate mode assignment is not conclusive. For 2-methylglyceric acid, the presence of a carbonyl stretch was observed at pH values below the pK_a, while anti-symmetric and symmetric carboxylate group stretches were observed above the pK_a for 2-methylglyceric acid sulfate ester. Raman spectra of ambient particles from the southeastern United States showed peaks at frequencies consistent with the intense $\nu(RO\text{-}SO_3)$ and $\nu_s(SO_3)$ modes, suggesting the presence of isoprene- and terpene-derived organosulfates. The Raman peak assignments determined in this study by combining experimental measurements, literature reports, and theoretical calculations can be used in future

studies to identify these species within individual SOA particles, which will assist in improving understanding of the abundance and atmospheric implications of these key SOA constituents.

4.5. Acknowledgements

A.L.B. performed the Raman analysis with assistance from R.L.C. Z.Z. and A.V. synthesized the isoprene-organosulfate standards with assistance from J.D.S. This project was supported by Prof. Ault's National Science Foundation (NSF) CAREER Award CHE-1654149 and NSF Collaborative Research Awards to Prof. Ault (AGS-1703019) and Prof. Surratt (AGS-1703535). Chris Johnson (SUNY-Stonybrook) and Bruce Ault (University of Cincinnati) are acknowledged for helpful conversations regarding the calculated structures and spectra. Kendra Souther (University of Michigan) is thanked for her NMR assistance. Paul Shepson (Purdue University), Steven Bertman (Western Michigan University), and Kerri Pratt (University of Michigan), as well as Manelisi V. Nhliziyo are acknowledged for facilitating collection of the ambient particle during the Southern Oxidant and Aerosol Study (SOAS) through EPA (R835409). Additionally, we thank Annmarie Carlton (Rutgers University, now UC-Irvine), Lindsay Yee (UC-Berkeley), and Allen Goldstein (UC-Berkeley) for organizing SOAS and the filter sampling effort, as well as Karsten Baumann and others for logistical assistance.

4.6. References

Allen, H. M., Draper, D. C., Ayres, B. R., Ault, A. P., Bondy, A. L., Takahama, S., Modini, R. L., Baumann, K., Edgerton, E., Knote, C., Laskin, A., Wang, B., and Fry, J. L.: Influence of crustal dust and sea spray supermicron particle concentrations and acidity on inorganic NO_3^- aerosol during the 2013 Southern Oxidant and Aerosol Study, Atmos. Chem. Phys., 15, 10669-10685, 2015.

An, Z. W., Daloisio, R., and Venturello, C.: A new, facile synthesis of methyltartronic acid, Synthesis-Stuttgart, 273-275, 1992.

Ault, A. P., Zhao, D., Ebben, C. J., Tauber, M. J., Geiger, F. M., Prather, K. A., and Grassian, V. H.: Raman microspectroscopy and vibrational sum frequency generation spectroscopy as probes of the bulk and surface compositions of size-resolved sea spray aerosol particles, PCCP, 15, 6206-6214, 2013.

Ault, A. P., Guasco, T. L., Baltrusaitis, J., Ryder, O. S., Trueblood, J. V., Collins, D. B., Ruppel, M. J., Cuadra-Rodriguez, L. A., Prather, K. A., and Grassian, V. H.: Heterogeneous reactivity of nitric acid with nascent sea spray aerosol: Large differences observed between and within individual particles, J. Phys. Chem. Lett., 5, 2493-2500, 2014.

Ault, A. P., and Axson, J. L.: Atmospheric aerosol chemistry: Spectroscopic and microscopic advances, Anal. Chem., 89, 430-452, 2017.

Avzianova, E., and Brooks, S. D.: Raman spectroscopy of glyoxal oligomers in aqueous solutions, Spectrochim. Acta, Part A, 101, 40-48, 2013.

Barnes, P. J., Shapiro, S. D., and Pauwels, R. A.: Chronic obstructive pulmonary disease: molecular and cellular mechanisms, Eur. Respir. J., 22, 672-688, 2003.

Bates, K. H., Crounse, J. D., St. Clair, J. M., Bennett, N. B., Nguyen, T. B., Seinfeld, J. H., Stoltz, B. M., and Wennberg, P. O.: Gas phase production and loss of isoprene epoxydiols, J. Phys. Chem. A, 118, 1237-1246, 2014.

Baustian, K. J., Cziczo, D. J., Wise, M. E., Pratt, K. A., Kulkarni, G., Hallar, A. G., and Tolbert, M. A.: Importance of aerosol composition, mixing state, and morphology for heterogeneous ice nucleation: A combined field and laboratory approach, J. Geophys. Res.: Atmos., 117, DOI: 10.1029/2011JD016784, 2012.

Ben Mabrouk, K., Kauffmann, T. H., Aroui, H., and Fontana, M. D.: Raman study of cation effect on sulfate vibration modes in solid state and in aqueous solutions, J. Raman Spectrosc., 44, 1603-1608, 2013.

Bondy, A. L., Wang, B., Laskin, A., Craig, R. L., Nhliziyo, M. V., Bertman, S. B., Pratt, K. A., Shepson, P. B., and Ault, A. P.: Inland sea spray aerosol transport and incomplete chloride depletion: Varying degrees of reactive processing observed during SOAS, Environ. Sci. Technol., 51, 9533-9542, 2017.

Boone, E. J., Laskin, A., Laskin, J., Wirth, C., Shepson, P. B., Stirm, B. H., and Pratt, K. A.: Aqueous processing of atmospheric organic particles in cloud water collected via aircraft sampling, Environ. Sci. Technol., 49, 8523-8530, 2015.

Budisulistiorini, S. H., Li, X., Bairai, S. T., Renfro, J., Liu, Y., Liu, Y. J., McKinney, K. A., Martin, S. T., McNeill, V. F., Pye, H. O. T., Nenes, A., Neff, M. E., Stone, E. A., Mueller, S., Knote, C., Shaw, S. L., Zhang, Z., Gold, A., and Surratt, J. D.: Examining the effects of anthropogenic emissions on isoprene-derived secondary organic aerosol formation during the 2013 Southern Oxidant and Aerosol Study (SOAS) at the Look Rock, Tennessee ground site, Atmos. Chem. Phys., 15, 8871-8888, 2015.

Budisulistiorini, S. H., Baumann, K., Edgerton, E. S., Bairai, S. T., Mueller, S., Shaw, S. L., Knipping, E. M., Gold, A., and Surratt, J. D.: Seasonal characterization of submicron aerosol chemical composition and organic aerosol sources in the southeastern United States: Atlanta, Georgia,and Look Rock, Tennessee, Atmos. Chem. Phys., 16, 5171-5189, 2016.

Budisulistiorini, S. H., Nenes, A., Carlton, A. G., Surratt, J. D., McNeill, V. F., and Pye, H. O. T.: Simulating aqueous-phase isoprene-epoxydiol (IEPOX) secondary organic aerosol production during the 2013 Southern Oxidant and Aerosol Study (SOAS), Environ. Sci. Technol., 51, 5026-5034, 2017.

Carlton, A. G., Wiedinmyer, C., and Kroll, J. H.: A review of secondary organic aerosol (SOA) formation from isoprene, Atmos. Chem. Phys., 9, 4987-5005, 2009.

Catelani, T., Pratesi, G., and Zoppi, M.: Raman characterization of ambient airborne soot and associated mineral phases, Aerosol Sci. Technol., 48, 13-21, 2014.

Chan, M. N., Surratt, J. D., Claeys, M., Edgerton, E. S., Tanner, R. L., Shaw, S. L., Zheng, M., Knipping, E. M., Eddingsaas, N. C., Wennberg, P. O., and Seinfeld, J. H.: Characterization and quantification of isoprene-derived epoxydiols in ambient aerosol in the southeastern United States, Environ. Sci. Technol., 44, 4590-4596, 2010.

Chihara, G.: Medical and biochemical application of infrared spectroscopy. V. : Infrared absorption spectra of organic sulfate esters., Chem. Pharm. Bull., 8, 988-994, 1960.

Cooney, T. F., Wang, L., Sharma, S. K., Gauldie, R. W., and Montana, A. J.: Raman spectral study of solid and dissolved poly(vinyl alcohol) and ethylene-vinyl alcohol copolymer Journal of Polymer Science Part B-Polymer Physics, 32, 1163-1174, 1994.

Craig, R. L., Bondy, A. L., and Ault, A. P.: Surface enhanced Raman spectroscopy enables observations of previously undetectable secondary organic aerosol components at the individual particle level, Anal. Chem., 87, 7510-7514, 2015.

Craig, R. L., Bondy, A. L., and Ault, A. P.: Computer-controlled Raman microspectroscopy (CC-Raman): A method for the rapid characterization of individual atmospheric aerosol particles, Aerosol Sci. Technol., 51, 1099-1112, 2017a.

Craig, R. L., Nandy, L., Axson, J. L., Dutcher, C. S., and Ault, A. P.: Spectroscopic determination of aerosol pH from acid–base equilibria in inorganic, organic, and mixed systems, J. Phys. Chem. A, 121, 5690-5699, 2017b.

Darer, A. I., Cole-Filipiak, N. C., O'Connor, A. E., and Elrod, M. J.: Formation and stability of atmospherically relevant isoprene-derived organosulfates and organonitrates, Environ. Sci. Technol., 45, 1895-1902, 2011.

De Gelder, J., De Gussem, K., Vandenabeele, P., and Moens, L.: Reference database of Raman spectra of biological molecules, J. Raman Spectrosc., 38, 1133-1147, 2007.

Deng, C., Brooks, S. D., Vidaurre, G., and Thornton, D. C. O.: Using Raman microspectroscopy to determine chemical composition and mixing state of airborne marine aerosols over the Pacific Ocean, Aerosol Sci. Technol., 48, 193-206, 2014.

Dominici, F., Peng, R. D., Bell, M. L., and et al.: Fine particulate air pollution and hospital admission for cardiovascular and respiratory diseases, JAMA, 295, 1127-1134, 2006.

Ebben, C. J., Strick, B. F., Upshur, M. A., Chase, H. M., Achtyl, J. L., Thomson, R. J., and Geiger, F. M.: Towards the identification of molecular constituents associated with the surfaces of isoprene-derived secondary organic aerosol (SOA) particles, Atmos. Chem. Phys., 14, 2303-2314, 2014.

Estillore, A. D., Hettiyadura, A. P. S., Qin, Z., Leckrone, E., Wombacher, B., Humphry, T., Stone, E. A., and Grassian, V. H.: Water uptake and hygroscopic growth of organosulfate aerosol, Environ. Sci. Technol., 50, 4259-4268, 2016.

Farmer, D. K., Matsunaga, A., Docherty, K. S., Surratt, J. D., Seinfeld, J. H., Ziemann, P. J., and Jimenez, J. L.: Response of an aerosol mass spectrometer to organonitrates and organosulfates and implications for atmospheric chemistry, Proc. Natl. Acad. Sci. U. S. A., 107, 6670-6675, 2010.

Fayer, M. D.: Chapter 12 - An Introduction to Protein 2D IR Spectroscopy, in: Ultrafast Infrared Vibrational Spectroscopy, CRC Press, 371-372, 2013.

Frossard, A. A., Shaw, P. M., Russell, L. M., Kroll, J. H., Canagaratna, M. R., Worsnop, D. R., Quinn, P. K., and Bates, T. S.: Springtime Arctic haze contributions of submicron organic particles from European and Asian combustion sources, J. Geophys. Res.: Atmos., 116, DOI: 10.1029/2010jd015178, 2011.

Froyd, K. D., Murphy, S. M., Murphy, D. M., de Gouw, J. A., Eddingsaas, N. C., Wennberg, P. O., and Thiemens, M. H.: Contribution of isoprene-derived organosulfates to free tropospheric aerosol mass, Proc. Natl. Acad. Sci. U. S. A., 107, 21360-21365, 2010.

Furić, K., Mohaček, V., Bonifačić, M., and Štefanić, I.: Raman spectroscopic study of H_2O and D_2O water solutions of glycine, J. Mol. Struct., 267, 39-44, 1992.

Glasius, M., and Goldstein, A. H.: Recent discoveries and future challenges in atmospheric organic chemistry, Environ. Sci. Technol., 50, 2754-2764, 2016.

Gomez-Gonzalez, Y., Surratt, J. D., Cuyckens, F., Szmigielski, R., Vermeylen, R., Jaoui, M., Lewandowski, M., Offenberg, J. H., Kleindienst, T. E., Edney, E. O., Blockhuys, F., Van Alsenoy, C., Maenhaut, W., and Claeys, M.: Characterization of organosulfates from the photooxidation of isoprene and unsaturated fatty acids in ambient aerosol using liquid chromatography/(-) electrospray ionization mass spectrometry, J. Mass Spectrom., 43, 371-382, 2008.

Guenther, A., Karl, T., Harley, P., Wiedinmyer, C., Palmer, P. I., and Geron, C.: Estimates of global terrestrial isoprene emissions using MEGAN (Model of Emissions of Gases and Aerosols from Nature), Atmos. Chem. Phys., 6, 3181-3210, 2006.

Hallquist, M., Wenger, J. C., Baltensperger, U., Rudich, Y., Simpson, D., Claeys, M., Dommen, J., Donahue, N. M., George, C., Goldstein, A. H., Hamilton, J. F., Herrmann, H., Hoffmann, T., Iinuma, Y., Jang, M., Jenkin, M. E., Jimenez, J. L., Kiendler-Scharr, A., Maenhaut, W.,

McFiggans, G., Mentel, T. F., Monod, A., Prévôt, A. S. H., Seinfeld, J. H., Surratt, J. D., Szmigielski, R., and Wildt, J.: The formation, properties and impact of secondary organic aerosol: current and emerging issues, Atmos. Chem. Phys., 9, 5155-5236, 2009.

Hatch, L. E., Creamean, J. M., Ault, A. P., Surratt, J. D., Chan, M. N., Seinfeld, J. H., Edgerton, E. S., Su, Y., and Prather, K. A.: Measurements of isoprene-derived organosulfates in ambient aerosols by aerosol time-of-flight mass spectrometry - part 1: Single particle atmospheric observations in Atlanta, Environ. Sci. Technol., 45, 5105-5111, 2011a.

Hatch, L. E., Creamean, J. M., Ault, A. P., Surratt, J. D., Chan, M. N., Seinfeld, J. H., Edgerton, E. S., Su, Y., and Prather, K. A.: Measurements of isoprene-derived organosulfates in ambient aerosols by aerosol time-of-flight mass spectrometry-part 2: Temporal variability and formation Mechanisms, Environ. Sci. Technol., 45, 8648-8655, 2011b.

He, Q. F., Ding, X., Wang, X. M., Yu, J. Z., Fu, X. X., Liu, T. Y., Zhang, Z., Xue, J., Chen, D. H., Zhong, L. J., and Donahue, N. M.: Organosulfates from pinene and isoprene over the Pearl River Delta, South China: seasonal variation and implication in formation mechanisms, Environ. Sci. Technol., 48, 9236-9245, 2014.

Hettiyadura, A. P. S., Stone, E. A., Kundu, S., Baker, Z., Geddes, E., Richards, K., and Humphry, T.: Determination of atmospheric organosulfates using HILIC chromatography with MS detection, Atmos. Meas. Tech., 8, 2347-2358, 2015.

Hidy, G. M., Blanchard, C. L., Baumann, K., Edgerton, E., Tanenbaum, S., Shaw, S., Knipping, E., Tombach, I., Jansen, J., and Walters, J.: Chemical climatology of the southeastern United States, 1999-2013, Atmos. Chem. Phys., 14, 11893-11914, 2014.

Hu, K. S., Darer, A. I., and Elrod, M. J.: Thermodynamics and kinetics of the hydrolysis of atmospherically relevant organonitrates and organosulfates, Atmos. Chem. Phys., 11, 8307-8320, 2011.

Iinuma, Y., Boge, O., Kahnt, A., and Herrmann, H.: Laboratory chamber studies on the formation of organosulfates from reactive uptake of monoterpene oxides, PCCP, 11, 7985-7997, 2009.

Ivleva, N. P., McKeon, U., Niessner, R., and Poeschl, U.: Raman microspectroscopic analysis of size-resolved atmospheric aerosol particle samples collected with an ELPI: Soot, humic-like substances, and inorganic compounds, Aerosol Sci. Technol., 41, 655-671, 2007.

Ivleva, N. P., Huckele, S., Weinzierl, B., Niessner, R., Haisch, C., and Baumann, T.: Identification and characterization of individual airborne volcanic ash particles by Raman microspectroscopy, Anal. Bioanal. Chem., 405, 9071-9084, 2013.

Jacobson, M. C., Hansson, H. C., Noone, K. J., and Charlson, R. J.: Organic atmospheric aerosols: review and state of the science, Rev. Geophys., 38, 267-294, 2000.

Kartha, V. B., Leitch, L. C., and Mantsch, H. H.: Infrared and Raman-spectra of alkali palmityl sulfates, Can. J. Chem., 62, 128-132, 1984.

Kato, Y., and Kurimoto, T.: Polarized Raman-spectra of lanthanum ethylsulfate nonahydrate and potassium ethylsulfate crystals, Spectrochim. Acta, Part A, 33, 1033-1040, 1977.

Koda, S., and Nomura, H.: Aqueous-solutions of sodium methylsulfate by Raman-scattering, NMR, ultrasound, and density-measurements, J. Solution Chem., 14, 355-366, 1985.

Kramer, A. J., Rattanavaraha, W., Zhang, Z., Gold, A., Surratt, J. D., and Lin, Y.-H.: Assessing the oxidative potential of isoprene-derived epoxides and secondary organic aerosol, Atmos. Environ., 130, 211-218, 2016.

Lappi, S. E., Smith, B., and Franzen, S.: Infrared spectra of $H_2{}^{16}O$, $H_2{}^{18}O$ and D_2O in the liquid phase by single-pass attenuated total internal reflection spectroscopy, Spectrochim. Acta, Part A, 60, 2611-2619, 2004.

Larkin, P.: Chapter 8 - Illustrated IR and Raman Spectra Demonstrating Important Functional Groups, in: Infrared and Raman Spectroscopy, Elsevier, Oxford, 135-176, 2011.

Lee, A. K. Y., and Chan, C. K.: Single particle Raman spectroscopy for investigating atmospheric heterogeneous reactions of organic aerosols, Atmos. Environ., 41, 4611-4621, 2007.

Lee, A. Y., and Chan, C.: Raman spectroscopy of single particles levitated by an electrodynamic balance for atmospheric studies, in: Fundamentals and Applications in Aerosol Spectroscopy, CRC Press, 155-191, 2010.

Leyton, P., Córdova, I., Lizama-Vergara, P. A., Gómez-Jeria, J. S., Aliaga, A. E., Campos-Vallette, M. M., Clavijo, E., García-Ramos, J. V., and Sanchez-Cortes, S.: Humic acids as molecular assemblers in the surface-enhanced Raman scattering detection of polycyclic aromatic hydrocarbons, Vib. Spectrosc, 46, 77-81, 2008.

Liao, J., Froyd, K. D., Murphy, D. M., Keutsch, F. N., Yu, G., Wennberg, P. O., St Clair, J. M., Crounse, J. D., Wisthaler, A., Mikoviny, T., Jimenez, J. L., Campuzano-Jost, P., Day, D. A., Hu, W. W., Ryerson, T. B., Pollack, I. B., Peischl, J., Anderson, B. E., Ziemba, L. D., Blake, D. R., Meinardi, S., and Diskin, G.: Airborne measurements of organosulfates over the continental US, J. Geophys. Res.: Atmos., 120, 2990-3005, 2015.

Lin, Y.-H., Zhang, Z., Docherty, K. S., Zhang, H., Budisulistiorini, S. H., Rubitschun, C. L., Shaw, S. L., Knipping, E. M., Edgerton, E. S., Kleindienst, T. E., Gold, A., and Surratt, J. D.: Isoprene epoxydiols as precursors to secondary organic aerosol formation: acid-catalyzed reactive uptake studies with authentic compounds, Environ. Sci. Technol., 46, 250-258, 2012.

Lin, Y.-H., Arashiro, M., Martin, E., Chen, Y., Zhang, Z., Sexton, K. G., Gold, A., Jaspers, I., Fry, R. C., and Surratt, J. D.: Isoprene-derived secondary organic aerosol induces the expression of oxidative stress response genes in human lung cells, Environ. Sci. Technol. Lett., 3, 250-254, 2016.

Lin, Y.-H., Arashiro, M., Clapp, P. W., Cui, T., Sexton, K. G., Vizuete, W., Gold, A., Jaspers, I., Fry, R. C., and Surratt, J. D.: Gene expression profiling in human lung cells exposed to isoprene-derived secondary organic aerosol, Environ. Sci. Technol., 51, 8166-8175, 2017.

Lin, Y. H., Knipping, E. M., Edgerton, E. S., Shaw, S. L., and Surratt, J. D.: Investigating the influences of SO_2 and NH_3 levels on isoprene-derived secondary organic aerosol formation using conditional sampling approaches, Atmos. Chem. Phys., 13, 8457-8470, 2013.

Maria, S. F., Russell, L. M., Turpin, B. J., Porcja, R. J., Campos, T. L., Weber, R. J., and Huebert, B. J.: Source signatures of carbon monoxide and organic functional groups in Asian Pacific Regional Aerosol Characterization Experiment (ACE-Asia) submicron aerosol types, J. Geophys. Res.: Atmos., 108, DOI: 10.1029/2003JD003703, 2003.

Martin, S. T., Andreae, M. O., Artaxo, P., Baumgardner, D., Chen, Q., Goldstein, A. H., Guenther, A., Heald, C. L., Mayol-Bracero, O. L., McMurry, P. H., Pauliquevis, T., Pöschl, U., Prather, K. A., Roberts, G. C., Saleska, S. R., Silva Dias, M. A., Spracklen, D. V., Swietlicki, E., and Trebs, I.: Sources and properties of Amazonian aerosol particles, Rev. Geophys., 48, DOI: 10.1029/2008RG000280, 2010.

McLaughlin, R. P., Bird, B., and Reid, P. J.: Vibrational analysis of isopropyl nitrate and isobutyl nitrate, Spectrochim. Acta, Part A, 58, 2571-2580, 2002.

Minerath, E. C., and Elrod, M. J.: Assessing the potential for diol and hydroxy sulfate ester formation from the reaction of epoxides in tropospheric aerosols, Environ. Sci. Technol., 43, 1386-1392, 2009.

Nguyen, T. B., Bates, K. H., Crounse, J. D., Schwantes, R. H., Zhang, X., Kjaergaard, H. G., Surratt, J. D., Lin, P., Laskin, A., Seinfeld, J. H., and Wennberg, P. O.: Mechanism of the hydroxyl radical oxidation of methacryloyl peroxynitrate (MPAN) and its pathway toward secondary organic aerosol formation in the atmosphere, PCCP, 17, 17914-17926, 2015.

Okabayashi, H., Okuyama, M., Kitagawa, T., and Miyazawa, T.: The Raman spectra and molecular conformations of surfactants in aqueous solution and crystalline states, Bull. Chem. Soc. Jpn., 47, 1075-1077, 1974.

Picquart, M.: Vibrational model behavior of SDS aqueous solutions studied by Raman scattering, J. Phys. Chem., 90, 243-250, 1986.

Popovicheva, O., Kireeva, E., Persiantseva, N., Timofeev, M., Bladt, H., Ivleva, N. P., Niessner, R., and Moldanova, J.: Microscopic characterization of individual particles from multicomponent ship exhaust, J. Environ. Monit., 14, 3101-3110, 2012.

Pure, I. U. o., Data, A. C. C. o. E., Serjeant, E. P., Dempsey, B., Pure, I. U. o., and Data, A. C. C. o. E.: Ionisation constants of organic acids in aqueous solution, Pergamon Press, 1979.

Rattanavaraha, W., Chu, K., Budisulistiorini, S. H., Riva, M., Lin, Y. H., Edgerton, E. S., Baumann, K., Shaw, S. L., Guo, H., King, L., Weber, R. J., Neff, M. E., Stone, E. A., Offenberg, J. H., Zhang, Z., Gold, A., and Surratt, J. D.: Assessing the impact of anthropogenic pollution on isoprene-derived secondary organic aerosol formation in $PM_{2.5}$ collected from the Birmingham, Alabama, ground site during the 2013 Southern Oxidant and Aerosol Study, Atmos. Chem. Phys., 16, 4897-4914, 2016.

Rattanavaraha, W., Canagaratna, M. R., Budisulistiorini, S. H., Croteau, P. L., Baumann, K., Canonaco, F., Prevot, A. S. H., Edgerton, E. S., Zhang, Z., Jayne, J. T., Worsnop, D. R., Gold, A., Shaw, S. L., and Surratt, J. D.: Source apportionment of submicron organic aerosol collected from Atlanta, Georgia, during 2014–2015 using the aerosol chemical speciation monitor (ACSM), Atmos. Environ., 167, 389-402, 2017.

Reid, J. P., Meresman, H., Mitchem, L., and Symes, R.: Spectroscopic studies of the size and composition of single aerosol droplets, Int. Rev. Phys. Chem., 26, 139-192, 2007.

Repine, J. E., Bast, A., Lankhorst, I., deBacker, W., Dekhuijzen, R., Demedts, M., vanHerwaarden, C., vanKlaveren, R., Lammers, J. W., Larsson, S., Lundback, B., Petruzelli, S., Postma, D., Riise, G., Vermeire, P., Wouters, E., Yernault, J. C., and vanZandwijk, N.: Oxidative stress in chronic obstructive pulmonary disease, Am. J. Respir. Crit. Care Med., 156, 341-357, 1997.

Rindelaub, J. D., Craig, R. L., Nandy, L., Bondy, A. L., Dutcher, C. S., Shepson, P. B., and Ault, A. P.: Direct measurement of pH in individual particles via Raman microspectroscopy and variation in acidity with relative humidity, J. Phys. Chem. A, 120, 911-917, 2016.

Riva, M., Budisulistiorini, S. H., Zhang, Z., Gold, A., and Surratt, J. D.: Chemical characterization of secondary organic aerosol constituents from isoprene ozonolysis in the presence of acidic aerosol, Atmos. Environ., 130, 5-13, 2016.

Russell, L. M., Takahama, S., Liu, S., Hawkins, L. N., Covert, D. S., Quinn, P. K., and Bates, T. S.: Oxygenated fraction and mass of organic aerosol from direct emission and atmospheric processing measured on the R/V Ronald Brown during TEXAQS/GoMACCS 2006, J. Geophys. Res.: Atmos., 114, DOI: 10.1029/2008JD011275, 2009.

Schwartz, R. E., Russell, L. M., Sjostedt, S. J., Vlasenko, A., Slowik, J. G., Abbatt, J. P. D., Macdonald, A. M., Li, S. M., Liggio, J., Toom-Sauntry, D., and Leaitch, W. R.: Biogenic oxidized organic functional groups in aerosol particles from a mountain forest site and their similarities to laboratory chamber products, Atmos. Chem. Phys., 10, 5075-5088, 2010.

Schweiger, G.: Raman scattering on single aerosol particles and on flowing aerosols: a review, J. Aerosol Sci, 21, 483-509, 1990.

Siebert, F., and Hildebrandt, P.: Theory of Infrared Absorption and Raman Spectroscopy, in: Vibrational Spectroscopy in Life Science, Wiley-VCH Verlag GmbH & Co. KGaA, 11-61, 2008.

Stone, E. A., Yang, L., Yu, L. E., and Rupakheti, M.: Characterization of organosulfates in atmospheric aerosols at four Asian locations, Atmos. Environ., 47, 323-329, 2012.

Surratt, J. D., Murphy, S. M., Kroll, J. H., Ng, N. L., Hildebrandt, L., Sorooshian, A., Szmigielski, R., Vermeylen, R., Maenhaut, W., Claeys, M., Flagan, R. C., and Seinfeld, J. H.: Chemical composition of secondary organic aerosol formed from the photooxidation of isoprene, J. Phys. Chem. A, 110, 9665-9690, 2006.

Surratt, J. D., Kroll, J. H., Kleindienst, T. E., Edney, E. O., Claeys, M., Sorooshian, A., Ng, N. L., Offenberg, J. H., Lewandowski, M., Jaoui, M., Flagan, R. C., and Seinfeld, J. H.: Evidence for organosulfates in secondary organic aerosol, Environ. Sci. Technol., 41, 517-527, 2007a.

Surratt, J. D., Lewandowski, M., Offenberg, J. H., Jaoui, M., Kleindienst, T. E., Edney, E. O., and Seinfeld, J. H.: Effect of acidity on secondary organic aerosol formation from isoprene, Environ. Sci. Technol., 41, 5363-5369, 2007b.

Surratt, J. D., Gómez-González, Y., Chan, A. W. H., Vermeylen, R., Shahgholi, M., Kleindienst, T. E., Edney, E. O., Offenberg, J. H., Lewandowski, M., Jaoui, M., Maenhaut, W., Claeys, M., Flagan, R. C., and Seinfeld, J. H.: Organosulfate formation in biogenic secondary organic aerosol, J. Phys. Chem. A, 112, 8345-8378, 2008.

Surratt, J. D., Chan, A. W. H., Eddingsaas, N. C., Chan, M., Loza, C. L., Kwan, A. J., Hersey, S. P., Flagan, R. C., Wennberg, P. O., Seinfeld, J. H., and Finlayson-Pitts, B. J.: Reactive intermediates revealed in secondary organic aerosol formation from isoprene, Proc. Natl. Acad. Sci. U. S. A., 107, 6640-6645, 2010.

Takahama, S., Schwartz, R. E., Russell, L. M., Macdonald, A. M., Sharma, S., and Leaitch, W. R.: Organic functional groups in aerosol particles from burning and non-burning forest emissions at a high-elevation mountain site, Atmos. Chem. Phys., 11, 6367-6386, 2011.

Tolocka, M. P., and Turpin, B.: Contribution of organosulfur compounds to organic aerosol mass, Environ. Sci. Technol., 46, 7978-7983, 2012.

Upshur, M. A., Strick, B. F., McNeill, V. F., Thomson, R. J., and Geiger, F. M.: Climate-relevant physical properties of molecular constituents for isoprene-derived secondary organic aerosol material, Atmos. Chem. Phys., 14, 10731-10740, 2014.

Vargas Jentzsch, P., Kampe, B., Ciobota, V., Rosch, P., and Popp, J.: Inorganic salts in atmospheric particulate matter: Raman spectroscopy as an analytical tool, Spectrochim. Acta, Part A, 115, 697-708, 2013.

Yassine, M. M., Dabek-Zlotorzynska, E., Harir, M., and Schmitt-Kopplin, P.: Identification of weak and strong organic acids in atmospheric aerosols by capillary electrophoresis/mass spectrometry and ultra-high-resolution fourier transform ion cyclotron resonance mass spectrometry, Anal. Chem., 84, 6586-6594, 2012.

Zhou, Q., Pang, S.-F., Wang, Y., Ma, J.-B., and Zhang, Y.-H.: Confocal Raman studies of the evolution of the physical state of mixed phthalic acid/ammonium sulfate aerosol droplets and the effect of substrates, J. Phys. Chem. B, 118, 6198-6205, 2014.

Chapter 5.

Atomic Force Microscopy-Infrared Spectroscopy of Individual Atmospheric Aerosol Particles: Sub-Diffraction Limit Vibrational Spectroscopy and Morphological Analysis

Adapted with permission from Bondy, A. L., Kirpes, R. M., Merzel, R. L., Pratt, K. A., Banaszak Holl, M. M., and Ault, A. P.: Atomic force microscopy-infrared spectroscopy of individual atmospheric aerosol particles: Subdiffraction limit vibrational spectroscopy and morphological analysis, Anal. Chem., 89, 8594-8598, 2017.

5.1. Introduction

Atmospheric aerosol particles < 1 μm in diameter impact climate by scattering and absorbing solar radiation, nucleating cloud droplets and ice crystals, and acting as surfaces for heterogeneous reactions in the atmosphere (Poschl, 2005). Additionally, through inhalation, these particles can penetrate deeply into the lungs, depositing in the alveoli (Hinds, 1999). This has large consequences as air pollution accounts for 10 % of global deaths annually (Evaluation-IHME, 2016). The size, chemical composition, and physical structure (e.g. well-mixed, core-shell, partially engulfed) of individual particles is critical for determining their climate and health impacts (Zhang and Thompson, 2014; Laskina et al., 2015; Fierce et al., 2016). However methods that can provide detailed molecular information at ambient pressure, allowing detection of volatile components for individual particles near the mode of the atmospheric number size distribution (~100 nm), are limited (Ault and Axson, 2017).

Vibrational spectroscopy has great potential to provide insight into chemical processes within aerosols (Ault and Axson, 2017), as it has been used to provide detail on functional groups, such as $\nu(SO_4^{2-})$, $\nu(NO_3^-)$, ν(C-H), and ν(O-H) (Ault et al., 2013). Vibrational methods provide molecular information that complements elemental information and electronic

transitions from energy dispersive X-ray spectroscopy and near edge X-ray absorption fine structure spectroscopy, respectively (Laskin et al., 2016; Moffet et al., 2010). Additionally, vibrational modes are sensitive to surrounding molecular environments, such as whether ions are free or bound to specific cations ($NO_{3\,(aq)}^-$ vs. $NO_{3\,(s)}^-$). These peak shifts can probe processes like phase separation and hydrogen bonding (Ault et al., 2013).

The greatest challenge of using optical microscopy-based vibrational spectroscopy for analysis of submicron particles has been the diffraction limit of visible and infrared (IR) light. Both Raman microspectroscopy and micro-IR spectroscopy of individual atmospheric particles provide insights for particles > 1 μm (Ault and Axson, 2017; Craig et al., 2017; Ghorai et al., 2014; Baustian et al., 2012), but have limited ability to probe accumulation mode particles (< 1 μm) and the atmospheric surface area mode (Seinfeld and Pandis, 2016). To probe smaller particles, surface-enhance Raman spectroscopy (SERS) (Craig et al., 2015) and tip-enhanced Raman spectroscopy (TERS) (Ofner et al., 2016) have been used, but uneven enhancements require further development for quantification. To understand the relationship between chemical composition and morphology in a critical size range for aerosol impacts, vibrational methods are needed that chemically analyze particles < 500 nm at atmospheric pressure and probe intra-particle compositional variability.

Atomic force microscopy with infrared spectroscopy (AFM-IR) has the potential to overcome size limitations with imaging capabilities on the scale of nanometers, and ~50 nm chemical resolution (Dazzi et al., 2012). This combines simultaneous single particle measurements of physical properties (hygroscopicity (Morris, 2016), surface tension (Morris et al., 2015; Hritz et al., 2016), phase, morphology (Krueger et al., 2005) by AFM) with chemical composition (functional groups by IR absorption). In this study, AFM-IR was used to analyze accumulation mode aerosol particles ($\geq$ 150 nm) for the first time. Inorganic and organic functional groups were characterized for laboratory-generated standards and ambient particles. Several substrates commonly used for AFM and Fourier transform IR spectroscopy (FTIR) were tested to determine the best substrate for aerosol particle analysis. Phase separation and spatial variation of chemical species were observed on spatial scales of 100 nm, demonstrating that AFM-IR can analyze particles below the diffraction limit.

5.2. Methods

5.2.1. AFM-IR Technique Overview

A nanoIR2 system (Anasys Instruments, Santa Barbara, CA) was used to test single-component, atmospherically-relevant standards in contact mode. The principle of AFM-IR, shown in Figure 5.1, is explained in detail by Dazzi et al. (2012). Briefly, the sample is pulsed with a tunable IR source (2.5-12 μm, 1 kHz) over a frequency range of 900-3600 cm^{-1}. Upon absorption of IR radiation, thermal expansion of the sample occurs, causing the AFM probe in contact with the surface to oscillate at its resonant frequency. The oscillations are detected by the deflection laser's position on the photodiode, and the amplitude of oscillation is proportional to IR absorbance, yielding an IR spectrum as a function of wavelength with 4 cm^{-1}/point resolution (instrument limit is 4 cm^{-1}) (Dazzi et al., 2012).

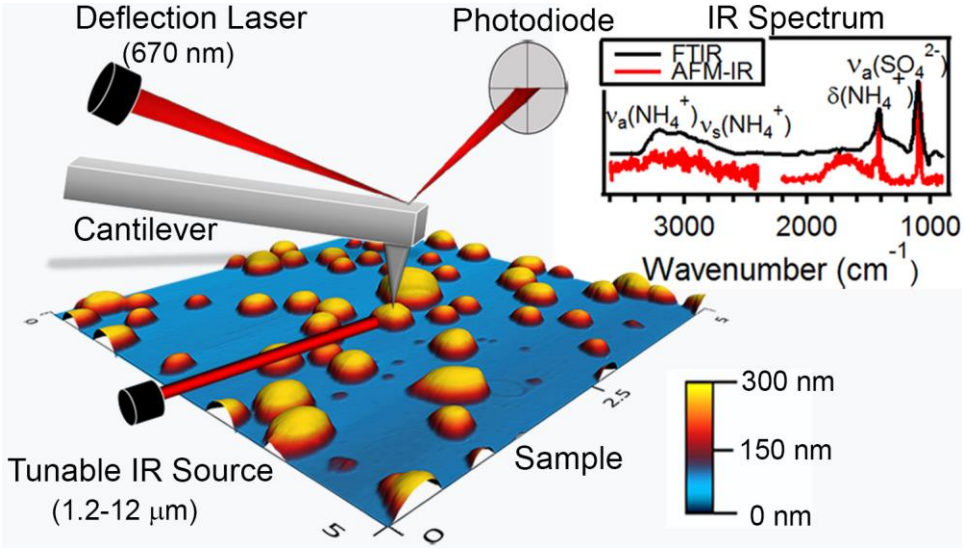

Figure 5.1. Schematic of AFM-IR operation. Local thermal expansion from the IR laser is detected by the cantilever, allowing IR spectra with ~50 nm resolution to be collected. IR spectra were collected from individual ammonium sulfate particles using AFM-IR (this study) and micro-FTIR (Liu et al., 2008).

5.2.2. Laboratory Standard Aerosol Generation and Impaction

Laboratory-generated aerosol samples were created by atomizing and impacting particles from 0.05 M standard solutions of ammonium sulfate (Alfa Aesar, 99 %), sodium nitrate (Sigma Aldrich 99.0 %), succinic acid (Alfa Aesar, 99 %), and D-sucrose (Fisher Scientific 99.9 %) onto substrates using a microanalysis particle sampler (MPS-3, California Measurements, Inc.).

Particles were impacted on stage 3 of the MPS (70-400 nm equivalent aerodynamic diameter). Succinic acid was generated via dissolution of succinic anhydride in Millipore water. Generated aerosols were passed through two diffusion dryers (drying to ~15 % relative humidity) prior to impaction. Core-shell particles were generated by atomizing a 1 % by weight solution of ammonium sulfate and polyethylene glycol 400 (Fluka) in a 1:1 ratio. Before impaction, ammonium sulfate-polyethylene glycol particles were not passed through diffusion dryers, resulting in liquid-liquid phase separation. Particles with AFM heights < 250 nm were used in the subsequent analysis.

5.2.3. AFM-IR Imaging and Spectral Acquisition

AFM-IR was performed on a nanoIR2 system (Anasys Instruments) with room relative humidity varying seasonally from 10-40 %. AFM height/deflection images and IR spectra of ammonium sulfate, sodium nitrate, succinic acid, and sucrose particles were collected in contact mode (IR power 21.27 %, filter in) at a scan rate of 1 Hz using a gold-coated contact mode silicon nitride probe (Anasys Instruments, 13 ± 4 kHz resonant frequency, 0.07-0.4 N/m spring constant). AFM height/phase images of phase separated ammonium sulfate and polyethylene glycol particles were collected in tapping mode at a scan rate of 0.4 Hz using a dual-purpose gold-coated silicon nitride tapping probe for NIR2 (Anasys Instruments, 75 ± 15 kHz resonant frequency, 1-7 N/m spring constant). To collect IR spectra, the dual-purpose tapping probe was put in contact mode (since on the nanoIR2 this is required to detect the sample photothermal expansion). The amplitude of cantilever oscillations was mapped using 128 co-averages, with a resolution of 4 cm^{-1}/point. Eight spectra with an IR power of 38.46 % (filter in) were averaged for the PEG reference spectrum, and four spectra collected with an IR power of 21.27 % (filter in) were averaged for IR spectra collected from both the core and shell of the phase separated ammonium sulfate/PEG particle. For the IR spectral maps of an ambient aerosol particle, maps were collected in contact mode using a gold-coated contact mode probe at 1476 cm^{-1} and 1580 cm^{-1} with a trace rate of 0.1 Hz and retrace rate of 1 Hz so that the update of the IR-peak, IR-amplitude and frequency data approximated the pixel rate of the image. The amplitude of cantilever oscillations was mapped using 16 co-averages, 300 pt. resolution for X and Y, and IR power at 1.03 %.

The IR ratio map was generated in Analysis Studio (Anasys analysis software) by cross-correlating the spatial distribution of the two AFM height images and calculating the ratio between the two IR intensities at each point. Since the ratio map correlates the IR maps with the height image, changes in intensity due to topography are normalized. Furthermore, thermal drift is accounted for in this analysis, hence the resulting ratio map is an accurate representation of the particles. Thermal drift of the sample between IR frequency maps is noted by the solid purple regions along the top and right edge of the image.

5.3. Results and Discussion

5.3.1. Single-Component Aerosol Particles

Aerosol particles were generated from single-component solutions to evaluate AFM-IR for model aerosol particles. Two inorganic salts (sodium nitrate and ammonium sulfate), and two organic compounds (succinic acid and sucrose), were aerosolized, dried, and impacted onto Si substrates using a microanalysis particle sampler (MPS-3, California Measurements Inc.). Particles with volume equivalent diameters (D_{ve}) ~200-350 nm were selected for IR analysis (Table D.1), where D_{ve} corresponds to the diameter of a sphere with volume equivalent to the impacted particle. Measured IR peak positions in submicron particles were compared to conventional FTIR mode frequencies, with good agreement observed. Ammonium sulfate was chosen as it is ubiquitous in aerosols and frequently used as a benchmark compound in aerosol studies (Seinfeld and Pandis, 2016), while $NaNO_3$ is readily formed in the atmosphere from reactions of HNO_3 with sea spray aerosol and mineral dust (Weis and Ewing, 1999). Succinic acid was chosen as dicarboxylic acids are the most abundant organic species in aerosols (Kawamura and Bikkina, 2016), while sucrose is used as a model compound for glassy secondary organic aerosol in lab studies (Zobrist et al., 2011).

In Figure 5.2, representative AFM height and deflection images and IR spectra are shown for individual particles generated from the four standards. The spectrum for ammonium sulfate particles showed $\nu(SO_4^{2-})$ at 1091 cm^{-1} and $\delta(NH_4^+)$ at 1422 cm^{-1}, which agree with spectra of ~1 μm particles observed by Liu et al. (2008) in a micro-FT-IR study. Although less intense, a weak mode at 3139 cm^{-1} consistent with $\nu(NH_4^+)$ (Liu et al., 2008; Weis and Ewing, 1996) was also observed. In the sodium nitrate particles, the sharp $\nu(NO_3^-)$ at 1356 cm^{-1} aligns well with

literature $\nu_a(NO_3^-)$ for particles at low relative humidity (Liu et al., 2008). Table D.2 comparing observed AFM-IR modes with FTIR literature modes is available in Appendix D.

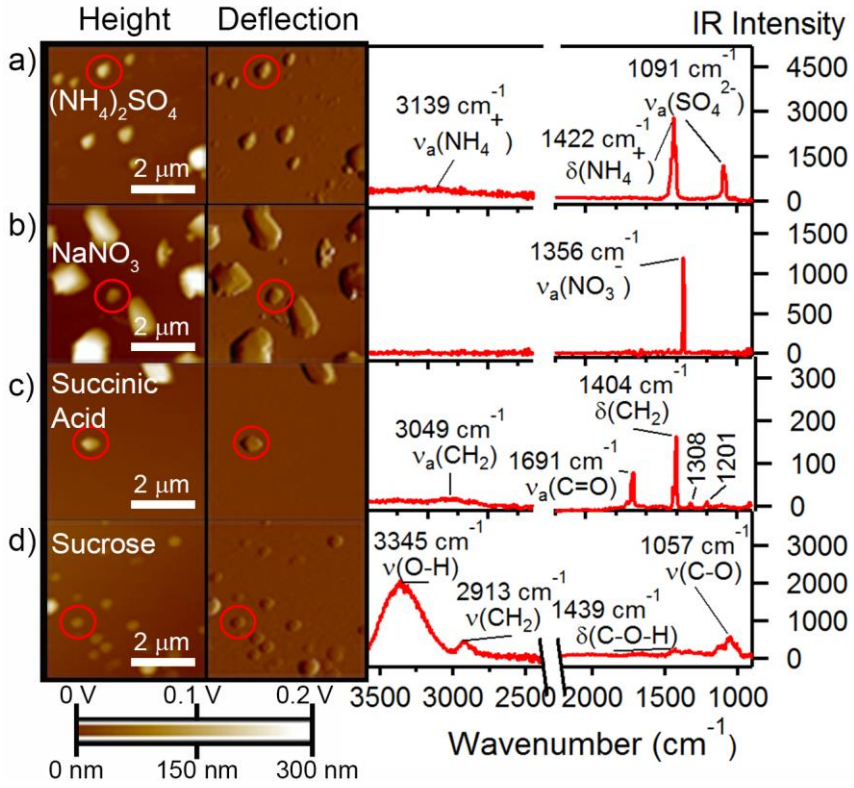

Figure 5.2. AFM height, deflection, and IR spectra of single-component particles: a) $(NH_4)_2SO_4$, b) NaNO3, c) succinic acid, and d) sucrose. D_{ve} of analyzed particle from each standard: 346 nm, 303 nm, 335 nm, and 202 nm (further information in Table D.1).

For the more complex organic particle spectra, IR mode assignments also matched prior IR studies, particularly in the fingerprint region (Table D.2). Peaks at 1201, 1308, and 3049 cm^{-1} consistent with ν(C-C), ν(C-O), and $\nu(CH_2)$, were observed in succinic acid particles (Larkin, 2011; Miñambres et al., 2010). A strong vibrational mode at 1691 cm^{-1}, ν(C=O), and a very strong vibration at 1404 cm^{-1}, $\delta(CH_2)$, were also observed (Miñambres et al., 2010; Larkin, 2011). For the sucrose particles, a variety of functional groups were observed including ν(C-O) at 1057 cm^{-1}, δ(C-O-H) at 1439 cm^{-1}, $\nu(CH_2)$ at 2913 cm^{-1}, and an intense ν(O-H) mode at 3345 cm^{-1} (Max and Chapados, 2001). Aside from the ν(O-H) stretch in sucrose, the IR intensity of the vibrational modes in the fingerprint region were most intense for all compounds. Although many vibrational modes are possible in this region, these results indicate that the fingerprint region could be used to make tentative assignments in multi-component particles.

5.3.2. Substrate-Dependent Spectral Response

The potential for substrate-dependent spectral responses was examined using ammonium sulfate particles (D_{ve} ~150-350 nm, Table D.3) impacted onto common microscopy and IR substrates: Si wafers, Ge, ZnSe, and chemical vapor deposition (CVD) diamond windows, and TEM grids, consisting of Formvar (polymer) coated copper grids (Figure 5.3). Particle spreading ratios were also calculated for each substrate to determine how substrate affected particle thickness (Figure D.1). Si, Ge, ZnSe, and CVD diamond provided good surfaces for imaging since these substrates are flat. However, the Cu grid bar on the TEM grid was rough, making particles difficult to distinguish from the surrounding substrate. Spectroscopically, particles on Si, Ge, ZnSe, and CVD diamond yielded strong IR signal and had minimal background interference, with average vibrational modes for $\nu(SO_4^{2-})$ at 1103 ± 5 cm^{-1} and $\delta(NH_4^+)$ at 1427 ± 3 cm^{-1}. In contrast, the TEM grid had sizeable background interferences including a Formvar out-of-plane bend δ(-CH) at 1020 cm^{-1} and the acetate carbonyl stretch at 1732 cm^{-1} (Hossain et al., 2014). One challenge observed for single particle AFM-IR data, was variation in the peak ratio and full width half maximum between the $\delta(NH_4^+)$ and $\nu(SO_4^{2-})$ modes, which is discussed in Appendix D (Figures D.2 and D.3). Si was found to be the best substrate for this AFM-IR analysis because it is microscopically flat and has minimal IR background, is inexpensive, and is nontoxic (unlike Ge and ZnSe).

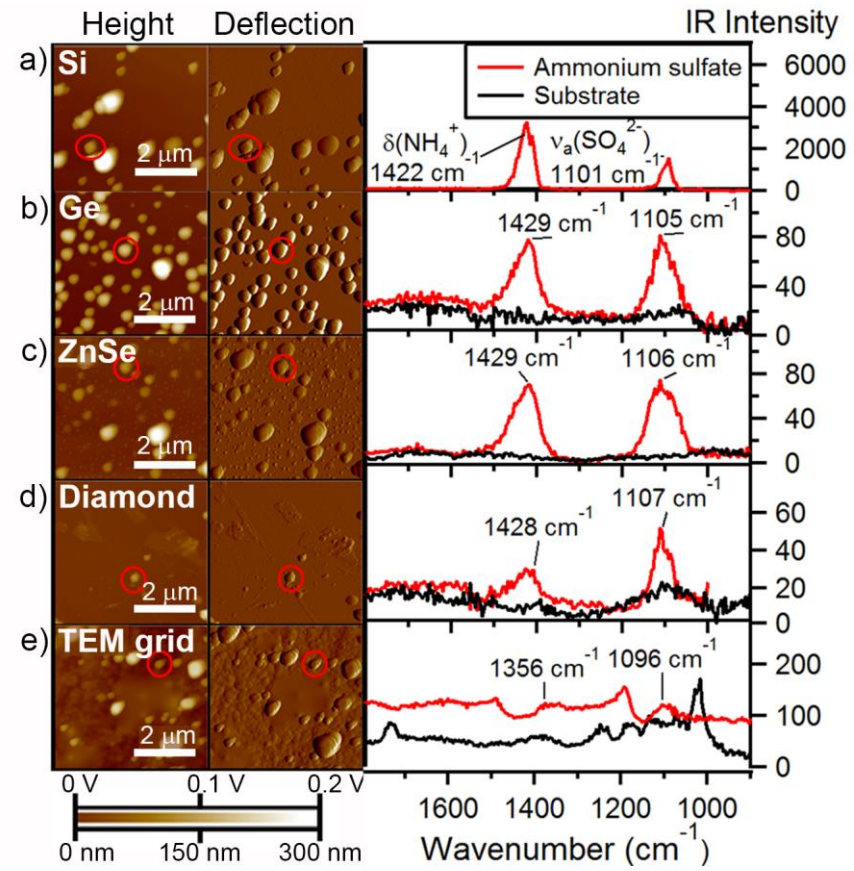

Figure 5.3. AFM height and deflection images, as well as IR spectra of individual ammonium sulfate aerosol particles (red trace) collected on the following substrates: a) Si, b) Ge, c) ZnSe, d) CVD diamond, and e) Cu grid bar from a TEM grid. An IR spectrum of each substrate from a region without particles is the background (black trace). Dve of analyzed particle from each substrate: 283 nm, 352 nm, 189 nm, 238 nm, 160 nm (Table D.3).

5.3.3. Core-Shell Aerosol Particles

To examine capabilities for more complex morphologies, core-shell particles were generated similar to prior microscopy studies (You et al., 2014; Veghte et al., 2013). Particles with an ammonium sulfate core and a polyethylene glycol (PEG) shell were impacted onto Si and analyzed by AFM (tapping mode). Although the height images appear similar to the single-component particles, the phase images clearly show two distinct phases (Figure 5.4a-b). AFM phase imaging has been used previously to detect phase separation of submicron particles including partially engulfed and core-shell morphologies (Laskina et al., 2015; Freedman et al., 2010), however chemical characterization of each phase in this size range has been limited due to the optical diffraction limit. Since AFM-IR has spatial resolution on the scale of 50-100 nm,

dual-purpose AFM tips were used to collect images (tapping mode) and IR spectra (tapping mode; probe in contact with sample) from each phase. Spectra collected from the core and shell of the 550 nm particle (D_{ve}) show two distinct compositions (Figure 5.4c). The core has an intense vibrational mode at 1090 cm^{-1}, $\nu(SO_4^{2-})$ of ammonium sulfate (Liu et al., 2008; Cziczo et al., 1997; Weis and Ewing, 1996), while the shell shows two modes at 1105 cm^{-1} and 1256 cm^{-1}, the ν(C-O-C) and CH_2 twisting modes in PEG (Larkin, 2011; Lu et al., 2014). Since the PEG shell covers the particle, a small mode at 1266 cm^{-1} in the "core" spectrum is observed from PEG located on the top of the impacted particle. Similarly, the shoulder at 1090 cm^{-1} is likely due to a less intense PEG vibration ~1105 cm^{-1}. Thus, AFM-IR chemically distinguished the core and shell for a 550 nm particle.

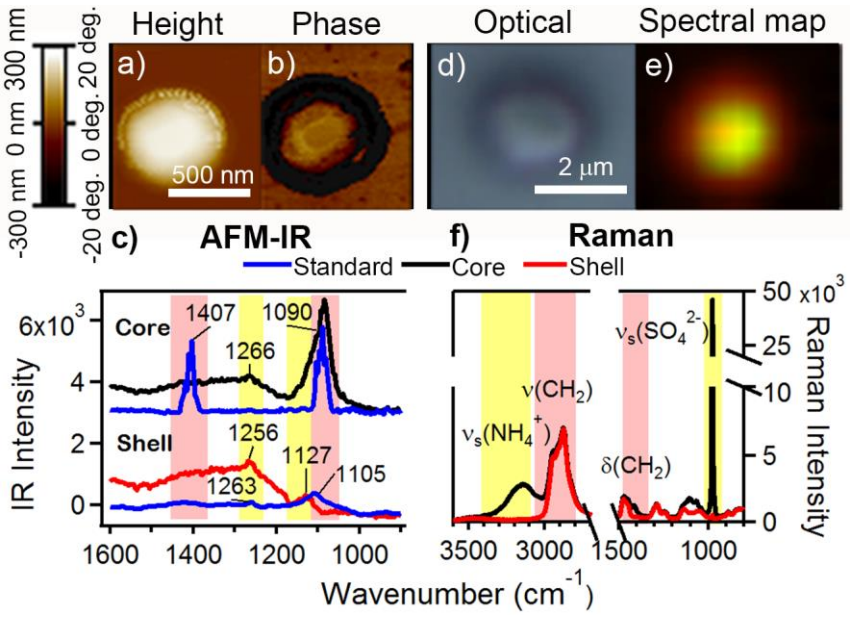

Figure 5.4. a) AFM height and b) phase images, as well as c) IR spectra of a submicron core-shell morphology particle consisting of $(NH_4)_2SO_4$ coated with polyethylene glycol (PEG) The blue traces are AFM-IR spectra for $(NH_4)_2SO_4$ and PEG. d) Optical image, e) Raman spectral map, and f) Raman spectra of a supermicron $(NH_4)_2SO_4$/PEG particle. Black and red traces were collected from the core and shell, respectively. $(NH_4)_2SO_4$ modes (yellow), and PEG modes (red) are highlighted.

To compare AFM-IR results to more traditional vibrational spectroscopy techniques, Raman microspectroscopy was used to collect spectra and chemical maps of supermicron core-shell ammonium sulfate/PEG particles (Figure 5.4d-f). The resulting Raman spectra agree with the AFM-IR results, with the shell containing solely PEG, while the "center" of the particles has both ammonium sulfate and PEG. The Raman map (Figure 5.4e), with regions corresponding to

the PEG modes at 1465 cm^{-1} and 2874 cm^{-1}, and the sulfate and ammonium modes at 974 cm^{-1} and 3150 cm^{-1}, clearly depict a core-shell morphology, similar to the AFM phase image. However while Raman microspectroscopy can analyze particles > 1 μm, the greatest advantage of AFM-IR is that it can investigate submicron particles. One limitation of the ammonium sulfate/PEG system studied here is that an IR spectral map could not be collected because PEG is a liquid, necessitating AFM analysis in tapping mode. As contact mode is currently needed for collecting IR spectra with the nanoIR2, only discreet point spectra could be collected.

5.3.4. Ambient Aerosol Particles

To demonstrate spatial resolution for spectral mapping of ambient particles with numerous chemical components, ambient aerosol particles were collected on Si substrates in Ann Arbor, MI (August 2016). IR spectral maps were collected for particles with $D_{ve} \leq$ 800 nm (Figure 5.5). Two modes, 1476 cm^{-1} and 1580 cm^{-1} suggestive of $\delta(CH_2)$ (Larkin, 2011) and ν(C=C) (Larkin, 2011; Miñambres et al., 2010), respectively, were observed for these particles, with different spatial distributions (Figure 5.5d-f). The ratio map (Figure 5.5f) most clearly highlights differences in spatial distribution of these two modes, as areas enriched in CH_2 (1476 cm^{-1}) appear red, while those enriched with C=C (1580cm^{-1}) appear blue. Within the smaller particles (P1-P2), approximately half the particle contains significant IR intensity from 1476 cm^{-1}, while the other half contains signatures from the 1580 cm^{-1} mode. Additionally, the two large agglomerate particles (P3-P4) exhibit chemical heterogeneity within localized regions. These results show that AFM-IR can effectively and simultaneously determine particle physical parameters, chemical composition, and distribution of chemical species within individual atmospheric particles, with a focus on organic functional groups.

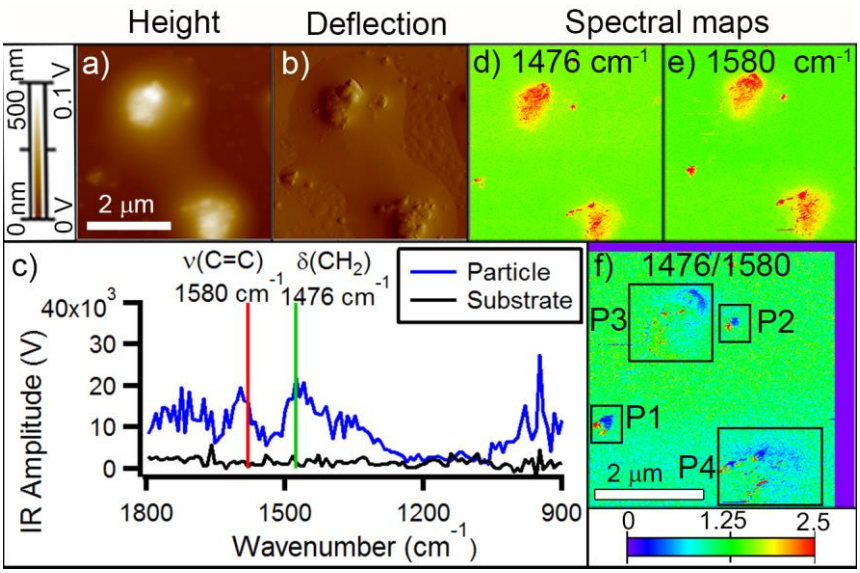

Figure 5.5. AFM height (a) and deflection images (b), IR spectrum (c), as well as IR spectral maps at 1476 cm^{-1} (d) 1580 cm^{-1}, and the ratio of 1476/1580 cm-1 shown for an ambient aerosol particle from Ann Arbor, MI. Four particles (P1-P4) exhibiting chemical heterogeneity are identified (e). Purple edge on (e) represents thermal drift between each map.

5.4. Conclusions

The simultaneous spectroscopic and morphological analysis of accumulation mode aerosol particles (< 1 µm) is challenging since techniques that are currently available either do not provide the detailed vibrational analysis necessary to identify distinct moieties, such as organic functional groups, or are diffraction limited and cannot investigate particles in this size range. Traditionally, AFM has been limited by its lack of chemical information, and micro-FTIR is limited by the diffraction of light to > 3 µm particles. AFM-IR however, has great potential to analyze submicron aerosol particles by imaging and providing vibrational information for species within < 500 nm particles at ambient pressure. As shown in this study, AFM-IR was applied to the study of single-component model systems, phase-separated particles, and ambient aerosol particles for the first time, detecting functional groups in particles concurrently imaged, so that particle diameter, height, morphology, phase, and chemical composition were all discerned. The novel application of this analytical method to atmospheric particles enabled detection of organic and inorganic vibrational modes in standards and ambient particles, as well as identified the composition of phase-separated components within a particle size range that has previously been unstudied by vibrational spectroscopy. The enhanced spatial scale for analysis of

atmospheric particles using AFM-IR has the potential to provide key insights regarding size-dependent phase-separated atmospheric particles within an atmospherically critical size range.

5.5. Acknowledgments

This project was supported by NSF CAREER Award CHE-1654149 and startup funds from the University of Michigan. A.L.B. generated aerosol particles from solutions in the laboratory and performed the AFM-IR and Raman microspectroscopy analysis. R.M.K. collected the ambient aerosol particles and initially collected AFM-IR images and spectra of the ambient particles. R.L.M. assisted with AFM-IR operation and along with M.M.B.H., data interpretation.

5.6. References

Ault, A. P., Zhao, D., Ebben, C. J., Tauber, M. J., Geiger, F. M., Prather, K. A., and Grassian, V. H.: Raman microspectroscopy and vibrational sum frequency generation spectroscopy as probes of the bulk and surface compositions of size-resolved sea spray aerosol particles, PCCP, 15, 6206-6214, 2013.

Ault, A. P., and Axson, J. L.: Atmospheric aerosol chemistry: Spectroscopic and microscopic advances, Anal. Chem., 89, 430-452, 2017.

Baustian, K. J., Cziczo, D. J., Wise, M. E., Pratt, K. A., Kulkarni, G., Hallar, A. G., and Tolbert, M. A.: Importance of aerosol composition, mixing state, and morphology for heterogeneous ice nucleation: A combined field and laboratory approach, J. Geophys. Res.: Atmos., 117, DOI: 10.1029/2011JD016784, 2012.

Craig, R. L., Bondy, A. L., and Ault, A. P.: Surface enhanced Raman spectroscopy enables observations of previously undetectable secondary organic aerosol components at the individual particle level, Anal. Chem., 87, 7510-7514, 2015.

Craig, R. L., Bondy, A. L., and Ault, A. P.: Computer-controlled Raman microspectroscopy (CC-Raman): A method for the rapid characterization of individual atmospheric aerosol particles, Aerosol Sci. Technol., 51, 1099-1112, 2017.

Cziczo, D. J., Nowak, J. B., Hu, J. H., and Abbatt, J. P. D.: Infrared spectroscopy of model tropospheric aerosols as a function of relative humidity: Observation of deliquescence and crystallization, J. Geophys. Res.: Atmos., 102, 18843-18850, 1997.

Dazzi, A., Prater, C. B., Hu, Q., Chase, D. B., Rabolt, J. F., and Marcott, C.: AFM-IR: Combining atomic force microscopy and infrared spectroscopy for nanoscale chemical characterization, Appl. Spectrosc., 66, 1365-1384, 2012.

Fierce, L., Bond, T. C., Bauer, S. E., Mena, F., and Riemer, N.: Black carbon absorption at the global scale is affected by particle-scale diversity in composition, Nature Communications, 7, 2016.

Freedman, M. A., Baustian, K. J., Wise, M. E., and Tolbert, M. A.: Characterizing the morphology of organic aerosols at ambient temperature and pressure, Anal. Chem., 82, 7965-7972, 2010.

Ghorai, S., Wang, B., Tivanski, A., and Laskin, A.: Hygroscopic properties of internally mixed particles composed of NaCl and water-soluble organic acids, Environ. Sci. Technol., 48, 2234-2241, 2014.

Hinds, W. C.: Aerosol technology: properties, behavior, and measurement of airborne particles, 2nd ed., 483 p., John Wiley & Sons, New York, 483 p. pp., 1999.

Hossain, U. H., Seidl, T., and Ensinger, W.: Combined in situ infrared and mass spectrometric analysis of high-energy heavy ion induced degradation of polyvinyl polymers, Polym. Chem., 5, 1001-1012, 2014.

Hritz, A. D., Raymond, T. M., and Dutcher, D. D.: A method for the direct measurement of surface tension of collected atmospherically relevant aerosol particles using atomic force microscopy, Atmos. Chem. Phys., 16, 9761-9769, 2016.

Kawamura, K., and Bikkina, S.: A review of dicarboxylic acids and related compounds in atmospheric aerosols: Molecular distributions, sources and transformation, Atmos. Res., 170, 140-160, 2016.

Krueger, B. J., Ross, J. L., and Grassian, V. H.: Formation of microcrystals, micropuddles, and other spatial inhomogenieties in surface reactions under ambient conditions: An atomic force microscopy study of water and nitric acid adsorption on MgO(100) and CaCO3(1014), Langmuir, 21, 8793-8801, 2005.

Larkin, P.: Chapter 8 - Illustrated IR and Raman Spectra Demonstrating Important Functional Groups, in: Infrared and Raman Spectroscopy, Elsevier, Oxford, 135-176, 2011.

Laskin, A., Gilles, M. K., Knopf, D. A., Wang, B., and China, S.: Progress in the analysis of complex atmospheric particles, in: Annual Review of Analytical Chemistry, Vol 9, edited by: Bohn, P. W., and Pemberton, J. E., Annual Review of Analytical Chemistry, 117-143, 2016.

Laskina, O., Morris, H. S., Grandquist, J. R., Qin, Z., Stone, E. A., Tivanski, A. V., and Grassian, V. H.: Size matters in the water uptake and hygroscopic growth of atmospherically relevant multicomponent aerosol particles, J. Phys. Chem. A, 119, 4489-4497, 2015.

Liu, Y., Yang, Z., Desyaterik, Y., Gassman, P. L., Wang, H., and Laskin, A.: Hygroscopic behavior of substrate-deposited particles studied by micro-FT-IR spectroscopy and complementary methods of particle analysis, Anal. Chem., 80, 633-642, 2008.

Lu, F., Jin, M. Z., and Belkin, M. A.: Tip-enhanced infrared nanospectroscopy via molecular expansion force detection, Nat. Photonics, 8, 307-312, 2014.

Max, J.-J., and Chapados, C.: Sucrose hydrates in aqueous solution by IR spectroscopy, J. Phys. Chem. A, 105, 10681-10688, 2001.

Miñambres, L., Sánchez, M. N., Castaño, F., and Basterretxea, F. J.: Hygroscopic properties of internally mixed particles of ammonium sulfate and succinic acid studied by infrared spectroscopy, J. Phys. Chem. A, 114, 6124-6130, 2010.

Moffet, R. C., Henn, T., Laskin, A., and Gilles, M. K.: Automated chemical analysis of internally mixed aerosol particles using X-ray spectromicroscopy at the carbon K-edge, Anal. Chem., 82, 7906-7914, 2010.

Morris, H. S., Grassian, V. H., and Tivanski, A. V.: Humidity-dependent surface tension measurements of individual inorganic and organic submicrometre liquid particles, Chemical Science, 6, 3242-3247, 2015.

Morris, H. S. S.: Quantifying the hygroscopic growth of individual submicrometer particles with atomic force microscopy, Analytical chemistry (Washington), 88, 3647-3654, 2016.

Ofner, J., Deckert-Gaudig, T., Kamilli, K. A., Held, A., Lohninger, H., Deckert, V., and Lendl, B.: Tip-enhanced Raman spectroscopy of atmospherically relevant aerosol nanoparticles, Anal. Chem., 88, 9766-9772, 2016.

Poschl, U.: Atmospheric aerosols: Composition, transformation, climate and health effects, Angew. Chem. Int. Ed., 44, 7520-7540, 2005.

Seinfeld, J. H., and Pandis, S. N.: Atmospheric chemistry and physics: from air pollution to climate change, John Wiley & Sons, 2016.

Veghte, D. P., Altaf, M. B., and Freedman, M. A.: Size dependence of the structure of organic aerosol, J. Am. Chem. Soc., 135, 16046-16049, 2013.

Weis, D. D., and Ewing, G. E.: Infrared spectroscopic signatures of $(NH_4)_2SO_4$ aerosols, J. Geophys. Res.: Atmos., 101, 18709-18720, 1996.

Weis, D. D., and Ewing, G. E.: The reaction of nitrogen dioxide with sea salt aerosol, J. Phys. Chem. A, 103, 4865-4873, 1999.

You, Y., Smith, M. L., Song, M., Martin, S. T., and Bertram, A. K.: Liquid-liquid phase separation in atmospherically relevant particles consisting of organic species and inorganic salts, Int. Rev. Phys. Chem., 33, 43-77, 2014.

Zhang, Q., and Thompson, J. E.: Effect of particle mixing morphology on aerosol scattering and absorption: A discrete dipole modeling study, GeoResJ, 3–4, 9-18, 2014.

Zobrist, B., Soonsin, V., Luo, B. P., Krieger, U. K., Marcolli, C., Peter, T., and Koop, T.: Ultra-slow water diffusion in aqueous sucrose glasses, PCCP, 13, 3514-3526, 2011.

Chapter 6.
Phase Separated Secondary Organic Aerosol Internal Structure Is Determined By Temperature and Relative Humidity History

6.1. Introduction

Secondary organic aerosol (SOA), formed from the oxidation of volatile organic compounds (VOCs), contribute substantially to aerosol mass globally, with estimates of 20-380 Tg y^{-1} (Hallquist et al., 2009; Glasius and Goldstein, 2016). SOA impact climate directly by scattering/absorbing solar radiation or indirectly by modifying cloud properties, and the potential toxicity of organic particles has made them a point of study (Jacobson et al., 2000). Despite its ubiquitous presence, models struggle to replicate SOA concentrations and distributions, in part due to uncertainties related to particle phase state, acidity, and internal structure (McNeill, 2015; Pye et al., 2017; Zuend and Seinfeld, 2012). Traditionally, SOA particles have been depicted as well-mixed aqueous droplets in models (Shiraiwa et al., 2017). However, as the study of phase separated and viscous organic-inorganic particles has expanded rapidly in the past decade, increasingly complex liquid-liquid phase separation (LLPS) structures, such as partially engulfed, have been observed (Veghte et al., 2014; Reid et al., 2011; Veghte et al., 2013; Fraund et al., 2017; Rachel E. O'Brien, 2015). Furthermore, numerous studies have recently focused on the role of viscosity and glass transition phase states, improving our understanding of how O:C elemental ratios, relative humidity (RH), and temperature affect LLPS (Bateman et al., 2015; Hosny et al., 2016; Rothfuss and Petters, 2016, 2017; Song et al., 2016; Dette and Koop, 2015; Koop et al., 2011; Shiraiwa et al., 2017). In order to more accurately predict SOA formation and minimize discrepancies between models and measurements, additional studies are needed to determine, quantify, and parameterize the factors involved in SOA formation and LLPS.

Herein, microchemical analyses (scanning electron microscopy with energy dispersive X-ray spectroscopy – SEM-EDX and scanning transmission X-ray microscopy with near edge X-ray absorption fine structure spectroscopy– STXM-NEXAFS) are used to probe LLPS and complex structure within ambient SOA-inorganic particles. Image processing was used to quantify the extent of complex phase separation relative to homogeneous and core-shell structures as a function of size, RH, temperature, and atmospheric age during the Southern Oxidant and Aerosol Study (SOAS) in the southeastern U.S. during the summer of 2013. The variation of complexity throughout the study suggests that complex structures are dependent on multiple factors including aerosol lifetime, as well as temperature and RH history.

6.2. Methods

6.2.1. SOAS Field Site Description and Sample Collection

Sampling was conducted at Centreville, AL in a heavily forested area from June 5, 2013 to July 11, 2013 as part of the SOAS field campaign (Bondy et al., 2017). Aerosol particles were collected on 200 mesh Carbon Type B with Formvar TEM grids (Ted Pella Inc.) and silicon wafers (Ted Pella Inc.) using a micro-orifice uniform deposit impactor (MOUDI, MSP Corp., Model 110) with a flow rate of 30 L/min. In order to exclude collection of particles > 10 μm, a PM_{10} cyclone (URG model 786) was paired with the MOUDI. The 50 % aerodynamic diameter size cut-points for the MOUDI stages used in this analysis were 0.56, 0.32 0.18, 0.10, and 0.056 μm (Marple et al., 1991).

Sampling was conducted daily from 8:00-19:00 Central Standard Time (CST) and 20:00-7:00 CST, with one hour for substrate exchange, aside from intensive periods on June 10-12, June 14-16, June 29-July 1, and July 7-9, 2013. Sampling during intensive periods, scheduled based on predicted gas-phase concentrations and meteorological parameters (Budisulistiorini et al., 2015), was conducted from 8:00-11:00, 12:00-15:00, 16:00-19:00, and 20:00-7:00 CST. Following collection, substrates were stored in a freezer at -22°C prior to analysis.

6.2.2. Scanning Electron Microscopy with Energy Dispersive X-ray Spectroscopy (SEM-EDX)

The majority of the SEM-EDX analysis was conducted at the Michigan Center for Materials Characterization $(MC)^2$ at the University of Michigan. For this analysis, a FEI Helios

NanoLab SEM/FIB equipped with a field emission gun operating at 15 kV and a high angle annular dark field detector (HAADF) was used to analyze particles on TEM grids. On silicon substrates, the SEM was operated at 10 kV with an Everhart-Thornley secondary electron imaging detector (ETD). An EDAX X-ray spectrometer (Si) was coupled with the SEM to determine elemental composition of particles. A portion of the SEM analysis of particles from SOAS was conducted at the Pacific Northwest National Laboratory (PNNL) using a FEI Quanta environmental SEM equipped with a field emission gun operating at 20 kV and a HAADF detector (Bondy et al., 2017; Laskin et al., 2006). The SEM was also equipped with an EDX spectrometer (EDAX, Inc.).

6.2.3. Image Segmentation

Particles in SEM images were automatically identified by segmenting each image using thresholds determined from Otsu's method (Figure 6.6) (Otsu, 1979). After segmentation, the area and perimeter of each particle larger than eight pixels was calculated using the regionprops function of Matlab's Image Processing Toolbox. To obtain a quantitative metric for particle complexity, each particle was extracted from the image and individually segmented and analyzed using the methods previously described to quantify the area and perimeter of the particles sub-structure, which are subsequently referred to as the inner area and inner perimeter respectively. The ratio of the inner perimeter to particle perimeter was used to quantify the complexity of each particle in the image. Both the SEM image and images of randomly selected particles were manually compared to thresholded images to verify proper performance of the automated threshholding algorithm.

6.2.4. Scanning Transmission X-ray Microscopy/Near Edge X-ray Absorption Fine Structure (STXM-NEXAFS)

STXM-NEXAFS measurements of two MOUDI samples, June 10, 2013 16:00-19:00 CST and July 7, 2013 8:00-19:00 were taken at the carbon (C) (280-320 eV), nitrogen (N) (395-430 eV), and oxygen (O) (525-550 eV) K-absorption edges and at the sulfur (S) (168-176 eV) L-absorption edge. STXM instruments at the Advanced Light Source at Lawrence Berkeley National Laboratory on beamlines 5.3.2 and 11.0.2 were used for this analysis. The operation of the microscope has been explained in detail by Kilcoyne et al. (2003) The soft X-ray beam was

focused to a spot size of 40 nm using a Fresnel zone plate and was raster scanned. X-rays transmitted through the samples and the TEM grid-substrates were detected using a phosphor-coated Lucite pipe coupled to a photomultiplier for single photon counting. As described by Moffet et al. (2010), Matlab and Axis 2000 were both used for spectral analysis of the STXM-NEXAFS data. Stacks of images taken at sequentially increasing photon energies were used to obtain spatially resolved spectroscopic data at the K-absorption edges. At the C K-edge, organic regions were identified where the post edge minus the pre-edge (optical density (OD) at 320 eV minus OD 278 eV) was > 0. For the inorganic identification, particles with a ratio of the pre edge and the post edge (OD 278 / OD 320) > 0.5 were identified. To identify soot inclusions within particles, individual pixels of a particle were analyzed and if a pixel contained 35 % or greater C=C, a peak identified as soot using graphitic carbon as a standard, then that pixel was identified as a soot region. For inorganic material identification, peak energies at the O K-edge, N K-edge, and S L-edge identified the composition as $(NH_4)_2SO_4$ (Hopkins et al., 2008; Zelenay et al., 2011). Based on STXM-NEXAFS analysis of organic and inorganic regions, particle internal complexity was identified as phase separation of these two components.

6.2.5. HYSPLIT Backward Air Mass Trajectory Analysis

NOAA's Hybrid Single Particle Lagrangian Integrated Trajectory (HYSPLIT) model (Draxler and Hess, 1997) was run at 500 m above ground level (48 h backward) to model the sources of air masses for samples collected during SOAS, air mass transport times, temperature, and relative humidity along the air mass trajectories. HYSPLIT backward air mass trajectories were run at the middle of each sampling time point (i.e. June 11 2:00 CST for a sample collected June 10 20:00-June 11 7:00) for June 10-June 17, 2013 and July 9, 2013.

6.2.6. Calculations of RH-Dependent Glass Transition Temperature (T_g) During SOAS

As the glass transition temperature (T_g) can vary substantially due to RH, the RH-dependent T_g for SOA during SOAS was estimated using the Gordon-Taylor approach (Koop et al., 2011; Wang et al., 2015):

$$T_g(RH) = \frac{T_{g,w} * k_{GT} + f(RH) * T_{g,org}}{k_{GT} + f(RH)} \quad (6.1)$$

where $T_{g,w}$ is the glass transition temperature of water; k_{GT} is the Gordon-Tayler constant for the specific organic material representing the interaction between water and organic solute; $T_{g,org}$ is

the glass transition temperature of the pure organic component, and *f(RH)* was calculated as expressed below.

$$f(RH) = \frac{100-RH}{RH}\frac{1}{\kappa_{org}}\frac{\rho_{org}}{\rho_w} \quad (6.2)$$

where k_{org} is the hygroscopicity parameter of the organic component; ρ_{org} is the density of the organic component; and ρ_w is the density of water. $T_{g,w}$, k_{GT}, κ_{org}, ρ_{org}, and ρ_w of 136 K (Wang et al., 2015), 2.5 (± 1.0) (Wang et al., 2012; Wang et al., 2015; Koop et al., 2011), 0.05 (0-0.3) (Brock et al., 2015), 1.4 (± 0.2) g cm^{-3} (Shilling et al., 2008), and1.0 g cm^{-3} were used, respectively. As the organic material within ambient SOA contains more than a single component, $T_{g,org}$ (~308 K) was estimated using an equation derived from the organic aerosol module ORACLE, based on a computationally efficient description of primary and secondary organic aerosol sources, phase-partitioning and chemical evolution (Shiraiwa et al., 2017).

$$T_g = -21.57(\pm 13.47) + 1.51(\pm 0.14)M - 1.7\,x + 131.4(\pm 16.01)(O{:}C) - 0.25(\pm 0.085)M(O{:}C) \quad (6.3)$$

where the average O:C ratio during SOAS was 0.58 (± 0.06) (Cerully et al., 2015) and the molar mass of biogenic SOA was estimated as 293 g mol^{-1} (Shiraiwa et al., 2017).

6.3. Results and Discussion

6.3.1. Complexity of Internal Structures within SOA-AS

The most abundant type of particle observed at the rural, forested sampling site during SOAS was SOA mixed with inorganic sulfate, particularly at small sizes near the mode of the ambient size distribution. Though these particles often had inorganic material homogeneously distributed throughout, phase separation between organic and inorganic material was frequently observed (Figure 6.1). Examples of different phase-separated internal structures observed from STXM-NEXAFS and SEM included: homogeneous, core-shell, and complex (Figure 6.2a-c). Furthermore, some particles contained inclusions identified as soot by NEXAFS (Figure 6.2d), although these particles accounted for < 10 % of SOA.

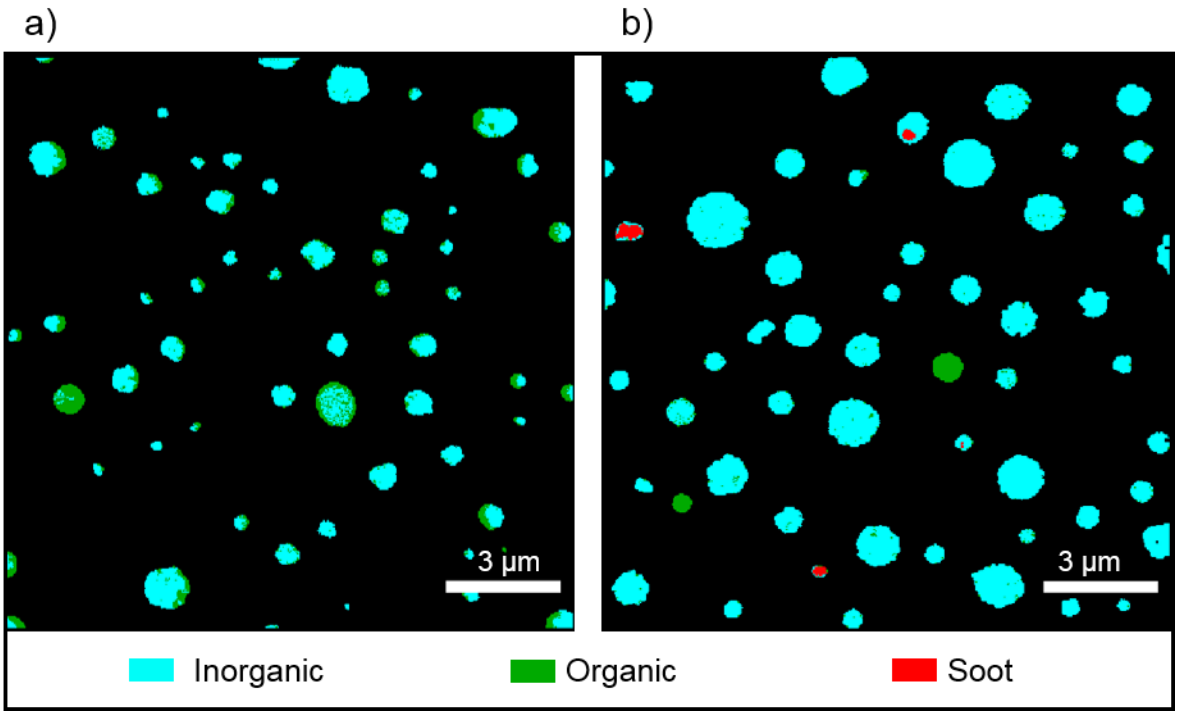

Figure 6.1. STXM particle maps with different spectral components for two SOAS samples: a) June 10 and b) July 7, 2013. The ratio of the optical density (OD) of the pre-edge to the post-edge (OD_{pre}/OD_{post}) indicates inorganic material (cyan), the OD_{COOH} is a map of carboxylic acid groups indicating organic material (green), and $sp^2 > 0.35$ indicates elemental carbon, or soot inclusions (red).

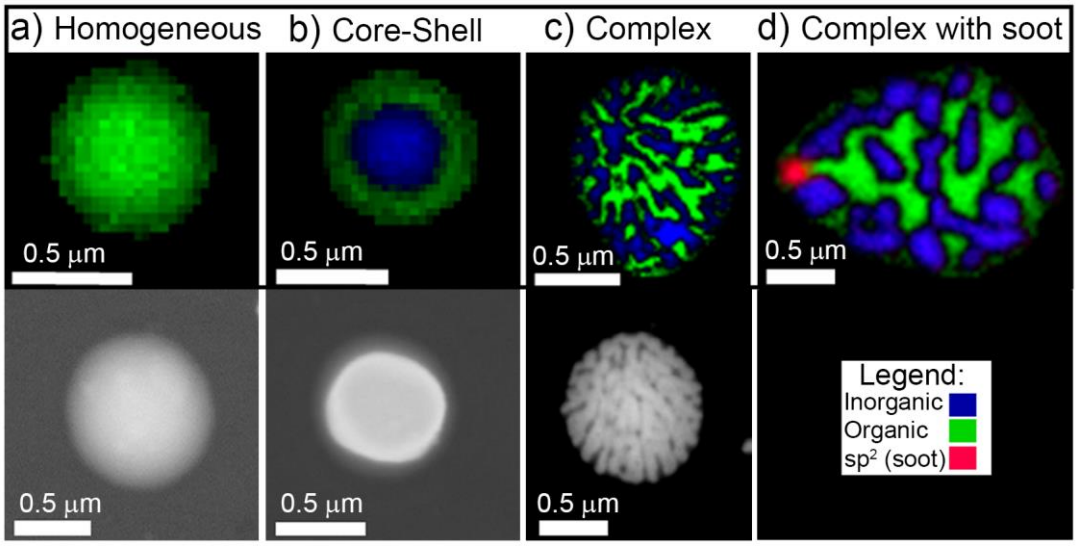

Figure 6.2. a) Homogeneous, b) core-shell, c) complex, and d) complex with soot morphologies were observed using STXM-NEXAFS and SEM performed on SOA-AS particles sampled on 6/10/2013 and 7/7/2013. STXM-NEXAFS singular value decomposition maps show inorganic (blue), organic (green), and sp^2 carbon (red). No complex particle with soot was available from the SEM analysis.

The blue inorganic regions (Figure 6.2) were identified through NEXAFS and atomic force microscopy-infrared spectroscopy (AFM-IR) as ammonium sulfate (Figures 6.3-6.4), which is likely aqueous for the RH range observed during SOAS (~60-90 %) (Guo et al., 2015) as the RH was above the efflorescence RH of ammonium sulfate. Although recent modelling incorporated phase separation into predictions to more accurately predict the role of aerosol water during SOAS (Pye et al., 2017), LLPS has not been examined during SOAS. Laboratory measurements predict a liquid organic component because a large fraction of the organic aerosol is from isoprene SOA (Xu et al., 2015), which are liquids at RH $\geq$ 60 % (Song et al., 2015). Additionally, measurements of aerosol bounce during SOAS indicate that at typical ambient RH and temperature, organic-dominated particles stay mostly liquid (Pajunoja et al., 2016), potentially allowing for LLPS to occur. However, the initial observation of phase separation, specifically forming complex internal structures (Figure 6.2c-d), was unexpected. Subsequent analysis of samples from a range of field sites, both forested and urban (Figure 6.5), suggest that these structures are not unique to SOAS and isoprene SOA, but are prevalent in ambient aerosol populations. Therefore, further analysis of SOA-ammonium sulfate (SOA-AS) structure and properties are needed as structure and morphology of organic aerosol affect the reactive uptake of important gas-phase species (McNeill et al., 2006) and influence the ice nucleation properties of particles (Schill and Tolbert, 2013).

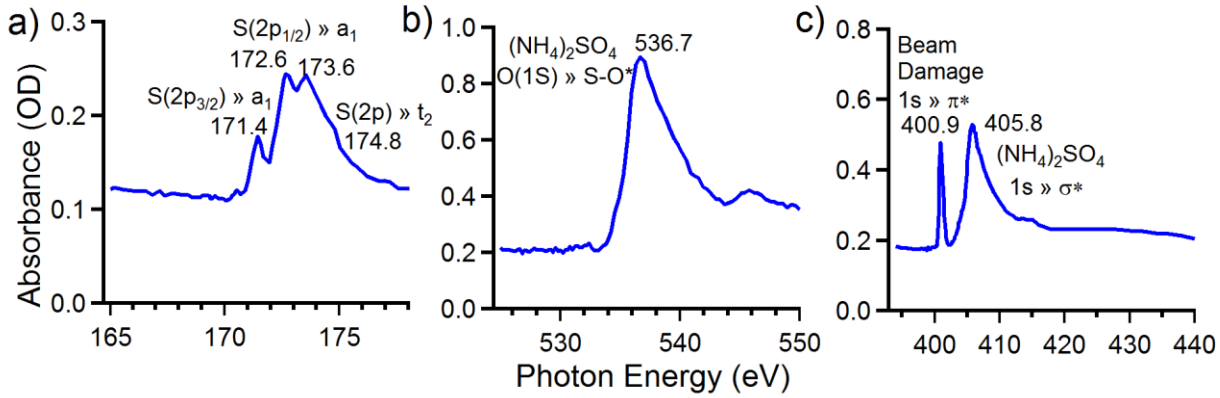

Figure 6.3. a) Sulfur L-edge NEXAFS spectrum, b) nitrogen K-edge spectrum, and c) oxygen K-edge spectrum collected from inorganic regions within phase-separated SOA-AS particles from SOAS.

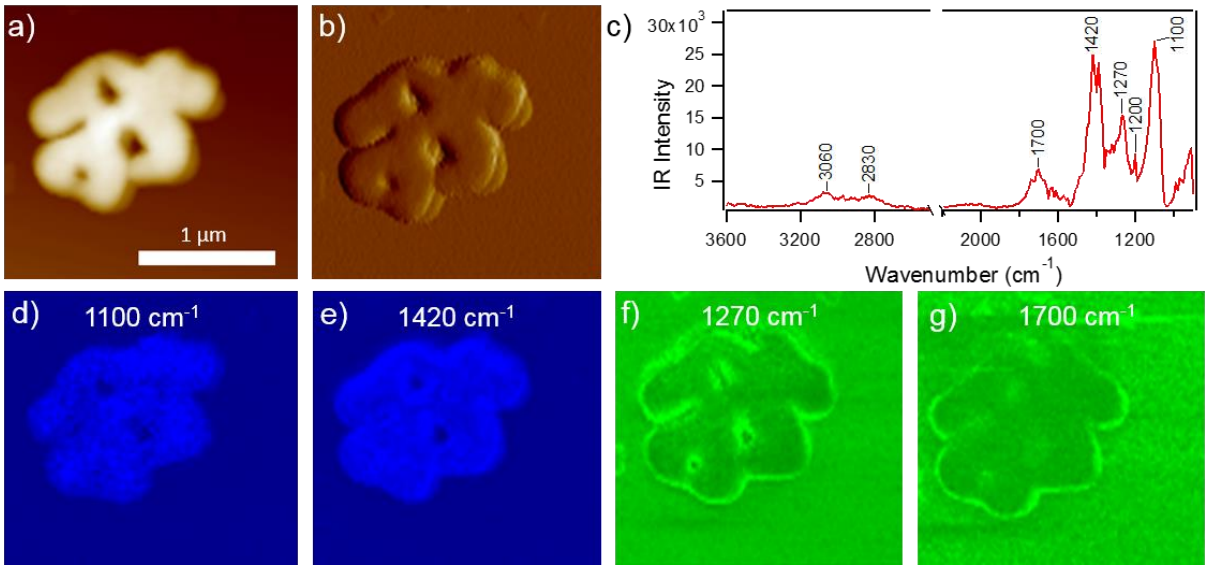

Figure 6.4. AFM a) height and b) deflection images and c) IR spectrum of an SOA-AS particle from SOAS exhibiting complex structure. IR maps collected at d) 1100, e) 1420, f) 1270, and g) 1700 cm^{-1} show the distribution of inorganic and organic species with inorganic (ammonium sulfate) on the interior and organic on the particle exterior. Modes at 1100 cm^{-1} likely corresponds to $\nu(SO_4^{2-})$, 1420 cm^{-1} corresponds to $\delta(NH_4^+)$, 1270 cm^{-1} corresponds to $\delta(CH_2)$, and the mode at 1700 cm^{-1} corresponds to $\nu(C=O)$.

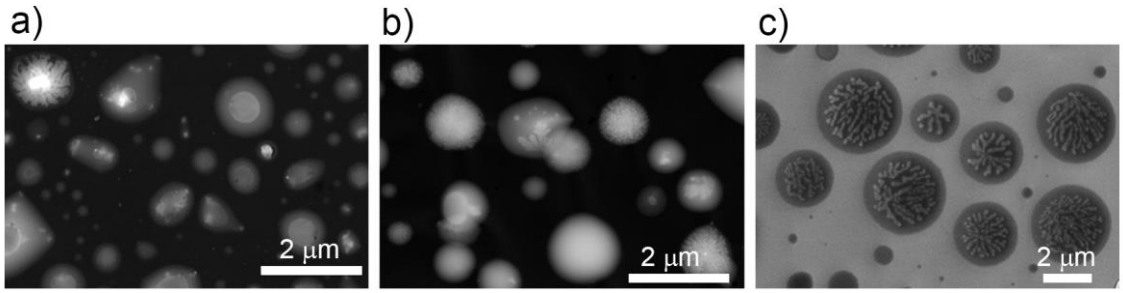

Figure 6.5. Evidence of complex structures from other field and chamber studies from samples not frozen during storage. SEM images of ambient SOA-inorganic particles from a) Pellston, MI and b) Atlanta, GA, and c) generated ammonium bisulfate and α-pinene from a chamber study.

To quantify the internal structure of SOA-AS particles from SEM images, an image processing method was developed to analyze a statistically significant number of particles (Figure 6.6), which was corroborated through extensive manual checking. Briefly, brightness to contrast was automatically adjusted and the external perimeter and internal perimeter(s) were traced. The brighter portion of complex particles (Figures 6.2 and 6.7a,f) results from the higher atomic number (Z) of sulfur versus oxygen and carbon in the darker portion. Based on analysis of multiple images such as Figures 6.7a and f, the ratio of inner perimeter to outer perimeter was

used to classify particles by internal structure (Figures 6.7b,g). Homogeneous particles, with mixed organic and inorganic material, had no inner perimeter and thus a perimeter ratio of 0. The delineation between complex and core-shell was based on an inner perimeter > outer perimeter, thus a ratio > 1. Though some particles could have a complex inner structure despite an inner perimeter < outer perimeter, this was rarely observed during manual classification and spot checking of the image processing code.

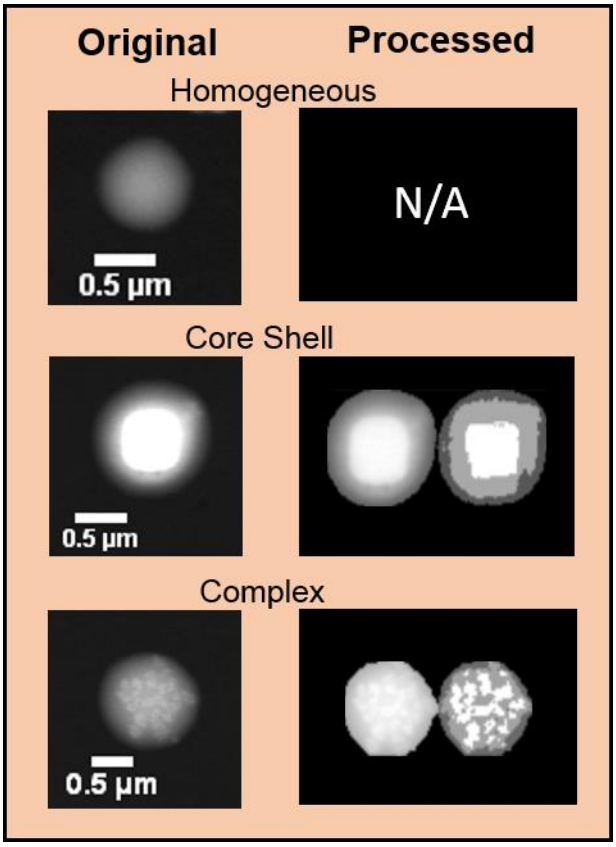

Figure 6.6. Image processing of example SEM images differentiates SOA-AS particles with homogeneous, core-shell, and complex structures and calculates outer and inner perimeter(s) for each particle analyzed.

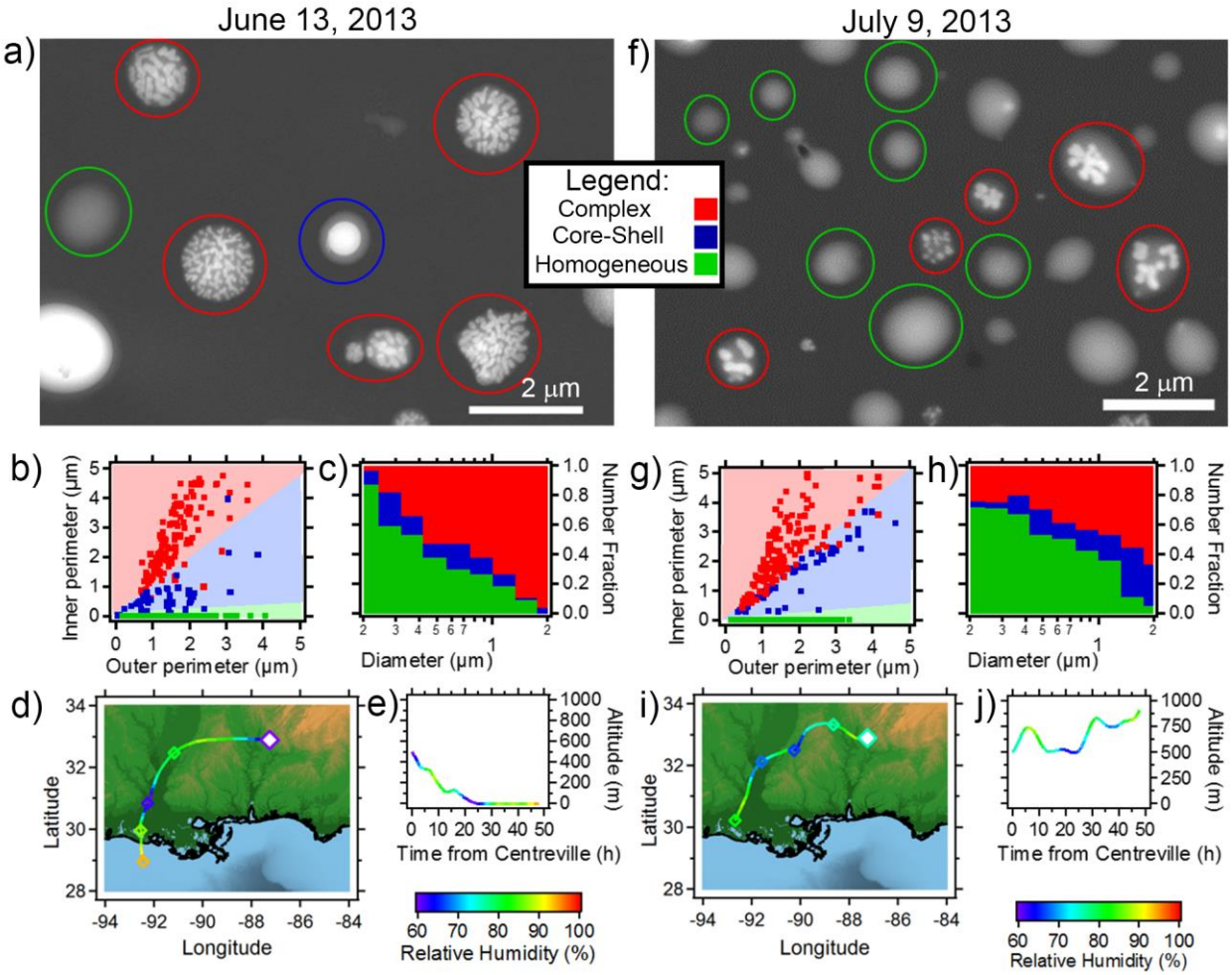

Figure 6.7. SOA-AS structure from two days during SOAS, June 13 and July 9, 2013. a) and f) SEM images with structures identified –complex (red), core-shell (blue) and homogeneous (green). b) and g) Particle inner perimeter versus outer perimeter was used for classification. c) and h) Size distributions of SOA-AS particles as a function of structure. The pie chart insets show SOA on June 13 (34 % homogeneous, 11 % core-shell, 55 % complex) and July 9 (51 % homogeneous, 14 % core-shell, 35 % complex). HYSPLIT backward air mass trajectories at 500 m on d) June 13, 2013 14:00 CST and i) July 9, 2013 18:00 CST (sample collection midpoints). The RH (%) is shown in the color scale where cooler colors represent lower RH and warmer colors represent higher RH values. e) and j) Altitude from HYSPLIT as a function of RH (color).

6.3.2. Effect of Particle Size on Structure Complexity

The relationship between particle size (volume equivalent diameter) and complexity is shown in Figures 6.7c,h for two days with differing $PM_{2.5}$ mass loadings of organic carbon (13 June 2013 – 2.9 μg/m^3 and 9 July 2013 – 1.7 μg/m^3). Because particles often spread upon impaction, volume equivalent diameters for SOA were calculated in this study by dividing the

projected area diameter obtained from SEM by a factor of 2. Accounting for particle spreading to represent diameters of particles before impaction, the number fraction of homogeneous particles is the highest at the smallest sizes measured in Figures 6.7c,h (~200 nm), similar to observations of laboratory-generated aerosol focused on core-shell and partially-engulfed morphologies (Veghte et al., 2013; Veghte et al., 2014). Furthermore, although core-shell particles are observed at all sizes, increasing numbers of complex particles are observed at the largest sizes. The size range where core-shell and complex particles are a large fraction of SOA-AS particles is where the surface area size distribution peaks (~300 nm during SOAS) (Seinfeld, 2006), which is a critical size for heterogeneous reactivity (Thornton and Abbatt, 2005; Ravishankara, 1997). In addition to variation in SOA-AS complexity as a function of size, the two case study days show differing relative abundances of complex particles, with much higher number fractions on June 13, 2013 (55 % complex, 34 % homogeneous) compared to July 9, 2013 (35 % complex, 51 % homogeneous), which is related to temperature and RH history, discussed below.

6.3.3. Temporal Variation of Structure Complexity

To determine whether the fraction of complex (and core-shell) particles observed in Figure 6.7 can be explained primarily by the RH lifetime experienced by aerosols, HYSPLIT backward air mass trajectories were run for June 13, 2013 and July 9, 2013. 48 hour HYSPLIT backward air mass trajectories (Draxler and Hess, 1997) at 500 m (with additional checks at other altitudes) showed slow moving air masses, barely reaching the Gulf of Mexico within 36 h, which is only 320 km from the sampling site (Figure 6.7d,i). The RH from the back trajectories was modelled for each sample, with the hourly average RH shown in color in Figures 6.7d,e,i,j as a function of time and air mass altitude. In both cases aerosols experienced a range of RH values (60-95 % and 63-89 %), varying temporally, across which LLPS has been observed to occur (Bertram et al., 2011; You et al., 2014; Song et al., 2012; Marcolli and Krieger, 2006; Ciobanu et al., 2009; Song et al., 2013; You et al., 2013). The RH values never decrease below the efflorescence RH (35 %) of ammonium sulfate (Ciobanu et al., 2010), and because the efflorescence RH is lower (or may be completely absent) for particles with a sufficient volume fraction of organic material (Smith et al., 2012; Smith et al., 2013), the aqueous phase is not expected to crystallize. However, the constant diurnal variation of RH alone, does not explain the

differences in SOA-AS structures observed. While the air mass on July 9, 2013 “cycled” RH more frequently, particles sampled from this air mass were less complex.

6.3.4. Temporal variation of structure complexity

To further explore the temporal variation of LLPS structure complexity and elucidate meteorological effects on SOA structure, the number fraction of particles with homogeneous, core-shell, and complex structures was evaluated for a single size cut (MOUDI, stage 7, aerodynamic diameter 50 % cut-point of 0.56 μm) (Marple et al., 1991) over a week period (Figure 6.8a). Relative number fractions of homogeneous (22 - 67 %), core-shell (0 – 65 %), and complex (0 – 46 %) particles all varied dramatically indicating that complex particles are frequently, but not always, a significant fraction of SOA-AS particles. To explain the variation in SOA-AS complexity observed, the phase state and glassy or viscous nature of SOA-AS at SOAS was investigated. As previous studies have shown that SOA-AS may adopt liquid, semisolid, and solid states (Kidd et al., 2014; You et al., 2014) under ambient conditions which could affect separation of inorganic and organic material, the phase state and role of liquid water are important to understand in order to predict organic aerosol mass in the southeastern U.S. (Pye et al., 2017).

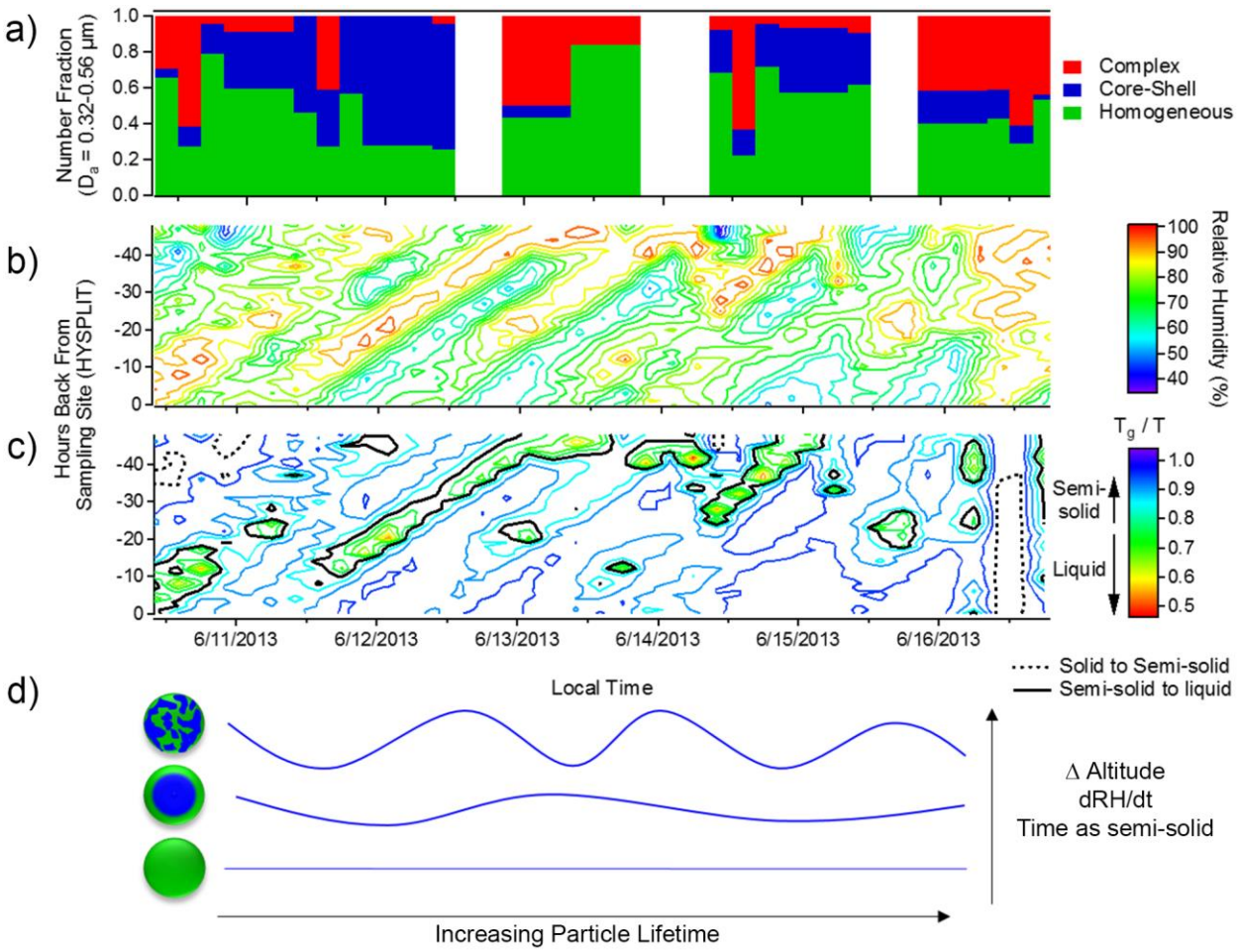

Figure 6.8. a) Week-long time series of SOA-AS particle complexity during SOAS. b) RH experienced by particle air masses and c) inverse ambient temperature (1/T) scaled by the RH-dependent glass transition temperature (T_g/T) modelled from HYSPLIT backward air mass trajectories. T_g/T is an indicator of the particle phase state—$T_g/T \geq 1$, solid; $0.8 < T_g/T < 1$, semi-solid; $T_g/T \leq 0.8$, liquid. d) Schematic of SOA-AS particle structure as a function of particle lifetime, altitude, particle drying rate, RH, and temperature.

6.3.5. Effect of T_g on SOA-AS structure complexity

To investigate particle phase states, the RH-dependent glass transition temperature (T_g) was used to estimate whether particles were liquids, solids, or semi-solids (Dette and Koop, 2015; Koop et al., 2011). Figure 6.8b shows the HYSPLIT-modelled RH experienced by particle air masses and Figure 6.8c shows the T_g calculated from HYSPLIT backward air mass trajectories from June 10, 2013 through June 16, 2013. When the ambient temperature is below T_g ($T_g/T \geq 1$), a particle behaves as a solid and kinetic limitations occur. In contrast, when $T_g/T <$

1, a particle exists as a semisolid ($0.8 < T_g/T < 1$) or a liquid ($T_g/T \leq 0.8$) (Shiraiwa et al., 2017). T_g of aerosol particles is affected by both water content (RH) and temperature (Wang et al., 2012). As water acts as a plasticizer, decreasing the viscosity of the organic material (Koop et al., 2011), we hypothesize that the initial loss of water causes a LLPS below the T_g of the organic material, resulting in a viscous organic phase surrounding an aqueous ammonium sulfate core. As the RH increases again leading to temperatures above the T_g of the organic material, the organic material can flow and begin to mix, but does not fully mix before the RH drops again due to its diurnal cycle. When the next cycle begins, the flow is again random, and insufficient for full mixing to a core-shell or homogeneous morphology (Figure 6.8d).

While previous laboratory studies have shown with simple model systems that an increasing number of factors including particle size, chemical composition, drying rate, and RH affect LLPS (Altaf and Freedman, 2017; Losey et al., 2016; Veghte et al., 2013; Dette and Koop, 2015; Koop et al., 2011; Smith et al., 2013; You et al., 2013; You et al., 2012; You et al., 2014; O'Brien et al., 2015), our results suggest that additional factors affected the structure of ambient SOA-AS particles during SOAS. One additional factor that needs to be considered that could also affect LLPS structure is the amount of time organic material can freely flow as a liquid with low viscosity. Previous work in the laboratory by Wang et al. (2015) showed for organic-inorganic particles of NaCl with secondary organic carbon from ozonolysis of limonene and α-pinene that the extent of reaction of secondary organic carbon with NaCl was influenced by the phase state and viscosity, temperature, and RH with more complex structures observed for particles in a liquid-like state for longer periods of time prior to dehydration. As ambient particles in the current work collected on June 13, 2013 during SOAS experienced more time above the estimated separation RH (SRH, 84 %) (Song et al., 2012) and with a liquid-like organic component (T_g ~308 K, estimated T_g during SOAS) (Shiraiwa et al., 2017) than on July 9, 2013 and exhibited more complex structures, these results suggests that the time spent in a liquid-like state could also have significant effects on SOA internal structure.

6.4. Conclusion

This work shows that in addition to homogeneous and core-shell morphologies, ambient SOA/inorganic aerosol particles frequently adopt complex internal morphologies. These structures vary as a function of size, with homogeneous particles present at the smallest sizes and

complex particles dominating at larger sizes. Additionally, the fraction of complex, core-shell, and homogeneous particles is not constant, but varies over time as a function of temperature, RH, and length of time the organic material spends as a liquid versus a glassy solid. These internal structures could affect the reactive uptake of important gas-phase species and influence the ice nucleation properties of particles. Thus, if each type of particle (homogeneous - no effect, core-shell – inhibitory, and complex – unknown) has a different effect on heterogeneous uptake and ice nucleation properties, a method needs to be derived that can be parameterized for inclusion in models.

6.5. Acknowledgements

Funding was provided by the National Science Foundation CAREER grant to A.P.A. (CHE-1654149) and the University of Michigan (startup funds). CCSEM was performed at the Environmental Molecular Sciences Laboratory (EMSL), a science user facility located at Pacific Northwest National Laboratory (PNNL), sponsored by the Office of Biological and Environmental Research. PNNL is operated for the U.S Department of Energy by Battelle Memorial Institute under contract number DE-AC06-76RL0 1830. Travel funds to PNNL were provided by UM Rackham Graduate School and the UM Office of the Provost. The Michigan Center for Materials Characterization (MC^2) is acknowledged for manual SEM-EDX of additional samples from SOAS. We thank Steven Bertman (Western Michigan University), Paul Shepson (Purdue University), and Kerri Pratt (University of Michigan) for their assistance with sampling design and funding for SOAS sampling through EPA grant R835409. Additionally, we thank Annmarie Carlton (Rutgers University, now UC-Irvine), Lindsay Yee (UC-Berkeley), Jason Surratt (UNC-Chapel Hill), and Allen Goldstein (UC Berkeley) for organizing SOAS and the filter sampling effort, as well as Karsten Baumann and others for logistical assistance. Finally, we thank Nga Lee (Georgia Tech) and Jason Surratt for collecting ambient and chamber-generated particles, shown for comparison in this work.

Chapter 6 is in preparation for submission to *Nature Geosciences:* Amy L. Bondy, Sydney L. Niles, Peter K. Peterson, Josie L. Little, Rashad C. Pace, Ryan C. Moffet, Rachel O'Brien, Bingbing Wang, Alexander Laskin, Manelisi V. Nhliziyo, Andrew P. Ault. Aerosol Internal Structure is Determined by Atmospheric Lifetime and Relative Humidity History.

6.6. References

Altaf, M. B., and Freedman, M. A.: Effect of Drying Rate on Aerosol Particle Morphology, The Journal of Physical Chemistry Letters, 10.1021/acs.jpclett.7b01327, 3613-3618, 2017.

Bateman, A. P., Bertram, A. K., and Martin, S. T.: Hygroscopic influence on the semisolid-to-liquid transition of secondary organic materials, J. Phys. Chem. A, 119, 4386-4395, 2015.

Bertram, A. K., Martin, S. T., Hanna, S. J., Smith, M. L., Bodsworth, A., Chen, Q., Kuwata, M., Liu, A., You, Y., and Zorn, S. R.: Predicting the relative humidities of liquid-liquid phase separation, efflorescence, and deliquescence of mixed particles of ammonium sulfate, organic material, and water using the organic-to-sulfate mass ratio of the particle and the oxygen-to-carbon elemental ratio of the organic component, Atmos. Chem. Phys., 11, 10995-11006, 2011.

Bondy, A. L., Wang, B., Laskin, A., Craig, R. L., Nhliziyo, M. V., Bertman, S. B., Pratt, K. A., Shepson, P. B., and Ault, A. P.: Inland sea spray aerosol transport and incomplete chloride depletion: Varying degrees of reactive processing observed during SOAS, Environ. Sci. Technol., 51, 9533-9542, 2017.

Brock, C. A., Wagner, N. L., Anderson, B. E., Attwood, A. R., Beyersdorf, A., Campuzano-Jost, P., Carlton, A. G., Day, D. A., Diskin, G. S., Gordon, T. D., Jimenez, J. L., Lack, D. A., Liao, J., Markovic, M. Z., Middlebrook, A. M., Ng, N. L., Perring, A. E., Richardson, M. S., Schwarz, J. P., Washenfelder, R. A., Welti, A., Xu, L., Ziemba, L. D., and Murphy, D. M.: Aerosol optical properties in the southeastern United States in summer – Part 1: Hygroscopic growth, Atmos. Chem. Phys. Discuss., 2015, 25695-25738, 2015.

Budisulistiorini, S. H., Li, X., Bairai, S. T., Renfro, J., Liu, Y., Liu, Y. J., McKinney, K. A., Martin, S. T., McNeill, V. F., Pye, H. O. T., Nenes, A., Neff, M. E., Stone, E. A., Mueller, S., Knote, C., Shaw, S. L., Zhang, Z., Gold, A., and Surratt, J. D.: Examining the effects of anthropogenic emissions on isoprene-derived secondary organic aerosol formation during the 2013 Southern Oxidant and Aerosol Study (SOAS) at the Look Rock, Tennessee ground site, Atmos. Chem. Phys., 15, 8871-8888, 2015.

Cerully, K. M., Bougiatioti, A., Hite Jr, J. R., Guo, H., Xu, L., Ng, N. L., Weber, R., and Nenes, A.: On the link between hygroscopicity, volatility, and oxidation state of ambient and water-soluble aerosols in the southeastern United States, Atmos. Chem. Phys., 15, 8679-8694, 2015.

Ciobanu, V. G., Marcolli, C., Krieger, U. K., Weers, U., and Peter, T.: Liquid-liquid phase separation in mixed organic/inorganic aerosol particles, J. Phys. Chem. A, 113, 10966-10978, 2009.

Ciobanu, V. G., Marcolli, C., Krieger, U. K., Zuend, A., and Peter, T.: Efflorescence of ammonium sulfate and coated ammonium sulfate particles: evidence for surface nucleation, J. Phys. Chem. A, 114, 9486-9495, 2010.

Dette, H. P., and Koop, T.: Glass formation processes in mixed inorganic/organic aerosol particles, J. Phys. Chem. A, 119, 4552-4561, 2015.

Draxler, R. R., and Hess, G.: Description of the HYSPLIT4 modeling system, 1997.

Fraund, M., Pham, D., Bonanno, D., Harder, T., Wang, B., Brito, J., de Sá, S., Carbone, S., China, S., Artaxo, P., Martin, S., Pöhlker, C., Andreae, M., Laskin, A., Gilles, M., and Moffet,

R.: Elemental mixing state of aerosol particles collected in Central Amazonia during GoAmazon2014/15, Atmosphere, 8, 173, 2017.

Glasius, M., and Goldstein, A. H.: Recent discoveries and future challenges in atmospheric organic chemistry, Environ. Sci. Technol., 50, 2754-2764, 2016.

Guo, H., Xu, L., Bougiatioti, A., Cerully, K. M., Capps, S. L., Hite, J. R., Jr., Carlton, A. G., Lee, S. H., Bergin, M. H., Ng, N. L., Nenes, A., and Weber, R. J.: Fine-particle water and pH in the southeastern United States, Atmos. Chem. Phys., 15, 5211-5228, 2015.

Hallquist, M., Wenger, J. C., Baltensperger, U., Rudich, Y., Simpson, D., Claeys, M., Dommen, J., Donahue, N. M., George, C., Goldstein, A. H., Hamilton, J. F., Herrmann, H., Hoffmann, T., Iinuma, Y., Jang, M., Jenkin, M. E., Jimenez, J. L., Kiendler-Scharr, A., Maenhaut, W., McFiggans, G., Mentel, T. F., Monod, A., Prévôt, A. S. H., Seinfeld, J. H., Surratt, J. D., Szmigielski, R., and Wildt, J.: The formation, properties and impact of secondary organic aerosol: current and emerging issues, Atmos. Chem. Phys., 9, 5155-5236, 2009.

Hopkins, R. J., Desyaterik, Y., Tivanski, A. V., Zaveri, R. A., Berkowitz, C. M., Tyliszczak, T., Gilles, M. K., and Laskin, A.: Chemical speciation of sulfur in marine cloud droplets and particles: Analysis of individual particles from the marine boundary layer over the California current, J. Geophys. Res.: Atmos., 113, 2008.

Hosny, N. A., Fitzgerald, C., Vysniauskas, A., Athanasiadis, A., Berkemeier, T., Uygur, N., Poschl, U., Shiraiwa, M., Kalberer, M., Pope, F. D., and Kuimova, M. K.: Direct imaging of changes in aerosol particle viscosity upon hydration and chemical aging, Chemical Science, 7, 1357-1367, 2016.

Jacobson, M. C., Hansson, H. C., Noone, K. J., and Charlson, R. J.: Organic atmospheric aerosols: review and state of the science, Rev. Geophys., 38, 267-294, 2000.

Kidd, C., Perraud, V., Wingen, L. M., and Finlayson-Pitts, B. J.: Integrating phase and composition of secondary organic aerosol from the ozonolysis of α-pinene, Proc. Natl. Acad. Sci., 111, 7552-7557, 2014.

Kilcoyne, A. L. D., Tyliszczak, T., Steele, W. F., Fakra, S., Hitchcock, P., Franck, K., Anderson, E., Harteneck, B., Rightor, E. G., Mitchell, G. E., Hitchcock, A. P., Yang, L., Warwick, T., and Ade, H.: Interferometer-controlled scanning transmission X-ray microscopes at the Advanced Light Source, Journal of Synchrotron Radiation, 10, 125-136, 2003.

Koop, T., Bookhold, J., Shiraiwa, M., and Poeschl, U.: Glass transition and phase state of organic compounds: Dependency on molecular properties and implications for secondary organic aerosols in the atmosphere, PCCP, 13, 19238-19255, 2011.

Laskin, A., Cowin, J. P., and Iedema, M. J.: Analysis of individual environmental particles using modern methods of electron microscopy and X-ray microanalysis, J. Electron. Spectrosc. Relat. Phenom., 150, 260-274, 2006.

Losey, D. J., Parker, R. G., and Freedman, M. A.: pH Dependence of Liquid–Liquid Phase Separation in Organic Aerosol, The Journal of Physical Chemistry Letters, 7, 3861-3865, 2016.

Marcolli, C., and Krieger, U. K.: Phase changes during hygroscopic cycles of mixed organic/inorganic model systems of tropospheric aerosols, J. Phys. Chem. A, 110, 1881-1893, 2006.

Marple, V. A., Rubow, K. L., and Behm, S. M.: A microorifice uniform deposit impactor (MOUDI)-description, calibration and use, Aerosol Sci. Technol., 14, 434-446, 1991.

McNeill, V. F., Patterson, J., Wolfe, G. M., and Thornton, J. A.: The effect of varying levels of surfactant on the reactive uptake of N_2O_5 to aqueous aerosol, Atmos. Chem. Phys., 6, 1635-1644, 2006.

McNeill, V. F.: Aqueous organic chemistry in the atmosphere: Sources and chemical processing of organic aerosols, Environ. Sci. Technol., 10.1021/es5043707, 2015.

Moffet, R. C., Henn, T., Laskin, A., and Gilles, M. K.: Automated chemical analysis of internally mixed aerosol particles using X-ray spectromicroscopy at the carbon K-edge, Anal. Chem., 82, 7906-7914, 2010.

O'Brien, R. E., Wang, B. B., Kelly, S. T., Lundt, N., You, Y., Bertram, A. K., Leone, S. R., Laskin, A., and Gilles, M. K.: Liquid-liquid phase separation in aerosol particles: Imaging at the nanometer scale, Environ. Sci. Technol., 49, 4995-5002, 2015.

Otsu, N.: Threshold selection method from gray-level histograms, Ieee Transactions on Systems Man and Cybernetics, 9, 62-66, 1979.

Pajunoja, A., Hu, W., Leong, Y. J., Taylor, N. F., Miettinen, P., Palm, B. B., Mikkonen, S., Collins, D. R., Jimenez, J. L., and Virtanen, A.: Phase state of ambient aerosol linked with water uptake and chemical aging in the southeastern US, Atmos. Chem. Phys., 16, 11163-11176, 2016.

Pye, H. O. T., Murphy, B. N., Xu, L., Ng, N. L., Carlton, A. G., Guo, H. Y., Weber, R., Vasilakos, P., Appel, K. W., Budisulistiorini, S. H., Surratt, J. D., Nenes, A., Hu, W. W., Jimenez, J. L., Isaacman-VanWertz, G., Misztal, P. K., and Goldstein, A. H.: On the implications of aerosol liquid water and phase separation for organic aerosol mass, Atmos. Chem. Phys., 17, 343-369, 2017.

Rachel E. O'Brien, B. W., Stephen T. Kelly, Nils LUndt, Yuan You, Allan K. Bertram, Stephen R. Leone, Alexander Laskin, Mary K. Gilles: Liquid-liquid phase separation in Aerosol Particles: Imaging at the Nanometer Scale, Environ. Sci. Technol., 10.1021, 2015.

Ravishankara, A. R.: Heterogeneous and multiphase chemistry in the troposphere, Science, 276, 1058-1065, 1997.

Reid, J. P., Dennis-Smither, B. J., Kwamena, N.-O. A., Miles, R. E. H., Hanford, K. L., and Homer, C. J.: The morphology of aerosol particles consisting of hydrophobic and hydrophilic phases: hydrocarbons, alcohols and fatty acids as the hydrophobic component, PCCP, 13, 15559-15572, 2011.

Rothfuss, N. E., and Petters, M. D.: Influence of functional groups on the viscosity of organic aerosol, Environ. Sci. Technol., 10.1021/acs.est.6b04478, 2016.

Rothfuss, N. E., and Petters, M. D.: Characterization of the temperature and humidity-dependent phase diagram of amorphous nanoscale organic aerosols, PCCP, 19, 6532-6545, 2017.

Schill, G. P., and Tolbert, M. A.: Heterogeneous ice nucleation on phase-separated organic-sulfate particles: effect of liquid vs. glassy coatings, Atmos. Chem. Phys., 13, 4681-4695, 2013.

Seinfeld, J. H. P., S. N.: Atmospheric Chemistry and Physics: From Air Pollution to Climate Change, 2nd ed. ed., Wiley, New York, 2006.

Shilling, J. E., Chen, Q., King, S. M., Rosenoern, T., Kroll, J. H., Worsnop, D. R., McKinney, K. A., and Martin, S. T.: Particle mass yield in secondary organic aerosol formed by the dark ozonolysis of α-pinene, Atmos. Chem. Phys., 8, 2073-2088, 2008.

Shiraiwa, M., Li, Y., Tsimpidi, A. P., Karydis, V. A., Berkemeier, T., Pandis, S. N., Lelieveld, J., Koop, T., and Pöschl, U.: Global distribution of particle phase state in atmospheric secondary organic aerosols, Nature Communications, 8, 15002, 2017.

Smith, M. L., Bertram, A. K., and Martin, S. T.: Deliquescence, efflorescence, and phase miscibility of mixed particles of ammonium sulfate and isoprene-derived secondary organic material, Atmos. Chem. Phys., 12, 9613-9628, 2012.

Smith, M. L., You, Y., Kuwata, M., Bertram, A. K., and Martin, S. T.: Phase transitions and phase miscibility of mixed particles of ammonium sulfate, toluene-derived secondary organic material, and water, J. Phys. Chem. A, 117, 8895-8906, 2013.

Song, M., Marcolli, C., Krieger, U. K., Zuend, A., and Peter, T.: Liquid-liquid phase separation in aerosol particles: Dependence on O:C, organic functionalities, and compositional complexity, Geophys. Res. Lett., 39, 2012.

Song, M., Marcolli, C., Krieger, U. K., Lienhard, D. M., and Peter, T.: Morphologies of mixed organic/inorganic/aqueous aerosol droplets, Faraday Discuss., 165, 289-316, 2013.

Song, M., Liu, P. F., Hanna, S. J., Li, Y. J., Martin, S. T., and Bertram, A. K.: Relative humidity-dependent viscosities of isoprene-derived secondary organic material and atmospheric implications for isoprene-dominant forests, Atmos. Chem. Phys., 15, 5145-5159, 2015.

Song, Y. C., Haddrell, A. E., Bzdek, B. R., Reid, J. P., Bannan, T., Topping, D. O., Percival, C., and Cai, C.: Measurements and predictions of binary component aerosol particle viscosity, J. Phys. Chem. A, 120, 8123-8137, 2016.

Thornton, J. A., and Abbatt, J. P. D.: N_2O_5 reaction on submicron sea salt aerosol: kinetics, products, and the effect of surface active organics, J. Phys. Chem. A, 109, 10004-10012, 2005.

Veghte, D. P., Altaf, M. B., and Freedman, M. A.: Size dependence of the structure of organic aerosol, J. Am. Chem. Soc., 135, 16046-16049, 2013.

Veghte, D. P., Bittner, D. R., and Freedman, M. A.: Cryo-transmission electron microscopy imaging of the morphology of submicrometer aerosol containing organic acids and ammonium sulfate, Anal. Chem., 86, 2436-2442, 2014.

Wang, B., Lambe, A. T., Massoli, P., Onasch, T. B., Davidovits, P., Worsnop, D. R., and Knopf, D. A.: The deposition ice nucleation and immersion freezing potential of amorphous secondary organic aerosol: Pathways for ice and mixed-phase cloud formation, J. Geophys. Res.: Atmos., 117, 2012.

Wang, B., O'Brien, R. E., Kelly, S. T., Shilling, J. E., Moffet, R. C., Gilles, M. K., and Laskin, A.: Reactivity of liquid and semisolid secondary organic carbon with chloride and nitrate in atmospheric aerosols, J. Phys. Chem. A, 119, 4498-4508, 2015.

Xu, L., Guo, H., Boyd, C. M., Klein, M., Bougiatioti, A., Cerully, K. M., Hite, J. R., Isaacman-VanWertz, G., Kreisberg, N. M., Knote, C., Olson, K., Koss, A., Goldstein, A. H., Hering, S. V., de Gouw, J., Baumann, K., Lee, S.-H., Nenes, A., Weber, R. J., and Ng, N. L.: Effects of

anthropogenic emissions on aerosol formation from isoprene and monoterpenes in the southeastern United States, Proc. Natl. Acad. Sci., 112, 37-42, 2015.

You, Y., Renbaum-Wolff, L., Carreras-Sospedra, M., Hanna, S. J., Hiranuma, N., Kamal, S., Smith, M. L., Zhang, X., Weber, R. J., Shilling, J. E., Dabdub, D., Martin, S. T., and Bertram, A. K.: Images reveal that atmospheric particles can undergo liquid-liquid phase separations, Proc. Natl. Acad. Sci. U. S. A., 109, 13188-13193, 2012.

You, Y., Renbaum-Wolff, L., and Bertram, A. K.: Liquid-liquid phase separation in particles containing organics mixed with ammonium sulfate, ammonium bisulfate, ammonium nitrate or sodium chloride, Atmos. Chem. Phys., 13, 11723-11734, 2013.

You, Y., Smith, M. L., Song, M., Martin, S. T., and Bertram, A. K.: Liquid-liquid phase separation in atmospherically relevant particles consisting of organic species and inorganic salts, Int. Rev. Phys. Chem., 33, 43-77, 2014.

Zelenay, V., Huthwelker, T., Krepelova, A., Rudich, Y., and Ammann, M.: Humidity driven nanoscale chemical separation in complex organic matter, Environ. Chem., 8, 450-460, 2011.

Zuend, A., and Seinfeld, J. H.: Modeling the gas-particle partitioning of secondary organic aerosol: the importance of liquid-liquid phase separation, Atmos. Chem. Phys., 12, 3857-3882, 2012.

Chapter 7.
Conclusions and Future Directions

7.1. Conclusions

Understanding single particle chemical composition and mixing state of aerosol particles generated from a variety of sources is critical for determining the effect of these particles on climate and human health. This dissertation has focused on the development and use of single particle microscopic and spectroscopic methods to study the chemical composition of fresh and aged primary and secondary atmospheric aerosols, particularly in the southeastern United States. During SOAS in 2013, electron microscopy was used to identify classes of particles aside from SOA present at the rural, forested sampling site in Centreville, Alabama. Additionally, the degree of chemical mixing was calculated during time periods influenced by specific particle classes using diversity measures developed for aerosol populations by Riemer and West (2013). One particular class, SSA, was studied in further detail as it was found to contribute significantly to aerosol number concentrations at Centreville during two events with varying degrees of reactivity. In addition to SSA observed at Centreville, an important class of compounds present in organic aerosol in the southeastern United States is isoprene-derived organosulfates. As these compounds are ubiquitous, Raman microspectroscopy and DFT calculations were used to determine a spectral fingerprint for organosulfates, allowing identification within individual particles from SOAS. Though electron microscopy and Raman microspectroscopy are valuable techniques for analyzing the size, morphology, and chemical composition of individual particles, a new method, AFM-IR, was applied to the analysis of aerosol particles for the first time in this work, allowing physicochemical characterization of submicron particles in particular. Using AFM-IR in addition to electron microscopy and STXM-NEXAFS, the physicochemical mixing state of liquid-liquid phase separated SOA was investigated, illustrating the separation of organic and inorganic material is dependent on aerosol lifetime, as well as temperature and relative humidity history. These findings have strengthened our understanding of the physicochemical mixing state of aerosol particles and provided motivation for additional future studies.

Chapter 2 discussed the chemical mixing state of primary and secondary particles both generated and transported from regional sources during the summer 2013 SOAS field campaign. Particles that were dominated by secondary organic aerosol (SOA) mixed with inorganic salts, such as ammonium sulfate, were the majority of particles by number fraction from 0.2-5 microns with an average of ~65 % SOA at submicron sizes. However, important contributions by other particle classes such as SSA, mineral dust, primary biological particles, fly ash, and biomass burning aerosol led to more external mixing and distinct chemical compositions per class, particularly at sizes below one micron. In addition to temporal variability of particle classes, secondary processing of particles by NO_x and SO_2 led to heterogeneity within particle classes. To quantify population diversity during periods with significant influence from SSA and dust, mixing state indices were calculated from mass estimates of the aerosol elemental components, determined using CCSEM-EDX. The mixing state indices for supermicron particles were generally the highest (χ = 19 %, 15 %, and 11 % during SSA, dust, and SOA periods, respectively), signifying that supermicron particles were less diverse than submicron particles. The mixing state index for accumulation mode particles during the SOA period was comparable (χ = 10 %), suggesting that submicron particles were more internally mixed during this time period compared to the dust and SSA periods.

Chapter 3 delved further into one particular class of particles, SSA, collected during SOAS at a site > 320 km from the Gulf of Mexico. SSA was observed in 93% of 42 time periods analyzed. During two marine air mass periods, SSA represented significant number fractions of particles in the accumulation (0.2-1.0 μm, 11 %) and coarse (1.0-10.0 μm, 35 %) modes. Chloride content of SSA particles ranged from fully to partially depleted, with 24 % of SSA particles containing chloride (mole fraction of Cl/Na $\geq$ 0.1, 90 % chloride depletion). Both the frequent observation of SSA at an inland site and the range of chloride depletion observed, suggest that SSA may represent an underappreciated inland sink for NO_x/SO_2 and source of halogen gases.

Chapter 4 further develops our understanding of the basic molecular structure and spectroscopic properties of isoprene-derived organosulfates, a significant component of SOA. Raman microspectroscopy and density functional theory (DFT) at the CAM-B3LYP level of theory were combined to analyze the vibrational modes and molecular structure of key organosulfates, 3-methyltetrol sulfate esters (two isomers) and 2-methylglyceric acid sulfate

ester, as well as hydrolysis products, 2-methyltetrols and 2-methylglyceric acid. Two intense vibrational modes were identified, ν(RO-SO_3) (846 ± 4 cm^{-1}) and $\nu_s(SO_3)$ (1065 ± 2 cm^{-1}), as well as a lower intensity $\delta(SO_3)$ mode (586 ± 2 cm^{-1}). For 2-methylglyceric acid and its sulfate ester, deprotonation of the carboxylic acid group above the pK_a (3.5) decreased the carbonyl stretch (1724 cm^{-1}) and increased carboxylate modes $\nu_s(COO^-)$ and $\nu_a(COO^-)$ at 1594 and 1413 cm^{-1}, respectively. The ν(RO-SO_3) and $\nu_s(SO_3)$ modes were observed in individual atmospheric particles and can be used in future studies of complex SOA mixtures to distinguish organosulfates from inorganic sulfate or hydrolysis products.

In Chapter 5, we showed the first application of AFM-IR to detect trace organic and inorganic species and probe intraparticle chemical variation in individual particles down to 150 nm. By detecting photothermal expansion at frequencies where particle species absorb IR photons from a tunable laser, AFM-IR provided vibrational spectroscopy information about particles smaller than the optical diffraction limit. Combining strengths of AFM (ambient pressure, height, morphology, and phase measurements) with photothermal IR spectroscopy, the potential of AFM-IR was shown for a diverse set of single-component particles, liquid-liquid phase separated particles (core-shell morphology), and ambient atmospheric particles. The spectra from atmospheric model systems (ammonium sulfate, sodium nitrate, succinic acid, and sucrose) had clearly identifiable features that correlated with absorption frequencies for infrared-active modes. Additionally, molecular information was obtained with < 100 nm spatial resolution for phase separated particles with a ~150 nm shell and 300 nm core. The sub-diffraction limit capability of AFM-IR has the potential to advance understanding of particle impacts on climate and health by improving analytical capabilities to study water uptake, heterogeneous reactivity, and viscosity.

Chapter 6 discussed the morphology and structure of ambient SOA during SOAS. As previous work has indicated that SOA are frequently present in a glassy state in the atmosphere, not the well-mixed aqueous conditions parameterized in models, measurements are needed to improve our understanding of structure and better model particle properties. Ambient SOA-inorganic particles observed in a remote, isoprene-rich site, had liquid-liquid phase separation with a range of internal structures, including core-shell and more complex internal morphologies. Complex structures were frequently observed and determined to be dependent on aerosol lifetime and RH and temperature history often with complex internal structures, which has important

implications for heterogeneous reactions and SOA formation. The presence of complex organic-inorganic structures challenges the traditional picture of aqueous SOA particles, indicating a more detailed picture of SOA structure may be needed to accurately predict atmospheric SOA concentrations.

7.2. Future Directions

The research experiences described in this dissertation provide insight into the chemical mixing state of aerosol particles using existing single particle microscopy and spectroscopy methods, though the results have led to further questions that can be investigated. In Chapter 2, our mixing state indices from SOAS derived from CCSEM-EDX mass fractions were significantly lower than previous studies which used both CCSEM-EDX and STXM-NEXAFS to quantify mixing state (O'Brien et al., 2015; Fraund et al., 2017). Though our method differs from the previous CCSEM-EDX analyses in that we quantify the mass fraction of sulfur due to aging rather than the mass fraction of each individual element (since particle classes such as SSA and dust contain inherently more elements than SOA, regardless of aging), our analysis omits carbon, nitrogen, and oxygen due to quantitation limitations. Additional STXM-NEXAFS analysis of particles from SOAS and mixing state indices calculated from these results would allow a more direct comparison of our method to previous studies. Furthermore, instead of using solely sulfur as a metric of aging, aging due to organic carbon can also be quantified, leading to more accurate mixing state results as significant aging by secondary organic carbon is expected at this rural, forested site.

In Chapter 3, our single particle characterization of particles from SOAS detected large number fractions of SSA at this inland location during distinct events. Furthermore, SSA with varying degrees of chloride depletion were observed within particles, with partially-aged SSA potentially serving as an inland sink for NO_x and source of oxidants. As few single particle methods capable of identifying aged and partially aged SSA have been utilized at inland locations, additional single particle studies are needed to determine whether partially-aged SSA are prevalent elsewhere. In particular, studies $\geq$ 300 km from the coast (comparable to Centreville which is ~320 km from the Gulf of Mexico) would be interesting to determine how far inland partially-aged SSA can be transported before complete reaction occurs, as Chapter 3 was the first single particle study that analyzed SSA so far inland.

The identification of a Raman fingerprint for isoprene organosulfates and the application of AFM-IR to aerosol particles in Chapters 4 and 5 provide the foundation for numerous research projects utilizing these methods to analyze ambient and chamber-generated aerosols. Using the Raman organosulfate fingerprint modes identified in Chapter 4, future work could involve a thorough analysis of organosulfates within single particles from SOAS. As our study only examined a few ambient particles to demonstrate the capability of the method, extensive analysis of the dataset and collection of additional Raman spectra would be useful to determine the number fraction of particles containing organosulfates at this isoprene-rich site. This dataset could be compared to mass spectrometry organosulfate mass fractions measured during SOAS (Budisulistiorini et al., 2015; Boone et al., 2015; Hu et al., 2015; Hettiyadura et al., 2015; Riva et al., 2016; Budisulistiorini et al., 2017; Rattanavaraha et al., 2016), linking organosulfate mass and number concentrations to better understand organosulfate abundance in the southeastern U.S. Furthermore, these organosulfate number fraction results could be compared to previous single particle mass spectrometry studies by Hatch et al. (2011a, b) to understand the prevalence of organosulfates at a rural location (Centreville, SOAS) compared to an urban site (Atlanta). Work is ongoing in our lab to further characterize the Raman modes of additional organosulfates from standards and chamber studies, as dialkyl sulfates may also be an important component within organic aerosol in the southeastern U.S.

While the application of AFM-IR to aerosol particles described in Chapter 5 successfully characterized a range of organic and inorganic particles and studied the effect of substrate on AFM image and IR signal, further characterization of standards would be useful to understand the diameter/height of particles necessary for sufficient IR signal intensity. A simple and interesting experiment could involve impacting various size poly styrene latex spheres or size selecting ammonium sulfate particles of varying diameters on substrates and collecting AFM images and IR spectra for particles of decreasing size. The IR signal intensity could then be examined as both a function of particle diameter and height, allowing the IR limit of detection to be determined for a simple system. In addition to this systematic analysis of standards, AFM-IR characterization of submicron ambient particles from SOAS would be interesting, as it would provide detailed molecular information for individual particles near the mode of the atmospheric number size distribution. A key starting place would be analyzing particle sizes that overlap with particles analyzed by Raman, comparing the two techniques. Additionally, characterizing

particles near the IR detection limit would allow for vibrational analysis of the complete size range of particles from SOAS. Particular vibrational modes of interest would include organosulfate modes, using previous IR studies of small molecule organosulfates to identify these frequencies.

The analysis and discussion of organic-inorganic SOA internal structure in Chapter 6 leaves open many possibilities to improve the automated image processing method and confirm the presented hypotheses through laboratory experiments. One way to improve the Matlab script for differentiating homogeneous, core-shell, and complex SOA to minimize false identification (i.e. script classifies complex or core-shell particle as homogeneous and does not trace inner perimeter) is to develop a machine learning algorithm based on a hand-sorted data set. This would reduce the time involved hand-sorting particles into each respective class, and would reduce the false identification rate, which currently necessitates modification of the script threshold so that inner perimeters are calculated for all complex and core-shell particles. In addition to modification of the image processing method, additional analysis of the ambient particles would be useful to improve our understanding of the liquid-liquid phase separation properties. An additional step would involve collecting AFM phase images of homogeneous, core-shell, and complex particles at ambient pressure, determining whether differences in properties between the inorganic and organic components (i.e. differences in viscosity) result in images similar to those collected using SEM and STXM under vacuum. Finally, an additional experiment that would be difficult, but potentially very interesting would involve RH cycling using ambient SOA from SOAS. The number of RH cycles and length of time above the glass transition temperature would be studied to understand the length of time necessary in liquid-like state before dehydration, and the number of RH cycles needed to achieve changes in internal structure. For this experiment, samples composed of primarily homogeneous SOA from SOAS would undergo changes in RH to understand whether resulting changes in organic-inorganic internal structure support the hypotheses presented in Chapter 6.

This thesis sought to address limitations in the current understanding of the chemical composition and mixing state of primary and secondary aerosol particles through single particle microscopic and spectroscopic investigations. The five data chapters highlight the need for additional laboratory studies and studies of ambient particles at diverse locations to fully understand the mixing state of particles to better predict particle properties. Future work in the

field will continue to focus on quantifying chemical mixing state and connecting physicochemical composition to properties to minimize discrepancies between models and measurements.

7.3. References

Boone, E. J., Laskin, A., Laskin, J., Wirth, C., Shepson, P. B., Stirm, B. H., and Pratt, K. A.: Aqueous processing of atmospheric organic particles in cloud water collected via aircraft sampling, Environ. Sci. Technol., 49, 8523-8530, 2015.

Budisulistiorini, S. H., Li, X., Bairai, S. T., Renfro, J., Liu, Y., Liu, Y. J., McKinney, K. A., Martin, S. T., McNeill, V. F., Pye, H. O. T., Nenes, A., Neff, M. E., Stone, E. A., Mueller, S., Knote, C., Shaw, S. L., Zhang, Z., Gold, A., and Surratt, J. D.: Examining the effects of anthropogenic emissions on isoprene-derived secondary organic aerosol formation during the 2013 Southern Oxidant and Aerosol Study (SOAS) at the Look Rock, Tennessee ground site, Atmos. Chem. Phys., 15, 8871-8888, 2015.

Budisulistiorini, S. H., Nenes, A., Carlton, A. G., Surratt, J. D., McNeill, V. F., and Pye, H. O. T.: Simulating aqueous-phase isoprene-epoxydiol (IEPOX) secondary organic aerosol production during the 2013 Southern Oxidant and Aerosol Study (SOAS), Environ. Sci. Technol., 51, 5026-5034, 2017.

Fraund, M., Pham, D., Bonanno, D., Harder, T., Wang, B., Brito, J., de Sá, S., Carbone, S., China, S., Artaxo, P., Martin, S., Pöhlker, C., Andreae, M., Laskin, A., Gilles, M., and Moffet, R.: Elemental mixing state of aerosol particles collected in Central Amazonia during GoAmazon2014/15, Atmosphere, 8, 173, 2017.

Hatch, L. E., Creamean, J. M., Ault, A. P., Surratt, J. D., Chan, M. N., Seinfeld, J. H., Edgerton, E. S., Su, Y., and Prather, K. A.: Measurements of isoprene-derived organosulfates in ambient aerosols by aerosol time-of-flight mass spectrometry - part 1: Single particle atmospheric observations in Atlanta, Environ. Sci. Technol., 45, 5105-5111, 2011a.

Hatch, L. E., Creamean, J. M., Ault, A. P., Surratt, J. D., Chan, M. N., Seinfeld, J. H., Edgerton, E. S., Su, Y., and Prather, K. A.: Measurements of isoprene-derived organosulfates in ambient aerosols by aerosol time-of-flight mass spectrometry-part 2: Temporal variability and formation Mechanisms, Environ. Sci. Technol., 45, 8648-8655, 2011b.

Hettiyadura, A. P. S., Stone, E. A., Kundu, S., Baker, Z., Geddes, E., Richards, K., and Humphry, T.: Determination of atmospheric organosulfates using HILIC chromatography with MS detection, Atmos. Meas. Tech., 8, 2347-2358, 2015.

Hu, W. W., Campuzano-Jost, P., Palm, B. B., Day, D. A., Ortega, A. M., Hayes, P. L., Krechmer, J. E., Chen, Q., Kuwata, M., Liu, Y. J., de Sá, S. S., McKinney, K., Martin, S. T., Hu, M., Budisulistiorini, S. H., Riva, M., Surratt, J. D., St. Clair, J. M., Isaacman-Van Wertz, G., Yee, L. D., Goldstein, A. H., Carbone, S., Brito, J., Artaxo, P., de Gouw, J. A., Koss, A., Wisthaler, A., Mikoviny, T., Karl, T., Kaser, L., Jud, W., Hansel, A., Docherty, K. S., Alexander, M. L., Robinson, N. H., Coe, H., Allan, J. D., Canagaratna, M. R., Paulot, F., and Jimenez, J. L.: Characterization of a real-time tracer for isoprene epoxydiols-derived secondary organic aerosol (IEPOX-SOA) from aerosol mass spectrometer measurements, Atmos. Chem. Phys., 15, 11807-11833, 2015.

O'Brien, R. E., Wang, B., Laskin, A., Riemer, N., West, M., Zhang, Q., Sun, Y., Yu, X.-Y., Alpert, P., Knopf, D. A., Gilles, M. K., and Moffet, R. C.: Chemical imaging of ambient aerosol particles: Observational constraints on mixing state parameterization, J. Geophys. Res.: Atmos., 120, 9591-9605, 2015.

Rattanavaraha, W., Chu, K., Budisulistiorini, S. H., Riva, M., Lin, Y. H., Edgerton, E. S., Baumann, K., Shaw, S. L., Guo, H., King, L., Weber, R. J., Neff, M. E., Stone, E. A., Offenberg, J. H., Zhang, Z., Gold, A., and Surratt, J. D.: Assessing the impact of anthropogenic pollution on isoprene-derived secondary organic aerosol formation in $PM_{2.5}$ collected from the Birmingham, Alabama, ground site during the 2013 Southern Oxidant and Aerosol Study, Atmos. Chem. Phys., 16, 4897-4914, 2016.

Riemer, N., and West, M.: Quantifying aerosol mixing state with entropy and diversity measures, Atmos. Chem. Phys., 13, 11423-11439, 2013.

Riva, M., Budisulistiorini, S. H., Zhang, Z., Gold, A., and Surratt, J. D.: Chemical characterization of secondary organic aerosol constituents from isoprene ozonolysis in the presence of acidic aerosol, Atmos. Environ., 130, 5-13, 2016.

Appendix A.
Diverse Chemical Mixing State of Aerosol Particles at SOAS in the Southeastern United States Supplemental Information

A.1. SEARCH Network $PM_{2.5}$ and Meteorological Measurements

The SouthEastern Aerosol Research and Characterization Network (SEARCH) is a multi-pollutant network designed to address regulatory and scientific questions related to ozone and its precursors, particulate matter mass and composition, and atmospheric visibility in addition to other research concerns. Active since 1992, Centreville, AL is one of a handful of sites that is part of SEARCH. During SOAS, meteorological conditions including wind direction, wind speed, solar radiation, precipitation, and relative humidity were monitored from the SEARCH network, plotted in Figure A.1. The box green boxes overlaid on the meteorological data in Figure A.1 identify the two SOA-rich time periods analyzed in this study. Similarly, tan boxes indicate the dust-rich time periods and blue boxes the SSA-rich time periods which were analyzed in this study.

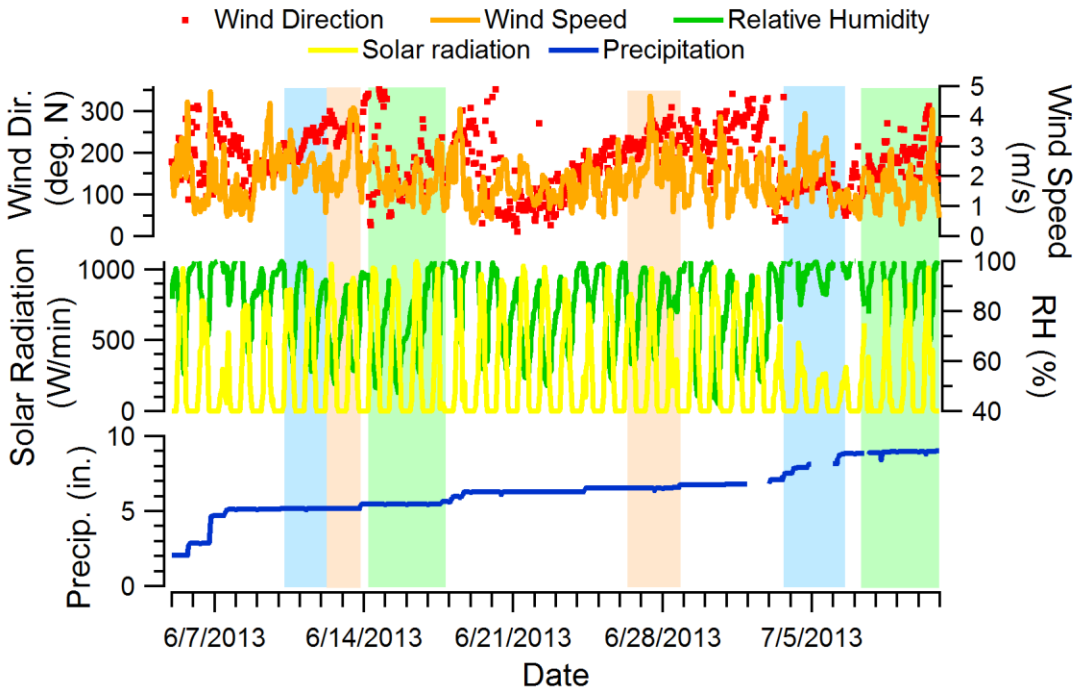

Figure A.1. SEARCH meteorological data for Centreville, AL during SOAS with green boxes overlaid for the two SOA-rich time periods, tan boxes for the dust-rich time periods, and blue boxes overlaid for the SSA-rich time periods.

A.2. CCSEM-EDX Analysis

SOAS intensive time periods, selected based on meteorological conditions, had shorter MOUDI collection times (3 hours rather than 11 hours.) The intensive dates are shown in Table A.1 below, with the sample times highlighted in blue showing periods where CCSEM-EDX was run.

Table A.1. Intensive sample collection times. Samples highlighted in blue were analyzed using CCSEM-EDX.

Intensive Date	Time (CST)
6/10/13	8:00-11:00
6/10/13	12:00-15:00
6/10/13	16:00-19:00
6/10/13	20:00-7:00
6/11/13	8:00-11:00
6/11/13	12:00-15:00
6/11/13	16:00-19:00
6/11/13	20:00-7:00
6/12/13	8:00-11:00
6/12/13	12:00-15:00
6/12/13	16:00-19:00
6/12/13	20:00-7:00
6/14/13	8:00-11:00
6/14/13	12:00-15:00
6/14/13	16:00-19:00
6/14/13	20:00-7:00
6/15/13	8:00-11:00
6/15/13	12:00-15:00
6/15/13	16:00-19:00
6/15/13	20:00-7:00
6/16/13	8:00-11:00
6/16/13	12:00-15:00
6/16/13	16:00-19:00
6/16/13	20:00-7:00
6/29/13	8:00-11:00
6/29/13	12:00-15:00
6/29/13	16:00-19:00
6/29/13	20:00-7:00
6/30/13	8:00-11:00
6/30/13	12:00-15:00
6/30/13	16:00-19:00
6/30/13	20:00-7:00
7/1/13	8:00-11:00
7/1/13	12:00-15:00
7/1/13	16:00-19:00
7/1/13	20:00-7:00
7/9/13	8:00-11:00
7/9/13	12:00-15:00
7/9/13	16:00-19:00
7/9/13	20:00-7:00

All sampling periods that were analyzed using CCSEM-EDX are indicated in Table A.2 below. The MOUDI stage(s) that were analyzed, in addition to the number of particles per sample, are

also indicated. The aerodynamic diameter 50 % cut points, detailed in Marple et al (1991), are as follows: stage 5 (1.8 µm), stage 6 (1.00 µm), stage 7 (0.56 µm), stage 8 (0.32 µm), stage 9 (0.18 µm), stage 10 (0.100 µm), and stage 11 (0.056 µm). Not every sample collected was analyzed due to time/funding constraints and damaged substrates.

Table A.2. Sampling times of all CCSEM-analyzed MOUDI samples and the number of particles analyzed per stage.

Sample Date	Time (CST)	Stage(s)	# of particles
6/5/13	10:00-19:00	7	145
6/6/13	20:00-7:00	6 / 7	23 / 43
6/7/13	8:00-19:00	7	305
6/7/13	20:00-7:00	6	222
6/8/13	8:00-19:00	6	167
6/10/13	8:00-11:00	6 / 8	395 / 580
6/10/13	12:00-15:00	6 / 8	518 / 497
6/10/13	16:00-19:00	8	281
6/10/13	20:00-7:00	7	567
6/11/13	8:00-11:00	7	431
6/11/13	16:00-19:00	7	450
6/11/13	20:00-7:00	7	553
6/12/13	8:00-11:00	6 / 8	305 / 151
6/12/13	12:00-15:00	5 / 7 / 8	129 / 474 / 1314
6/12/13	16:00-19:00	6 / 7	365 / 220
6/12/13	20:00-7:00	7 / 9	581 / 2313
6/13/13	8:00-19:00	5 / 8 / 10	462 / 653 / 688
6/13/13	20:00-7:00	7	122
6/14/13	8:00-11:00	6 / 7	101 / 355
6/14/13	12:00-15:00	6 / 7 / 8	22 / 343 / 402
6/14/13	16:00-19:00	8	512
6/14/13	20:00-7:00	6	100
6/15/13	8:00-11:00	7 / 8	384 / 380
6/15/13	20:00-7:00	6 / 7 / 8	84 / 532 / 2304
6/16/13	8:00-11:00	7	239
6/16/13	16:00-19:00	7	338
6/16/13	20:00-7:00	6 / 8	514 / 791
6/17/13	8:00-19:00	7	2707
6/20/13	8:00-19:00	6 / 7	134 / 938
6/26/13	20:00-7:00	6 / 7	295 / 539
6/28/13	20:00-7:00	7	95
7/1/13	12:00-15:00	7	392
7/3/13	20:00-7:00	7	711
7/4/13	8:00-19:00	7	1826
7/5/13	8:00-19:00	7	448
7/6/13	8:00-19:00	6 / 10 / 11	369 / 64 / 342
7/7/13	8:00-19:00	7 / 10	209 / 690
7/7/13	20:00-7:00	9	153
7/8/13	8:00-19:00	6 / 9 / 11	137 / 755 / 1246
7/8/13	20:00-7:00	9	260
7/9/13	16:00-19:00	5 / 6 / 10 / 11	527 / 446 / 846 / 879
7/11/13	8:00-19:00	9	1262

A.3. Calculation of Particle Volume Equivalent Diameters

To describe the impact of size on aerosol chemical diversity during SOAS, projected area diameters (D_{pa}) measured using CCSEM-EDX were converted to volume equivalent diameters (D_{ve}) using a conversion factor determined from atomic force microscopy (AFM) height images of organic particles from SOAS collected on silicon substrates (Ted Pella Inc.). As particles can undergo spreading upon impaction on substrates, D_{ve} represents the size of particles before impaction. AFM images from organic aerosol particles collected during SOAS on June 14, 2013 were used in the subsequent analysis to calculate a conversion factor between D_{pa} and D_{ve} for SOA and biomass burning particles. As SSA during SOAS was predominately aged by HNO_3 leading to $NaNO_3$ in the particle phase (Bondy et al., 2017b), a SSA spreading conversion factor was calculated using laboratory-generated $NaNO_3$ (Bondy et al., 2017a). Though organic aerosol particles and SSA are expected to spread upon impaction as they are generally liquids at the temperatures and relative humidities presented, mineral dust, fly ash and primary biological particles are not expected to spread as they are solid. Thus, D_{pa} is equivalent to D_{ve} for mineral dust, fly ash and biological particles.

AFM was performed on a nanoIR2 system (Anasys Instruments). AFM height/deflection images were collected in contact mode (IR power 21.27 %, filter in) at a scan rate of 1 Hz using a gold-coated contact mode silicon nitride probe (Anasys Instruments, 13 ± 4 kHz resonant frequency, 0.07-0.4 N/m spring constant). Volumes of particles were measured using SPIP software (v6.2.6, Image Metrology, Hørsholm, Denmark), and from these volumes, D_{ve} was calculated for each particle. Table A.3 shows the measured height and diameter, calculated volume, and calculated D_{ve} for select organic particles from SOAS (~100 particles were actually used to calculate the conversion factor). From these results, SOA and biomass burning particles were multiplied by a conversion factor of 0.49 to convert D_{pa} to D_{ve}.

Table A.3. AFM-measured and volume-calculated diameters of organic aerosol collected during SOAS on June 14, 2013. *Note, the physical characteristics of ~100 particles were analyzed in the volume calculations, however only a fraction are shown here for brevity.

Particle #	D_{pa} (nm)	Height (nm)	Volume (nm^3)	D_{ve} (nm)
1	437	61	6947798	237
2	959	154	71964608	516
3	814	52	23869656	357
4	1030	85	52498328	465
5	368	40	3808314	194
6	354	67	5322988	217
7	332	44	2505523	169
8	367	48	3452574	188
9	519	62	6793956	235
10	551	60	7362516	241
11	1092	133	43055348	435
12	559	51	8345108	252
13	513	57	7491997	243
14	227	2	519373.6	100
15	431	46	4841927	210
16	500	83	8957392	258
17	495	50	6785424	235
18	499	56	5260008	216
19	444	43	4814164	210
20	414	54	4637069	207
21	296	40	2351715	165
22	393	79	5153589	214
23	329	44	3074541	180
24	483	51	5008449	212

Similarly, volumes were calculated for $NaNO_3$ particles representative of SSA from SOAS in Table A.4. From these results, SSA particles were multiplied by a conversion factor of 0.67 to convert D_{pa} to D_{ve}.

Table A.4. AFM-measured and volume-calculated diameters of NaNO3 particles impacted on silicon substrates, representative of SSA.

Particle #	D_{pa} (nm)	Height (nm)	Volume (nm^3)	D_{ve} (nm)
1	448	84	8981224	258
2	68	17	102174	58
3	171	29	821752	116
4	136	19	435493	94
5	100	13	205804	73
6	105	12	228540	76
7	250	58	2467066	168
8	258	77	2776954	174
9	153	29	648760	107
10	284	72	3454101	188
11	251	51	2288227	164
12	217	24	1243357	133
13	265	57	2718737	173
14	89	15	169364	69
15	320	67	4208101	200
16	745	108	24432611	360
17	273	55	2854158	176
18	217	40	1542059	143
19	458	79	8608666	254
20	199	33	1133683	129
21	319	69	4500131	205
22	383	64	5131053	214
23	187	9	676804	109
24	250	50	2184633	161

A.4. Fresh Soot Calculation

Soot was difficult to detect using CCSEM-EDX due to interference from the Formvar B coating on the TEM grid. Therefore, the size distribution for soot was manually calculated from SEM images using samples on various stages from one day, and then a correction factor was applied to each sampling period based on the SEARCH network mass concentrations of elemental carbon (EC). This method likely overestimates the contribution of fresh soot since organic carbon/elemental carbon (OC/EC) SEARCH measurements include both fresh and aged soot, however the EC mass was used as an approximation of soot's contribution. To calculate the size distribution of soot particles during SOAS, all SEM images from July 9, 2013 4pm-7pm

CST were inspected for soot agglomerates. This sample was chosen for analysis because stages 7-11 of the MOUDI (0.056-0.56 µm 50 % size cut; relevant sizes for soot) were available for imaging. Once a soot particle was identified, the particle was traced in ImageJ software to calculate the area. From this area, similar to the CCSEM software output, the projected area diameter (D_{pa}) was calculated and a size distribution using all soot D_{pa} was generated, shown below.

Table A.5. Size distribution for fresh soot calculated for July 9, 2013 stages 7-11.

Projected Area Diameter (µm)	Frequency	Fraction of soot per bin
0.133352	0	0
0.177828	0	0
0.237137	5	0.065789474
0.316228	14	0.184210526
0.421697	27	0.355263158
0.562341	18	0.236842105
0.749894	11	0.144736842
1	0	0
1.333521	0	0
1.778279	1	0.013157895
2.371374	0	0
3.162278	0	0
4.216965	0	0
5.623413	0	0
7.498942	0	0
10	0	0
Total	76	

The fraction of soot per size bin was then used with the SEARCH network EC mass concentrations, measured using oxidative combustion, to calculate an approximate number of soot particles within each size range. First, the average EC mass was calculated for each time period of interest during SOAS. Then, the average $PM_{2.5}$ mass, measured using a tapered element oscillating microbalance (TEOM), was calculated for each time period. A scaling factor was generated by dividing EC mass/TEOM mass. The scaling factor calculated for each time period is: SOA (0.022), mineral dust (0.018), and SSA (0.029). This scaling factor was then multiplied

by the size distributions in Table A.5, giving results for the fraction of soot within the designated size bins for each of the three time periods.

A.5. Mass Calculations and Mixing State Parameters

To calculate the mixing state parameters, atomic percentages were converted to mass fractions as described in the experimental section. To calculate elemental diversity, the mass of each element was used in the mixing state calculations shown below. To calculate mixing state due to aging during the SOA-rich, dust-rich, and SSA-rich time periods, elemental masses were assigned to specific source-based particle classes with the compositions described below. The elemental mass fractions for each of the three time periods are shown in Figure A.2 depicting each element's contribution as a function of size. For the source-based elemental assignments, SOA particles consisted of solely S, biomass burning particles contained K and Cl, fly ash particles consisted of Si and Al, dust particles contained Na, Mg, Al, Si, K, Ca, Ti, and Fe, SSA particles contained Na, Mg, Cl, K, and Ca, and biological particles consisted of P, Cl, and K. Secondary species in this study were represented by S in every particle class, since organic (C, O) and nitrogen-containing species (N) are not quantitative using SEM-EDX (Laskin et al., 2006).

In addition to mass calculations, mixing state parameters were calculated for each elemental class to quantify diversity, and for the SOA, dust, and SSA time periods to quantify aging. The experimental section describes the equations used to calculate the entropy and mixing state index. Below are the definitions and equations for aerosol mass and mass fraction used to calculate the entropy along with equations for particle, species, and bulk population diversity (Riemer and West, 2013). The mass of species a in particle i is termed $\mu^a{}_i$ where $a = 1,\ldots, A$ and $i = 1,\ldots, N$. The total mass of particle i (μ_i) is given by

$$\mu_i = \sum_{a=1}^{A} \mu_i^a \quad \text{(A.1)}$$

The total mass of species a in the population (μ^a) is given by

$$\mu^a = \sum_{i=1}^{N} \mu_i^a \quad \text{(A.2)}$$

The total mass of the population (μ) is given by

$$\mu = \sum_{i=1}^{N} \mu_i \quad \text{(A.3)}$$

The mass fraction of species a in particle i ($p^a{}_i$) is given by

$$p_i^a = \frac{\mu_i^a}{\mu_i} \tag{A.4}$$

The mass fraction of particle *i* in the population (p_i) is given by

$$p_i = \frac{\mu_i}{\mu} \tag{A.5}$$

The mass fraction of species *a* in the population (p^a) is given by

$$p^a = \frac{\mu^a}{\mu} \tag{A.6}$$

The particle diversity of particle *i* (D_i) is given by

$$D_i = e^{H_i} \tag{A.7}$$

where H_i is the mixing entropy of particle *i*. The average particle species diversity (D_α) is given by

$$D_\alpha = e^{H_\alpha} \tag{A.8}$$

where H_α is the average particle mixing entropy. The bulk population species diversity (D_γ) is given by

$$D_\gamma = e^{H_\gamma} \tag{A.9}$$

where H_γ is the population bulk mixing entropy. D_α was used as a quantitative measure of elemental diversity for each particle class during SOAS (SOA, biomass burning particles, fly ash, dust, SSA, and biological particles.) However to quantify particle aging due to S during SOAS, the mixing state index (χ), a ratio between the average particle species diversity and bulk population species diversity, was calculated. While D_α is a useful metric to quantify elemental diversity, χ quantifies the degree of internal versus external mixing present within particle populations.

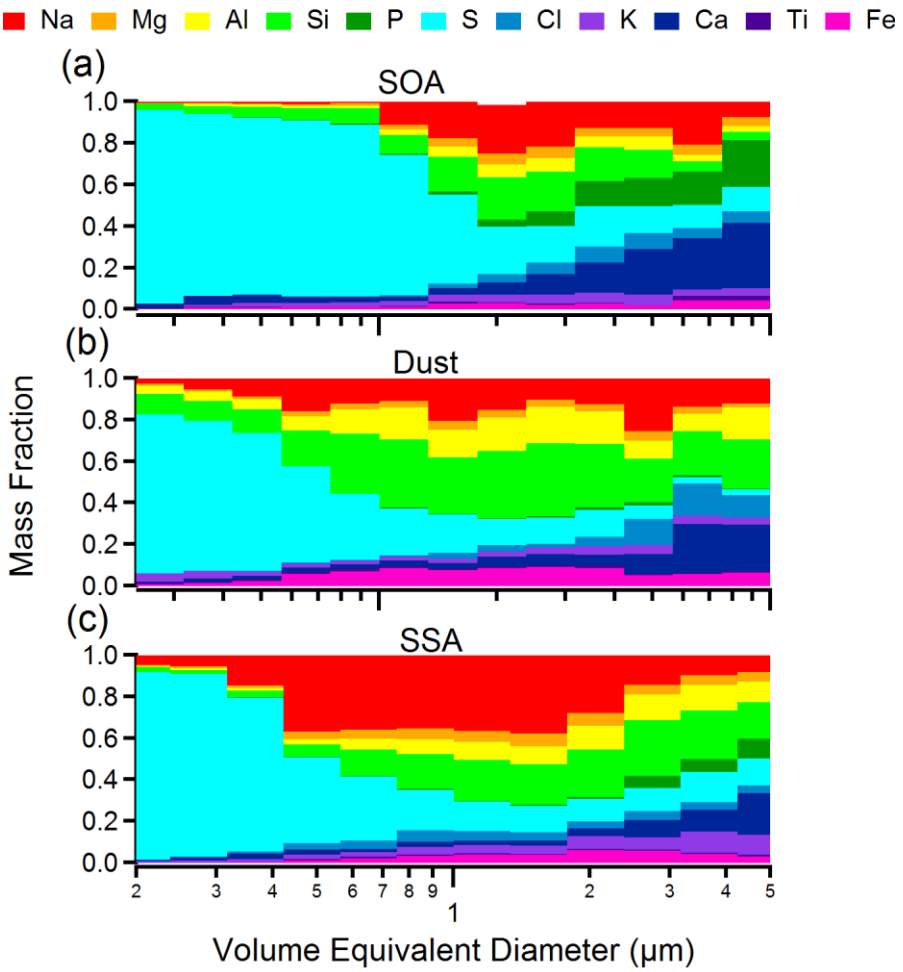

Figure A.2. Mass fractions as a function of volume equivalent diameter for particle-rich time periods: (a) SOA-rich periods (June 14-17 and July 7-11, 2013), (b) dust-rich periods (June 12-13 and June 26-28, 2013), and (c) SSA-rich periods (June 10-11 and July 3-6, 2013.) C and O are not included in element quantification due to substrate interferences. *Only particles with a diameter between 0.2 - 5 μm are shown due to too few particles present at larger sizes for quantitative analysis.

A.6. STXM-NEXAFS Soot Identification

Two samples, June 10 and July 7, 2013, were analyzed using STXM-NEXAFS. In order to calculate the number fraction of particles from each sample that contained sp^2 C in the form of soot, Matlab was used to visualize every particle in the sample. Each particle was screened on a per pixel basis for regions of high C=C content (> 35 % C=C). If a pixel contained > 35 % C=C, then the script rendered a red pixel, stating that it was safe to call that region soot. The same was performed for the other colors (i.e. blue=inorganic, green=organic). Using this data, 6.9 % of

particles by number contained soot collected June 10, 2013 and 9.9 % of particles collected July 7, 2013 contained soot.

A.7. EDX of SOA on Silicon

Most of the CCSEM-EDX analysis in this study was conducted on Formvar-coated TEM grids. However, since Formvar (a polymer) interferes with particle carbon and oxygen X-ray signals, additional EDX spectra of SOA particles were collected on Si substrates. EDX spectra from 61 particles (June 15, 2013 8pm-7am St. 8 sample) were collected and quantified with respect to C, N, O, and S. Figure A.3 shows an example spectrum of an SOA/sulfate particle collected on Si. Note, the signal for Si extend beyond 80 counts, however the y-axis range shown here was selected to view the elements of interest (C, N, O, S). The average weight % of elements within SOA/sulfate from this analysis was 40 % C, 11 % N, 28 % O, and 20 % S. Though SOA/sulfate only contained 20 % sulfur from this analysis, the mixing state indices for aerosol populations were calculated based on SOA/sulfate containing only sulfur, since CCSEM-EDX is not quantitative for C, N, and O.

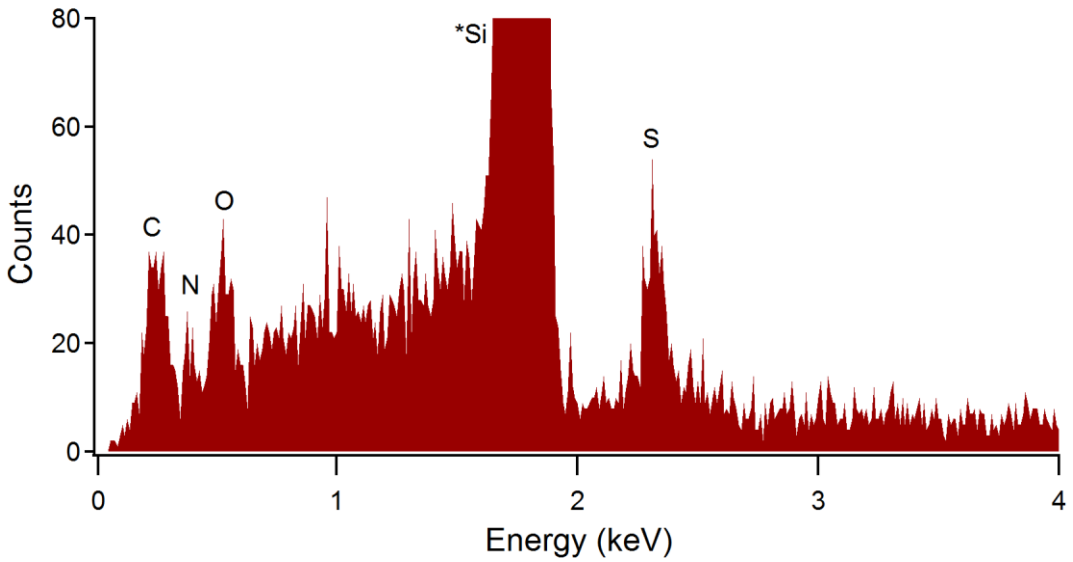

Figure A.3. Example EDX spectrum of an SOA/sulfate particle collected on a silicon substrate.

A.8. Circularity Equation

To determine the average circularity for SOA, biomass burning aerosol, and fly ash classes, the mode circularity was averaged across the k-means clusters assigned to that class in Equation A.10:

$$C = 4\pi A/p^2 \tag{A.10}$$

where C is circularity, A is area of the particle, and p is the particle perimeter.

A.9. Nonvolatile Cations

The number fraction of particles containing nonvolatile cations (Na, Mg, K, Ca, Fe) in sub- and supermicron sizes is shown in Figure A.4 for the dust and SSA periods. In general, the number fraction of metal-containing particles is consistent for each class across the different periods (although there are minor differences between the sub- and super micron size ranges), suggesting that nonvolatile cations don't vary with processing, but are inherent to each class.

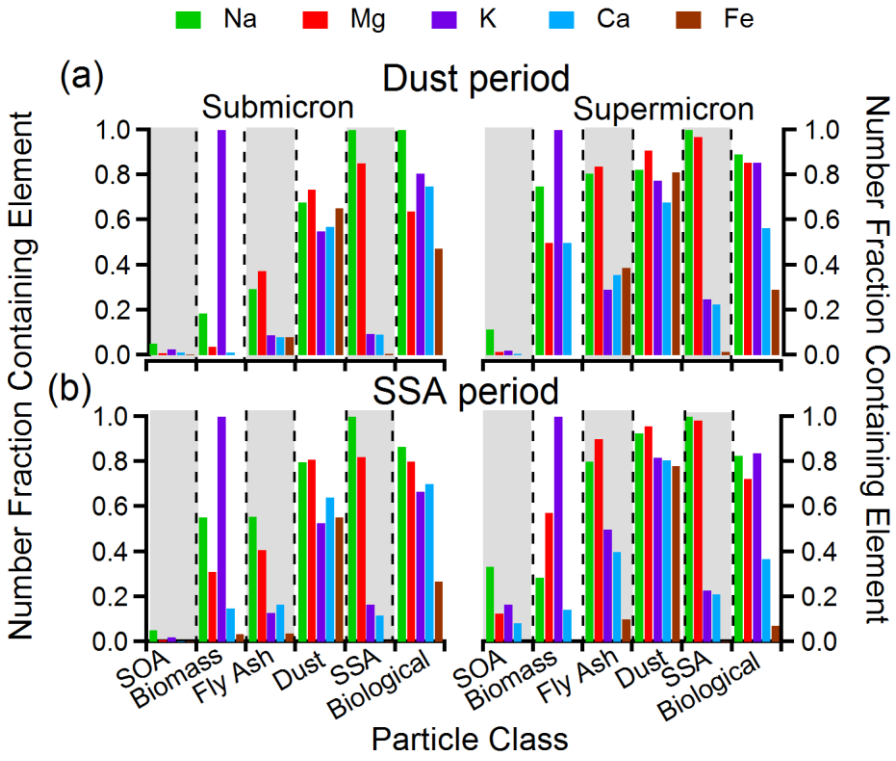

Figure A.4. Size-resolved particle class compositions indicate the number fraction of particles in each class containing non-volatile cations Na, Mg, K, Ca, and Fe during the (a) dust period and (b) SSA period in the submicron and supermicron size range.

A.10. Significance of Aging by Sulfur during Three Events

The degree of secondary processing for each particle class was calculated as the average mass fraction of sulfur per particle (Figure A.5). This parameter was used to calculate average sulfur diversity and along with the bulk population diversity, mixing state indices could be quantified. However, the mass fraction calculations here exclude C, N, and O since low Z elements are only semiquantitative with CCSEM. Excluding C, N, and O, SOA/sulfate have average sulfur mass fractions of 0.98 ± 0.08, 0.96 ± 0.13, 0.96 ± 0.16, during the SOA-influenced, dust-influenced, and SSA-influenced events, respectively. However, analysis of SOA on a non-carbonaceous substrate, which allowed C, N, and O to be quantified, demonstrated that the average mass fraction of sulfur in SOA was actually 0.20 ± 0.04. This "actual" mass value for SOA was used to scale the average mass fraction of sulfur for each period and is portrayed in Figure A.5 by red markers. Using this scaled mass fraction of sulfur, the "actual" mass of sulfur was 0.197 during the SOA-influenced events, 0.193 during the dust periods, and 0.192 during the SSA periods.

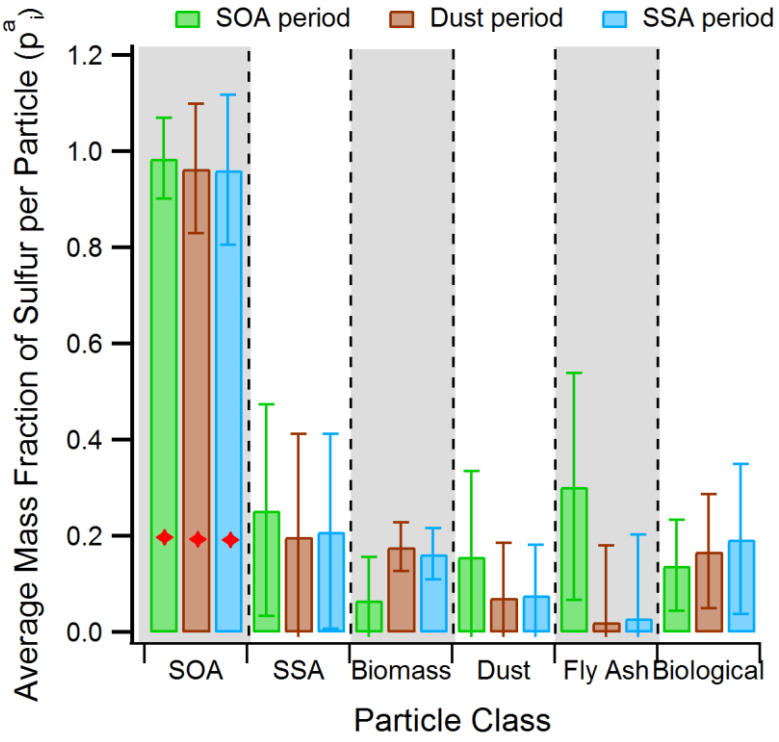

Figure A.5. The secondary processing of particles by sulfate was calculated for each class during the three time periods of interest as the average mass fraction of sulfur per particle. Red markers indicate the scaled "actual" mass fraction of sulfur for SOA including mass contributions from C, N, and O.

A student's t-test was used to compare the average mass fraction of sulfur per particle for six main particle classes (SOA/sulfate, biomass burning aerosol, fly ash, dust, SSA, and biological) during the SOA events, dust events, and SSA events. The standard deviation, s_{pooled}, was calculated using the following equation,

$$s_{pooled} = \sqrt{\frac{s_1^2(n_1-1)+s_2^2(n_2-1)}{n_1+n_2-2}} \quad \text{(A.11)}$$

where s_1 and s_2 are the standard deviations from the two samples, and n_1 and n_2 are the number of samples in each category. Then the student's t-test was calculated,

$$t_{calculated} = \frac{x_1-x_2}{s_{pooled}} \sqrt{\frac{n_1 n_2}{n_1+n_2}} \quad \text{(A.12)}$$

where x_1 and x_2 are the mean mass fraction of sulfur per particle class. The results of the student t-tests are located in Table A.6, Table A.7, and Table A.8. The student's t-test was calculated to compare the aging of particle classes during the SOA vs. dust events, SOA vs. SSA events, and dust vs. SSA events. The difference in average sulfur mass fractions for all particle classes was found to be significant for the SOA vs. dust events and SOA vs. SSA events, but the difference was not statistically significant for the dust vs. SSA events at the 95 % confidence interval.

Table A.6. Student's t-test comparing average sulfur mass fractions among particle classes for the SOA vs. dust events

	SOA	**Biomass**	**Fly Ash**	**Dust**	**SSA**	**Biological**
x_1	0.985	0.260	0.070	0.169	0.306	0.140
x_2	0.964	0.177	0.022	0.072	0.199	0.168
s_1	0.081	0.221	0.091	0.179	0.235	0.096
s_2	0.134	0.214	0.051	0.114	0.156	0.119
s_{pooled}	0.095	0.048	0.006	0.128	0.194	0.099
degrees of freedom	120	120	120	120	120	120
$t_{calculated}$	10.97	3.95	5.67	19.82	13.49	2.50
95 % CI t_{table}	1.98	1.98	1.98	1.98	1.98	1.98
significantly different?	yes	yes	yes	yes	yes	yes

Table A.7. Student's t-test comparing average sulfur mass fractions among particle classes for the SOA vs. SSA events

	SOA	**Biomass**	**Fly Ash**	**Dust**	**SSA**	**Biological**
x_1	0.985	0.260	0.070	0.169	0.306	0.140
x_2	0.962	0.163	0.029	0.077	0.209	0.193
s_1	0.081	0.221	0.091	0.179	0.235	0.096
s_2	0.155	0.202	0.053	0.104	0.173	0.156
s_{pooled}	0.098	0.047	0.083	0.132	0.193	0.108
degrees of freedom	120	120	120	120	120	120
$t_{calculated}$	10.71	3.98	3.50	16.56	13.62	5.04
95 % CI t_{table}	1.98	1.98	1.98	1.98	1.98	1.98
significantly different?	yes	yes	yes	yes	yes	yes

Table A.8. Student's t-test comparing average sulfur mass fractions among particle classes for the dust vs. SSA events

	SOA	**Biomass**	**Fly Ash**	**Dust**	**SSA**	**Biological**
x_1	0.985	0.177	0.022	0.072	0.199	0.168
x_2	0.964	0.163	0.029	0.077	0.209	0.193
s_1	0.081	0.214	0.051	0.114	0.158	0.119
s_2	0.134	0.202	0.053	0.104	0.173	0.156
s_{pooled}	0.144	0.209	0.052	0.111	0.168	0.142
degrees of freedom	120	120	120	120	120	120
$t_{calculated}$	0.568	0.57	0.94	1.63	1.78	1.29
95 % CI t_{table}	1.98	1.98	1.98	1.98	1.98	1.98
significantly different?	no	no	no	no	no	no

A.11. References

Bondy, A. L., Kirpes, R. M., Merzel, R. L., Pratt, K. A., Banaszak Holl, M. M., and Ault, A. P.: Atomic force microscopy-infrared spectroscopy of individual atmospheric aerosol particles: Subdiffraction limit vibrational spectroscopy and morphological analysis, Anal. Chem., 89, 8594-8598, 2017a.

Bondy, A. L., Wang, B., Laskin, A., Craig, R. L., Nhliziyo, M. V., Bertman, S. B., Pratt, K. A., Shepson, P. B., and Ault, A. P.: Inland sea spray aerosol transport and incomplete chloride depletion: Varying degrees of reactive processing observed during SOAS, Environ. Sci. Technol., 51, 9533-9542, 2017b.

Laskin, A., Cowin, J. P., and Iedema, M. J.: Analysis of individual environmental particles using modern methods of electron microscopy and X-ray microanalysis, J. Electron. Spectrosc. Relat. Phenom., 150, 260-274, 2006.

Marple, V. A., Rubow, K. L., and Behm, S. M.: A microorifice uniform deposit impactor (MOUDI)-description, calibration and use, Aerosol Sci. Technol., 14, 434-446, 1991.

Riemer, N., and West, M.: Quantifying aerosol mixing state with entropy and diversity measures, Atmos. Chem. Phys., 13, 11423-11439, 2013.

Appendix B.

Inland Sea Spray Aerosol Transport and Incomplete Chloride Depletion: Varying Degrees of Reactive Processing Observed during SOAS Supplemental Information

B.1. Inland SSA Studies

Numerous locations impacted by transported SSA have been previously studied (Figure B.1, Table B.1) (Gard et al., 1998; Noble and Prather, 1997; Ueda et al., 2014), however in this work only SSA detected at locations ranging from 100-1100 km from the coast are considered inland (O'Brien et al., 2015; Moffet et al., 2013; Laskin et al., 2012; Foner and Ganor, 1992; Giannoni et al., 2016; Silva et al., 2007; Gustafsson and Franzen, 2000; Dos Santos et al., 2012; Manders et al., 2010; Chalbot et al., 2013; Shaw, 1991; Hara et al., 2004; Udisti et al., 2012). Although most of these studies have used bulk analysis methods, studies during CARES (Carbonaceous Aerosols and Radiative Effects Study) (O'Brien et al., 2015; Moffet et al., 2013; Laskin et al., 2012) in Sacramento and Cool, CA used single particle techniques including computer-controlled scanning electron microscopy with energy dispersive X-ray spectroscopy (CCSEM-EDX) and scanning transmission x-ray microscopy with near edge X-ray absorption fine structure (STXM-NEXAFS) to study SSA. Of the bulk analysis studies, a variety of methods were used including electrical conductivity (Gustafsson and Franzen, 2000), which detects the mass of all salts, and ion chromatography or inductively coupled plasma spectroscopy, which detect SSA using chloride content, sodium content, or a ratio of SSA containing species (Ueda et al., 2014; Foner and Ganor, 1992; Giannoni et al., 2016; Dos Santos et al., 2012; Chalbot et al., 2013; Udisti et al., 2012; Hara et al., 2004; Manders et al., 2010; Silva et al., 2007). In most of the inland studies, the mass fraction or number fraction (denoted by #) of SSA was quantified. However particles which have undergone complete chloride depletion would not be recognized as SSA using these methods, necessitating single particle analysis.

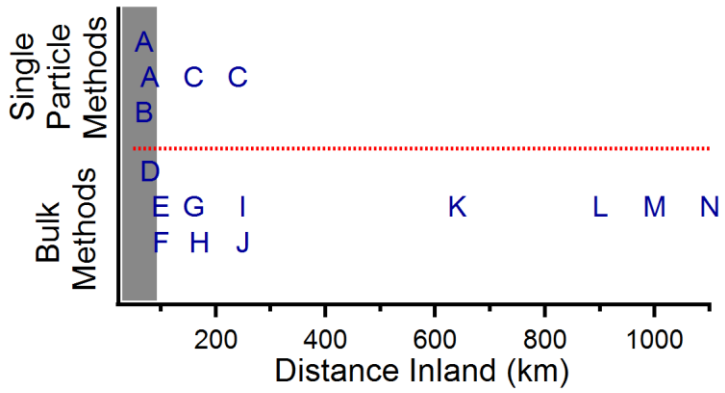

Figure B.1. Previous SSA studies use primarily bulk techniques and have sampled particles at distances ranging 70-1100 km from the coast (Gard et al., 1998; Noble and Prather, 1997; Moffet et al., 2013; O'Brien et al., 2015; Laskin et al., 2012; Ueda et al., 2014; Foner and Ganor, 1992; Giannoni et al., 2016; Silva et al., 2007; Gustafsson and Franzen, 2000; Dos Santos et al., 2012; Manders et al., 2010; Chalbot et al., 2013; Shaw, 1991; Hara et al., 2004; Udisti et al., 2012). In this work, only studies $\geq$ 100 km are considered "inland." (Moffet et al., 2013; O'Brien et al., 2015; Silva et al., 2007; Udisti et al., 2012; Manders et al., 2010; Gustafsson and Franzen, 2000; Dos Santos et al., 2012; Chalbot et al., 2013; Shaw, 1991; Foner and Ganor, 1992; Giannoni et al., 2016; Hara et al., 2004; Laskin et al., 2012)

Table B.1. Previous studies of transported SSA depicted in Figure B.1.

Letter	Author (Year)	Location(s)	Distance from coast (km)	Single particle (S.P) or Bulk	SSA composition	Fraction of SSA
A	Gard et al. (1998)	Upland, CA and Tanbark Flats, CA	70, 80	S.P.	0.3-0.5 mole fraction NO_3^-	--
B	Noble et al. (1997)	Riverside, CA	70	S.P.	--	12-80 % (#)
C	Moffet et al. (2013) O'Brien et al. (2015) Laskin et al. (2012)	Sacramento, CA Cool, CA	160, 240	S.P.	Cl/(Na+0.5Mg) = 0-0.9	40-50 % (#)
D	Ueda et al. (2014)	Mt. Oyama, Japan	80	Bulk	Cl/Na = 0-0.35	0-89 % (#)
E	Foner and Ganor (1992)	Arad, Israel	100	Bulk	--	3-18 % TSP (mass)
F	Giannoni et al. (2016)	Ecuador	100	Bulk	Na/Cl = 0-2	3-30 % (mass)
G	Silva et al. (2007)	Galicia, Spain	160	Bulk	Cl/Na = 0.56-0.67	0.1-0.14 $meql^{-1}$
H	Gustafsson and Franzen (2000)	Southern Sweden	170	Bulk	Cl/Na = 1.8	1-3 $\mu g/m^3$
I	Dos Santos et al. (2012)	Buenos Aires	250	Bulk	Cl/Na = 1.38-1.81	$PM_{2.5-10}$ = 3-20 % (mass) $PM_{2.5}$ = 4-10 % (mass)
J	Manders et al. (2010)	Across Europe	200-300	Bulk	--	2-5 $\mu g/m^3$
K	Chalbot et al. (2013)	Little Rock, AR	640	Bulk	Cl/Na = 0.1	10 % (mass)
L	Shaw (1991)	Central AK	900	Bulk	Cl/Na = 0.46-0.94	800-1300 ng Na^+
M	Hara et al. (2004)	Dome Fuji, Antarctica	1000	Bulk	Cl/Na = 0.48	0.44-2.7 $nmol/m^3$ Na^+
N	Udisti et al. (2012)	Dome C, Antarctica	1100	Bulk	2-3 ng/m^3 $ssNa^+$ (summer) 15.6-24.7 ng/m^3 $ssNa^+$ (winter)	11-85 % (mass)

B.2. Identification of SSA

The molar ratio of Na:Mg, approximately 10:1 (actual 10.1:1 ± 2.1) (Pilson, 1998), was used to identify SSA using SEM-EDX with k-means clustering. This ratio of Na:Mg is the same in particles as that found in seawater since the seawater cations are not volatile and unlikely to be displaced (Pilson, 1998; Laskin et al., 2012; Hopkins et al., 2008; Ault et al., 2013). SSA particles were separated into three categories based on their chemical composition. Partially aged SSA had Cl/Na molar ratios $\geq$ 0.1 (approximately 10 % of the ratio present within seawater, 1.16) (Pilson, 1998). Particles in the aged categories had little chloride, Cl/Na molar ratio < 0.1, and nitrate and/or sulfate. Particles in the aged-sulfate class contained sulfate (mole % S $\geq$ 1,

mole % N < 1 %), while particles in the aged-nitrate/sulfate contained sulfate (mole % S $\geq$ 1) and nitrate (mole % N $\geq$ 1). The number fraction of particles belonging to each SSA class IS detailed in Table B.2.

Table B.2. Number fractions and standard error associated with SSA classes.

Class	Particles per class	Number Fraction	Standard Error
Partially aged	977	0.241	0.007
Aged-S	594	0.147	0.006
Aged-N/S	2476	0.612	0.008

B.3. Raman Microspectroscopy: Analysis of Secondary Species within SSA Particles

Computer-controlled Raman microspectroscopy (CC-Raman) was used to analyze secondary species in aerosol particles (Craig et al., 2017). Divisive clustering analysis (DCA) was used to cluster and classify particles based on distinct features in their Raman spectra. Raman spectra and morphological parameters, such as particle diameter and circularity, were measured for 209 particles from June 12, 2013 12:00-15:00 CST (Event 1), and 198 particles from July 4, 2013 8:00-19:00 (Event 2). These SSA-rich time periods were selected in order to identify whether CCSEM results showing sulfur and nitrogen in SSA corresponded to secondary species such as sulfate and nitrate. Although Raman spectroscopy cannot differentiate SSA from other particle types since it cannot detect sodium or magnesium, this technique can identify nitrate and sulfate. Because SSA-rich time periods were selected for Raman analysis, likely most of the supermicron particles analyzed are SSA. Representative average Raman spectra of the nitrate- and sulfate-containing DCA clusters (37 % of particles, by number, analyzed for Event 1, and 36 % of particles, by number, analyzed for Event 2) are shown in Figure B.2. During Event 1, all of the particles which were likely SSA contained nitrate, while < 2 % of the particles, by number, contained sulfate. Conversely, during Event 2, 33 % of the particles analyzed, by number, contained nitrate, 56 %, by number, contained nitrate and sulfate, and 11 %, by number, contained solely sulfate. Additionally the presence of organic functionalities, indicative of an organic coating which may inhibit the rate of chloride depletion, were detected within all nitrate- and sulfate-containing particles.

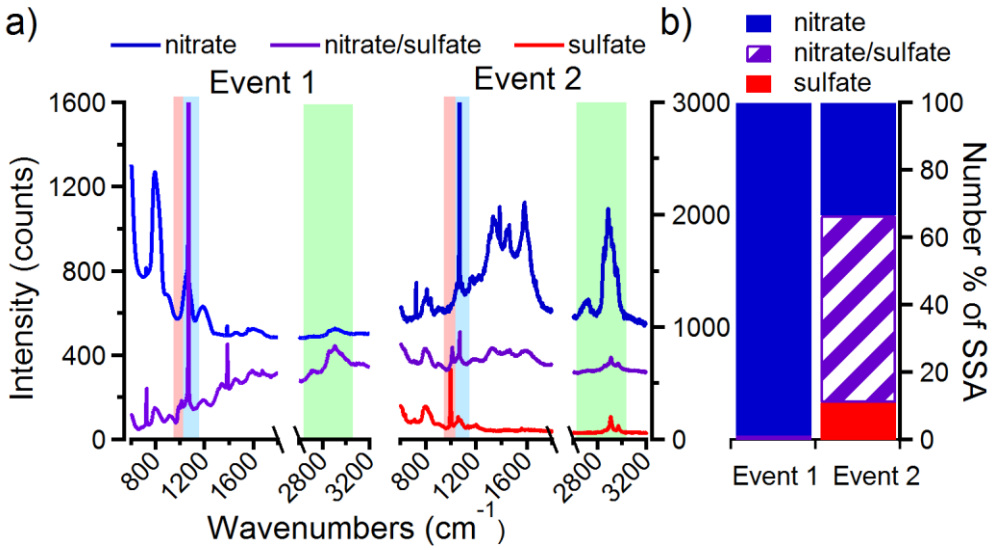

Figure B.2. a) Average Raman spectra of DCA clusters from Event 1 and Event 2 containing nitrate and/or sulfate. The vibrational modes highlighted in red correspond to sulfate, blue to nitrate, and green to organic functional groups. b) Percent of particles, by number, containing nitrate and/or sulfate vibrational modes from Event 1 and Event 2 using CC-Raman.

B.4. Two SSA Events Identified

Two SSA events, June 10, 2013 8:00 – June 13, 2013 19:00 CST and July 3, 2013 20:00 – July 8, 2013 7:00 CST were identified by high number fractions of SSA compared to particles analyzed during other times throughout SOAS (Figure B.3). During these two events, SSA comprised a significant fraction of both the submicron (up to 48 %, by number, with an average of 11 %) and supermicron (up to 81 %, by number, with an average of 35 %) size ranges. Data from July 4 20:00 - July 5 7:00 and July 5 8:00-19:00 were excluded due to possible influence from fireworks. Data from June 19- 26 were not analyzed because the samples were damaged during transport.

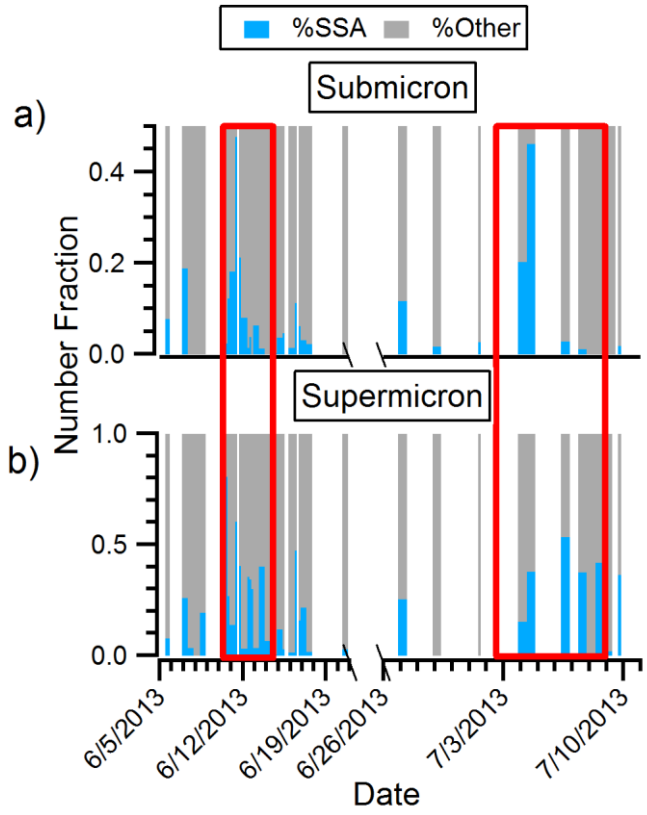

Figure B.3. SSA contributes substantially to the total number fraction of particles in both the a) submicron (0.2-1.0 µm) and b) supermicron (1.0-10.0 µm) projected area diameter size ranges. Two time periods, June 10-13 and July 3-8 highlighted with red boxes, contain a high number fraction of SSA. Data from July 4 20:00 – July 6 8:00 UTC were excluded due to possible influence by fireworks.

B.5. Estimation of Theoretical Uptake of HNO_3 onto SSA

The theoretical uptake of HNO_3 on SSA particles was calculated based on experimental results by Liu et al. (2007) to examine whether the observed chloride depletion during the two SOAS events occurred slower than diffusion-limited kinetics would predict. This calculation involves numerous assumptions including: HNO_3 is in excess over NaCl over the entire time of transport, the HNO_3 concentration remains constant in the entire region as particles are transported, the relative humidity remains constant throughout transport, and the rate constant for the reaction is valid for the size of SSA and concentration of HNO_3 from SOAS. The following equation was used to predict the reaction time at which chloride was 99 % depleted (aged-SSA category):

$$t = -\frac{1}{k}\ln\frac{[Cl]_t}{[Cl]_0} \quad \text{(B.1)}$$

where t is transport time in seconds and k is the first order rate constant under specified conditions. The rate constant was selected for the experimental conditions that most closely matched those during SOAS. The conditions selected compared to average conditions during SOAS are listed in Table B.3. Using these conditions and a rate constant (k) of 3.4 x 10^{-4} s^{-1}, the time needed for 99 % chloride depletion is ~3.8 hours, much less than average transport times from the Gulf during SOAS. The results of this calculation suggest that the particles were likely not diffusion limited, particularly during Event 1, but rather were thermodynamically limited by inorganic and organic acids.

Table B.3. Reaction conditions for theoretical HNO_3 uptake compared to the actual conditions during SOAS

	Liu et. al. (2007)	**SOAS average**
D_p (μm)	0.83 ± 0.02	1.64 ± 1.23
RH (%)	80	82
[HNO3] (ppb)	3.0	0.15
Particle surface density (cm^{-2})	2.0 ± 0.5 x 10^{-3}	--

B.6. HNO_3 and NO_y Concentrations during SOAS

HNO_3 and NO_y gas phase concentrations were measured by the SEARCH monitoring network. Data was obtained from the SEARCH monitoring network in Centreville, AL and downloaded from the site for the National Oceanographic and Atmospheric Administration (NOAA): https://esrl.noaa.gov/csd/groups/csd7/measurements/2013senex/Ground/DataDownload/. HNO_3 and NO_y gas phase measurements during SOAS are plotted in Figure B.4. Event 1 and Event 2, highlighted in the red boxes, show drastically different concentrations of nitrogen-containing gas-phase species. During Event 1, the concentration of HNO_3 was 0.23 ppb on average and the NO_y concentration was 1.28 ppb, which was very high compared to the concentrations of HNO_3 (0.03 ppb) and NO_y (0.51 ppb) during Event 2. The high concentrations of HNO_3 and NO_y during Event 1 may account for the highly nitrate-aged SSA analyzed during that period, compared to the high concentrations of partially aged SSA detected during Event 2.

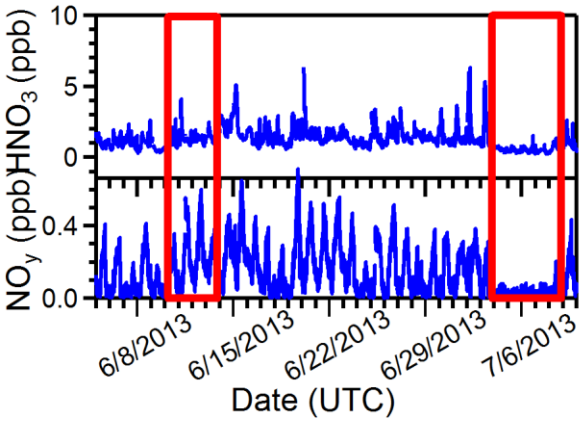

Figure B.4. NO_y and HNO_3 continuous gas phase measurements from SEARCH using chemiluminescence with 10 minute resolution. Red boxes highlight concentrations during the two SSA events. Data was obtained from the National Oceanic and Atmospheric Agency's Earth System Research Laboratory.

B.7. Chloride Depletion within SSA Particles

To determine the aged character of SSA particles in Figure 3.6, the molar % chloride depletion was calculated from the CCSEM-EDX data according to the following equation:

$$\%\ chloride\ depletion = \frac{[Cl]_0 - [Cl]_t}{[Cl]_0} * 100 \qquad \text{(B.2)}$$

where $[Cl^-]_0$ is the original mole % of chloride in the particle, and $[Cl^-]_t$ is the concentration, in mole %, of chloride in the particle at time *t* measured using EDX. Although $[Cl^-]_0$ cannot be measured directly, it can be inferred from $[Na^+]_t$. Since cations in sea water remain constant as a particle is aged and the molar ratio of Cl^- : Na^+ in sea water is 1.164 (Pilson, 1998), the original concentration of chloride in an SSA particle, in mole %, is equal to the concentration of sodium*1.164 at time *t*. Thus, equation B.3 was used in this study to determine the molar % chloride depletion in SSA:

$$\%\ chloride\ depletion = \frac{([Na]_t * 1.164) - [Cl]_t}{[Na]_t * 1.164} * 100 \qquad \text{(B.3)}$$

where $[Na]_t$ is the mole % of sodium in an SSA particle at time *t*.

B.8. Student T-test: Significance of Cl^- Depletion Due to Air Mass Transport Time

A student's t-test was used to compare the % depletion of Cl in SSA during Event 1 with 20-29 h and 30-68 h of transport from the ocean (median 30 h), and during Event 2 with 7-8 h and 10-14 h of transport from the ocean (median 10 h). The results of the student t-test are located in Table B.4. The difference in % Cl depletion for 20-29 h and 30-68 h was found to not be significant for Event 1, but the difference in % Cl depletion for Event 2 7-8 h and 10-14 h was statistically significant at the 90 % confidence interval with a t_{table} value of 2.57.

Table B.4. Student t-test results for % Cl remaining in SSA after transport.

	Event 1	**Event 2**
x_1	98.63	87.48
x_2	99.54	95.37
s_1	1.62	5.43
s_2	0.82	2.24
s_{pooled}	1.28	3.63
degrees of freedom	8	3
$t_{calculated}$	1.11	2.66
90 % CI t_{table}	1.86	2.35
significantly different?	no	yes

Two samples from Event 1, June 12th 8:00-19:00 and June 13th 8:00-19:00 were excluded from this analysis because these time periods were statistical outliers according to Grubb's test compared to the other 8 samples. Additionally as mentioned previously, samples from July 4th 20:00-7:00 and July 5th 8:00-19:00 were excluded from all analysis due to possible influence by fireworks.

B.9. References

Ault, A. P., Moffet, R. C., Baltrusaitis, J., Collins, D. B., Ruppel, M. J., Cuadra-Rodriguez, L. A., Zhao, D., Guasco, T. L., Ebben, C. J., Geiger, F. M., Bertram, T. H., Prather, K. A., and Grassian, V. H.: Size-dependent changes in sea spray aerosol composition and properties with different seawater conditions, Environ. Sci. Technol., 47, 5603-5612, 2013.

Chalbot, M. C., McElroy, B., and Kavouras, I. G.: Sources, trends and regional impacts of fine particulate matter in southern Mississippi valley: Significance of emissions from sources in the Gulf of Mexico coast, Atmos. Chem. Phys., 13, 3721-3732, 2013.

Craig, R. L., Bondy, A. L., and Ault, A. P.: Computer-controlled Raman microspectroscopy (CC-Raman): A method for the rapid characterization of individual atmospheric aerosol particles, Aerosol Sci. Technol., 10.1080/02786826.2017.1337268, 1-14, 2017.

Dos Santos, M., Dawidowski, L., Smichowski, P., Graciela Ulke, A., and Gomez, D.: Factors controlling sea salt abundances in the urban atmosphere of a coastal South American megacity, Atmos. Environ., 59, 483-491, 2012.

Foner, H. A., and Ganor, E.: The chemical and mineralogical composition of some urban atmospheric aerosols in Israel, Atmos. Environ., Part B, 26, 125-133, 1992.

Gard, E. E., Kleeman, M. J., Gross, D. S., Hughes, L. S., Allen, J. O., Morrical, B. D., Fergenson, D. P., Dienes, T., Galli, M. E., Johnson, R. J., Cass, G. R., and Prather, K. A.: Direct observation of heterogeneous chemistry in the atmosphere, Science, 279, 1184-1187, 1998.

Giannoni, S. M., Trachte, K., Rollenbeck, R., Lehnert, L., Fuchs, J., and Bendix, J.: Atmospheric salt deposition in a tropical mountain rainforest at the eastern Andean slopes of south Ecuador - Pacific or Atlantic origin?, Atmos. Chem. Phys., 16, 10241-10261, 2016.

Gustafsson, M. E. R., and Franzen, L. G.: Inland transport of marine aerosols in southern Sweden, Atmos. Environ., 34, 313-325, 2000.

Hara, K., Osada, K., Kido, M., Hayashi, M., Matsunaga, K., Iwasaka, Y., Yamanouchi, T., Hashida, G., and Fukatsu, T.: Chemistry of sea-salt particles and inorganic halogen species in Antarctic regions: compositional differences between coastal and inland stations, J. Geophys. Res.: Atmos., 109, 2004.

Hopkins, R. J., Desyaterik, Y., Tivanski, A. V., Zaveri, R. A., Berkowitz, C. M., Tyliszczak, T., Gilles, M. K., and Laskin, A.: Chemical speciation of sulfur in marine cloud droplets and particles: Analysis of individual particles from the marine boundary layer over the California current, J. Geophys. Res.: Atmos., 113, 2008.

Laskin, A., Moffet, R. C., Gilles, M. K., Fast, J. D., Zaveri, R. A., Wang, B., Nigge, P., and Shutthanandan, J.: Tropospheric chemistry of internally mixed sea salt and organic particles: Surprising reactivity of NaCl with weak organic acids, J. Geophys. Res.: Atmos., 117, 2012.

Liu, Y., Cain, J. P., Wang, H., and Laskin, A.: Kinetic study of heterogeneous reaction of deliquesced NaCl particles with gaseous HNO_3 using particle-on-substrate stagnation flow reactor approach, J. Phys. Chem. A, 111, 10026-10043, 2007.

Manders, A. M. M., Schaap, M., Querol, X., Albert, M. F. M. A., Vercauteren, J., Kuhlbusch, T. A. J., and Hoogerbrugge, R.: Sea salt concentrations across the European continent, Atmos. Environ., 44, 2434-2442, 2010.

Moffet, R. C., Roedel, T. C., Kelly, S. T., Yu, X. Y., Carroll, G. T., Fast, J., Zaveri, R. A., Laskin, A., and Gilles, M. K.: Spectro-microscopic measurements of carbonaceous aerosol aging in central California, Atmos. Chem. Phys., 13, 10445-10459, 2013.

Noble, C. A., and Prather, K. A.: Real-time single particle monitoring of a relative increase in marine aerosol concentration during winter rainstorms, Geophys. Res. Lett., 24, 2753-2756, 1997.

O'Brien, R. E., Wang, B., Laskin, A., Riemer, N., West, M., Zhang, Q., Sun, Y., Yu, X.-Y., Alpert, P., Knopf, D. A., Gilles, M. K., and Moffet, R. C.: Chemical imaging of ambient aerosol particles: Observational constraints on mixing state parameterization, J. Geophys. Res.: Atmos., 120, 9591-9605, 2015.

Pilson, M. E. Q.: An introduction to the chemistry of the sea, Cambridge University Press, 1998.

Shaw, G. E.: Aerosol chemical-components in Alaska air masses. 2. Sea salt and marine product, J. Geophys. Res.: Atmos., 96, 22369-22372, 1991.

Silva, B., Rivas, T., Garcia-Rodeja, E., and Prieto, B.: Distribution of ions of marine origin in Galicia (NW Spain) as a function of distance from the sea, Atmos. Environ., 41, 4396-4407, 2007.

Udisti, R., Dayan, U., Becagli, S., Busetto, M., Frosini, D., Legrand, M., Lucarelli, F., Preunkert, S., Severi, M., Traversi, R., and Vitale, V.: Sea spray aerosol in central Antarctica. Present atmospheric behaviour and implications for paleoclimatic reconstructions, Atmos. Environ., 52, 109-120, 2012.

Ueda, S., Hirose, Y., Miura, K., and Okochi, H.: Individual aerosol particles in and below clouds along a Mt. Fuji slope: modification of sea-salt-containing particles by in-cloud processing, Atmos. Res., 137, 216-227, 2014.

Appendix C.

Isoprene-Derived Organosulfates: Vibrational Mode Analysis by Raman Spectroscopy, Acidity-Dependent Spectral Modes, and Observation in Individual Atmospheric Particles Supplemental Information

C.1. Synthesis of the 3-Methyltetrol Sulfate Esters (from δ-IEPOX)

2-Methyl-2-vinyloxirane (~1 g) was dissolved in acetonitrile (ACN)/H_2O (50:50, 30 mL), a few drops of trifluoroacetic acid was added and the mixture was stirred at room temperature. The reaction was monitored by NMR spectroscopy until the complete disappearance of the oxiranyl proton signals. The mixture was distilled under reduced pressure on a rotary evaporator to remove the solvent. The resulting residue was dissolved in ACN (~30 mL) and cooled on ice water while *m*CPBA (1.2 equivalent based on the starting isoprene monoepoxide) was added. The mixture was allowed to warm to ambient temperature, stirred, and monitored by thin layer chromatography (TLC) until the reaction was complete. Precipitate that had formed was filtered off, the filtrate concentrated, and the residue purified by column chromatography (silicon gel/ether) to afford δ-IEPOX.

The δ-IEPOX was dissolved in anhydrous acetonitrile and cooled on ice water and Bu_4NHSO_4 (1 eq.) was added followed by a small amount of potassium bisulfate. The reaction was stirred and allowed to warm to room temperature overnight. The solvent was removed under reduced pressure on a rotary evaporator and the residue purified on an ion exchange column (Dowex 50 W x 4-100) neutralized with 1 N K_2CO_3 before being packed. The column was eluted with water and monitored by TLC. The fractions containing product were pooled and lyophilized to give the product as a white powder.

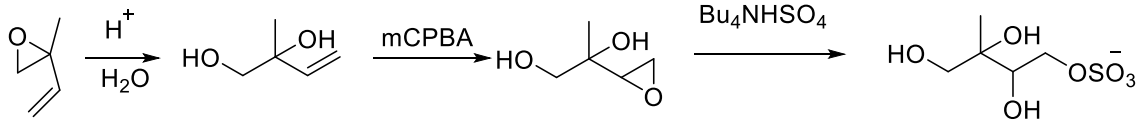

Scheme S1. Synthesis of the 3-methyltetrol sulfate esters.

C.2. Synthesis of the 2-Methyltetrols

To the aqueous solution of δ-IEPOX, a catalytic amount of trifluoroacetic acid was added and the mixture was allowed to stir at room temperature or heated under reflux until the NMR indicated the absence of oxiranyl protons. The reaction mixture was then concentrated under reduced pressure on a rotary evaporator and the concentrated solution lyophilized to yield the 2-methyltetrol mixture.

C.3. Nuclear Magnetic Resonance Spectroscopy (^{1}H NMR) of Organosulfate Esters and Polyols

^{1}H NMR spectra (400 MHz, D_2O) were acquired for the 3-methyltetrol sulfate esters, the 2-methyltetrols, 2-methylglyceric acid sulfate ester, and 2-methylglyceric acid. Spectra were collected using a 400 MHz Varian spectrometer. NMR spectra are consistent with previously reported spectra (Budisulistiorini et al., 2015; Rattanavaraha et al., 2016).

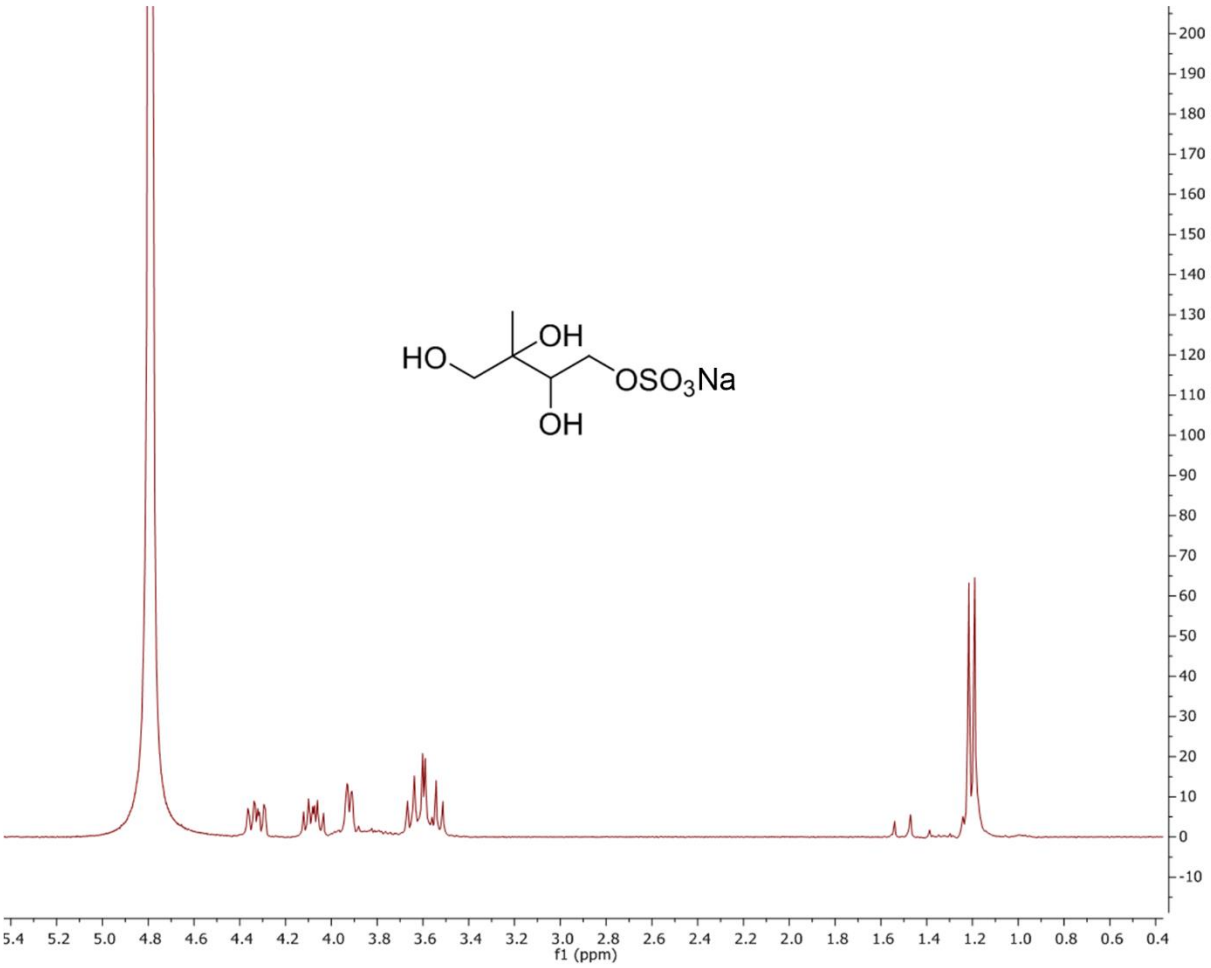

Figure C.1. ^{1}H NMR spectrum (400 MHz, D_2O) of the 3-methyltetrol sulfate esters formed from δ-IEPOX.

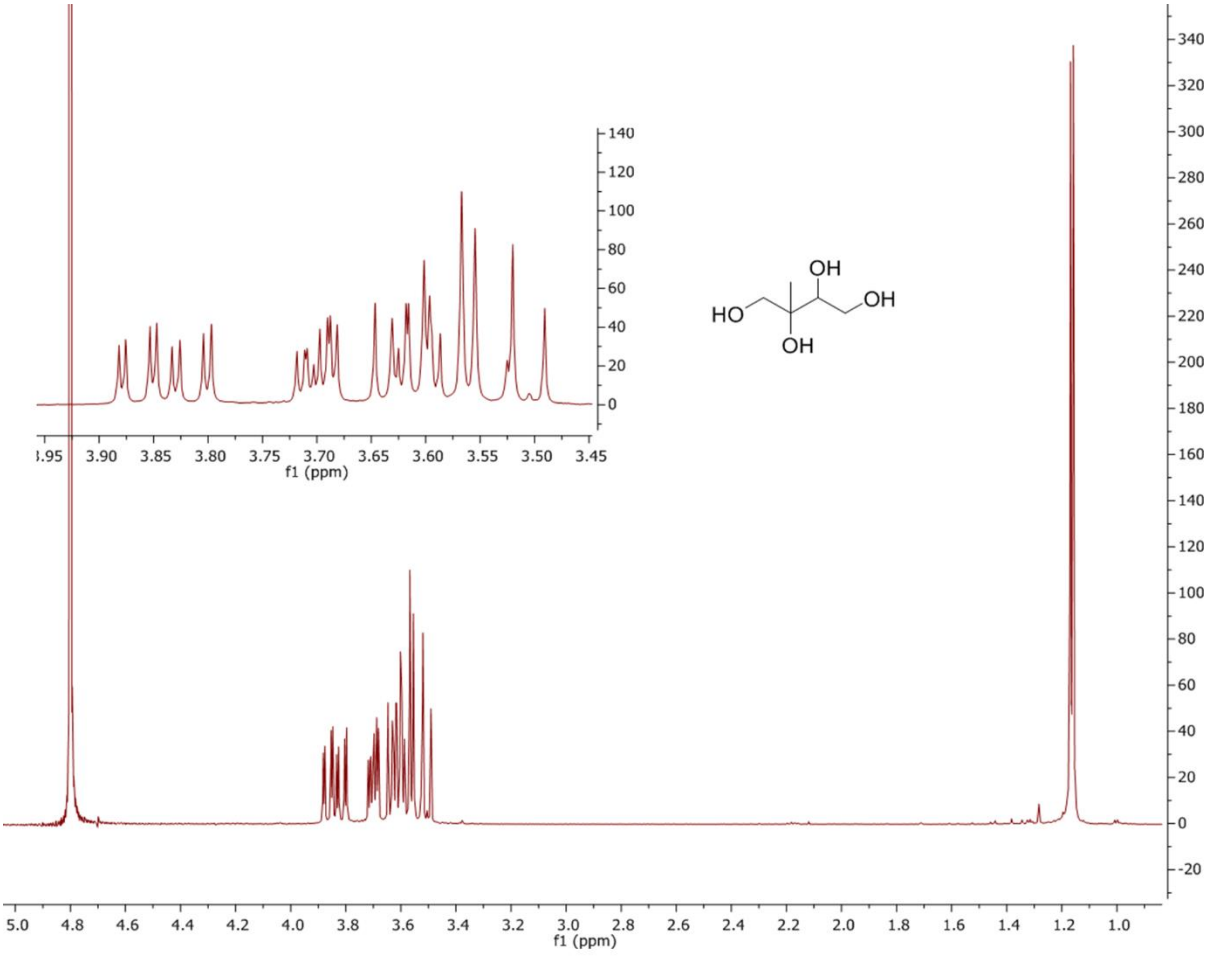

Figure C.2. ^{1}H NMR spectrum (400 MHz, D_2O) of the 2-methyltetrols formed from δ-IEPOX.

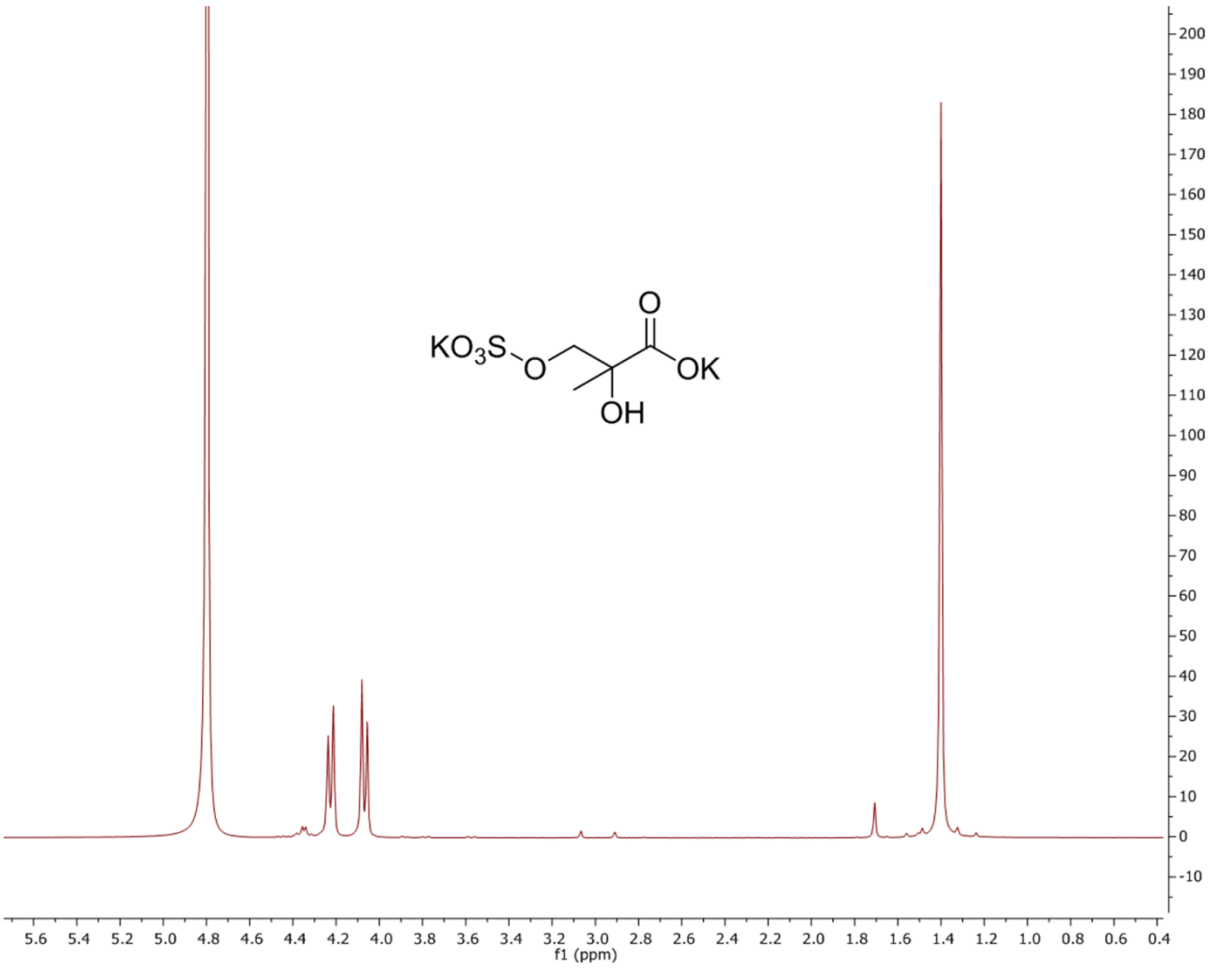

Figure C.3. ^{1}H NMR spectrum (400 MHz, D_2O) of 2-methylglyceric acid sulfate ester.

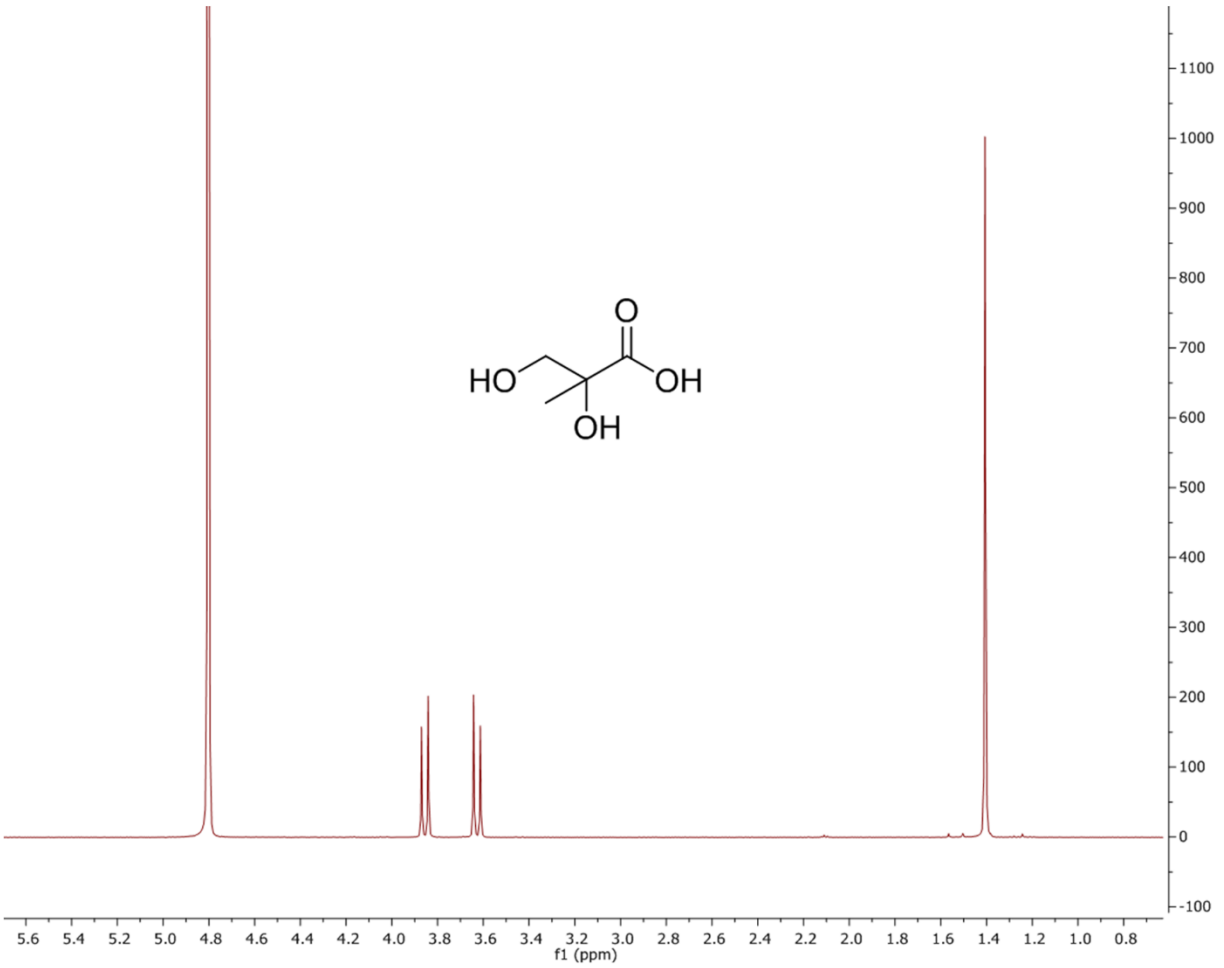

Figure C.4. ^{1}H NMR spectrum (400 MHz, D_2O) of 2-methylglyceric acid.

C.4. Fourier Transform Infrared Spectroscopy (FTIR) of Organosulfate Esters

Attenuated total reflection Fourier transform infrared spectroscopy (ATR-FTIR) spectra were collected for the 3-methyltetrol sulfate esters and 2-methylglyceric acid sulfate ester. Spectra were collected using a Shimadzu IRTracer-100, from 600-4700 cm^{-1} with 2 cm^{-1} resolution and 25 scans. Characteristic infrared absorption bands of organic sulfate esters appeared at 1212-1217cm^{-1} ($\nu_{as}(SO_3)$ 1200-1220 cm^{-1}), 1063-1065 cm^{-1} ($\nu_s(SO_3)$ 1040-1070 cm^{-1}), and 767-780 cm^{-1} (ν(S-O-C) 750-800 cm^{-1}), consistent with previous results (Chihara, 1958; Chihara, 1960; Larkin, 2011).

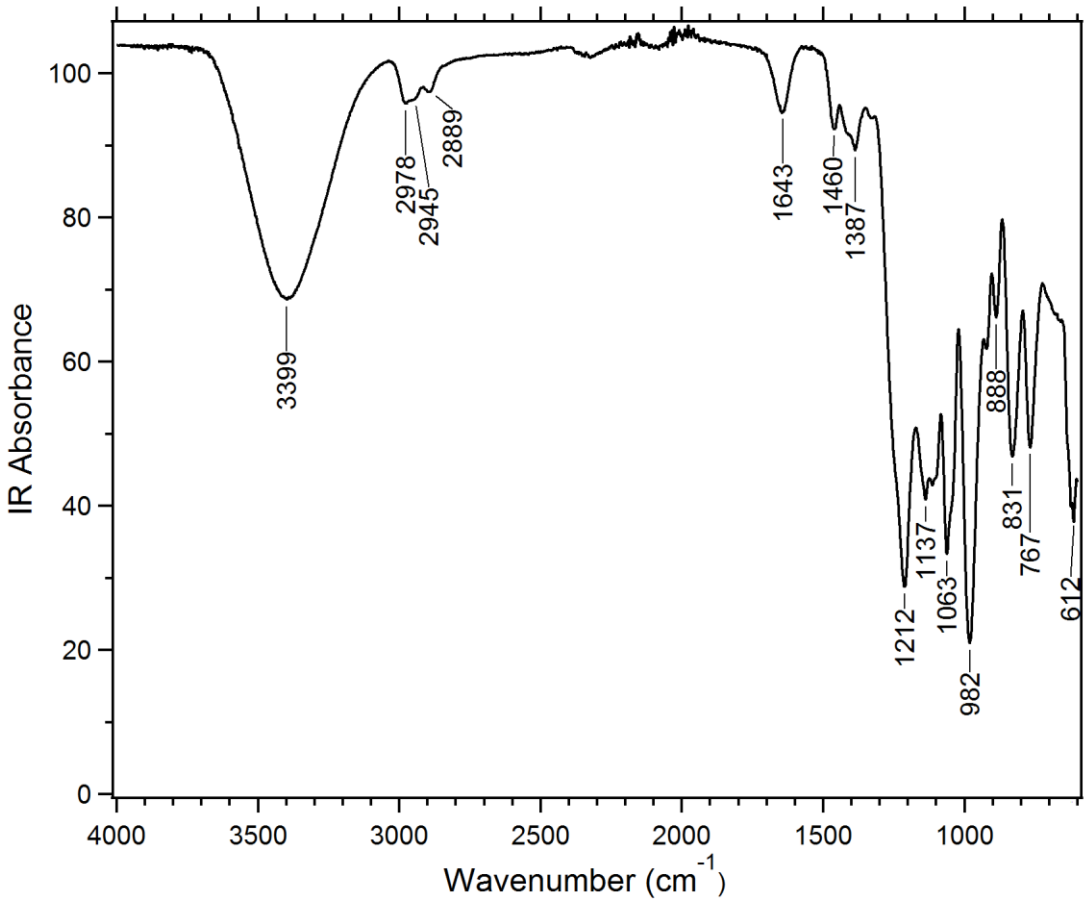

Figure C.5. FTIR spectrum of the solid (crystalline) 3-methyltetrol sulfate esters.

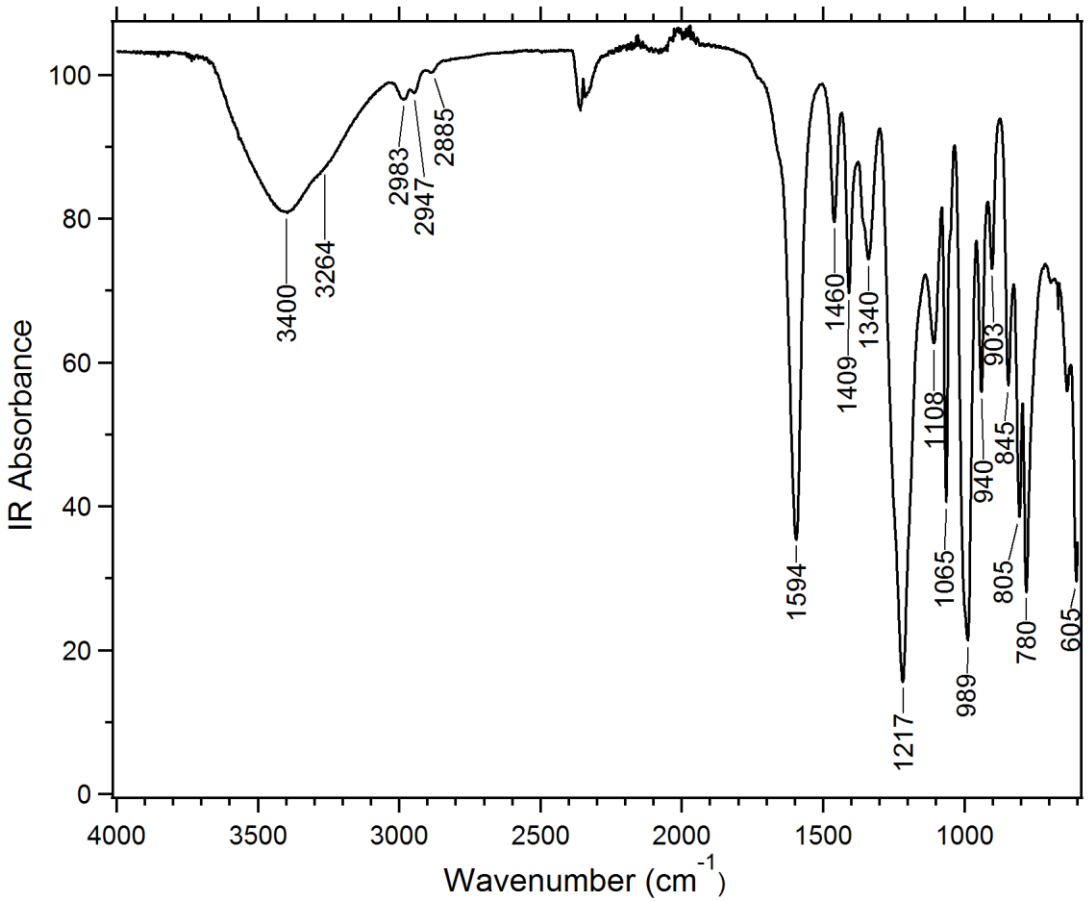

Figure C.6. FTIR spectrum of solid (crystalline) 2-methylglyceric acid sulfate ester.

C.5. Energy Dispersive X-Ray Spectroscopy (EDX) of Organosulfate Esters

EDX spectra were collected for crystals of the 3-methyltetrol and 2-methylglyceric acid sulfate esters to verify the identity of the counter-ions associated with the organosulfates. Crystals of each organosulfate were deposited on Si wafers and analyzed using a FEI Helios scanning electron microscope equipped with an EDX spectrometer (EDAX, Inc.). X-ray energies corresponding to carbon, oxygen, sodium, and sulfur were detected for the 3-methyltetrol sulfate esters. Similarly, X-ray energies corresponding to carbon, oxygen, sulfur, and potassium were detected for 2-methylglyceric acid sulfate ester. As the frequency of ν(C-O) in 2-methylglyceric acid sulfate ester was significantly lower than the modes in the 2-methyltetrols and 2-methylglyceric acid (1008 cm^{-1} compared to 1047 and 1056 cm^{-1}, respectively), EDX verified that the mode at 1008 cm^{-1} was not related to $CaSO_4$ ($\nu_s(SO_4^{2-})$ at 1005 cm^{-1}) (Vargas Jentzsch et

al., 2013). These results, with sodium associated with the 3-methyltetrol sulfate esters and potassium associated with 2-methylglyceric acid sulfate ester, are consistent with expected results based on the synthetic procedure. Note, the silicon signal is due to the substrate.

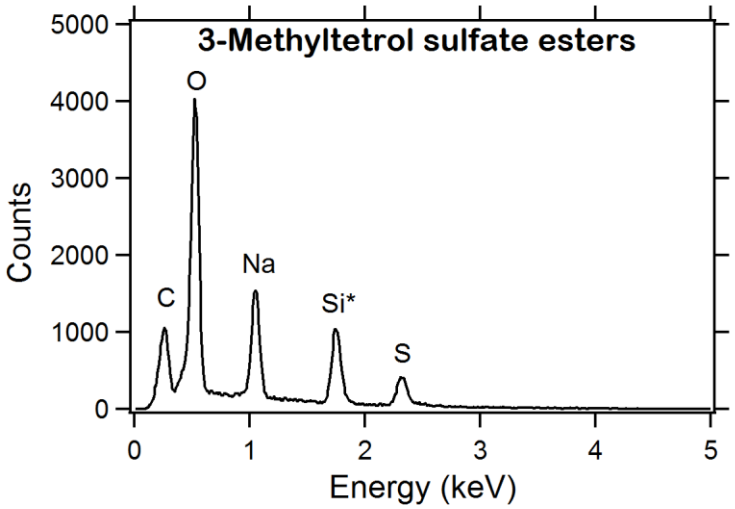

Figure C.7. EDX spectrum of the 3-methyltetrol sulfate esters. Note, the Si signal is due to the substrate.

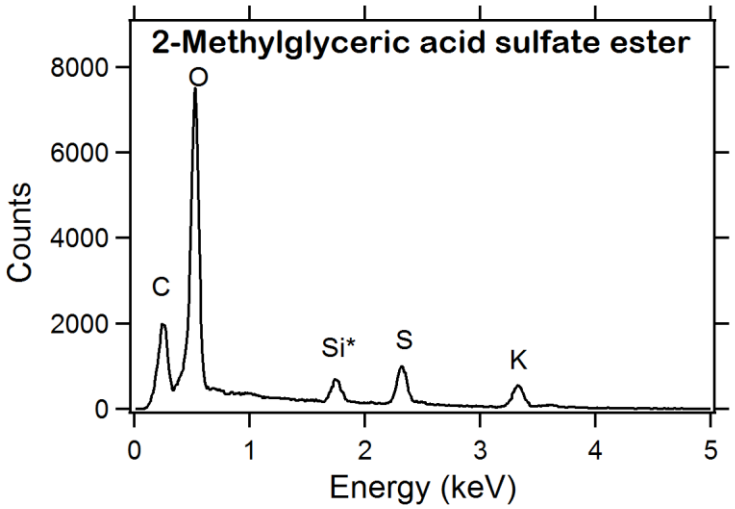

Figure C.8. EDX spectrum of 2-methylglyceric acid sulfate ester. Note, the Si signal is due to the substrate.

C.6. Experimental Raman Spectra of Compounds

Sample compounds were prepared for Raman analysis using the following three methods:

1. Crystals (3-methyltetrol sulfate esters, 2-methylglyceric acid sulfate ester, 2-methylglyceric acid) or a 2 µL droplet (2-methyltetrols) were placed on quartz substrates without further preparation for Raman analysis.
2. Aqueous droplets (2 µL) of 0.05 M solutions of each compound were placed on quartz substrates for Raman analysis.
3. Aerosol particles were generated on quartz substrates from liquid (2-methyltetrols and 2-methylglyceric acid) and aqueous 0.05M solutions (3-methyltetrol sulfate esters and 2-methylglyceric acid sulfate ester) for Raman analysis.

Raman spectra were collected for each compound, the 3-methyltetrol sulfate esters, 2-methylglyceric acid sulfate ester, 2-methyltetrols, and 2-methylglyceric acid using all three methods listed above. For this analysis, spectra were collected using the 600 g/mm diffraction grating (~1.7 cm^{-1} spectral resolution), a ND filter operated at 100 %, 30 second acquisition times, and 3 accumulations.

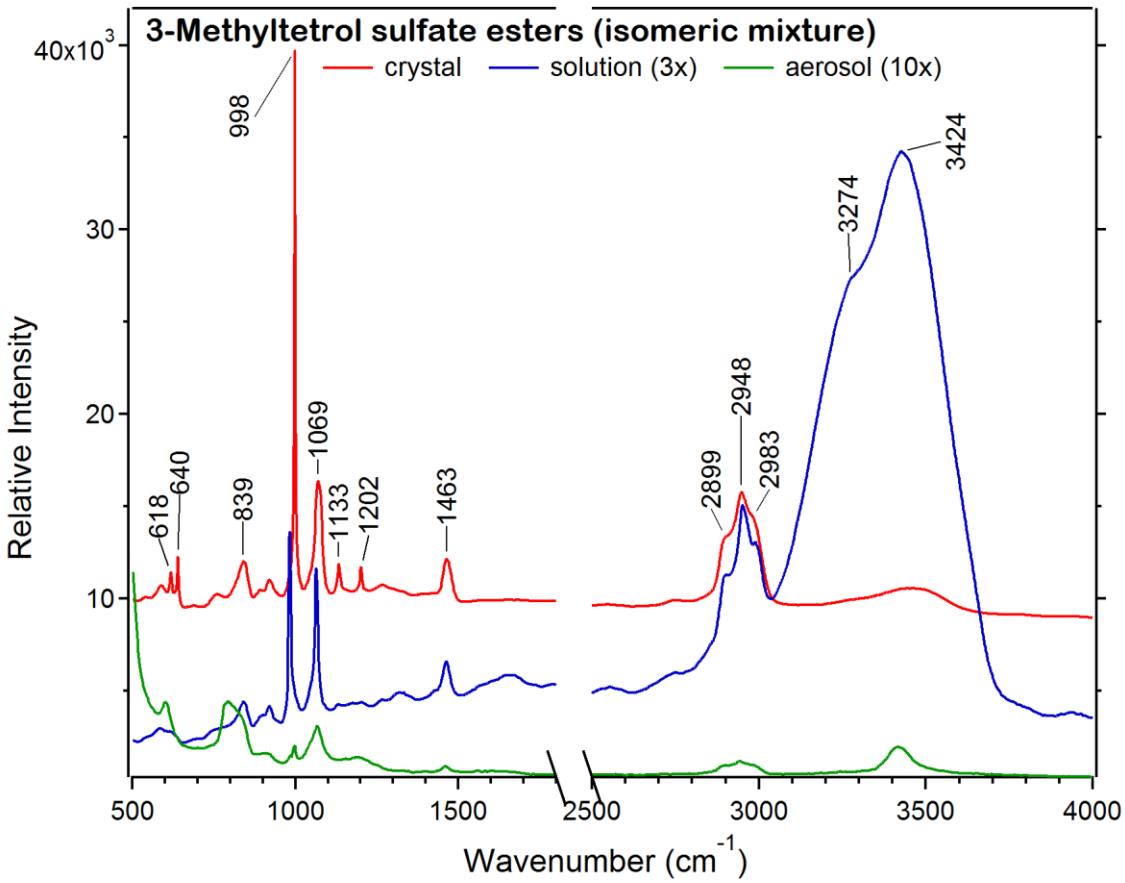

Figure C.9. Experimental Raman spectra collected for a crystal, a 1 mm diameter droplet of aqueous solution, and a 5 µm diameter aerosol particle of the 3-methyltetrol sulfate esters. Due to differences in Raman intensity between the three spectra, the intensity of the aqueous solution was multiplied by a factor of three and the intensity of the aerosol particle was multiplied by a factor of 10.

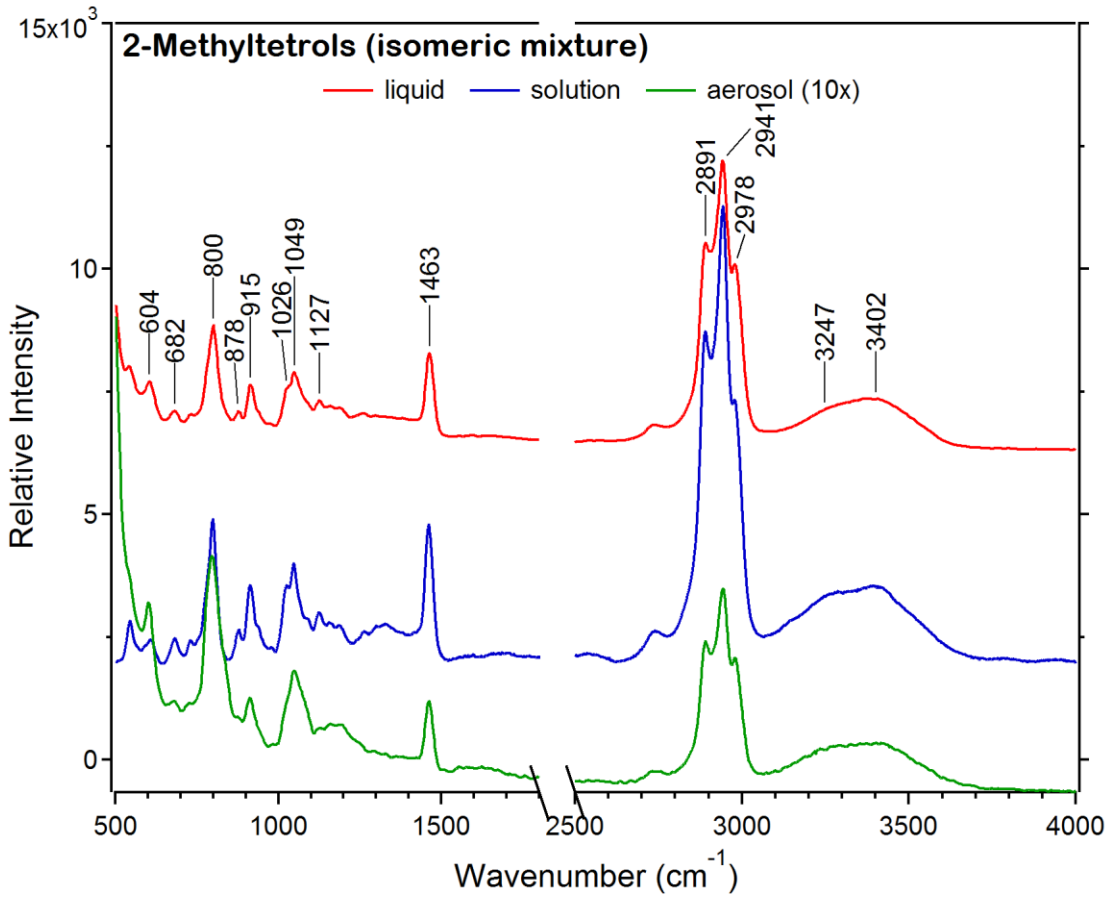

Figure C.10. Experimental Raman spectra collected for a 1 mm droplet of pure liquid, a 1 mm diameter droplet of aqueous solution, and a 8 μm diameter aerosol particle of the 2-methyltetrols. Due to differences in Raman intensity between the spectra, the intensity of the aerosol particle was multiplied by a factor of 10.

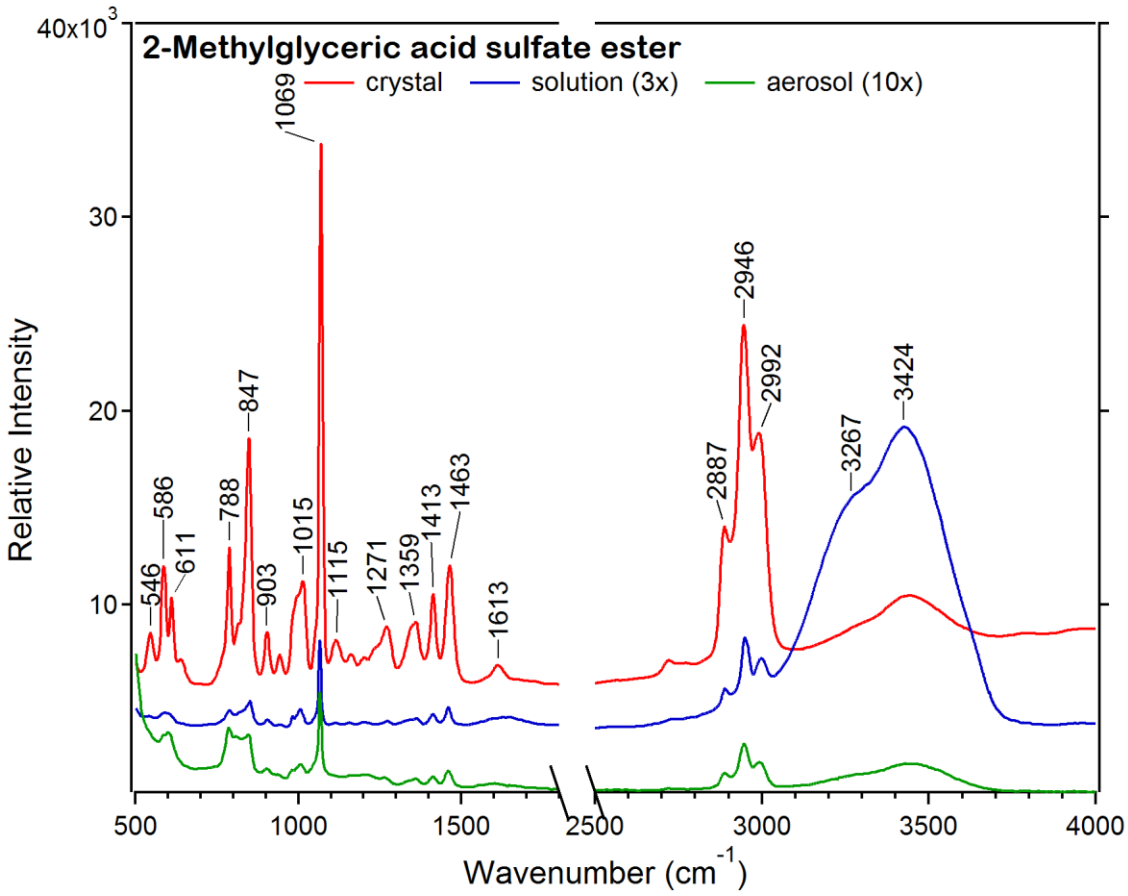

Figure C.11. Experimental Raman spectra collected for a crystal, a 1 mm diameter droplet of aqueous solution, and a 4 μm diameter aerosol particle of 2-methylglyceric acid sulfate ester. Due to differences in Raman intensity between the three spectra, the intensity of the aqueous solution was multiplied by a factor of three and the intensity of the aerosol particle was multiplied by a factor of 10.

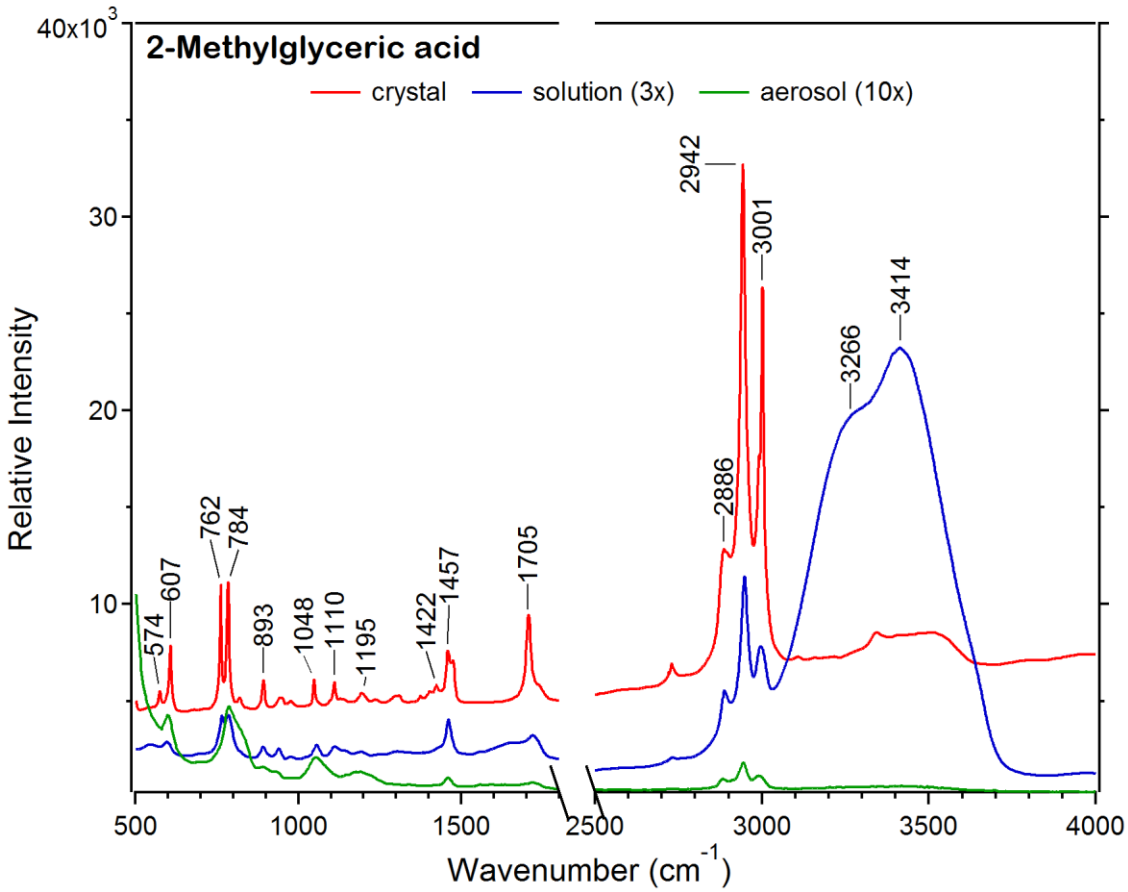

Figure C.12. Experimental Raman spectra collected for a crystal, a 1 mm diameter droplet of aqueous solution, and a 4 μm diameter aerosol particle of 2-methylglyceric acid. Due to differences in Raman intensity between the three spectra, the intensity of the aqueous solution was multiplied by a factor of three and the intensity of the aerosol particle was multiplied by a factor of 10.

C.7. Computed Raman Frequencies

Initially, molecular structures and vibrational spectra were computed for the organosulfates and their hydrolysis products using density functional theory (DFT) at the B3LYP level of theory. However, as calculated frequencies had large errors compared to the anticipated experimental modes based on published studies of small-molecule organosulfates, we evaluated the predicting performances of different functionals and basis sets using methyl sulfate as a surrogate. In Table C.1, the frequencies for the $\nu_s(SO_3)$ mode of methyl sulfate calculated using different parameters are shown. Based on these results, the DFT CAM-B3LYP level of theory was chosen for the work presented to compromise between prediction performance and computer-time requirement.

Table C.1. Computed Raman frequencies for the $\nu_s(SO_3)$ mode in methyl sulfate.

Experimental	B3LYP (solvated) 6-311 ++ G(2d,p)	CAM-B3LYP 6-31 ++ G(d)	CAM-B3LYP (solvated) 6-311 ++ G(2d,p)	M06-2X 6-31 ++ G(d)	MP2 6-31 ++ G(d)
1063	999	1023	1027	1039	1017

C.8. Raman Modes, Detailed DFT Frequencies, and Tentative Assignments

For each compound analyzed in this study, the 3-methyltetrol sulfate esters, 2-methyltetrols, 2-methylglyceric acid sulfate ester, and 2-methylglyceric acid, experimental Raman spectra were collected and the DFT Raman spectra were calculated at the CAM-B3LYP/6-311 ++ G(2d,p) level of theory. In Tables C.2-C.5 below, detailed analysis of the Raman modes are presented for each of the compounds. The experimental Raman shift and relative intensity is given, as well as the DFT-calculated frequency and Raman activity. Furthermore, assignments were made for the DFT Raman modes based on motions observed from 3D vibration animations and comparison to literature Raman mode assignments (Matyas et al., 2016; Cassanas et al., 1993; Leyton et al., 2008; Larkin, 2011; Avzianova and Brooks, 2013; De Gelder et al., 2007; McLaughlin et al., 2002; Furić et al., 1992; Lee and Chan, 2007; Craig et al., 2015; Cooney et al., 1994; Zhou et al., 2014; Fayer, 2013).

Table C.2. Detailed Raman modes for the 3-methyltetrol sulfate esters. The relative intensity and frequency of each vibration are given for the experimental spectrum, and the frequencies and Raman activities of the tentative DFT calculations are listed. Organosulfate-related stretching modes are highlighted in yellow and bending modes in blue.

	DFT Raman modes: 3-methylerythritol sulfate ester (cm^{-1})	**DFT Raman modes: 3-methylthreitol sulfate ester (cm^{-1})**	**Assignment**
	547[a] (6)	531[a] (1)	SO_3 scissor
584 (vw)[a,b]	561[a] (3)	546[a] (5)	SO_3 wag
		563 (3)	O-H bend
	596[a] (5)	602[a] (4)	SO_3 wag
619 (vw)	639 (1)	579 (1)	O-H bend
		681 (12)	C-C-O wag
842 (m)[a]	727[a] (6)	732[a] (6)	RO-SO_3 stretch
	672[a] (7)	827 (22)	C-C-O wag
	803 (26)	890 (4)	C-C bend
895 (sh)	903 (3)	944 (8)	C-C stretch, CH_2 twist
920 (w)	939 (7)	954 (5)	C-C stretch, CH_2 rock
	975 (5)	978 (5)	CH_2 rock, CH_3 rock
	997 (4)		CH_2 & CH_3 rock, C-C stretch
982 (vs)[c]			SO4 sym. Stretch (salt)
	1003 (40)		CH_2 & CH_3 rock
1047 (sh)		1006 (47)	C-O stretch
1063 (vs)[a]	1047 (31)	1054 (27)	SO_3 sym. Stretch
	1066[a] (13)	1063[a] (12)	C-O stretch
	1107 (8)	1117 (4)	C-O stretch
	1131 (3)	1128 (1)	C-O stretch, C-C stretch
	1161[a] (7)		CH_3 wag, CH_2 wag
	1174 (10)	1167 (11)	CH_3 wag, C-C stretch
	1184 (10)	1188 (12)	SO_3 asym. Stretch
	1206[a] (7)	1211[a] (8)	CH_3 wag, C-C stretch
	1245 (12)	1245 (13)	SO_3 asym. Stretch
	1262 (5)	1266 (3)	CH_2 twist
	1278 (14)	1285 (7)	CH_2 twist, C-H bend
	1300 (7)	1297 (15)	CH_2 twist, C-H bend
	1346 (8)	1345 (4)	CH_2 twist, C-H bend
	1367 (3)	1372 (6)	C-H bend
	1385 (3)	1386 (2)	CH_2 and CH_3 wag
	1409 (3)	1407 (5)	CH_2 wag, C-H bend, CH_3 wag
	1415 (5)		CH_2 wag
	1451 (2)	1419 (1)	CH, CH_2, &CH_3 wag

		1447 (2)	CH and CH_2 wag
	1484 (7)	1481 (8)	CH_2 and CH3 wag
	1500 (3)	1497 (1)	CH_3 scissor
1462 (m)	1500 (3)	1503 (27)	CH_3 scissor
	1510 (15)	1510 (4)	CH_2 scissor
	1516 (3)	1517 (4)	CH_2 scissor
2741 (w)	3018 (222)	3017 (170)	CH_2 sym. Stretch
2899 (s)	3055 (184)	3048 (175)	CH_2 sym. Stretch
2950 (vs)	3066 (366)	3066 (391)	C-H stretch
2992 (s)	3097 (205)	3110 (213)	CH_3 sym. Stretch
	3114 (118)	3134 (109)	CH_2 asym. Stretch
	3136 (117)	3138 (143)	CH_2 asym. Stretch
	3141 (115)	3145 (97)	CH_3 asym. Stretch
	3158 (104)	3167 (110)	CH_3 asym. Stretch
	3549 (227)	3562 (243)	O-H stretch
3243 (s)	3786 (136)	3795 (137)	O-H stretch
3454 (vs)	3877 (160)	3878 (158)	O-H stretch

[a] Frequencies highlighted in blue correspond to bending modes associated with the organosulfate group, while frequencies highlighted in yellow correspond to organosulfate-related stretching modes.

[b] Possible $\delta(SO_3)$ mode, however difficult to differentiate from background.

[c] Indicates contamination.

Table C.3. Detailed Raman modes for 2-methyltetrols. The relative intensity and frequency of each vibration are given for the experimental spectra, and the frequencies and Raman activities of the tentative DFT calculations are listed.

Experimental Raman modes (cm^{-1})	DFT Raman modes: 2-methylerythritol (cm^{-1})	DFT Raman modes: 2-methylthreitol (cm^{-1})	Assignment
545 (m)	550 (1)	566 (2)	CH_2 rock
611 (w)	669 (1)	682 (4)	O-H bend
730 (w)			CH_2 bend
799 (s)	792 (21)	814 (20)	C-OH bend
878 (w)	902 (3)	883 (4)	C-C stretch
914 (m)	942 (7)	946 (6)	CH_2 & CH_3 rock
940 (sh)	975 (5)	972 (4)	CH_2 & CH_3 rock
	997 (5)	980 (5)	CH_2 & CH_3 rock
1022 (sh)	1032 (3)	1040 (4)	C-O stretch, CH_2 rock
1047 (m)	1069 (25)	1078 (19)	C-O stretch
	1094 (3)	1099 (3)	C-O stretch, C-C stretch
	1111 (3)	1110 (2)	CH_2 twist
1125 (w)	1159 (9)	1142 (18)	C-OH stretch
1157 (vw)	1165 (14)	1185 (6)	C-C stretch, CH_2 wag
1192 (vw)	1204 (7)	1201 (6)	CH_3 wag, C-C stretch
	1224 (2)	1235 (3)	CH_3 wag, C-C stretch
	1254 (5)	1257 (8)	CH_2 twist
	1274 (13)	1265 (4)	CH_2 twist, C-H bend
	1280 (9)	1287 (20)	CH_2 twist, C-H bend
	1331 (6)	1320 (2)	CH_2 twist, C-H bend
	1363 (4)		
	1392 (6)	1382 (5)	C-H bend
	1407 (2)	1391 (2)	CH_2 & CH_3 wag
	1434 (7)	1421 (2)	CH_2 wag, C-H bend
		1435 (4)	CH_2 & CH_3 wag
	1454 (3)	1464 (3)	CH_2 wag
	1474 (2)	1468 (2)	CH_2 & CH bend
1462 (s)	1498 (13)	1505 (16)	CH_3 bend
	1504 (12)	1492 (9)	CH_3 bend
	1514 (1)	1517 (1)	CH_2 scissor
	1515 (9)	1519 (8)	CH_2 scissor
2751 (w)	3020 (236)	3027 (12)	CH Stretch
2895 (s)	3054 (215)	3035 (418)	CH_2 sym. Stretch
	3061 (57)	3061 (105)	CH_2 sym. Stretch
2942 (vs)	3067 (523)	3069 (436)	CH_3 sym. Stretch
2983 (s)	3110 (156)	3088 (137)	CH_2 asym. Stretch
	3112 (59)	3113 (95)	CH_2asym. Stretch
	3138 (113)	3138 (117)	CH_3 asym. Stretch
	3142 (119)	3153 (113)	CH_3 asym. stretch
3262 (s)	3785 (123)	3777 (172)	O-H stretch
	3809 (131)	3786 (77)	O-H stretch
	3872 (153)	3871 (156)	O-H stretch
3435 (s)	3875 (159)	3873 (159)	O-H stretch

Table C.4. Detailed Raman modes for the 2-methylglyceric acid sulfate ester. The relative intensity and frequency of each vibration are given for the experimental spectrum, and the frequencies and Raman activities of the tentative DFT calculations are listed. Organosulfate-related stretching modes are highlighted in yellow and bending modes in blue.

Experimental Raman modes (cm^{-1})	DFT Raman modes (cm^{-1})	Assignment
543 (w)	521 (2)	C-H bend
	556[a] (4)	S-O scissoring
587 (m)[a,b]	564[a] (3)	S-O scissoring
608 (m)	580 (4)	O-H bend
788 (m)		C-OH wag, O-H bend
834 (sh)	593 (4)	O-H bend
	664[a] (7)	C-OH wag, R-OSO_3 stretch
850 (s)[a]	748[a] (5)	RO-SO_3 stretch
905 (w)	788 1)	CH_3 rock
941 (vw)	815 (41)	C-C stretch, CH_2 rock, CH_3 wag
	916 (5)	CH_3 rock, C-C stretch
979 (m)[c]		SO_4^{2-} sym. stretch
1008 (m)	973 (4)	C-O stretch
	1006 (6)	CH_3 rock
1066 (vs)[a]	1031[a] (51)	SO_3 sym. stretch
1116 (vw)	1092 (12)	C-OH stretch
1158 (vw)	1146 (6)	C-C stretch, CH_3 rock
	1168 (5)	C-C stretch, CH_2 twist
	1204 (13)	SO_3 asym. stretch
1271 (w)	1211[a] (7)	CH_2 & CH_3 twist
	1235[a] (12)	SO_3 asym. stretch
1347 (sh)	1249 (10)	C-O stretch, CH_2 twist, CH_3 wag
1365 (m)	1310 (9)	CH_2 twist,
	1347 (5)	C-H bend
1413 (m)[d]		COO^- sym. stretch
	1404 (1)	CH_2 & CH_3 wag
	1427 (5)	CH_2 & CH_3 wag
	1442 (3)	CH_2 wag
1460 (s)	1491 (13)	CH_3 bend
	1495 (6)	CH_3 bend
	1512 (7)	CH_2 bend
1595 (vw)[d]		COO^- asym. stretch
	1792 (33)	C=O stretch
2731 (vw)	3067 (108)	CH_2 sym. stretch
2894 (s)	3072 (404)	CH_3 sym. stretch
	3126 (74)	CH_2 asym. stretch
2947 (vs)	3146 (118)	CH_3 asym. stretch
2994 (s)	3160 (113)	CH_3 asym. stretch
3259 (vs)	3745 (102)	O-H stretch
3465 (vs)	3761 (165)	O-H stretch

[a] Frequencies highlighted in blue correspond to bending modes associated with the organosulfate group, while frequencies highlighted in yellow correspond to organosulfate-related stretching modes.

[b] Possible $\delta(SO_3)$ mode, however difficult to differentiate from background.

[c] Indicates contamination.

[d] Experimental results indicate carboxylate ion rather than carboxylic acid group is present.

Table C.5. Detailed Raman modes for 2-methylglyceric acid. The relative intensity and frequency of each vibration are given for the experimental spectrum, and the frequencies and Raman activities of the tentative DFT calculations are listed.

Experimental Raman modes (cm^{-1})	DFT Raman modes (cm^{-1})	Assignment
551 (m)	531 (2)	C-H bend
599 (s)	602 (1)	O-H bend
	656 (2)	C-OH wag
764 (vs)	769 (26)	O-C-O bend
788 (vs)	794 (3)	C-OH wag, O-H bend
893 (m)	912 (3)	C-C stretch
940 (m)	958 (4)	C-C stretch, CH_2 rock, CH_3 wag
977 (vw)	997 (6)	CH_3 wag, C-O stretch
1056 (m)	1072 (5)	C-O stretch
1112 (m)	1136 (9)	C-OH stretch
1143 (w)	1152 (10)	C-O stretch, CH_2 twist
	1190 (3)	C-C stretch, CH_3 wag
1190 (w)	1222 (5)	C-C stretch, CH_2 twist
1246 (vw)	1269 (5)	CH_2 wag
1307 (vw)	1299 (8)	CH_2 twist
	1340 (9)	CH_2 twist
	1404 (1)	CH_3 wag
	1442 (5)	CH_3 wag
1430 (vw)	1455 (3)	CH_2 wag
1462 (s)	1491 (10)	CH_3 bend
	1501 (8)	CH_3 bend
	1516 (5)	CH_2 bend
1724 (s)	1794 (23)	C=O stretch
2737 (w)	3061 (108)	CH_2 sym. stretch
2896 (s)	3067 (426)	CH_3 sym. stretch
2946 (vs)	3116 (109)	CH_2 asym. stretch
	3143 (118)	CH_3 asym. stretch
2992 (s)	3147 (123)	CH_3 asym. stretch
3212 (vs)	3759 (166)	O-H stretch
3436 (vs)	3778 (118)	O-H stretch
	3875 (144)	O-H stretch

C.6. References

Avzianova, E., and Brooks, S. D.: Raman spectroscopy of glyoxal oligomers in aqueous solutions, Spectrochim. Acta, Part A, 101, 40-48, 2013.

Budisulistiorini, S. H., Li, X., Bairai, S. T., Renfro, J., Liu, Y., Liu, Y. J., McKinney, K. A., Martin, S. T., McNeill, V. F., Pye, H. O. T., Nenes, A., Neff, M. E., Stone, E. A., Mueller, S., Knote, C., Shaw, S. L., Zhang, Z., Gold, A., and Surratt, J. D.: Examining the effects of anthropogenic emissions on isoprene-derived secondary organic aerosol formation during the 2013 Southern Oxidant and Aerosol Study (SOAS) at the Look Rock, Tennessee ground site, Atmos. Chem. Phys., 15, 8871-8888, 2015.

Cassanas, G., Kister, G., Fabrègue, E., Morssli, M., and Bardet, L.: Raman spectra of glycolic acid, l-lactic acid and d,l-lactic acid oligomers, Spectrochimica Acta Part A: Molecular Spectroscopy, 49, 271-279, 1993.

Chihara, G.: Characteristic infrared absorption band of organic sulfate esters, Chem. Pharm. Bull., 6, 114-114, 1958.

Chihara, G.: Medical and biochemical application of infrared spectroscopy. V. : Infrared absorption spectra of organic sulfate esters., Chem. Pharm. Bull., 8, 988-994, 1960.

Cooney, T. F., Wang, L., Sharma, S. K., Gauldie, R. W., and Montana, A. J.: Raman spectral study of solid and dissolved poly(vinyl alcohol) and ethylene-vinyl alcohol copolymer Journal of Polymer Science Part B-Polymer Physics, 32, 1163-1174, 1994.

Craig, R. L., Bondy, A. L., and Ault, A. P.: Surface enhanced Raman spectroscopy enables observations of previously undetectable secondary organic aerosol components at the individual particle level, Anal. Chem., 87, 7510-7514, 2015.

De Gelder, J., De Gussem, K., Vandenabeele, P., and Moens, L.: Reference database of Raman spectra of biological molecules, J. Raman Spectrosc., 38, 1133-1147, 2007.

Fayer, M. D.: Chapter 12 - An Introduction to Protein 2D IR Spectroscopy, in: Ultrafast Infrared Vibrational Spectroscopy, CRC Press, 371-372, 2013.

Furić, K., Mohaček, V., Bonifačić, M., and Štefanić, I.: Raman spectroscopic study of H_2O and D_2O water solutions of glycine, J. Mol. Struct., 267, 39-44, 1992.

Larkin, P.: Chapter 8 - Illustrated IR and Raman Spectra Demonstrating Important Functional Groups, in: Infrared and Raman Spectroscopy, Elsevier, Oxford, 135-176, 2011.

Lee, A. K. Y., and Chan, C. K.: Single particle Raman spectroscopy for investigating atmospheric heterogeneous reactions of organic aerosols, Atmos. Environ., 41, 4611-4621, 2007.

Leyton, P., Córdova, I., Lizama-Vergara, P. A., Gómez-Jeria, J. S., Aliaga, A. E., Campos-Vallette, M. M., Clavijo, E., García-Ramos, J. V., and Sanchez-Cortes, S.: Humic acids as molecular assemblers in the surface-enhanced Raman scattering detection of polycyclic aromatic hydrocarbons, Vib. Spectrosc, 46, 77-81, 2008.

Matyas, R., Lycka, A., Jirasko, R., Jakovy, Z., Maixner, J., Miskova, L., and Kunzel, M.: Analytical characterization of erythritol tetranitrate, an improvised explosive, Journal of Forensic Sciences, 61, 759-764, 2016.

McLaughlin, R. P., Bird, B., and Reid, P. J.: Vibrational analysis of isopropyl nitrate and isobutyl nitrate, Spectrochim. Acta, Part A, 58, 2571-2580, 2002.

Rattanavaraha, W., Chu, K., Budisulistiorini, S. H., Riva, M., Lin, Y. H., Edgerton, E. S., Baumann, K., Shaw, S. L., Guo, H., King, L., Weber, R. J., Neff, M. E., Stone, E. A., Offenberg, J. H., Zhang, Z., Gold, A., and Surratt, J. D.: Assessing the impact of anthropogenic pollution on isoprene-derived secondary organic aerosol formation in $PM_{2.5}$ collected from the Birmingham, Alabama, ground site during the 2013 Southern Oxidant and Aerosol Study, Atmos. Chem. Phys., 16, 4897-4914, 2016.

Vargas Jentzsch, P., Kampe, B., Ciobota, V., Rosch, P., and Popp, J.: Inorganic salts in atmospheric particulate matter: Raman spectroscopy as an analytical tool, Spectrochim. Acta, Part A, 115, 697-708, 2013.

Zhou, Q., Pang, S.-F., Wang, Y., Ma, J.-B., and Zhang, Y.-H.: Confocal Raman studies of the evolution of the physical state of mixed phthalic acid/ammonium sulfate aerosol droplets and the effect of substrates, J. Phys. Chem. B, 118, 6198-6205, 2014.

Appendix D.

Atomic Force Microscopy-Infrared Spectroscopy: Sub-Diffraction Limit Spectroscopy and Morphological Analysis of Individual Atmospheric Aerosol Particles Supplemental Information

D.1. Calculations of Volume

Volumes of particles were measured using SPIP software (v6.2.6, Image Metrology, Hørsholm, Denmark), and from these volumes, volume equivalent diameters (D_{ve}) were calculated for each particle analyzed in Figure 5.2 and Figure 5.3.

Table D.1. Diameter, height, calculated volume, and calculated volume equivalent radii and diameters for particles of varying composition impacted on Si. The particles listed correspond to the circled particles in Figure 5.2.

Compound	Diameter (nm)	Height (nm)	Volume (nm^3)	r (nm)	D_{ve} (nm)
$(NH_4)_2SO_4$	535	188	2.17×10^7	173	346
$NaNO_3$	496	114	1.45×10^7	151	303
Succinic acid	556	149	1.97×10^7	167	335
Sucrose	425	55	4.31×10^6	101	202

The D_{ve} for the four particles shown in Figure 5.2 range from 202 nm to 346 nm.

Table D.2. Identification and comparison of AFM-IR vibrational modes in aerosol particles generated from standards compared to FTIR modes from previous studies.

	Mode	Experimental AFM-IR modes (cm^{-1})	Literature FTIR modes (cm^{-1})	Reference
$(NH_4)_2SO_4$	$\nu(SO_4^{2-})$	1091	1095	(Liu et al., 2008)
	$\delta(NH_4^+)$	1422	1415	(Liu et al., 2008)
	$\nu(NH_4^+)$	3139	2800-3300	(Liu et al., 2008) (Weis and Ewing, 1996)
$NaNO_3$	$\nu(NO_3^-)$	1356	~1350	(Liu et al., 2008) (Weis and Ewing, 1999)
Succinic acid	ν(C-C)	1201	1204	(Larkin, 2011) (Miñambres et al., 2010)
	ν(C-O)	1308	1310	(Larkin, 2011) (Miñambres et al., 2010)
	$\nu(CH_2)$	3049	2926	(Larkin, 2011) (Miñambres et al., 2010)
	ν(C=O)	1691	1696	(Larkin, 2011) (Miñambres et al., 2010)
Sucrose	$\delta(CH_2)$	1404	1419	(Max and Chapados, 2001)
	ν(C-O)	1057	1052	(Max and Chapados, 2001)
	δ(C-O-H)	1439	1431	(Max and Chapados, 2001)
	$\nu(CH_2)$	2913	2933	(Max and Chapados, 2001)
	ν(O-H)	3345	3290	(Max and Chapados, 2001)
PEG	ν(C-O-C)	1105	1130	(Larkin, 2011) (Lu et al., 2014)
	$\nu(CH_2)$	1256	1244	(Larkin, 2011) (Lu et al., 2014)

Table D.3. Diameter, height, calculated volume, and calculated volume equivalent radii and diameters for ammonium sulfate particles impacted on various substrates. The particles listed correspond to the circled particles in Figure 5.3.

Substrate	*Diameter (nm)*	*Height (nm)*	*Volume (nm^3)*	*r (nm)*	*D_{ve} (nm)*
Si	453	119	1.19×10^7	142	283
Ge	440	125	2.29×10^7	176	352
ZnSe	312	75	3.53×10^6	94	189
Diamond	341	101	7.03×10^6	119	238
TEM grid	290	57	2.16×10^6	80	160

The D_{ve} for the five ammonium sulfate particles shown in Figure 5.3 range from 160 nm to 352 nm.

D.2. Substrate-Dependent Spreading Ratios

Ammonium sulfate particles impacted on the five various substrates were examined to determine the spreading ratio, a factor which was substrate-dependent. To calculate the spreading ratio, the projected area diameter (D_{pa}) was divided by the height.

$$Spreading\ ratio = \frac{D_{pa}}{h} \tag{D.1}$$

The TEM grid and Ge were shown to cause the least particle spreading, Si caused intermediate spreading, and particles impacted on diamond and ZnSe spread the most. While substrate spreading proved to play a minor role in the study, the spreading (and hence D_{ve}) is important to consider when selecting particles for IR analysis since thicker samples can lead to a deterioration in spatial resolution, and features less than 100 nm in height are difficult to measure since the magnitude of sample thermomechanical expansion decreases with decreasing feature size, although the exact relation between particle size and IR spectral intensity requires further study.

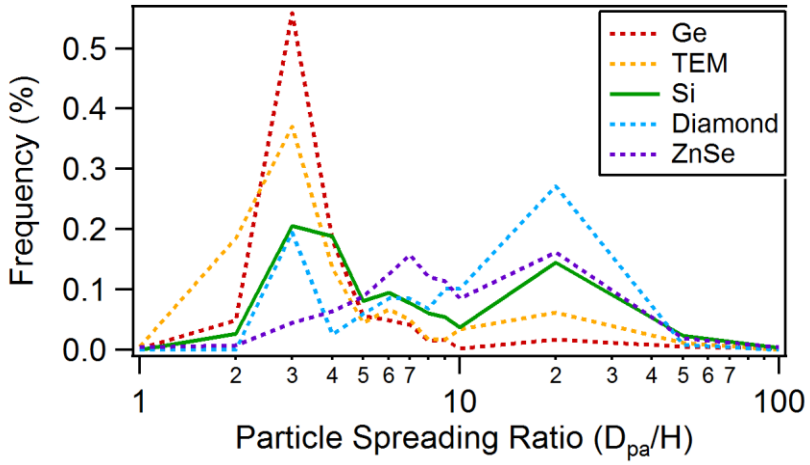

Figure D.1. Average spreading ratios (diameter/height) for ammonium sulfate particles on the following substrates: Ge, TEM grid, Si, Diamond, and ZnSe.

D.3. IR Spectral Resolution

The maximum IR spectral resolution that can be achieved for the nanoIR2 system is 4 cm^{-1}/point. Lower spectral resolution can result in less noise, but the peak full width half maximum (FWHM) tends to broaden and the peak shape is less defined (Figure D.2).

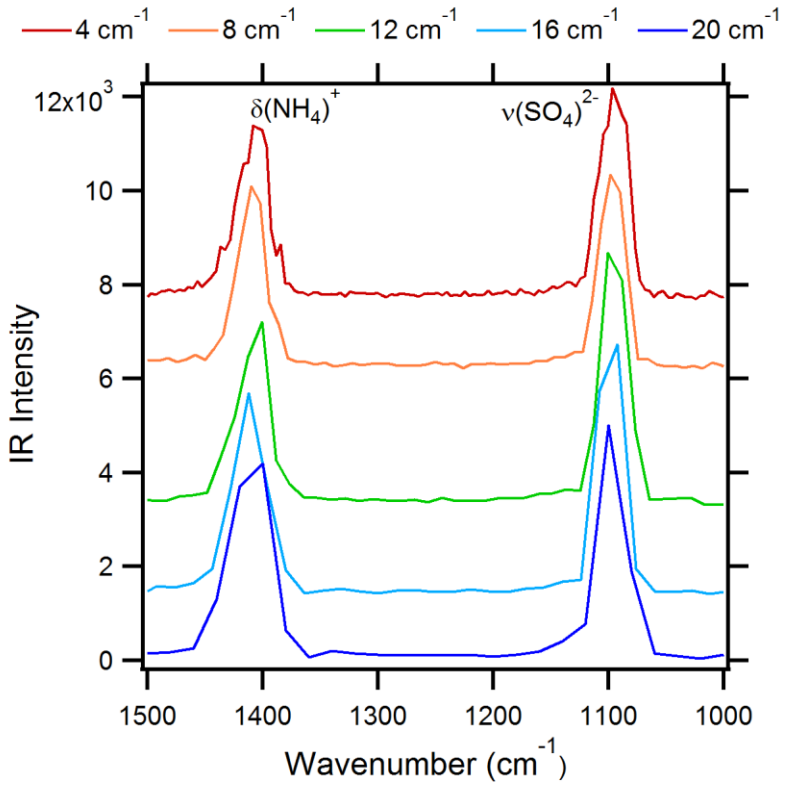

Figure D.2. AFM-IR spectra of ammonium sulfate particles show the peak FWHM increase as spectral resolution decreases and the peak shape becomes less defined.

D.4. IR Peak Ratios

One challenge observed with AFM-IR was peak ratio variation, such as ammonium sulfate peaks (1427 and 1103 cm^{-1}), as a function of particle analyzed (even within a single particle, Figure D.3.) We hypothesize that this results from material heterogeneity or IR photothermal response variation between spectra, however the exact cause this phenomenon requires further investigation. In the 99 % pure ammonium sulfate particles possible contaminants that could lead to variation in NH_4^+ (1427 cm^{-1}) and SO_4^{2-} (1103 cm^{-1}) include Na^+ and Cl^- ions. Furthermore differences in FWHM of NH_4^+ and SO_4^{2-} were likely due to differential hydration levels.

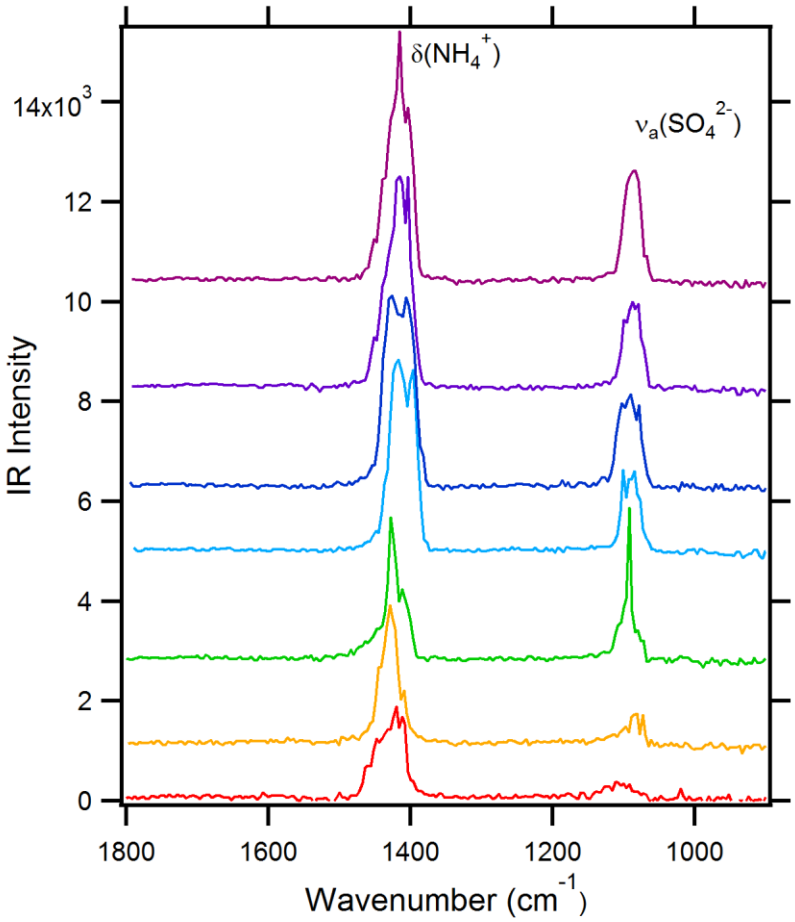

Figure D.3. AFM-IR spectra collected from one ammonium sulfate particle demonstrates variability in $\delta(NH_4^+)$ and $\nu_a(SO_4^{2-})$ peak ratios.

D.5. References

Larkin, P.: Chapter 8 - Illustrated IR and Raman Spectra Demonstrating Important Functional Groups, in: Infrared and Raman Spectroscopy, Elsevier, Oxford, 135-176, 2011.

Liu, Y., Yang, Z., Desyaterik, Y., Gassman, P. L., Wang, H., and Laskin, A.: Hygroscopic behavior of substrate-deposited particles studied by micro-FT-IR spectroscopy and complementary methods of particle analysis, Anal. Chem., 80, 633-642, 2008.

Lu, F., Jin, M. Z., and Belkin, M. A.: Tip-enhanced infrared nanospectroscopy via molecular expansion force detection, Nat. Photonics, 8, 307-312, 2014.

Max, J.-J., and Chapados, C.: Sucrose hydrates in aqueous solution by IR spectroscopy, J. Phys. Chem. A, 105, 10681-10688, 2001.

Miñambres, L., Sánchez, M. N., Castaño, F., and Basterretxea, F. J.: Hygroscopic properties of internally mixed particles of ammonium sulfate and succinic acid studied by infrared spectroscopy, J. Phys. Chem. A, 114, 6124-6130, 2010.

Weis, D. D., and Ewing, G. E.: Infrared spectroscopic signatures of $(NH_4)_2SO_4$ aerosols, J. Geophys. Res.: Atmos., 101, 18709-18720, 1996.

Weis, D. D., and Ewing, G. E.: The reaction of nitrogen dioxide with sea salt aerosol, J. Phys. Chem. A, 103, 4865-4873, 1999.